Innovative Frameworks for the Probabilistic Performance-Based Design of Inelastic Wind Excited Structures

by

Wei-Chu Chuang

A dissertation submitted in partial fulfillment
of the requirements for the degree of
Doctor of Philosophy
(Civil Engineering)
in the University of Michigan
2019

Doctoral Committee:

Assistant Professor Seymour M.J. Spence, Chair
Professor Seth Guikema
Associate Professor Ann Jeffers
Associate Professor Jason P. McCormick
Associate Professor Jeff Scruggs

Wei-Chu Chuang

wechuang@umich.edu

ORCID iD: 0000-0002-9147-2198

ACKNOWLEDGEMENTS

Over the past four years I have received a great deal of support and assistance. First, I would like to express my deepest appreciation to my advisor, Prof. Seymour Spence, for the patient guidance, motivation and support through each stage of the process. I have been extremely lucky to have an advisor who cared so much about my work, and who responded to my questions so promptly. His never ending enthusiasm and passion for research has inspired me to strive for excellence in every professional aspect. I would also like to thank my dissertation committee of Prof. Seth Guikema, Prof. Ann Jeffers, Prof. Jason McCormick, and Prof. Jeff Scruggs for their support and advice in completing this work.

The research presented in this dissertation was supported by the National Science Foundation (NSF) under Grant No. CMMI-1562388, CMMI-1462084 and the Magnusson Klemencic Associates (MKA) Foundation. This support is gratefully acknowledged.

To everyone in Prof. Spence's group, Arthriya, Zhicheng, Ahmed and Bowei, thank you for your support, advice and friendship. Thanks also to friends in CEE, Alyssa, Jason, Ning, Paul, Tung-Yu, Szu-Yun, Omar and Malcolm. I would also like to thank many friends I have made in Ann Arbor for providing much needed stress relief though dinners, game nights, exercising and traveling. Special thanks to Dian-Ru, Szu-Yun and Te-Yuh for being there whenever I needed a friend, and for making the journey much more pleasant.

Finally, I would like to thank my family. This journey would not have been possible without their unconditional love and support and for that I am extremely grateful.

TABLE OF CONTENTS

LIST OF TABLES

Table

LIST OF FIGURES

Figure

LIST OF APPENDICES

Appendix

ABSTRACT

Current prescriptive design provisions are moving towards performance-based design (PBD) approaches in which system-level probabilistic measures are used to explicitly describe performance. One of the key challenges in applying PBD in wind engineering is the evaluation of structural behavior over a full range of hazard levels, including extreme windstorms that could cause inelastic response. Despite the abundance of methods for inelastic response characterization of seismically excited systems, application of these methods to wind engineering is computationally challenging due to the extremely long duration of windstorms for which complex failure mechanisms can occur. The need to propagate uncertainties through the system in order to estimate the performance metrics further complicates the problem.

To address this situation, this research presents a performance-based wind engineering framework that integrates system-level collapse susceptibility models with non-collapse performance assessment frameworks. In particular, an efficient approach is proposed to rapidly estimate the inelastic behavior of wind excited systems based on the theory of dynamic shakedown. Safety against collapse susceptibility is then defined as the structure reaching the state of dynamic shakedown therefore ensuring safety against failure mechanisms such as low-cycle fatigue and/or incremental plastic collapse. To further account for failure due to excessive plastic deformations, a path-following algorithm is introduced for direct estimation of the residual displacements and plastic strains occurring at shakedown. The efficiency in estimating inelastic responses for any given wind load trace further allows simulation models to be directly applied for propagating uncertainty through the system and consequently estimating not only system-level reliability but also any other system-level performance metric

of interest. A full scale archetype building is then studied with the aim of understanding, as compared to conventional elastic design procedures, the possibility of designing wind excited buildings to have controlled plasticity at the ultimate load level.

Finally, in addition to this mechanics-based approach, alternative data-driven approaches are developed through applying advanced metamodeling techniques for estimating the dynamic responses of uncertain wind excited systems. The potential of this data-driven approach is investigated on a high-dimensional building system subject to stochastic wind excitation and system uncertainty.

CHAPTER I

Introduction

1.1 Overview

The current prescriptive design philosophy that relies simply on meeting requirements stipulated in standards is shifting towards a performance-based design (PBD) approach for achieving designs that rationally meet society's need for a truly safe built environment. While earthquake engineering has embraced these changes over the last few decades, the same cannot be said for wind engineering where design provisions have remained predominantly prescriptive. The development of performance-based wind engineering requires performance evaluation under various levels of wind hazards, including extreme windstorms that could cause excursions into the range of inelastic responses. To this end, the development of efficient methods for estimating the inelastic behavior of wind excited structures is investigated in this research. A brief overview of these areas is presented below.

1.1.1 Performance-based wind engineering

In the field of wind engineering, various frameworks based on the approach developed by the Pacific Earthquake Engineering Research Center (PEER) (*Federal Emergency Management Agency (FEMA)*, 2012a,b,c) for estimating performance in terms of probabilistic measures that are consistent with the needs of decision-makers have been proposed (*Ciampoli et al.*, 2011a; *Spence and Kareem*, 2014b). These works, however, have mainly focused on

the non-collapse performance assessment of certain specialized wind excited structures, such as tall buildings and long span bridges. Therefore, the next steps in applying performance-based design to wind engineering requires the development of methodologies that can model the behavior of general building systems subject to a full range of moderate to severe wind events and that can be integrated with probabilistic collapse models.

1.1.2 Inelastic behavior of wind excited structures

Current practice in designing wind excited structures is based on the assumption of linear elastic material at extreme loading levels. The lack of knowledge regarding the inelastic behavior of the structure has the potential to leave them exposed to undesirable post-yield behavior or possible collapse scenarios. In this respect, there has been increasing research efforts devoted to the problem of understanding and modeling the inelastic behavior of wind excited structures (*Vickery*, 1970; *Tamura et al.*, 2001; *Judd and Charney*, 2015; *Feng and Chen*, 2017, 2018). The main difficulty in developing an effective inelastic modeling procedure has been identified as: 1) the significant computational challenge associated with performing inelastic analysis over the long duration (order of hours) of typical windstorms; and 2) the general complexity of the inelastic response of wind excited systems that can involve phenomena such as low-cycle fatigue and ratcheting. In the application of modern probabilistic PBD, the need to propagate uncertainties through the system in order to estimate the performance metrics further complicates the problem. These challenges can only be overcome through the development of efficient approaches to rapidly provide a complete picture of the post-yield behavior of wind excited structures that can be integrated with general performance-based wind engineering frameworks.

1.2 Objectives

The primary goal of this research is to develop efficient frameworks, validated with conventional approaches, for estimating the inelastic behavior of wind excited building systems

within the setting of performance-based wind engineering. The major objectives are the following:

Objective I: A framework for the PBD of wind excited structures. Development of PBD methodologies for the assessment of the main wind force resisting system and non-structural components of multi-story buildings subject to a full range of wind intensities (from serviceability to collapse). In particular, the possibility of integrating efficient methods for estimating collapse susceptibility in the framework will be explored, as will methods that take into account both collapse and non-collapse losses.

Objective II: An efficient approach for estimating inelastic behavior of wind excited structures. The objective is to develop computationally tractable methods to rapidly estimate the inelastic behaviors of both steel and reinforced concrete structures subject to wind excitations based on the theory of plasticity. In particular, methods based on the theory of dynamic shakedown will be explored. Both concentrated plasticity and distributed plasticity models will be considered in modeling inelasticity. The efficiency and accuracy of this approach will be investigated through comparison with traditional direct integration methods.

Objective III: A probabilistic system-level collapse susceptibility estimation framework. Development of a simulation-based framework for estimating the system-level probability of collapse susceptibility based on the efficient methods developed in Objective II with a general description of failure including both local and global limit states. The possibility of using the framework to identify critical windstorms will also be explored.

Objective IV: Reliability of inelastic wind excited structures. The system and member reliabilities of an archetype structure designed in accordance with current code requirements will be estimated in terms of system-level inelastic limit states. This will provide insight into both the plastic reserves of current code compliant designs as

well as the potential of designing wind excited structures to satisfy inelastic system-level limit states at life safety. Furthermore, to address the computational limits of Monte Carlo methods, the possibility of integrating conditional simulation schemes for estimating the reliability of the system will be explored.

Objective V: Alternative approaches for nonlinear analysis of wind excited systems. Data-driven methods will be introduced as an alternative approach for estimating the dynamic responses of non-linear wind excited structures using metamodeling techniques. Methods will be introduced that can handle both stochastic excitations as well as parameter uncertainty.

1.3 Structure of the Dissertation

A brief description of each of the eight following chapters of the dissertation is provided below.

Chapter II: A performance-based design framework for the integrated collapse and non-collapse assessment of wind excited buildings. This chapter presents a simulation-based framework for multistory wind excited buildings that rigorously integrates system-level estimates of both collapse and non-collapse losses. In particular, it is proposed to use the theory of dynamic shakedown as an efficient means for describing the collapse probability of the main wind force resisting system. A full-scale case study is presented to illustrate the practicality and potential of the proposed framework.

Chapter III: A New Class of Shakedown Algorithms. An approach that enables the estimation of plastic strains and deformations together with the state of dynamic shakedown is introduced. In modeling the inelasticity, the dynamic shakedown framework is developed for both concentrated and distributed plasticity model.

Chapter IV: A Probabilistic Dynamic Shakedown Framework for Stochastic Ex-

citations. This chapter addresses the challenge inherent to modeling the long duration inelastic response of wind-excited systems through the development of a simulation framework based on the strain-driven dynamic shakedown models outlined in Chapter III. To model the record-to-record variability in simulating wind loads, stochastic wind load models are introduced.

Chapter V: Verification and Examples. The accuracy and applicability of the approach presented in Chapter III for estimating inelastic responses of wind excited systems is discussed through case studies formulated with concentrated and distributed plasticity. Applications of the simulation framework proposed in Chapter IV are also be illustrated.

Chapter VI: A Full Scale Case Study. This chapter presents a full scale three-dimensional case study for the illustration of the probabilistic dynamic shakedown framework of Chapter IV.

Chapter VII: Extension to Uncertain Systems and Reliability Analysis. In this chapter, a reliability assessment framework is developed based on the dynamic shakedown models for the estimation of both component and system-level reliabilities while considering uncertainties in both the system and wind loads. In particular, to efficiently estimate reliability associated with small failure probabilities, a conditional simulation scheme is integrated into the framework. Component reliabilities are evaluated with failure defined as the occurrence of inelasticity, which is consistent with current code requirements, while system reliability is determined through the proposed shakedown framework with general local and global limit states. Differences between the component and system reliabilities are discussed to better understand the strength reserves of systems designed to classic elastic limit states.

Chapter VIII: Rapid uncertainty quantification for non-linear and stochastic wind excited structures: a metamodeling approach. This chapter investi-

gates the possibility of using advanced metamodeling techniques in order to define a computationally tractable approach for propagating uncertainty through a class of multi-degree-of-freedom non-linear dynamic systems subject to multivariate stochastic wind excitation. To this end, a scheme is introduced that is based on combining model order reduction with a recently introduced metamodeling approach that has been seen to be particularly effective in describing the dynamic response of uncertain non-linear systems of low dimensions.

Chapter IX: Summary and Conclusions. Key findings and contributions of the proposed research are summarized.

1.4 Publications from this Dissertation

To date, three journal papers have been published from the work of this dissertation with another under review and a fifth in preparation. In particular, the work outlined in Chapter II has been published in a separate journal paper while the work of Chapter III to Chapter V has resulted in one journal paper published and another submitted for possible publication. Concerning the work of Chapter VI and Chapter VII, a journal paper is in preparation and will soon be submitted for possible publication. Finally, the work outlined in Chapter VIII has already been published. The following is a list of published papers:

Chuang, W.C., Spence, S.M.J. A performance-based design framework for the integrated collapse and non-collapse assessment of wind excited buildings. *Engineering Structures* 2017;150:746-758.

Chuang, W.C., Spence, S.M.J. An efficient framework for the inelastic performance assessment of structural systems subject to stochastic wind loads. *Engineering Structures* 2019;179:92-105.

Chuang, W.C., Spence, S.M.J. Probabilistic performance assessment of inelastic wind-

excited structures within the setting of distributed plasticity. *Structural Safety* Submitted.

Chuang, W.C., Spence, S.M.J. Rapid uncertainty quantification for non-linear and stochastic wind excited structures: a metamodeling approach. *Meccanica* 2019; https://doi.org/10.1007/s11012-019-00958-9

CHAPTER II

A Performance-based Design Framework for the Integrated Collapse and Non-collapse Assessment of Wind Excited Buildings

2.1 Overview

This chapter begins with an overview of the background and literature relevant to the development of the performance-based wind engineering and is followed by the presentation of a simulation-based PBD framework for estimating both system-level collapse and non-collapse losses of multistory wind excited buildings. A full scale case study is also presented to illustrate the practicality and potential of the proposed framework.

2.2 Literature Review

In traditional prescriptive provisions for seismic design, the concept of performance is implicitly considered through defining sets of rules that aim at achieving specific performance levels, such as collapse prevention or life safety. However, the significant economic losses from earthquake events, such as the 1989 Loma Prieta and 1994 Northridge earthquakes, has proved that in general implicit approaches are not reliable in ensuring the satisfaction of predetermined sets of performance levels (*Whittaker et al.*, 2003). As a consequence, a first

generation of performance-based seismic design (PBSD) methodologies were developed and introduced in the 1990s (*Federal Emergency Management Agency (FEMA)*, 1996; *Structural Engineers Association of California (SEAOC)*, 1996; *Applied Technology Council (ATC)*, 1996a,b). Notwithstanding how these procedures represent milestones in the development of PBSD, several shortcomings were identified which led to the development of what is commonly refereed to as second generation PBSD (*Moehle and Deierlein*, 2004; *Yang et al.*, 2009) and in particular, the publication by the Federal Emergency Management Agency (FEMA) of the P-58 volumes (*Federal Emergency Management Agency (FEMA)*, 2012a,b,c). These documents outline a general methodology that not only accounts for the inevitable uncertainty in accurately predicting the response of building systems subject to severe earthquakes, but also communicates performance through system-level measures that are easily understood by decision-makers and/or stakeholders, e.g. expected repair time and cost. In addition to these measures of direct economic losses, a more detailed downtime assessment methodology was recently proposed in the Resiliency-based Earthquake Design initiative (REDi) guidelines (*Almufti and Willford*, 2013). In these guidelines, aspects such as impeding factors and utility disruption are explicitly considered in the calculation of downtime.

While the framework outlined in the P-58 volumes–and more in general the model proposed by the Pacific Earthquake Engineering Research (PEER) center (*Moehle and Deierlein*, 2004; *Yang et al.*, 2009)–was developed for buildings subject to earthquake excitation, it is a relatively general procedure that can in theory be extended to other natural hazards such as wind. In this respect, several research efforts have been conducted over the past few years (*Ciampoli et al.*, 2011a; *Petrini and Ciampoli*, 2012; *Spence and Gioffrè*, 2012; *Bernardini et al.*, 2013; *Seo and Caracoglia*, 2013; *Caracoglia*, 2014; *Bobby et al.*, 2014; *Spence and Kareem*, 2014b; *Bernardini et al.*, 2015; *Larsen et al.*, 2016). These works have mainly focused on the performance assessment of specialized wind excited structures such as tall buildings and long span bridges. As outlined in *Larsen et al.* (2016), the next steps in applying performance-based design to wind engineering requires the continued development of these–

or similar–methodologies with the ultimate aim of defining general performance-based wind engineering (PBWE) frameworks that can model the behavior of systems subject to a full range of moderate to severe wind events.

To develop such a framework, models that estimate the performance in terms of probabilistic system-level losses, such as expected repair time and costs for a wide range of building systems, are necessary. In particular, the possibility of allowing the system to enter an inelastic response regime needs to be taken into consideration in order to avoid leaving the system exposed to undesirable post-yield behavior and possible collapse. In this respect, various contributions have been made towards better understanding how wind excited system respond inelastically to wind (*Vickery*, 1970; *Wyatt and May*, 1971; *Tsujita et al.*, 1998; *Ohkuma et al.*, 1998; *Chen and Davenport*, 2000; *Tamura et al.*, 2001; *Gani and Légeron*, 2011; *Judd and Charney*, 2015; *Feng et al.*, 2016; *Larsen et al.*, 2016). In particular, the computational challenge of estimating the nonlinear response has been identified as a major issue as, in a nonlinear response regime, the complete duration of the event must be considered if meaningful results are to be obtained. Because of the long duration of typical wind events (in the order of several hours), the possibility of applying robust numerical methods that require direct integration of the non-linear dynamic equations of motion over the entire duration of the storm, such as incremental dynamic analysis (IDA) (*Vamvatsikos and Cornell*, 2002), is lost. This is especially true if the probability of inelastic response, and ultimately collapse, is desired (which is necessary if frameworks such as the P-58 are to be developed for wind excited systems). Notwithstanding these issues, a number of studies have been carried out over the years using direct integration methods with the aim of better understading the inelastic behavior of wind excited systems *Vickery* (1970); *Tamura et al.* (2001); *Hong* (2004); *Judd and Charney* (2015); *Feng and Chen* (2017, 2018). These studies have provided insight into the inelastic failure mechanisms affecting wind excited structures, e.g. ratcheting in the alongwind direction and low cycle fatigue in the acrosswind direction.

In alternative to direct integration, methods have recently been proposed based on nonlin-

ear static pushover analysis (*Huang et al.*, 2015). While providing significant computational gains over direct integration, these methods are affected by the inherent difficulty of nonlinear static pushover analysis to capture cumulative damage mechanisms, e.g. ratcheting and low cycle fatigue (*Krawinkler and Seneviratna*, 1998; *Antoniou and Pinho*, 2004). This has led to the recent development of a computationally efficient approach for determining safety of wind excited systems against these inelastic failure mechanisms (*Tabbuso et al.*, 2016). This approach is based on applying the theory of dynamic shakedown (*Ceradini*, 1969; *Corradi and Maier*, 1974; *Ceradini*, 1980; *Polizzotto*, 1984; *Polizzotto et al.*, 1993) as a means to rapidly provide a complete picture of the inelastic structural behavior, from incremental plastic collapse to low cycle fatigue. Based on the extension of the classic Bleich-Melan and Koiter shakedown theorems (*Koiter*, 1960) to dynamic excitation, this approach was developed to determine if an elastoplastic structure subject to a given dynamic load history will eventually respond elastically after a finite amount of plastic deformation. While theoretical frameworks for dynamic shakedown of systems subject to excitation of finite duration have been proposed (*Polizzotto*, 1984; *Polizzotto et al.*, 1993), a special case that significantly facilitates the determination of the state of dynamic shakedown exists when the external loads can be considered of infinite duration and periodic. This special case is at the basis of the approaches outlined in *Tabbuso et al.* (2016) where the finite duration of real dynamic wind loads was considered by simply repeating indefinitely the windstorm of interest. In particular, if the yield domains of the structure are modeled as piece-wise linear, the limit state that separates plastic collapse from the safe state of dynamic shakedown can be efficiently identified through solving a linear programming problem (LPP) for each dynamic wind load trace of interest (*Tabbuso et al.*, 2016).

2.3 Performance-based Wind Engineering: Problem Setting

The PBWE framework that will be developed in this chapter will be based on the PBSD framework recently proposed by the FEMA (*Federal Emergency Management Agency*

(FEMA), 2012a). Within this framework, the performance of the system is measured in terms of the mean annual exceedance rates of decision variable thresholds (dv) that correspond to limiting values of measures such as repair costs and time. In particular, these rates are estimated by solving the following probabilistic integral (*Moehle and Deierlein*, 2004):

$$\lambda(dv) = \iiint G(dv|dm) \cdot \ |dG(dm|edp)| \cdot |dG(edp|im)| \cdot |d\lambda(im)| \tag{2.1}$$

where $G(a|b)$ is the complementary cumulative distribution function (CCDF) of A conditional on B (where the common convention of using capital letters to indicate random variables and lower case letters their realizations has been used); DM is the damage measure indicating the state of damage of structural and/or non-structural components; EDP is the engineering demand parameter, i.e. the structural response responsible for causing damage; and IM is the measure of the intensity of the event. By assuming that the various conditional probabilities in Eq. (2.1) are independent, each component of the equation can be obtained through separate analyses (sub-blocks), namely, hazard analysis providing the hazard curve $\lambda(im)$, structural analysis giving $G(edp|im)$ and damage and loss analysis giving $G(dm|edp)$ and $G(dv|dm)$ respectively.

In the case of wind engineering, an additional step is generally introduced to account for interaction of the structure with its wind environment (*Ciampoli et al.*, 2011a; *Petrini and Ciampoli*, 2012):

$$\lambda(dv) = \iiiint G(dv|dm) \cdot |dG(dm|edp)| \cdot |dG(edp|ip)| \cdot |dG(ip|im)| \cdot |d\lambda(im)| \tag{2.2}$$

where IP represents a set of interaction parameters (i.e. the aerodynamic loads acting on the structure).

In this chapter, instead of considering the mean annual rates of exceedance of the thresholds dv, structural performances will be measured in terms of the annual exceedance probability of the thresholds, P_f, as this measure is more commonly used in wind engineering.

Thus, Eq. (2.2) is rewritten in the following form:

$$P_f(dv) = \iiint G(dv|dm) \cdot |dG(dm|edp)| \cdot |dG(edp|ip)| \cdot |dG(ip|im)| \cdot p(im) \cdot dim \quad (2.3)$$

where $p(im)$ is the probability density function of the annual largest values of IM.

As in the case of the FEMA P-58 seismic framework, in this work Eq. (2.3) is used for estimating the performances of buildings that are repairable, i.e. for buildings that are not susceptible to collapse during the wind event. To separate collapse susceptibility from non-collapse susceptibility, a model based on dynamic shakedown theory will be developed. In particular, since collapse and non-collapse susceptibility are mutually exclusively events, the probability of the DV exceeding a threshold, dv, considering both scenarios can be expressed through the total probability theorem as:

$$P(DV > dv) = P(DV > dv|NC)P(NC) + P(DV > dv|C)P(C) \quad (2.4)$$

where $P(C)$ is the probability of collapse susceptibility, $P(NC)$ the complement of $P(C)$ (i.e. the probability non-collapse susceptibility), $P(DV > dv|NC)$ is the annual exceedance probability of dv given that the building is not susceptible to collapse, while $P(DV > dv|C)$ is the annual exceedance probability of dv given that the building is susceptible to collapse during the event. In this work, $P(NC)$ will be estimated through dynamic shakedown while $P(DV > dv|NC)$ will be estimated through solving Eq. (2.3). In particular, $P(DV > dv|C)$ is a probabilistic distribution representing the building performances if replacement is required, that is:

$$P(DV > dv|C) = G_C(DV) \quad (2.5)$$

where $G_C(DV)$ is the total losses if the MWFRS are susceptible to collapse, e.g. the total replacement cost if the decision variable is financial loss or the total replacement time if downtime is the decision variable.

In order to solve the above equation, models for each sub-analysis step will be proposed in the following section. Furthermore, a general simulation strategy for assessing the performance measures such as repair costs and downtime of the structure will also be presented in Section 2.4.3.

2.4 PBWE Framework

2.4.1 Non-collapse assessment

This section presents appropriate models for carrying out the sub-analyses for solving the non-collapse susceptibility problem of Eq. (2.3).

2.4.1.1 Wind hazard analysis

The first step towards performance assessment is identifying the intensity of the wind event to be considered. Unlike seismic engineering where probabilistic site-specific hazard curves are well-established, wind hazard curves are not explicitly defined. An appropriate intensity measure, IM, that is often used to describe the intensity of an extreme wind event, is the maximum wind speed to occur during the event at a height of interest z (e.g. building or eave height) averaged over a fixed time interval T (e.g. an hour). In general, meteorological data is collected at weather stations in the form of wind speeds v averaged over a period τ at a site characterized by a roughness length z_{01} and height H_{met}. In order to extrapolate this data to site-specific intensity measures IM, a probabilistic transformation, such as the following, is necessary (*Minciarelli et al.*, 2001):

$$im = \bar{v}_z(T, z_0) = e_7 e_3 \left(\frac{e_5 z_0}{e_6 z_{01}}\right)^{e_4 \cdot 0.0706} \cdot \frac{\ln[\frac{z}{e_5 z_0}]}{\ln[\frac{H_{met}}{e_6 z_{01}}]} e_1 e_2 v(\tau, H_{met}, z_{01}) \tag{2.6}$$

where e_1 and e_2 are random variables modeling sampling and observation errors in the wind speed data set v, e_3 is a random variable accounting for the uncertainty involved in converting the time interval τ to T, e_4 is a random variable associated with the uncertainty

Table 2.1: Probabilistic descriptions of the components of $\mathbf{U}_{IM}$.

Basic variables	Mean	Standard deviation	Coefficient of variation	Type of distribution	Reference
E_1	1.0	0.10	0.10	Normal	—
E_2	1.0	0.025	0.025	Normal	(*Minciarelli et al.*, 2001)
E_3	[a]	—	0.05	Normal	(*Diniz et al.*, 2004a)
E_4	1.0	0.10	0.10	Truncated Normal	(*Diniz et al.*, 2004a)
E_5	1.0	0.30	0.30	Truncated Normal	(*Diniz et al.*, 2004a)
E_6	1.0	0.30	0.30	Truncated Normal	(*Diniz et al.*, 2004a)
E_7	1.0	0.05	0.05	Normal	(*Minciarelli et al.*, 2001)

[a] Depends on averaging times τ and T.

in the empirical constant 0.0706, e_5 and e_6 are respectively random variables modeling the uncertainties in the roughness lengths z_0 and z_{01}, while e_7 is an uncertainty factor characterizing the epistemic model uncertainties when extreme wind events such as hurricanes and tornadoes are considered in place of straight winds (*Minciarelli et al.*, 2001). In the following, the random variables $e_1 \dots e_7$ are collected in vector $\mathbf{U}_{IM} = \{E_1 \dots E_7\}^T$. A possible probabilistic description of the components of $\mathbf{U}_{IM}$ is summarized in Table 2.1.

2.4.1.2 Aerodynamic analysis

After identifying the intensity of the wind event, aerodynamic loads, $\mathbf{F}$, acting on the structure need to be determined before the EDPs can be estimated through structural analysis. These loads, defined as the interaction parameters (IP), can be obtained from specific wind tunnel tests or associated databases, computational fluid dynamics or quasi-steady models, which will be discussed in Section 4.4. In general, the interaction parameters will depend on a vector of uncertain model parameters, $\mathbf{U}_{IP}$, as well as the intensity of the wind event $\bar{v}_z$:

$$\mathbf{ip} = \mathbf{F}(t; \bar{v}_z, \mathbf{u}_{IP}) \tag{2.7}$$

2.4.1.3 Structural analysis

The damage models for assessing the system-level building performance developed in this chapter are driven by a vector of EDPs defined by structural responses such as displacements

$\mathbf{u}$, velocities $\dot{\mathbf{u}}$ and accelerations $\ddot{\mathbf{u}}$. In particular, the EDPs are taken as the maximum responses to occur over the duration, T, of the wind event:

$$\mathbf{edp} = \max_{0 \leqslant t \leqslant T} \mathbf{R}(t; \mathbf{F}, \mathbf{u}_{EDP}) \tag{2.8}$$

where $\mathbf{R}(t; \mathbf{F}, \mathbf{u}_{EDP})$ is the vector collecting the response processes of interest while $\mathbf{U}_{EDP}$ is a vector containing the uncertain parameters associated with estimating the structural responses (e.g. the modal damping ratios or Young's modulus). In particular, the vector $\mathbf{R}$ can be formally defined as:

$$\mathbf{R}(t; \mathbf{F}, \mathbf{u}_{EDP}) = \mathbf{\Lambda}\tilde{\mathbf{u}} \tag{2.9}$$

where $\mathbf{\Lambda}$ is an indicator matrix extracting the responses, including combinations (e.g. inter-story drifts), from the augmented response vector $\tilde{\mathbf{u}} = \{\ddot{\mathbf{u}}, \dot{\mathbf{u}}, \mathbf{u}\}^T$ where $\mathbf{u}$, $\dot{\mathbf{u}}$ and $\ddot{\mathbf{u}}$ are the displacement, velocity and acceleration responses of the system. In particular, in order to determine the dynamic response of the structure, a floor-wise lumped mass model can in general be used. Under these conditions, while considering only the degrees-of-freedom (DOFs) of interest (e.g. the horizontal responses of the floors), the equations of motion can be expressed through static condensation as:

$$\begin{bmatrix} \mathbf{M}_{tt} & \mathbf{0} \\ \mathbf{0} & \mathbf{0} \end{bmatrix} \begin{bmatrix} \ddot{\mathbf{u}}_{\mathbf{t}}(t) \\ \ddot{\mathbf{u}}_{\mathbf{r}}(t) \end{bmatrix} + \begin{bmatrix} \mathbf{C}_{tt} & \mathbf{0} \\ \mathbf{0} & \mathbf{0} \end{bmatrix} \begin{bmatrix} \dot{\mathbf{u}}_{\mathbf{t}}(t) \\ \dot{\mathbf{u}}_{\mathbf{r}}(t) \end{bmatrix} + \begin{bmatrix} \mathbf{K}_{tt} & \mathbf{K}_{tr} \\ \mathbf{K}_{rt} & \mathbf{K}_{rr} \end{bmatrix} \begin{bmatrix} \mathbf{u}_t(t) \\ \mathbf{u}_r(t) \end{bmatrix} = \begin{bmatrix} \mathbf{F}(t) \\ \mathbf{0} \end{bmatrix} \tag{2.10}$$

where $\mathbf{u}_t(t)$ and $\mathbf{u}_r(t)$ are the vectors of the dynamically significant and secondary DOFs respectively; $\mathbf{C}_{tt}$ is the damping matrix associated with the dynamic DOFs; $\mathbf{K}_{tt}$, $\mathbf{K}_{tr}$, $\mathbf{K}_{rt}$ and $\mathbf{K}_{rr}$ are the stiffness submatrices obtained from the partitioning of the complete stiffness matrix $\mathbf{K}$; $\mathbf{M}_{tt}$ is the lumped mass matrix acting at the dynamic DOFs; and $\mathbf{F}(t)$ is the stochastic forcing function generated through the aerodynamic analysis of Section 2.4.1.2.

From the first row of Eq. (2.10), the following differential equation can be derived:

$$\mathbf{M}_{tt}\ddot{\mathbf{u}}_{\mathbf{t}}(t) + \mathbf{C}_{tt}\dot{\mathbf{u}}_{\mathbf{t}}(t) + \bar{\mathbf{K}}\mathbf{u}_t(t) = \mathbf{F}(t) \tag{2.11}$$

where $\bar{\mathbf{K}} = \mathbf{K}_{tt} - \mathbf{K}_{tr}\mathbf{K}_{tt}^{-1}\mathbf{K}_{rt}$ is the condensed stiffness matrix. The dynamic displacements, velocities and accelerations, can then be efficiently estimated through a modal analysis as:

$$\begin{cases} \mathbf{u}_t(t) = \mathbf{\Phi}_m \mathbf{q}_m(t) \\ \dot{\mathbf{u}}_t(t) = \mathbf{\Phi}_m \dot{\mathbf{q}}_m(t) \\ \ddot{\mathbf{u}}_t(t) = \mathbf{\Phi}_m \ddot{\mathbf{q}}_m(t) \end{cases} \tag{2.12}$$

where $\mathbf{\Phi}_m = [\boldsymbol{\phi}_1, \ldots, \boldsymbol{\phi}_m]$ is the mode shape matrix of order m calculated from the stiffness and mass matrix of the condensed system through solving the following eigenvalue problem:

$$\left(\bar{\mathbf{K}} - \omega_i^2 \mathbf{M}_{tt}\right) \boldsymbol{\phi}_i = 0 \tag{2.13}$$

where ω_i is the natural circular frequency of the ith mode, while $\mathbf{q}_m(t) = \{q_1(t), \ldots, q_m(t)\}^T$, $\dot{\mathbf{q}}_m(t) = \{q_1(t), \ldots, q_m(t)\}^T$, and $\ddot{\mathbf{q}}_m(t) = \{q_1(t), \ldots, q_m(t)\}^T$ are the vectors of the first m modal displacement, velocity and acceleration responses. In particular, the ith component of the modal response vectors can be determined by solving the following modal equation:

$$\ddot{q}_i(t) + 2\xi_i\omega_i\dot{q}_i(t) + \omega_i^2 q_i(t) = \boldsymbol{\phi}_i^T \mathbf{F}(t; \bar{v}_H, \mathbf{u}_F) \tag{2.14}$$

where ξ_i is the ith modal damping ratio.

To account for the uncertainties involved in the structural model and material properties, the modal damping ratios, ξ_i and Young's modulus, e_y, can be taken as random variables, as can any other parameter used in defining the structural model. For instance, in this work, in addition to the above mentioned parameters, a random variable ΔM is introduced to model

the uncertainty in the mass matrix. The aforementioned random variables are collected in vector $\mathbf{U}_{EDP} = \{\xi_1, \ldots, \xi_m, \Delta_M, E_y\}^T$.

2.4.1.4 Damage analysis

In general, a building system will have a large number of repeated components (e.g. windows, partition walls, ceiling elements, etc.). These groups of common elements have the same susceptibility to damage and consequences, and can therefore be grouped together to form what are commonly referred to as Fragility Groups (FGs). For each FG, a series of discrete damage states (DS_i for $i = 1, ...$) are generally identified and associated with appropriate fragility functions that formally represent the probability of exceeding each damage state DS_i given a demand level edp, or:

$$\text{Fragility}_{DS_i}(edp) = \text{Prob}(DS_i|edp) \tag{2.15}$$

Because in general, more than one component of a FG will be subject to the same demand, a number of FG subsets can be defined. These subsets are termed performance groups (PGs) and can be associated with one demand parameter or EDP. In particular, the possibility of correlation (or lack of) between damage occurrences can be assessed for the components of any given PG. In practice, once a demand (i.e. an EDP) value is obtained from the structural analysis, e.g. $EDP = EDP^*$, damage analysis is performed by entering into a suite of fragility functions at EDP^* (as illustrated in Figure 2.1) and considering as an ordinate the value assumed by a sample of a uniformly distributed random number in $[0, 1]$. As discussed in (*Yang et al.*, 2009; *Federal Emergency Management Agency (FEMA)*, 2012a), the value assumed by the sample can be used to identify which damage state has occurred.

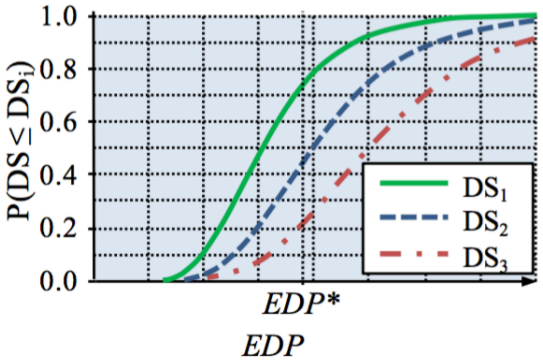

Figure 2.1: Example of fragility functions for a component with 3 possible damage states, DS_1, DS_2 and DS_3 (adapted from FEMA (2012a)).

2.4.1.5 Loss assessment

The approach adopted in this work for assessing losses is based on the framework proposed by FEMA (*Federal Emergency Management Agency (FEMA)*, 2012a). Accordingly, in order to translate the damage states identified through the fragility analysis outlined in Section 2.4.1.4 to losses, a unique set of consequence functions are defined. In particular, each fragility function is associated with a consequence function that translates the damage state described by the fragility function into a numerical value of the consequence, e.g. dollars for repair cost or number of days for repair time.

For the framework developed in this work, losses are restricted to estimated repair cost and time. However, the procedure is general and can be extended to other relevant loss measures, such as condition tagging or casualties.

Repair cost

Following the framework outlined above, for repair cost estimation, the consequence functions take the form of unit repair cost functions (i.e. functions that estimate, for example, the cost to repair a given damage state per square meter of partition wall, or the the cost to repair a single window subject to a given damage state (*Federal Emergency Management Agency (FEMA)*, 2012a)). In particular, the unit repair cost functions are described by the

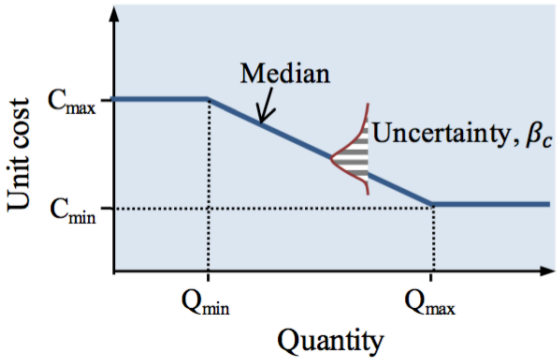

Figure 2.2: Example of a possible consequence function (adapted from FEMA (2012a)).

following parameters: maximum and minimum unit costs, associated maximum and minimum quantities, as well as dispersion parameters describing the uncertainty in translating damage into repair costs. An example of a unit repair cost function is shown in Figure 2.2. In particular, the reduction in unit repair costs as the quantity goes up (i.e. number of elements that require repair) models the economies of scale. In general, together with the dispersion parameter, a possible distribution is also indicated, for example log-normal.

In this work, once the number, N_{DS_i}, of elements in a given damage state (DS_i) are identified for a given PG, the repair cost for those elements can be estimated by sampling from the probability density function of the corresponding consequence function (at the ordinate N_{DS_i}) and then multiplying by the N_{DS_i}. Following this scheme, the total repair cost can be evaluated by aggregating over all damage states and performance groups.

Downtime

In addition to the direct financial losses, buildings are generally also vulnerable to indirect economic losses due to downtime, defined as the time required to achieve a recovery state such as, re-occupancy, functional recovery, or full recovery, after a wind event (*Bonowitz*, 2011). In this work, a downtime assessment model based on integrating the recently proposed methodology outlined in the REDi guidelines (*Almufti and Willford*, 2013) with that proposed in *Federal Emergency Management Agency (FEMA)* (2012a) will be developed.

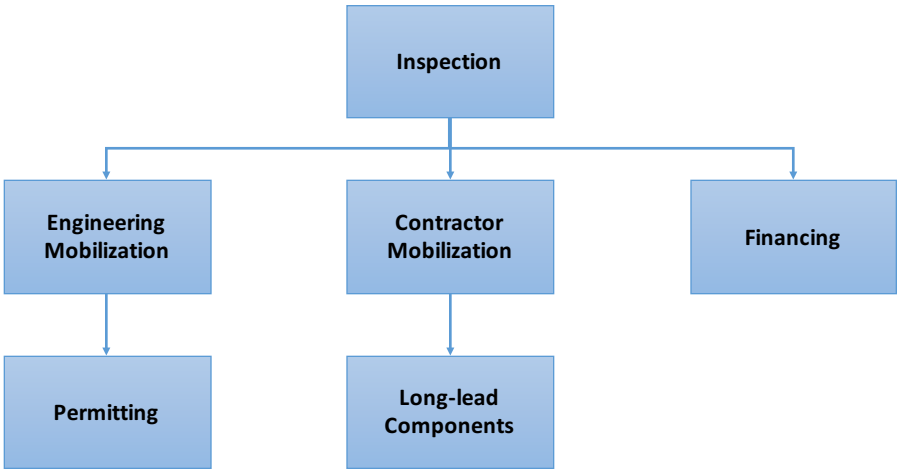

Figure 2.3: Sequences of delays due to impeding factors.

In assessing downtime, impeding factors that delay the initiation of repairs required to achieve a certain recovery state must be identified and included in the downtime estimate. As illustrated in Figure 2.3, some impeding factors occur in series while others occur simultaneously. In particular, after inspection the sequence producing the greatest delay among: (1) engineering mobilization and permitting; (2) contractor mobilizations; and (3) financing, must be used in calculating downtime. Furthermore, long-lead times due to the unavailability of certain building components will in general occur, therefore hindering the repair of the corresponding component. As illustrated in Figure 2.3, this source of potential delay should be included at the end of the contractor mobilization phase.

In order to estimate total repair time, delays due to impeding factors must then be added to repair work times (i.e. the time that workers require to carry out the repairs). To estimates these last, two extreme cases are considered in this work. In the first case, repair work is assumed to be carried out in series, i.e. repair for one component has to be finished before work on another can start. This will provide an upper bound on the repair time as in general some work can be carried out in parallel. In the second case, all repair work is assumed to be carried out simultaneously. This will provide a lower bound on the repair work time as, in general, some repair work will inevitably require the repair of certain elements before it can commence. The actual time required for the repair work will be somewhere between

the upper and lower bounds. To estimate these bounds, a model similar to that proposed in *Federal Emergency Management Agency (FEMA)* (2012a) is considered. Therefore, the time necessary for a single worker to repair the damage states described by the fragility functions is estimated through unit consequence functions. In particular, each consequence function is described by the following parameters: a maximum and minimum repair time; associated upper and lower quantities; as well as a dispersion parameter modeling the uncertainty in the repair time. The maximum and minimum repair times mentioned above, are associated with the increased efficiency that is likely to occur if multiple components in the same damage state are repaired. It should be observed that, because it is assumed that only a single worker is available, the repair work time can be reduced proportionally if multiple workers are considered.

Utility disruption is also considered in estimating downtime to full or functional recovery. In particular, for wind storms, only disruption to the electrical systems is considered. Finally, the overall downtime is estimated as:

$$\text{Downtime} = \text{Max}\{\text{utility disruption}, \text{impeding factors}\} + \text{repair work} \tag{2.16}$$

2.4.2 Collapse assessment

Section 2.4.1 outlined a procedure for assessing the performance of building systems that are not susceptible to collapse during the wind event. In order to determine whether a building is susceptible to collapse or not, a definition of collapse susceptibility must be given. This can range from the instability of a numerical model of the structural system, to the exceedence of a predetermined deformation limit. As already mentioned, the difficulty of estimating collapse susceptibility in the case of wind excited systems lies in treating the long duration of typical wind events (order of hours), which creates both computational as well as theoretical challenges (i.e. collapse could occur due not only to incremental plasticity but also phenomena such as low cycle fatigue). To overcome this, in this work it is proposed to

define collapse susceptibility of the MWFRS, as the failure of the system to achieve "dynamic shakedown", where "dynamic shakedown" is defined as a state in which plastic deformation is produced only during a first phase of finite duration whilst the whole subsequent phase is purely elastic (*Ceradini*, 1980; *Polizzotto*, 1984; *Polizzotto et al.*, 1993; *Tabbuso et al.*, 2016). This state not only precludes the occurrence of incremental plastic collapse but also low cycle fatigue, and would therefore seem well adapt for defining the separation between a safe inelastic state and collapse in the case of wind excited systems.

2.4.2.1 Dynamic shakedown: classic solution

In order to introduce how the state of dynamic shakedown is estimated, consider an elastoplastic structure with the vectors $\mathbf{q}(t)$ and $\mathbf{Q}(t)$ collecting the time varying generalized strains and stresses induced by the external wind loads $\mathbf{F}(t)$. Equilibrium and geometric compatibility can then be expressed in terms of $\mathbf{q}(t)$ and $\mathbf{Q}(t)$ as:

$$\mathbf{B}^T\mathbf{Q}(t) = \mathbf{F}(t) - \mathbf{M}_{tt}\ddot{\mathbf{u}}_t(t) - \mathbf{C}_{tt}\dot{\mathbf{u}}_t(t) \tag{2.17}$$

$$\mathbf{q}(t) = \mathbf{B}\mathbf{u}_t(t) \tag{2.18}$$

where $\mathbf{B}$ is the strain-displacement (compatibility) matrix that depends on the undeformed geometry of the system. The strain matrix $\mathbf{q}(t)$ is defined as the sum of an elastic, $\mathbf{e}(t)$, and a plastic, $\mathbf{p}(t)$, strain. The elasticity equations for this system can be expressed as:

$$\mathbf{Q}(t) = \mathbf{D}\mathbf{e}(t) + \mathbf{Q}^*(t) \tag{2.19}$$

where $\mathbf{D}$ is the block diagonal matrix collecting the elastic stiffness matrices of each element while $\mathbf{Q}^*$ is a vector of the perfectly clamped element generalized stresses.

In order to satisfy the yield criterion, the generalized stresses, i.e. the internal forces, at each cross section cannot lie outside the yield surface. This implies that the following must

hold:

$$\mathbf{f} = \mathbf{N}^T \mathbf{Q}(t) - \mathbf{R} \leq \mathbf{0} \tag{2.20}$$

where $\mathbf{f}$ is a piece-wise linearized yield vector, $\mathbf{N}$ is the block diagonal matrix of unit external normals to the yield surface while $\mathbf{R}$ is a plastic resistance vector that depends on the yield stress, σ_y, of the material. To account for possible uncertainty in the material strength, σ_y can be taken as uncertain. Under these circumstances, σ_y would be a component of the uncertain vector $\mathbf{U}_{sh}$ that collects uncertain parameters associated with the dynamic shakedown analysis.

A necessary and sufficient condition for dynamic shakedown (*Ceradini*, 1980; *Polizzotto*, 1984) to occur is that there exists a finite time $r \geq 0$ such that the sum of a free motion stress field $\mathbf{Q}^F(t)$, a time independent self-stress distribution $\boldsymbol{\rho}$ representing the initial plastic strains along with the elastic stress response to the loads backward truncated at r, $\mathbf{Q}^E(r+\tau)$, proves to be inside the yield surface at any time $\tau \geq 0$:

$$\mathbf{f} = \mathbf{N}^T[\mathbf{Q}^E(r+\tau) + \mathbf{Q}^F(\tau) + \boldsymbol{\rho}] - \mathbf{R} < \mathbf{0}, \quad \forall \tau \geq 0 \tag{2.21}$$

In order to estimate the safety factor against inadaptation (i.e. non-shakedown) of the structure, a scalar multiplier $s > 0$ of the forcing function is introduced so that the following scaled loads can be defined $\mathbf{F}_s(t) = s\mathbf{F}(t)$. For this time dependent loading system, the shakedown safety factor is defined as the threshold value s, indicated by s_p, for which shakedown will always occur if $s < s_p$.

In the case of periodic external actions, s_p can be estimated by dropping the free vibration stress and setting $r = 0$ as it is always possible to find some particular initial conditions that will make the purely elastic response of the system coincide with its forced vibration counterpart (*Ceradini*, 1980; *Polizzotto*, 1984; *Polizzotto et al.*, 1993). Accordingly, the elastic backward truncated stress response $\mathbf{Q}^E(r+\tau)$ can be represented by the steady state response $\mathbf{Q}^S$. Therefore, the shakedown safety factor can be estimated by solving the

following linear programming problem:

$$
\begin{aligned}
& s_p = \max_{s,\boldsymbol{\rho}} s \\
& \text{subject to} \\
& \bar{\mathbf{Q}}^s = \max_{0 \leqslant t \leqslant T} \mathbf{N}^T \mathbf{Q}^s(t) \\
& \mathbf{f} = s\bar{\mathbf{Q}}^s + \mathbf{N}^T \boldsymbol{\rho} - \mathbf{R} \leqslant \mathbf{0} \\
& \mathbf{B}^T \boldsymbol{\rho} = \mathbf{0}
\end{aligned}
\tag{2.22}
$$

where $\bar{\mathbf{Q}}^s$ is the vector of elastic envelope stress defined as the maximum of the plastic demand for each yielding mode in time, $\mathbf{Q}^S(t)$ is the purely elastic steady state response while T represents the period of the forcing function.

It is interesting to observe that, together with optimization problem outlined above, the following linear programming problem may also be defined for identifying the the load multiplier s_e that separates a perfectly elastic response state from the initiation of plasticity:

$$
\begin{aligned}
& s_e = \max_{s} s \\
& \text{subject to} \\
& \bar{\mathbf{Q}}^s = \max_{0 \leqslant t \leqslant T} \mathbf{N}^T \mathbf{Q}^s(t) \\
& \mathbf{f} = s\bar{\mathbf{Q}}^s - \mathbf{R} \leqslant 0
\end{aligned}
\tag{2.23}
$$

where now the vector of plastic strains $\boldsymbol{\rho}$ are considered equal to zero.

2.4.2.2 Application to wind engineering

In real world applications, the approach introduced in the previous section cannot be immediately applied because of the finite length and non-periodic nature of, for instance, real wind storms. However, as detailed in *Tabbuso et al.* (2016), by considering the wind storm of duration T as a finite realization of a stationary stochastic process of period T, then

an artificial wind storm is defined that is periodic and of infinite duration. For this artificial wind storm, the linear programming problems of Eqs. (2.22) and (2.23) can be directly applied for estimating the multipliers s_p and s_e. The significance of the results obtained for the artificial wind storm outlined above, lies in the fact that if the structure shakes down for the artificial infinite duration and periodic wind storm, then it cannot undergo plastic fatigue failure or incremental plastic collapse during the actual wind storm of duration T (*Tabbuso et al.*, 2016). This result is extremely useful as it allows the state of shakedown or non-shakedown (i.e. non-collapse or collapse susceptibility) to be identified by solving a "linear programming problem" (i.e. the problem of (Eq. 2.22)), which does not present any particular computational issues even for events of long duration (T in the order of hours). In particular, a value of $s_p \geqslant 1$ implies that, under the loads $\mathbf{F}(t)$, the structure will shakedown and is therefore safe against fatigue failure or incremental plastic collapse. This implies that, within a simulation framework, if for a given wind load realization it is found that $s_p \geqslant 1$, it can be stated that the system is not susceptible to collapse where collapse susceptibility is defined as the failure to reach a state of dynamic shakedown. It is this definition of collapse/non-collapse susceptibility that is used in the proposed framework.

Before closing this section, it should be observed that local failure mechanisms (e.g. local buckling deformations of web and flange of a connection) are included in this framework through the damage states and associated fragility functions considered in the non-collapse damage analysis of Section 2.4.1.4.

2.4.3 Simulation Strategy

Section 2.4.1 presented models for assessing the repair costs and downtime associated with the occurrence of a severe wind storm while Section 2.4.2 presented a model for determining the integrity of the MWFRS with respect to collapse. This section presents a simulation framework for assessing Eq. (2.4) in terms of the aforementioned models. In particular, the

approach is based on Monte Carlo simulation and therefore estimating Eq. (2.4) as follows:

$$P(DV > dv) \approx \frac{1}{N_s} \sum_{i=1}^{N_s} I(\mathbf{u}^{(i)}) \tag{2.24}$$

where N_s is the total number of simulations while I is an indicator function defined as:

$$I(\mathbf{u}^{(i)}) = \begin{cases} 1 \text{ if } dv^{(i)}(\mathbf{u}^{(i)}) > dv \\ 0 \text{ if } dv^{(i)}(\mathbf{u}^{(i)}) \leq dv \end{cases} \tag{2.25}$$

where $\mathbf{u}^{(i)}$ is the ith realization of the random vector $\mathbf{U} = \{V, \mathbf{U}_{IM}, \mathbf{U}_{IP}, \mathbf{U}_{EDP}, \mathbf{U}_{sh}\}^T$ with V the random variable probabilistically defining the wind speeds, v, collected at the meteorogical station. A flowchart of the simulation-based framework is shown in Figure 2.4. In particular, the steps defining the Monte Carlo algorithm are as follows:

1. Generate a realization $v^{(i)}$ of V and of the random vector $\mathbf{U}_{IM}$, $\mathbf{u}_{IM}^{(i)}$, and use Eq. (2.6) to estimate the intensity measure, $\bar{v}_z(T, z_0)$, at all heights of interest.

2. Generate a realization $\mathbf{u}_{IP}^{(i)}$ of $\mathbf{F}(t)$ to use together with $\bar{v}_z(T, z_0)$ of the previous step in order to estimate a realization of the interaction parameters, i.e. the aerodynamic loads $\mathbf{F}(t)$ of Eq. (2.7).

3. Generate a realization $\mathbf{u}_{EDP}^{(i)}$ of $\mathbf{U}_{EDP}$ to use together with the aerodynamic loads of the previous step, for estimating the response vector $\tilde{\mathbf{u}}$.

4. Generate a realization $\mathbf{u}_{sh}^{(i)}$ of $\mathbf{U}_{sh}$ and use it together with the responses from step 3 to determine the shakedown safety factor, s_p, by solving the linear programming problem of Eq. (2.22). Check if the structure is susceptible to collapse during the wind event, i.e. if $s_p < 1$.

5. If the structure does not shakedown (i.e. $s_p < 1$), it is deemed to be susceptible to collapse and repair cost and downtime for the ith realization, $dv^{(i)}$, are set equal to the

building replacement cost and time.

6. If the structure is not susceptible to collapse, i.e. $s_p \geqslant 1$, a realization of the demand vector $\mathbf{edp}^{(i)}$ (Eq. (2.8)) is generated. The vector $\mathbf{edp}^{(i)}$ is then used to estimate damage to the components of the performance groups through their respective fragility functions. Values of downtime and repair cost are then estimated for each performance group through the consequence functions associated with each damage state. By aggregating over all performance groups, non-collapse values for $dv^{(i)}$ are obtained.

7. Use Eq.(2.25) to determine the value of $I(\mathbf{u}^{(i)})$.

By repeating steps 1 to 7 for N_s samples of the random vector $\mathbf{U}$, estimates of the probability of the performance variables exceeding a threshold value, $P(DV > dv)$, can be obtained from Eq. (2.24).

2.5 Case Study

2.5.1 Description

As a case study, the 40-story four-span plane steel frame of Figure 2.5 is considered. The geometry of the frame is described by beam span lengths of 6.1 m (20 ft) and by the inter-story heights of 6.1 m (20 ft) at ground level and 3.8 m (12.5 ft) for all other floors. The overall height of the structure is 154.7 m (507.5 ft). Column splices occur every three floors. The columns are built-up box members while the beams are wide flange standard W sections. A summary of the section sizes is reported in Table 2.2. The steel composing the frame is assumed to be elastic perfectly plastic and is therefore completely described by the yield stress σ_y and Young's modulus E_y, which are considered as uncertain parameters with log-normal distributions. In particular, the yield stress is assigned a mean 355 MPa and a standard deviation of 15 MPa while the Young's modulus has a mean of 210 GPa and standard deviation of 15 GPa. The mass of the structure is lumped at each floor and

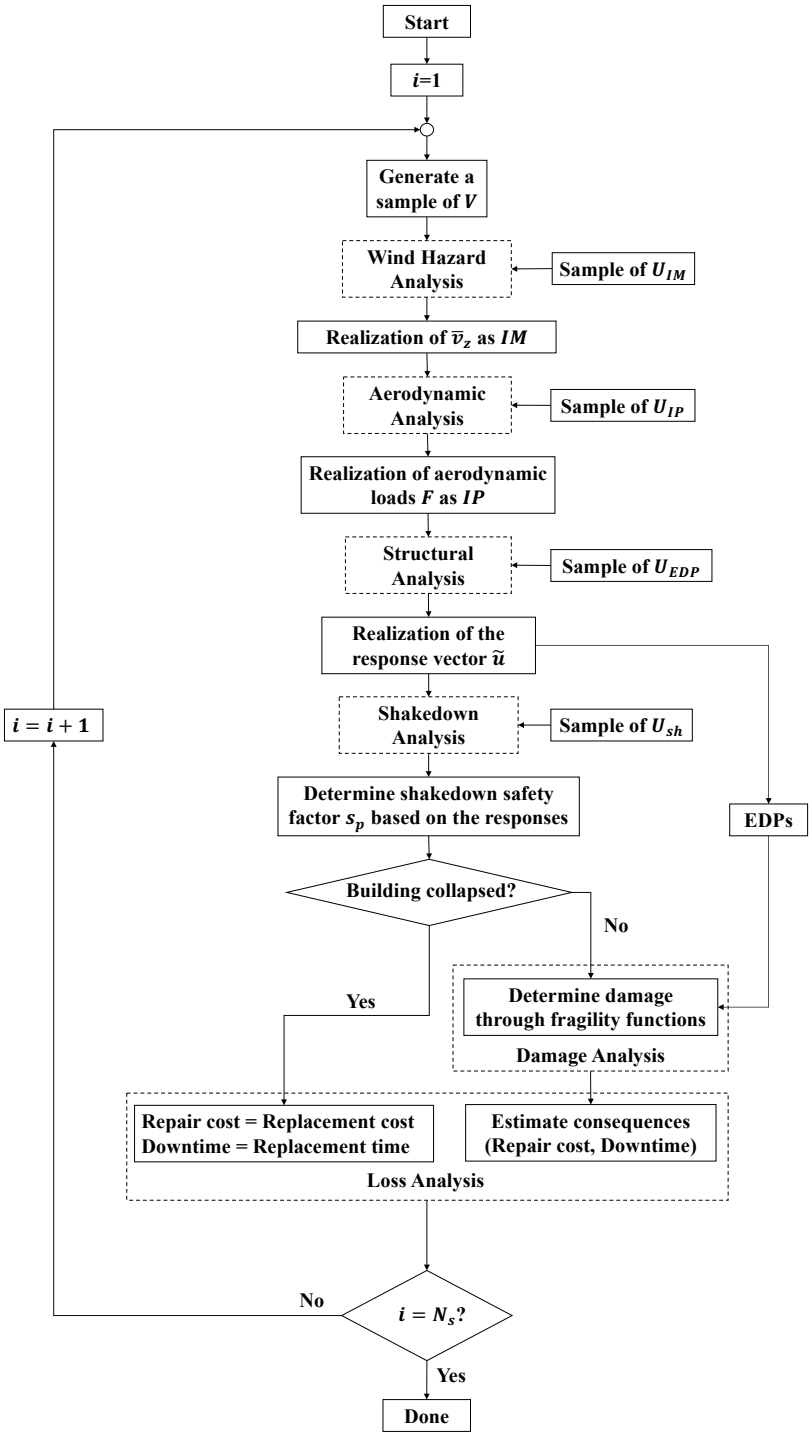

Figure 2.4: Flowchart of the overall simulation strategy.

Table 2.2: Section sizes defining the steel frame.

Level range	Wide-flange Beams	Box columns	
		Interior (in.)	Exterior (in.)
1-10	W36 × 282	22 × 22	20 × 20
		$t = 3$	$t = 2.5$
11-20	W36 × 194	20 × 20	20 × 20
		$t = 2$	$t = 2$
21-30	W33 × 169	18 × 18	18 × 18
		$t = 1$	$t = 1$
31-40	W27 × 84	18 × 18	18 × 18
		$t = 0.75$	$t = 0.75$

is calculated as as the sum of the element mass and dead load mass $M = q_o L/g$, where g is the gravitational acceleration while $q_o = 11.96[\text{kN}/m^2]\times h$ is the dead load with h and L the height and width of each floor respectively. To model uncertainty, the mass at each floor is multiplied by a log-normal random variable, Δ_M, with unit mean and standard variation 0.05. To complete the calibration of $\mathbf{U}_{EDP}$, the modal damping ratios are also taken as log-normal random variables with mean 0.05 and standard deviation 0.005 (*Spence and Kareem*, 2014a; *Spence et al.*, 2014).

For analyzing the dynamic shakedown multipliers, rigid-perfectly plastic hinges are assumed at the extremes of all beams and columns. The yield domain associated with the plastic hinges of the columns (defined by the interaction between the the axial stress N and bending moment M) is modeled through the piece-wise linear domain shown in Figure 2.6, where N_y is the axial generalized yield stress given by $N_y = \sigma_y A$ while M_y is the yield moment given by $M_y = \sigma_y S$ with A and S the area and section modulus of the cross section respectively. For plastic hinges located in the beams, the yield domain is simply defined by the yield moments due to the action of the floor diaphragms.

For the application described in this section, the distribution characterizing the largest yearly meteorological wind speeds v was taken as a Type II distribution with mean value of 30 m/s and standard deviation 3.5 m/s. In calibrating the the transformation of Eq. (2.6), τ was assumed as 1 hour while a roughness length of $z_{01} = 0.05$ m and a meteorological height of $H_{met} = 10$ m were considered. The roughness length at the site of the structure,

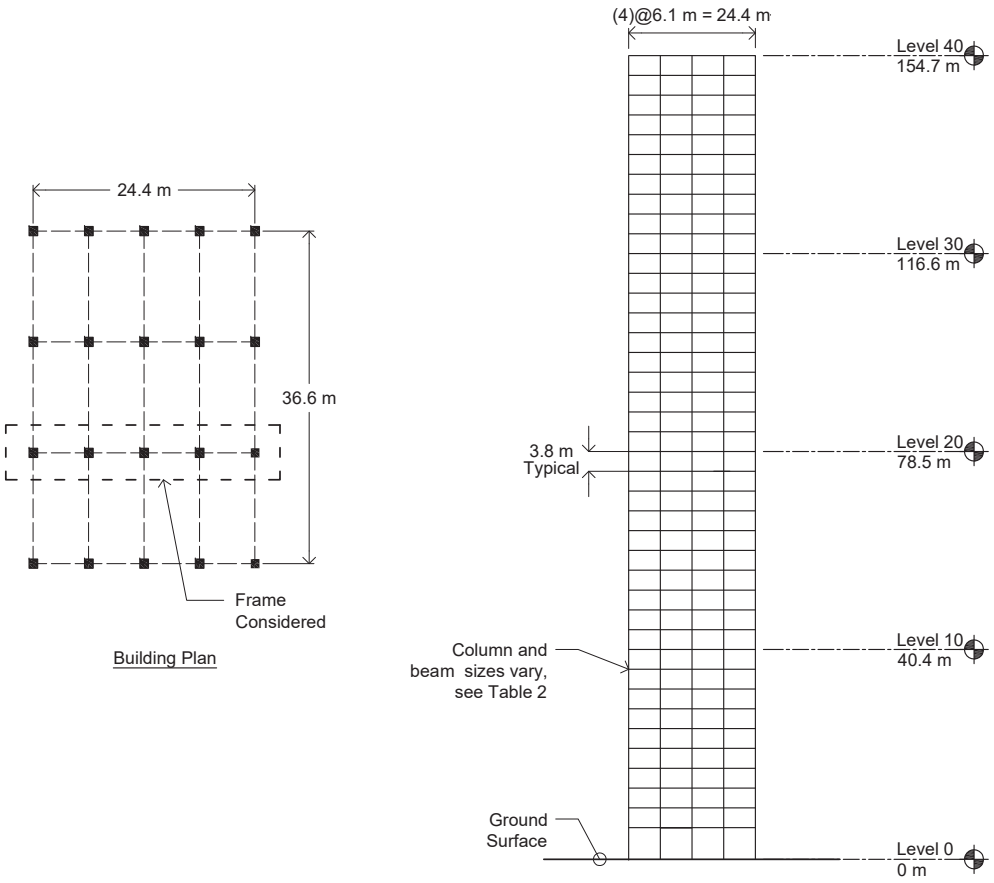

Figure 2.5: Schematic of the 40 story steel frame of the case study.

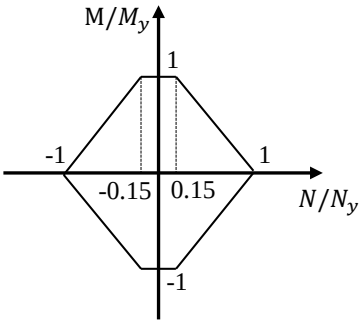

Figure 2.6: Piecewise linear failure domain of the plastic hinges in the columns.

z_0, was taken as a random variable with uniform distribution between 0.01 m and 0.03 m. It should be observed that in this work a "time-based" P-58 style assessment of the building system is carried out, i.e. losses for all possible wind intensities over a duration of 1 year are estimated. To perform an "intensity based" assessment, it would simply be necessary to consider a fixed wind speed value with desired mean recurrence interval.

In order to model the aerodynamic loads acting on the frame, the quasi-steady model outlined in 4.4.2 was adopted while considering an influence width for each floor of 12.2 m (40 ft), a pressure coefficient of $\bar{C}_j = 1.3$, and an air density of $\rho = 1.25$ kg/m^3. In calibrating the model, N was chosen to be 2048 therefore yielding wind storms with a stationary duration of $T = 16,085$ s with a sampling frequency of 1.27 Hz. In order to generate realizations of the forcing functions $\boldsymbol{F}(t)$, a total of 81920 independent and uniformly distributed random numbers in $[0, 2\pi]$ are required. In the proposed framework, these random numbers are collected in the random vector $\mathbf{U}_{IP}$. A typical realization of the 40th floor forcing function, $F_{40}(t)$, and the corresponding interstory drift ratio response are shown in Figure 2.7 while Figure 2.8 shows the target and simulated power spectral density (PSD) functions.

In defining the fragility and consequence functions, building components were grouped into five main categories, as follows: (1) structure; (2) façade; (3) egress; (4) mechanical, electrical and plumbing (MEP); and (5) office fitouts. The FGs included in the case study together with the characteristics of the fragility functions–chosen from the FEMA fragility

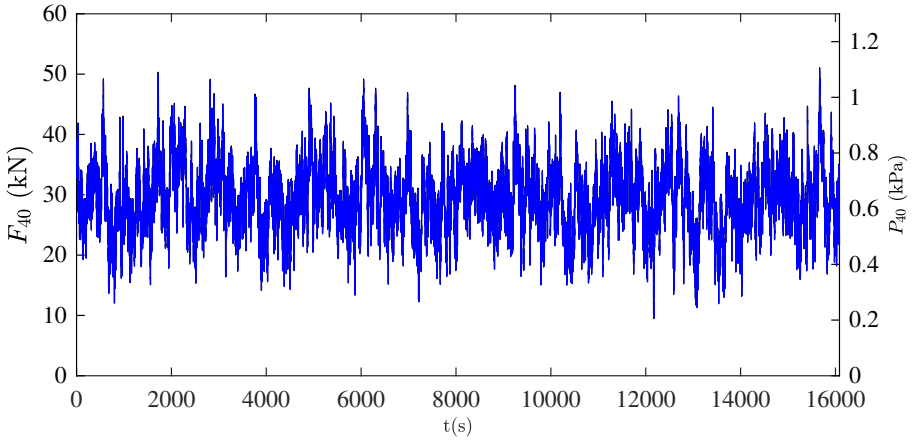

(a)

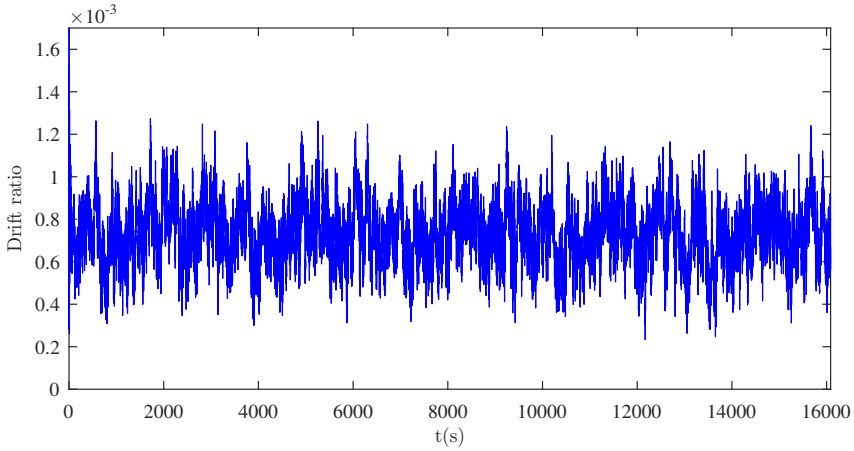

(b)

Figure 2.7: A realization of the top floor stochastic forcing function and corresponding interstory drift ratio response: (a) Net force and corresponding effective pressure, i.e. ratio between story force and building width times story height; (b) Interstory drift ratio response.

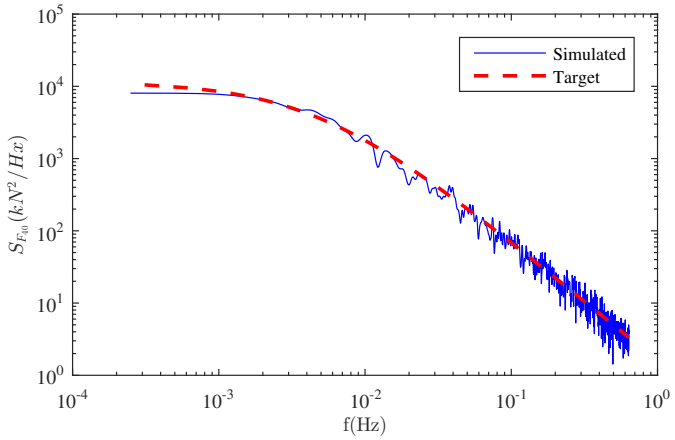

Figure 2.8: PSD functions for the target and simulated forcing function of floor 40.

Database (*Federal Emergency Management Agency (FEMA)*, 2012c)–and unit repair cost functions for the first damage state are summarized in Table 2.3. In practice, more than one damage state was considered for each FG (the definition of the fragility and consequence functions for each additional damage state can be found in *Federal Emergency Management Agency (FEMA)* (2012c) using the FEMA designation codes reported in Table 2.3). For failure modes occurring at the column splices and beam-column connections, 6 different FGs (FGs 2 to 7) were defined based on the total weight above the component and whether one or two beams were connected to the beam column joint. Both the fragility functions and the URCFs (unit repair cost functions) were assumed to be lognormally distributed with dispersion β_f for the fragility functions and $\beta_c = 0.25$ for all URCFs. The median of the fragility functions is indicated with m_f in Table 2.3, while the median of the URCF is defined by the four values C_{max}, C_{min}, Q_{max} and Q_{min} and is fixed for a given wind storm (i.e. simulation point) by the quantity of damaged components.

The PGs were identified as follows. PGs belonging to FGs 1 to 10 and 32 were defined by interstory drift sensitive components and were therefore assigned peak interstory drifts as EDPs. The PGs were therefore defined by grouping elements at each floor (e.g. for FG 32, 40 PGs are defined). Analogously, for FGs 11 to 26 that were sensitive to floor acceleration, the components were divided into 40 PGs, depending on the floor to which they belonged while the peak floor acceleration was assigned as the EDP. FGs 27 to 31 were MEP facilities assumed to be installed at the top floor, so 1 PG was assigned to each FG. As a result, a total of 899 PGs were considered.

2.5.2 Results

The analyses were carried out for $N_s = 26000$ simulation points. Figure 2.9 reports the distributions of s_p and s_e. In particular, for a threshold value $s_p = 1$, i.e. no amplification of the forcing function $\boldsymbol{F}(t)$, the annual system-level probability of the structure suffering plastic collapse was estimated to be $P(s_p < 1) = 0.0004$ while the annual probability of the structure

Table 2.3: Summary of the FGs and associated fragility and URCFs for the first Damage State.

FG number	Category	FEMA designation	Description	EDP type	Damage state 1					
					Fragility functions		Unit repair cost functions			
					m_f	β_f	C_{max}[$]	C_{min}[$]	Q_{max}	Q_{min}
1	Structure	B1031.011c	Steel column base plates	D direct.	0.04	0.4	25,812.00	17,208.00	15	5
2	Structure	B1031.021b	Column splice (150<W<300plf)	D direct.	0.04	0.4	12,168.00	8,112.00	15	5
3	Structure	B1031.021c	Column splice (W>300plf)	D direct.	0.04	0.4	13,608.00	9,072.00	15	5
4	Structure	B1035.041	Pre-Northridge Welded Unreinforced Flange-Bolted (WUF-B) beam-column joint, beam one side	D direct.	0.017	0.4	14,472.00	9,648.00	30	10
5	Structure	B1035.042	Pre-Northridge WUF-B beam-column joint, beam one side of column, beam depth >= W30	D direct.	0.017	0.4	15,072.00	10,048.00	30	10
6	Structure	B1035.051	Pre-Northridge WUF-B beam- column joint, beam both sides	D direct.	0.017	0.4	21,096.00	14,064.00	30	10
7	Structure	B1035.052	Pre-Northridge WUF-B beam-column joint, beam both sides of column, beam depth >= W30	D direct.	0.017	0.4	21,096.00	14,064.00	30	10
8	Façade	B2011.201a	Precast concrete panels with user- specified in-plane connection capacity	D direct.	0.005	0.5	17,160.00			
9	Fitout	C1011.001a	Wall Partition, Type: Gypsum with metal studs, Full Height, Fixed Below, Fixed Above (based upon 13'x100' Panels)	D direct.	0.0021	0.6	2.50	2.04	13000	1300
10	Fitout	C3011.001a	Wall Partition, Type: Gypsum + Wallpaper, Full Height, Fixed Below, Fixed Above (based upon 9'x100' Panels)	D direct.	0.0021	0.6	3.90	2.40	5000	500
11	Fitout	C3027.001	Raised Access Floor, non seismically rated.	Acc.	0.5	0.5	1.27	1.04	10000	1000
12	Fitout	C3032.001b	Suspended Ceiling, SDC A,B, Area (A): 250 < A < 1000, Vert support only	Acc.	0.55	0.4	1.89	1.31	2500	250
13	Fitout	C3034.001	Independent Pendant Lighting - non seismic	Acc.	0.6	0.4	643.50	396.00	10	5
14	Fitout	E2022.023	Desktop electronics including computers, monitors, stereos, etc, smooth surface	Acc.	0.4	0.5	1,000.00			
15	MEP	D2021.011a	Cold Water Piping (dia > 2.5 inches), SDC A or B, PIPING FRAGILITY	Acc.	1.5	0.4	700.00	210.00	10	5
16	MEP	D2022.011a	Hot Water Piping - Small Diameter Threaded Steel - (2.5 inches in diameter or less), SDC A or B, PIPING FRAGILITY	Acc.	0.55	0.5	279.00			
17	MEP	D2022.011b	Hot Water Piping - Small Diameter Threaded Steel - (2.5 inches in diameter or less), SDC A or B, BRACING FRAGILITY	Acc.	1.2	0.5	383.00			
18	MEP	D2022.021a	Hot Water Piping - Large Diameter Welded Steel - (greater than 2.5 inches in diameter), SDC A or B, PIPING FRAGILITY	Acc.	1.5	0.5	348.00			
19	MEP	D2031.021a	Sanitary Waste Piping - Cast Iron w/bell and spigot couplings, SDC A,B, PIPING FRAGILITY	Acc.	2.25	0.5	3,167.00			
20	MEP	D2031.021b	Sanitary Waste Piping - Cast Iron w/bell and spigot couplings, SDC A,B, BRACING FRAGILITY	Acc.	1.2	0.5	423.00			
21	MEP	D3041.011a	HVAC Stainless Steel Ducting less than 6 sq. ft in cross sectional area, SDC A or B	Acc.	1.5	0.4	1,300.00	390.00	10	5
22	MEP	D3041.012a	HVAC Stainless Steel Ducting less than 6 sq. ft in cross sectional area, SDC C	Acc.	1.5	0.4	1,900.00	570.00	10	5
23	MEP	D3041.031a	HVAC Drops / Diffusers in suspended ceilings - No independent safety wires, SDC A or B	Acc.	1.3	0.4	360.00	240.00	50	10
24	MEP	D3041.041a	Variable Air Volume (VAV) box with in-line coil, SDC A or B	Acc.	1.9	0.4	14,796.00			
25	MEP	D4011.021a	Fire Sprinkler Water Piping - Horizontal Mains and Branches - Old Style Victaulic - Thin Wall Steel - No bracing, SDC A or B, PIPING FRAGILITY	Acc.	1.1	0.4	348.00			
26	MEP	D4011.031a	Fire Sprinkler Drop Standard Threaded Steel - Dropping into unbraced lay-in tile SOFT ceiling - 6 ft. long drop maximum, SDC A or B	Acc.	0.75	0.4	526.00			
27	MEP	D5012.021a	Low Voltage Switchgear - Capacity: 100 to <350 Amp - Unanchored equipment that is not vibration isolated - Equipment fragility only	Acc.	1.28	0.4	550.00	450.00	3	1
28	MEP	D3031.011c	Chiller - Capacity: 350 to <750 Ton - Unanchored equipment that is not vibration isolated - Equipment fragility only	Acc.	0.2	0.4	2,420.00	1,980.00	4	1
29	MEP	D3031.021c	Cooling Tower - Capacity: 350 to <750 Ton - Unanchored equipment that is not vibration isolated - Equipment fragility only	Acc.	0.5	0.4	2,420.00	1,980.00	4	1
30	MEP	D3052.011d	Air Handling Unit - Capacity: 25000 to <40000 CFM - Unanchored equipment that is not vibration isolated - Equipment fragility only	Acc.	0.25	0.4	2,066.00			
31	MEP	D5012.013a	Transformer/primary service - Capacity: <100 kVA - Equipment that is either hard anchored or is vibration isolated with seismic snubbers/restraints - Anchorage fragility only	Acc.	0.73	0.45	4,167.00			
32	Egress	C2011.001b	Prefabricated steel stair with steel treads and landings with no seismic joint.	D direct.	0.005	0.6	520.00	320.00	5	1

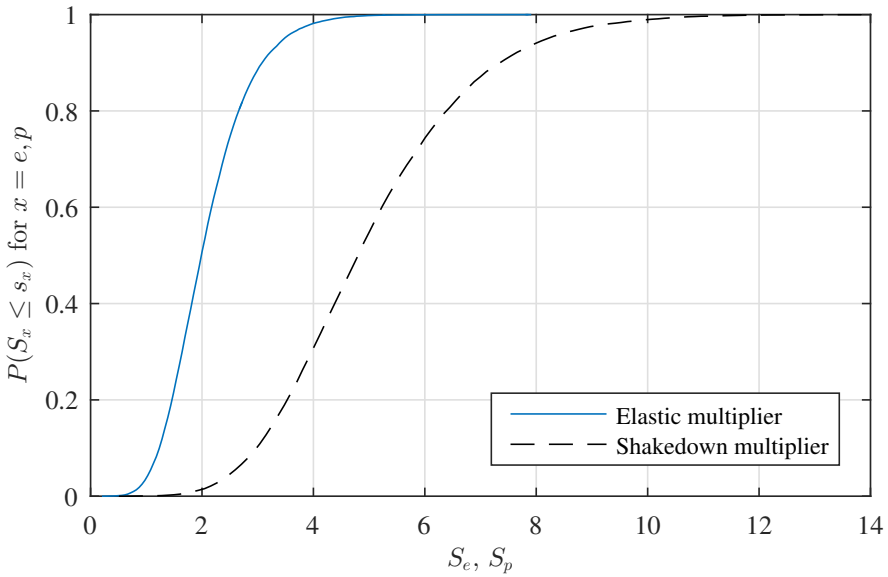

Figure 2.9: Distributions of the elastic, s_e, and dynamic shakedown, s_p, safety factors.

exiting the elastic regime was estimated to be $P(s_e < 1) = 0.039$. The difference between the two curves indicates the significant plastic reserves of the frame under investigation. It should also be noted that with $N_s = 26000$ samples, the variance of the estimate of the annual probability of the structure exiting the elastic regime is around 1.4×10^{-6}, which is considered adequate for this application. In addition to the information above, the distributions of s_p and s_e also provide useful information on the sensitivity of the probabilities associated with undergoing plastic collapse or exiting the elastic regime as a result of amplifications in the external excitation.

Figure 2.10 shows annual probability of exceedance associated with total repair costs. As can be seen, the total repair cost with a return period of 5 years ($P_f = 0.2$) is about \$2,267,000, indicating that the structure was poorly designed and underperformed, while the cost with a 50 year return period ($P_f = 0.02$) is approximately \$4,564,000. In interpreting these numbers, it should be observed that it is generally acknowledged that the time and cost consequences of the 2012 FEMA fragility database (as used in this work) associated with interior partitions, gravity shear tabs, and in plane precast panels, are somewhat conservative leading to relatively high repair cost and time estimates. In the proposed approach, the repair

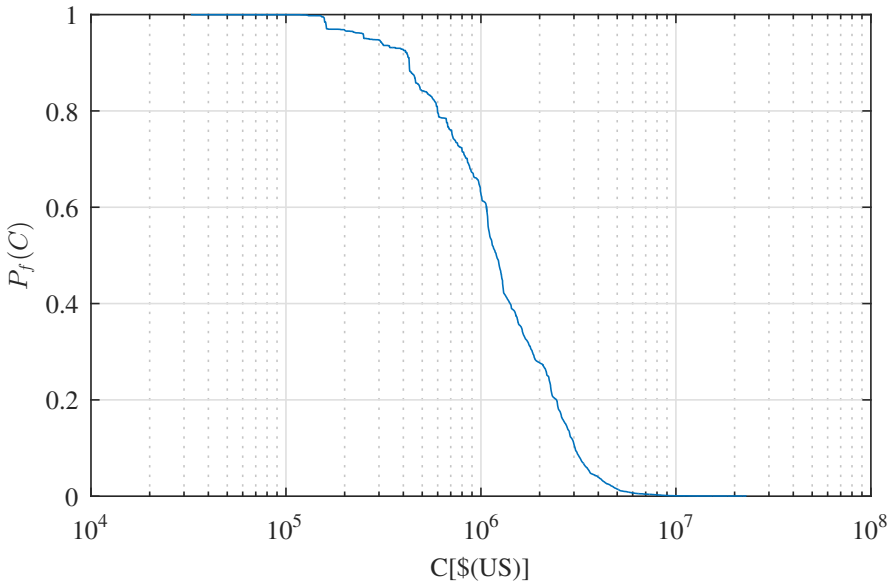

Figure 2.10: Annual probability of exceedance of the total repair cost C.

costs are calculated at an individual component level before being aggregated for estimating the total system-level consequence. Therefore, by deaggregating over all FGs, information on how the various FGs contribute to the total repair cost can be found. As can be seen from Figure 2.11, FG 8 to 14 (concrete panels and office fitouts) and 32 are responsible for the bulk of the repair costs while FG 4 to 7, 23, 24, 30, and 31 contribute minimally to the total cost. This information would be particularly useful in the redesign or retrofit of the building and illustrates the type of decision support information that the proposed framework has been developed to provide.

In parallel with the repair cost estimation, downtime for full recovery was also assessed. In this respect, Figure 2.12 shows the annual probability of exceedance of total downtime thresholds. In particular, upper and lower bounds were estimated considering the repair work done in series or parallel respectively. The corresponding total downtime with a return period of 5 years ($P_f = 0.2$) is about 726 and 230 days, respectively. In addition, a strategy in which repairs were carried out floor by floor in a serial manner (i.e. all structural and non-structural components repaired simultaneously at a certain floor before repairs can commence at the next floor) was also considered. In this case, the estimated downtime with a return period

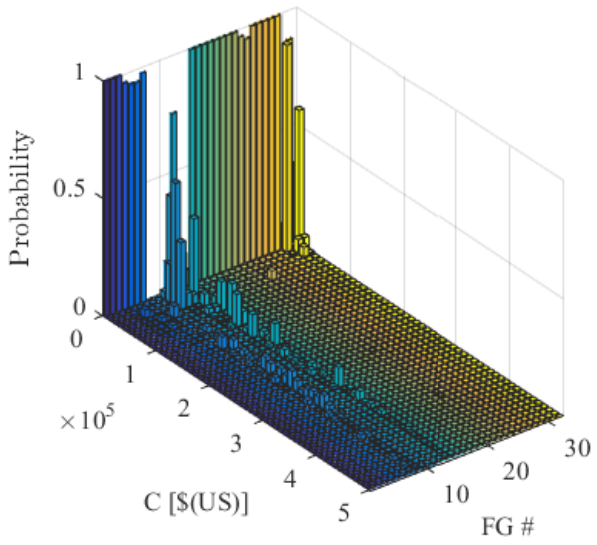

Figure 2.11: Deaggregation of the total repair cost among the fragility groups.

of 5 years ($P_f = 0.2$) is around 626 days which, consistent with how the repair strategy was defined, is between the two extreme scenarios.

Figure 2.13 shows the deaggregation of the system-level total repair time among all fragility groups. In particular, it can be seen that non-structural components, such as concrete panels and office fitouts, contribute mostly to the total repair time, independently of whether the repairs are assumed to be carried out in series or in parallel. A breakdown of the different downtime contributors for the intermediate repair strategy considered above as well as the deaggregation of the impeding factors are illustrated in Figure 2.14. It can be observed that the delay caused by the impeding factors, largely driven by the delays associated with contractor mobilization, contributes–in this example–almost as much as the repair work time to the total downtime. This simple example would suggest that, the total downtime may be greatly underestimated if delays that prevent the initiation of the repairs are neglected, as in the FEMA P-58 procedures. Moreover, for this case study, utility disruption does not control over impeding factors and therefore–in this case–does not have a direct impact on the downtime assessment.

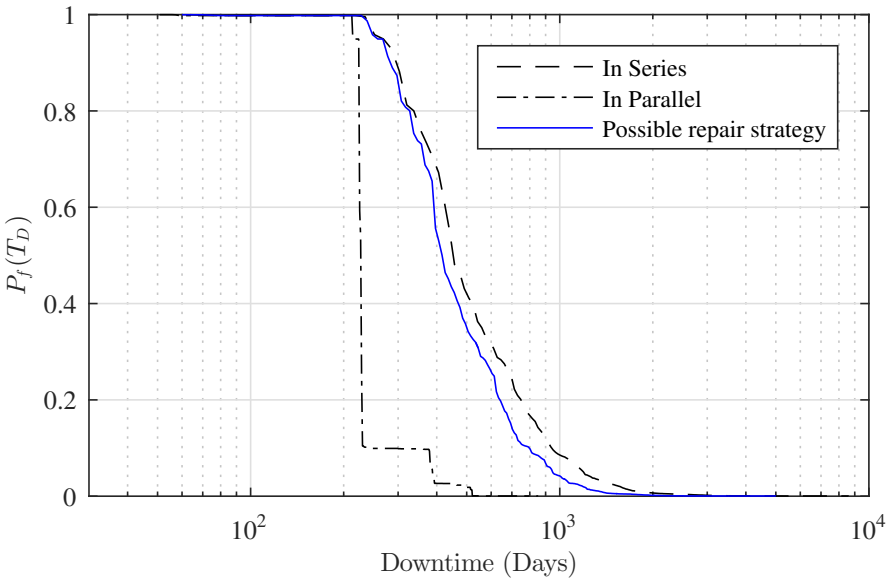

Figure 2.12: Annual probability of exceedance of the total downtime T_D.

2.5.3 Discussion

The primary objective of this work was the introduction of an efficient PBWE framework for the integrated collapse and non-collapse susceptibility assessment of multistory wind excited buildings systems. The case study presented in this section demonstrated the potential of the framework for assessing the performance of a system given a set of input data with associated probabilistic distributions. Obviously, the quality of the performance estimates obtained from the proposed framework depends on the correct estimation of the input parameters. Having said this, it should be kept in mind that the framework presented in this work is based on Monte Carlo simulation. Therefore, the sensitivity of the results can be studied in a straightforward manner with respect to any of the input parameters. This aspect was not investigated in this work as it was focused on the development of the framework itself. However, a separate study into this very aspect would be of sure interest.

Before closing this section, it should be mentioned that while the case study presented here is 2D, the extension to 3D problems would be straightforward. Indeed, due to the efficiency with which high dimensional linear programmimg problems can be solved, an extension to 3D would not present any particular computational difficulties.

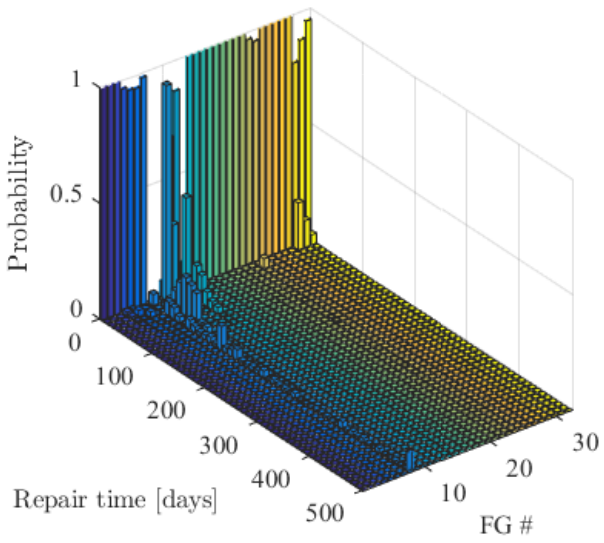

(a)

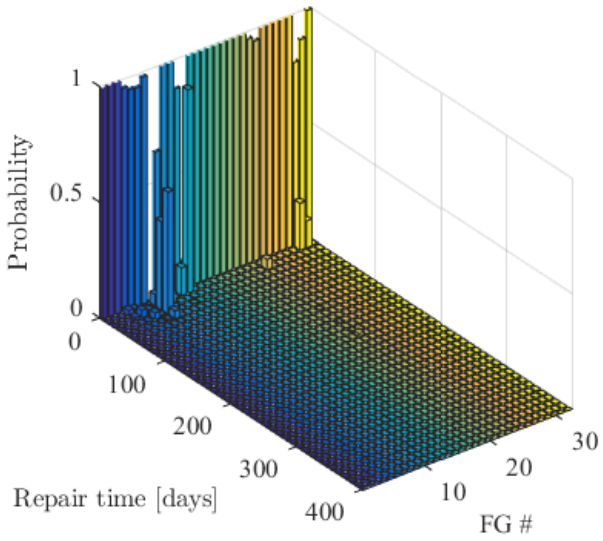

(b)

Figure 2.13: Deaggregation of the total repair time: (a) repair work carried out in series; (b) repair work carried out in parallel.

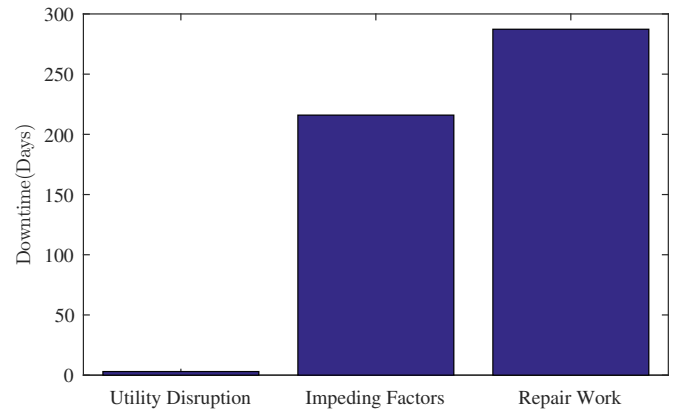

(a)

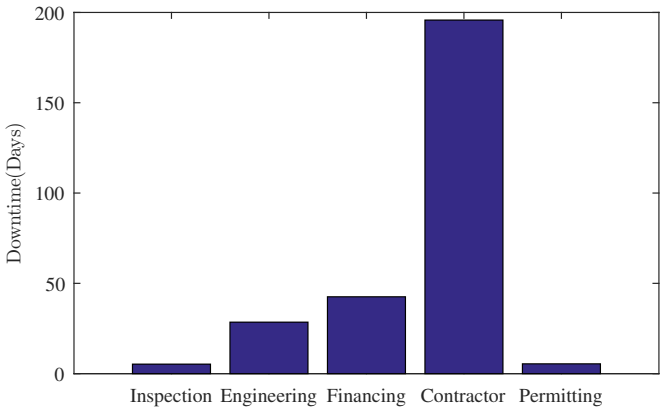

(b)

Figure 2.14: (a) Downtime contributors; (b) deaggregation of impeding factors for the structure.

2.6 Summary and Conclusions

A probabilistic PBWE framework is presented in this chapter that integrates probabilistic dynamic shakedown analysis with system-level damage and loss estimation models. In particular, performance is expressed at a system-level through metrics such as repair costs and downtime, therefore enabling straightforward interpretation by decision-makers of diverse technical backgrounds. With respect to downtime estimation, a model is developed that depends not only on the estimation of repair work time but also on the estimation of delays caused by impeding factors that prevent the start of actual repair work. By applying dynamic shakedown theory, an efficient model is defined for describing the post yield behavior of structural systems subject to long duration (order of hours) dynamic wind loads. By defining safety against collapse as the occurrence of dynamic shakedown, collapse scenarios for the MWFRS are efficiently estimated and integrated into the overall loss model. This classic solution method, however, does not provide an estimate of plastic deformation when the structure reaches the shakedown state. To further consider failure due to excessive plastic deformations, a strain-driven approach will be presented in the following chapter.

A case study consisting of a 40-story frame building was presented to illustrate the potential of the proposed PBWE framework. This allowed for the illustration of the capability of the framework for systematically estimating not only the integrated system-level collapse and non-collapse losses, but also the deaggregated non-collapse losses. Due to the efficiency of the procedure and its systematic estimation of both structural and non-structural damage, it is believed that the framework outlined in this work could be of significant and immediate interest to the designers of wind excited building systems.

CHAPTER III

A New Class of Shakedown Algorithms

3.1 Overview

The primary goals of the work outlined in this chapter are:

1. Development of a dynamic shakedown framework within the setting of concentrated plasticity that enables the estimation of plastic strains and deformations together with the state of shakedown. Classic shakedown theory outlined in Section 2.4.2.1 only allows for the determination of whether a structure shakes down to a safe state, but not of the strains and deformations involved in reaching this state.

2. Development of a dynamic shakedown framework that enables estimation of distributed plasticity along the element through application of fiber section model in dynamic shakedown analysis.

3.2 Introduction

A significant limitation of the approaches outlined in the Chapter II is the lack of any estimation of the plastic deformations and strains that occur during the process of dynamic shakedown. This limits the applicability of these approaches, as these quantities play a fundamental role in determining whether a building is repairable after an extreme wind

event, or, more critically, if the building is susceptible to collapse due to asymptotically limited but excessive plastic deformations.

To estimate plastic strains and deformations in the case of structural systems modeled through one-dimensional finite elements, two main approaches exist: 1) distributed plasticity, in which plastic strains are allowed to form anywhere along the member length; and 2) concentrated (or lumped) plasticity, where inelastic behavior is typically concentrated at the member ends in terms of plastic hinges (*Clough et al.*, 1965; *Giberson*, 1967). The main advantage of concentrated plasticity models is their efficiency. Indeed, they often allow large-scale problems to be treated with reasonable computational effort. Their main drawback resides in difficulties in systematically defining the parameters associated with the hysteretic force-deformation relationships of the locations of concentrated plasticity (i.e. plastic hinge locations) (*Spacone et al.*, 1996; *Spacone and El-Tawil*, 2004). Indeed, in the case of both axial force and bending moment (e.g. columns), it is common to ignore any interaction between these forces. This difficulty can lead to important errors in the estimation of the inelastic responses (*Filippou and Issa*, 1988). While more computationally involved, distributed plasticity models do not suffer these limitations. In particular, fiber-based distributed plasticity models allow plasticity to form not only along the member, but also over the height of the member. More importantly, the inelastic behavior can be simply and rationally defined through uniaxial fiber stress-strain relationships, i.e. uniaxial constitutive laws, leading to far greater accuracy in the estimation of the inelastic responses (*Spacone et al.*, 1996; *Spacone and El-Tawil*, 2004).

Within this context, this chapter is focused on the development of concentrated and distributed plasticity models for the efficient estimation of the plastic deformations and strains occurring during shakedown under a given dynamic wind load time history. In particular, the proposed approach is based on the reformulation to dynamic shakedown of the path-following algorithms recently proposed for static shakedown analysis *Casciaro and Garcea* (2002); *Malena and Casciaro* (2008). Indeed, these algorithms have proved to be both nu-

merically efficient and well suited for finite element implementation with applications to various structures subjected to a combination of static loads (*Casciaro and Garcea*, 2002; *Malena and Casciaro*, 2008; *Garcea et al.*, 2005).

3.3 A Strain-driven Concentrated Plasticity Model

Although the classic solution method, formulated as a linear programming problem in Section 2.4.2.1, can be used to evaluate in an extremely efficient fashion the shakedown limit state of structures subject to dynamic loads, the plastic strains and deformations remain unknown. Therefore, if the inelastic deformations are required, an alternative approach to estimate shakedown has to be explored. To this end, the algorithms proposed in *Casciaro and Garcea* (2002, 2006) for estimating the shakedown multiplier under static loads are of interest. By first extending these algorithms to dynamic shakedown problems, it can be observed that, under the conditions outlined in Section 4.3, accurate predictions of the plastic strains and deformations occurring during shakedown can be made. The first step towards this goal is the extension of the path-following algorithms outlined in *Casciaro and Garcea* (2002, 2006) to dynamic shakedown problems involving periodic and infinite duration dynamic loads.

3.3.1 Problem formulation

To formulate the dynamic shakedown problem for periodic and infinite duration dynamic loads in terms of strains and displacements, it is convenient to first consider a residual displacement increment $\mathbf{u}_r$ together with a load multiplier s satisfying $s_e \leq s \leq s_p$. From $\mathbf{u}_r$ the following strain increment can be defined (*Casciaro and Garcea*, 2002):

$$\boldsymbol{\epsilon}_r(\mathbf{u}_r) = \mathbf{B}\mathbf{u}_r \tag{3.1}$$

An admissible stress vector, $\boldsymbol{\rho}$, corresponding to $\mathbf{u}_r$ and s can be obtained through the following return mapping scheme:

$$\boldsymbol{\rho}(s, \mathbf{u}_r) = \boldsymbol{\rho}_E + \Delta\boldsymbol{\rho}, \quad \mathbf{f}(s, \boldsymbol{\rho}) \leq 0 \tag{3.2}$$

where $\boldsymbol{\rho}_E = \boldsymbol{\rho}_0 + \mathbf{EBu}_r$ is the elastic predictor of $\boldsymbol{\rho}$, while $\Delta\boldsymbol{\rho} = -\mathbf{E}\boldsymbol{\epsilon}_p$ with $\boldsymbol{\epsilon}_p$ is the plastic component of the strain increment $\boldsymbol{\epsilon}_r$ defined by the Kuhn-Tucker condition:

$$\boldsymbol{\epsilon}_p = \mu\mathbf{n}, \quad \mathbf{n} \in \partial\mathbf{f}(s, \mathbf{u}_r), \quad \mu = \begin{cases} = 0 & \text{if } \mathbf{f}(s, \boldsymbol{\rho}_E) < 0 \\ \geq 0 & \text{if } \mathbf{f}(s, \boldsymbol{\rho}_E) \geq 0 \end{cases} \tag{3.3}$$

with μ the plastic multiplier. Instead of estimating $\boldsymbol{\rho}(s, \mathbf{u}_r)$ by directly solving the return mapping of Eqs. (3.2) and (3.3), $\boldsymbol{\rho}(s, \mathbf{u}_r)$ can be more conveniently estimated by minimizing the Haar-Kármán function subject to the dynamic shakedown feasibility conditions:

$$\begin{aligned} &\min_{\boldsymbol{\Delta\rho}} \frac{1}{2}\boldsymbol{\Delta\rho}^T\mathbf{E}^{-1}\boldsymbol{\Delta\rho} \\ &\text{subject to} \\ &\bar{\mathbf{Q}}^s = \max_{0\leq t\leq T} \mathbf{N}^T\mathbf{Q}^s(t) \\ &\mathbf{f} = s\bar{\mathbf{Q}}^s + \mathbf{N}^T\boldsymbol{\rho} - \mathbf{R} \leq 0 \end{aligned} \tag{3.4}$$

Equation (3.4) represents a standard strictly convex quadratic programming problem that can be efficiently solved in high-dimensions through standard optimization algorithms.

By solving the return mapping scheme for a given s and $\mathbf{u}_r$, solutions in terms of $\boldsymbol{\rho}(s, \mathbf{u}_r)$ will be found that satisfy the shakedown feasibility condition $\mathbf{f}(s, \boldsymbol{\rho}) \leq 0$. However, for $\boldsymbol{\rho}(s, \mathbf{u}_r)$ to be a solution to the Shakedown Theorem, then it must also be self-equilibrated. This requirement can be imposed in terms of the internal force vector, $\mathbf{S}$, associated with

the displacement field $\mathbf{u}_r$ and assigned multiplier s as:

$$\mathbf{S}(\mathbf{u}_r, s) = \mathbf{B}^T \boldsymbol{\rho} = 0 \tag{3.5}$$

By combining this condition with the strain-driven scheme for the identification of admissible values of $\boldsymbol{\rho}(s, \mathbf{u}_r)$, the following dynamic shakedown problem can be stated directly in terms of the displacement increments:

$$s_p = \max s : \exists \mathbf{u}_r : \mathbf{S}(\mathbf{u}_r, s) = \mathbf{0} \tag{3.6}$$

To solve Eq. (3.6), an incremental iterative scheme can be adopted based on producing a sequence of admissible safe states that are self-equilibrated.

3.3.2 An iterative solution scheme

Starting from the elastic limit state $(s_e, \mathbf{0}, \mathbf{0})$, the iterative solution method estimates the shakedown multiplier s_p and the corresponding admissible self-equilibrated stress state $\boldsymbol{\rho}$ with associated deformation vector $\mathbf{u}_r$ by producing a sequence of admissible safe states $(s^{(k)}, \boldsymbol{\rho}^{(k)}, \mathbf{u}_r^{(k)})$ with $s^{(k)}$ monotonously increasing at each step and convergent to s_p. The overall procedure is outlined in the flowchart of Figure 3.1. In particular, at each step, the multiplier s and displacement field $\mathbf{u}_r$ are initialized through the following equations:

$$\begin{aligned} s_1 &= s^{(k-1)} + \beta(s^{(k-1)} - s^{(k-2)}) \\ \mathbf{u}_{r1} &= \mathbf{u}_r^{(k-1)} + \beta(\mathbf{u}_r^{(k-1)} - \mathbf{u}_r^{(k-2)}) \end{aligned} \tag{3.7}$$

where β is an appropriate scaling factor. The iterative process within each step produces a monotonically decreasing sequence, indexed with j, of nodal forces $\mathbf{S}(\mathbf{u}_r, s)$ until the self-equilibrated condition $\mathbf{S}(\mathbf{u}_{rj}, s_j) = \mathbf{0}$ is satisfied. To obtain this condition, corrections $\dot{\mathbf{u}}_{rj}$

and $\dot{s}$ for the jth iteration are defined as:

$$\begin{cases} \mathbf{S}(\mathbf{u}_{rj+1}, s_{j+1}) = \mathbf{S}(\mathbf{u}_{rj}, s_j) + \mathbf{K}_j \dot{\mathbf{u}}_{rj} + \mathbf{y}_j \dot{s}_j = \mathbf{0} \\ \mathbf{y}_j^T \dot{\mathbf{u}}_{rj} = \mathbf{0} \end{cases} \tag{3.8}$$

where $\mathbf{K}_j$ and $\mathbf{y}_j$ are the initial tangent in $(\mathbf{u}_{rj}, s_j)$ of the nodal force $\mathbf{S}(\mathbf{u}_{rj}, s_j)$, i.e.

$$\begin{cases} \mathbf{K}_j = \left. \frac{\partial \mathbf{S}(\mathbf{u}_r, s)}{\partial \mathbf{u}_r} \right|_{(\mathbf{u}_{rj}, s_j)} \\ \mathbf{y}_j = \left. \frac{\partial \mathbf{S}(\mathbf{u}_r, s)}{\partial s} \right|_{(\mathbf{u}_{rj}, s_j)} \end{cases} \tag{3.9}$$

To improve the efficiency of the solution process and to guarantee convergence of the iterative scheme, $\mathbf{K}_j$ is taken as the elastic stiffness matrix of the system $\mathbf{K}_e$, defined once and for all at the start of the process. This allows the new estimates to be calculated as:

$$\begin{cases} \mathbf{u}_{rj+1} = \mathbf{u}_{rj} + \dot{\mathbf{u}}_{rj} \\ s_{j+1} = s_j + \dot{s}_j \end{cases} \qquad \begin{cases} \dot{\mathbf{u}}_{rj} = -\mathbf{K}_e^{-1}(\mathbf{S}_j + \dot{s}_j \mathbf{y}_j) \\ \dot{s}_j = -\frac{\mathbf{y}_j^T \mathbf{K}_e^{-1} \mathbf{S}_j}{\mathbf{y}_j^T \mathbf{K}_e^{-1} \mathbf{y}_j} \end{cases} \tag{3.10}$$

The solution provided at each step k satisfies the plastic admissibility and self-equilibrium condition while the multiplier $s^{(k)}$ is less than or equal to s_p. As such, the solution process is terminated when $s^{(k)} = s^{(k-1)}$, providing the shakedown multiplier.

In addition to the self-stresses, $\boldsymbol{\rho}^{(k)}$ and displacements, $\mathbf{u}_r^{(k)}$, the solution process can also produce estimates of the total plastic strains to occur during the shakedown process, $\boldsymbol{\epsilon}_p$, through the following expression:

$$\boldsymbol{\epsilon}_p = \sum_{k=0}^{K} \boldsymbol{\epsilon}_p^{(k)} = \sum_{k=0}^{K} (\mathbf{B}\mathbf{u}_r^{(k)} - \mathbf{E}^{-1}\boldsymbol{\rho}^{(k)}) \tag{3.11}$$

with K the total number of steps required in obtaining s_p.

The plastic strains and deformations provided by this iterative scheme obviously follow

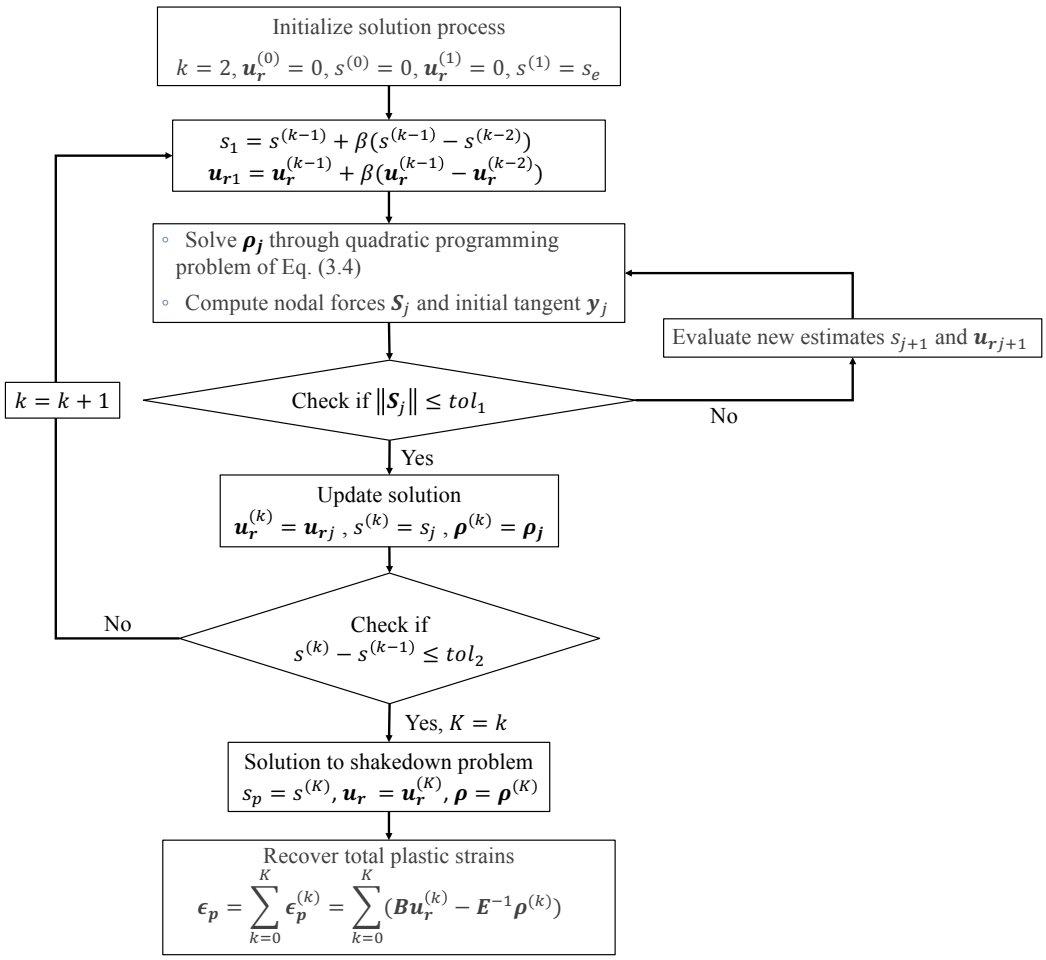

Figure 3.1: Flowchart of the strain-based iterative dynamic shakedown algorithm.

the simulated load path. In general, this load path will differ from the actual load path followed during the adaptation process under the prescribed load history $\mathbf{F}(t; \bar{v}_y, \alpha)$ calibrated to a mean wind speed $\bar{v}_y$ at the building top with a mean recurrence interval (MRI) of y years, where α is the direction of wind with respect to the building. However, as will be outlined in the following, under certain conditions of particular practical interest, the simulated load path will provide a good approximation of the actual load path followed by the structure under $\mathbf{F}(t; \bar{v}_y, \alpha)$.

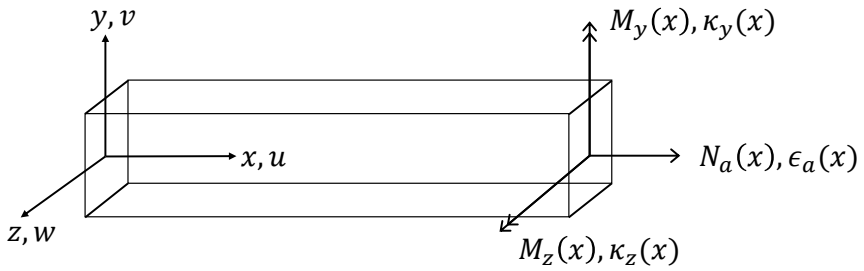

Figure 3.2: Displacements, section forces and deformations for three-dimensional beam-column elements.

3.4 A Strain-driven Distributed Plasticity Model

To model the distribution of plasticity along structural elements as they experience inelasticity, a fiber-based finite element formulation is outlined in this section. To this end, state-of-art displacement-based (DB) finite elements are first introduced for modeling distributed plasticity. The dynamic shakedown framework is then formulated within this setting.

3.4.1 Mechanical model

The fiber-based formulation considered in this work is based on Euler-Bernoulli beam theory for which the displacement field of a three-dimensional (3D) element is given by:

$$\mathbf{u}(x) = \begin{bmatrix} u(x) & v(x) & w(x) \end{bmatrix}^T \tag{3.12}$$

where $u(x)$, $v(x)$ and $w(x)$ are displacements in x, y and z-direction respectively, as shown in Figure 3.2. The section deformation vector, which contains the axial strain $\epsilon_a(x)$ and curvatures $\kappa_z(x)$ and $\kappa_y(x)$, is given by

$$\begin{aligned} \mathbf{d}(x) &= \begin{bmatrix} \epsilon_a(x) & \kappa_z(x) & \kappa_y(x) \end{bmatrix}^T \\ &= \begin{bmatrix} \dfrac{\partial u(x)}{\partial x} & \dfrac{\partial^2 v(x)}{\partial x^2} & -\dfrac{\partial^2 w(x)}{\partial x^2} \end{bmatrix}^T \end{aligned} \tag{3.13}$$

The behavior at a section is described in terms of several longitudinal fibers in which the section has be subdivided. The geometric location of each fiber can be fully described by the location of the centroid of the fiber area A_f with respect to a local reference system (y, z) with origin coinciding with the neutral axis of the section, as illustrated in Figure 3.3 for a rectangular section. From the assumption that plane sections remain plane during the element deformation history, the fiber strains and stresses act parallel to the neutral axis following a uniaxial relation. Hence, the vector collecting all fiber strains over the section, $\boldsymbol{\epsilon}(x)$, is related to section deformations as follows:

$$\boldsymbol{\epsilon}(x) = \mathbf{l}(x)\mathbf{d}(x) \tag{3.14}$$

where $\mathbf{l}(x)$ is the linear section compatibility matrix defined as:

$$\mathbf{l}(x) = \begin{bmatrix} 1 & -y_1 & z_1 \\ 1 & -y_2 & z_2 \\ \vdots & \vdots & \vdots \\ 1 & -y_{n_f} & z_{n_f} \end{bmatrix} \tag{3.15}$$

with (y_i, z_i) the location of the ith fiber of the section and n_f the total number of fibers of the section. The corresponding fiber stresses of the section are then obtained through the following constitutive relation:

$$\boldsymbol{\sigma}(x) = \mathbf{E}_f(x)\boldsymbol{\epsilon}(x) \tag{3.16}$$

where $\mathbf{E}_f(x)$ is a diagonal matrix containing the tangent moduli of all fibers, as follows:

$$\mathbf{E}_f(x) = \begin{bmatrix} E_{f_1} & 0 & \cdots & 0 \\ 0 & E_{f_2} & \cdots & 0 \\ \vdots & \vdots & \ddots & \vdots \\ 0 & 0 & \cdots & E_{f_{n_f}} \end{bmatrix} \tag{3.17}$$

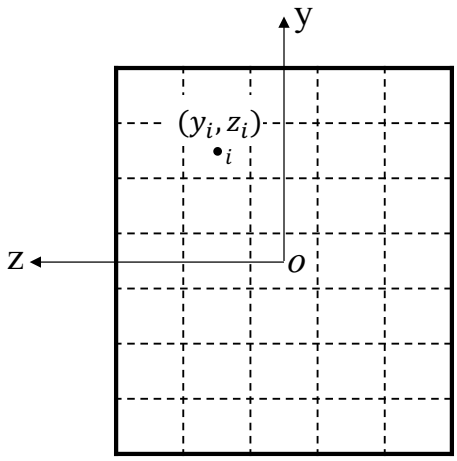

Figure 3.3: Discretization of fiber section.

Within this context, the constitutive relation of the section can be derived by integration of the fiber responses. Therefore, the section stiffness matrix $\mathbf{k}_s(x)$, assembled from the fiber stiffnesses, can be formulated as:

$$\mathbf{k}_s(x) = \mathbf{l}^T(x)\mathbf{E}_f(x)\mathbf{A}_f(x)\mathbf{l}(x) \tag{3.18}$$

where $\mathbf{A}_f(x)$ is a diagonal matrix collecting the areas of all fibers in the section:

$$\mathbf{A}_f(x) = \begin{bmatrix} A_{f_1} & 0 & \cdots & 0 \\ 0 & A_{f_2} & \cdots & 0 \\ \vdots & \vdots & \ddots & \vdots \\ 0 & 0 & \cdots & A_{f_{n_f}} \end{bmatrix} \tag{3.19}$$

The section forces, including axial force $N_a(x)$ and bending moments $M_z(x)$ and $M_y(x)$, corresponding to deformations $\mathbf{d}(x)$, are then defined through section constitutive relation,

as follows:

$$\begin{aligned}\mathbf{D}(x) &= \begin{bmatrix} N_a(x) & M_z(x) & M_y(x) \end{bmatrix}^T \\ &= \mathbf{k}_s(x)\mathbf{d}(x)\end{aligned} \tag{3.20}$$

3.4.2 Displacement-based element formulation

The displacement-based (DB) stiffness method follows the standard finite element approach, in which the displacement field of the element is expressed by the element end nodal displacements through appropriate interpolation functions (*Hughes*, 2000; *Cook et al.*, 2001). The most commonly used functions for beam-column elements are linear Lagrangian interpolation functions for the axial displacements and cubic Hermitian polynomials for the lateral translations and rotations. The degrees of freedom at each end node are three displacements and two rotations for a 3D beam-column element, as illustrated in Figure 3.4. The response in torsion is assumed linearly elastic and uncoupled from the axial and flexural response, therefore the associated displacements and forces are omitted in the following discussion. The displacement field along the element, $\mathbf{u}(x)$, can then be related to nodal displacements through the following expression:

$$\mathbf{u}(x) = \hat{\mathbf{N}}(x)\mathbf{q} \tag{3.21}$$

where $\mathbf{q} = [q_1, q_2, \cdots, q_{10}]^T$ is the nodal displacements at the element ends in local coordinate system while $\hat{\mathbf{N}}(x)$ is a matrix collecting the interpolation functions for all member end degrees of freedom, defined as:

$$\hat{\mathbf{N}}(x) = \begin{bmatrix} N_1(x) & 0 & 0 & 0 & 0 & N_2(x) & 0 & 0 & 0 & 0 \\ 0 & N_3(x) & 0 & 0 & N_4(x) & 0 & N_5(x) & 0 & 0 & N_6(x) \\ 0 & 0 & N_3(x) & -N_4(x) & 0 & 0 & 0 & N_5(x) & -N_6(x) & 0 \end{bmatrix} \tag{3.22}$$

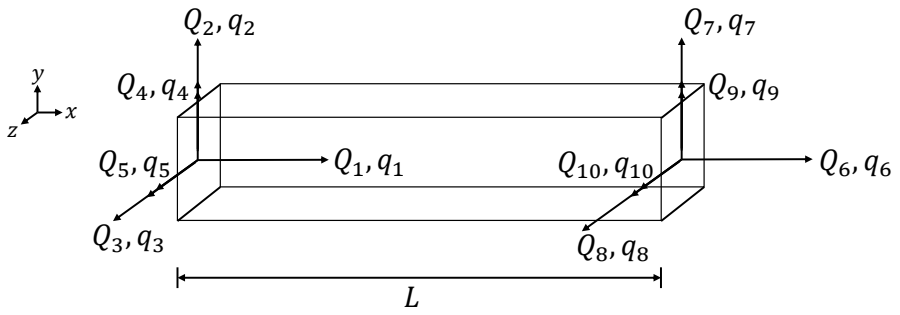

Figure 3.4: Element nodal forces and displacements.

where

$$N_1(x) = \frac{L-x}{L} \qquad N_2(x) = \frac{x}{L}$$

$$N_3(x) = 1 - \frac{3x^2}{L^2} + \frac{2x^3}{L^3} \qquad N_4(x) = x - \frac{2x^2}{L} + \frac{x^3}{L^2} \tag{3.23}$$

$$N_5(x) = \frac{3x^2}{L^2} - \frac{2x^3}{L^3} \qquad N_6(x) = -\frac{x^2}{L} + \frac{x^3}{L^2}$$

The section deformations $\mathbf{d}(x)$ are then related to the element end nodal displacements $\mathbf{q}$, as follows:

$$\mathbf{d}(x) = \hat{\mathbf{B}}(x)\mathbf{q} \tag{3.24}$$

where $\hat{\mathbf{B}}(x)$ is the strain-deformation matrix containing the first derivative of the axial displacement interpolation function and the second derivatives of the transverse displacement interpolation functions, that is

$$\hat{\mathbf{B}}(x) = \begin{bmatrix} N_1'(x) & 0 & 0 & 0 & 0 & N_2'(x) & 0 & 0 & 0 & 0 \\ 0 & N_3''(x) & 0 & 0 & N_4''(x) & 0 & N_5''(x) & 0 & 0 & N_6''(x) \\ 0 & 0 & N_3''(x) & -N_4''(x) & 0 & 0 & 0 & N_5''(x) & -N_6''(x) & 0 \end{bmatrix} \tag{3.25}$$

Since the displacement field is approximate, several displacement-based elements are required along the length of a member to represent the deformations. From the principle of virtual

displacements, the element force vector $\mathbf{Q} = [Q_1, Q_2, \cdots, Q_{10}]^T$, i.e. nodal forces at element ends, can be expressed through equilibrium in the following form:

$$\mathbf{Q} = \int_0^L \hat{\mathbf{B}}^T(x)\mathbf{D}(x)dx \tag{3.26}$$

with L being the length of the element. The corresponding element stiffness matrix $\mathbf{k}_e$, defined as derivative of the element forces with respect to the element displacements, can then be formulated in terms of section stiffness by substituting the section force vector $\mathbf{D}(x)$ in Eq. (3.26) with Eqs. (3.20) and (3.24), as follows:

$$\mathbf{k}_e = \frac{\partial \mathbf{Q}}{\partial \mathbf{q}} = \int_0^L \hat{\mathbf{B}}^T(x)\mathbf{k}_s(x)\hat{\mathbf{B}}(x)dx \tag{3.27}$$

To define a complete element stiffness matrix, the torsional stiffnesses, which are assumed uncoupled from axial and flexural stiffnesses and therefore omitted in the expression above, at the two element end nodes have to be added to the formulation of Eq. (3.27). The elastic stiffness matrix $\mathbf{K}$ for the overall system are then obtained by standard assemble over all n_b elements:

$$\mathbf{K} = \sum_{n_b} \mathcal{A}\left(\mathbf{k}_e\right) \tag{3.28}$$

The integrals involved in the element formulation, i.e. Eqs. (3.26) and (3.27), are evaluated numerically through a Gauss-Legendre integration scheme along the element, which can be expressed as:

$$I = \int_a^b f(x)dx = \sum_{n=1}^{NIP} w_n f(x_n) \tag{3.29}$$

where *NIP* is the number of integration points along the element while w_n is the weight for each integration point. Since Gauss quadrature is defined in a domain of $[-1,\ 1]$, a transformation of the interval $a \leq x \leq b$ into $-1 \leq \xi \leq 1$ is required to evaluate the integral.

The integral is then approximated by

$$\frac{b-a}{2}\sum_{n=1}^{NIP} w_n\, f(\frac{b+a}{2}+\frac{b-a}{2}\,\xi_n) \tag{3.30}$$

in which ξ_n are integration points on the abscissa. In particular in the case of Gauss-Legendre quadrature, the n-th Gauss node, ξ_n, is given by the n-th root of the *NIP*-th Legendre polynomials, $P_{NIP}(\xi)$, defined as:

$$P_{NIP}(\xi) = \frac{1}{2^{(NIP)}(NIP)!}\frac{d^{(NIP)}}{d\xi^{(NIP)}}\left(\xi^2-1\right)^{NIP} \tag{3.31}$$

The corresponding weight, w_n, is given by (*Abramowitz and Stegun*, 1972):

$$w_n = \frac{2}{(1-\xi_n^2)\left[P'_{NIP}(\xi)\right]^2} \tag{3.32}$$

Therefore, the DB element formulation involves both numerical integration error due to the approximate nature of the Gauss integration scheme and the discretization error due to the approximate nature of the displacement interpolation, which can be reduced by increasing the number of element sub-divisions (*Neuenhofer and Filippou*, 1997).

3.4.3 A fiber-based model

A finite element formulation that solves the dynamic shakedown problem through a strain-driven iterative scheme was developed in Section 3.3 in terms of generalized stress and strain, i.e. moments and rotations of plastic hinges at the element ends. In this section, this iterative scheme is further extended to account for plasticity distributed along the element. Two frameworks based on fiber stresses and section forces (axial forces and moments of a section along the element) are developed, as will be discussed in the following sections.

3.4.3.1 Problem formulation

The DB element with fiber model discussed in Sections 3.4.1 and 3.4.2 is adopted here for modeling distributed plasticity. Accordingly, the strain-driven dynamic shakedown framework has to be reformulated in terms of fiber stresses and strains instead of the generalized stresses and strains at the member ends of Section 3.3. Consider a structure, modeled by the fiber approach, subject to an external dynamic load of infinite duration and the corresponding fiber stress responses $\boldsymbol{\sigma}(t)$, the yield surfaces associated with the fibers can be expressed as:

$$\boldsymbol{\varphi}(t) = \mathbf{N}^T \boldsymbol{\sigma}(t) - \hat{\boldsymbol{\sigma}} \leq \mathbf{0} \tag{3.33}$$

where $\boldsymbol{\varphi}$ represents the yield function, $\mathbf{N}$ is the block diagonal matrix collecting the unit external normals to the yield surfaces, which, in the case of uniaxial fiber behavior, are positive and negative unit values for all fibers of the structure, leading to the following $N_f \times 2N_f$ matrix:

$$\mathbf{N} = \begin{bmatrix} 1 & -1 & & & & \\ & & 1 & -1 & & \\ & & & & \ddots & \\ & & & & 1 & -1 \end{bmatrix}_{N_f \times 2N_f} \tag{3.34}$$

where N_f is the total number of fibers used in the discretization of the structure. $\hat{\boldsymbol{\sigma}}$ is the vector collecting the yield stresses σ_y in both tension and compression (indicated with subscripts T and C) of each fiber, defined as follows:

$$\hat{\boldsymbol{\sigma}} = \begin{bmatrix} \sigma_{y_{1_T}} & \sigma_{y_{1_C}} & \sigma_{y_{2_T}} & \sigma_{y_{2_C}} & \cdots & \sigma_{y_{N_{f_T}}} & \sigma_{y_{N_{f_C}}} \end{bmatrix}^T_{1 \times 2N_f} \tag{3.35}$$

For a structure to reach the state of dynamic shakedown, i.e. the state in which a finite field of plastic strains has formed to enable the structure to respond purely elastically in

the subsequent load history, a necessary and sufficient condition is that there exists a finite time $t^* \geq 0$ and some arbitrary initial conditions such that the sum of the elastic stress solution and a time-independent self-equilibrated stress state $\boldsymbol{\sigma}_s$ lie within the elastic domain (*Polizzotto et al.*, 1993), i.e. such that the following holds:

$$\mathbf{N}^T \left(\boldsymbol{\sigma}^E(t) + \boldsymbol{\sigma}_s \right) - \hat{\boldsymbol{\sigma}} \leq \mathbf{0}, \qquad \forall t \geq t^* \tag{3.36}$$

where $\boldsymbol{\sigma}^E(t)$ is the purely elastic stress response to a dynamic load history, while $\boldsymbol{\sigma}_s$ is a time independent self stress distribution (associated with the time independent plastic distortions enabling shakedown). In this work, the special case of a not only infinite but also periodic load $\mathbf{F}(t)$ is considered, which significantly simplifies the dynamic shakedown problem. This artificial load is obtained by assuming an external load of duration T indefinitely repeated. Under these circumstances, shakedown will occur if a time independent stress distribution, $\boldsymbol{\sigma}_s$, can be found for which Eq. (3.36) is satisfied for the steady state elastic response in $[0, T]$.

To formulate the dynamic shakedown problem in terms of fiber stresses and strains, it is first convenient to consider a residual displacement increment of $\mathbf{u}_r$ and load multiplier s. The associated fiber strain increment $\boldsymbol{\epsilon}_r$, collected in a vector over the entire structure, is related through the fiber model as:

$$\boldsymbol{\epsilon}_r(\mathbf{u}_r) = \mathbf{L}\hat{\mathbf{B}}\mathbf{T}\mathbf{u}_r \tag{3.37}$$

where $\mathbf{L}$ and $\hat{\mathbf{B}}$ are respectively block-diagonal matrices collecting the section compatibility

matrix $\mathbf{l}(x)$ and strain-deformation matrix $\hat{\mathbf{B}}(x)$ of all sections of the structure:

$$\mathbf{L} = \begin{bmatrix} l(x_1) & 0 & \cdots & 0 \\ 0 & l(x_2) & \cdots & 0 \\ \vdots & \vdots & \ddots & \vdots \\ 0 & 0 & \cdots & l(x_{NIP^* n_b}) \end{bmatrix}, \quad \hat{\mathbf{B}} = \begin{bmatrix} \hat{\mathbf{B}}_{s_1} & 0 & \cdots & 0 \\ 0 & \hat{\mathbf{B}}_{s_2} & \cdots & 0 \\ \vdots & \vdots & \ddots & \vdots \\ 0 & 0 & \cdots & \hat{\mathbf{B}}_{s_{n_b}} \end{bmatrix} \tag{3.38}$$

where n_b is the total number of elements of the discretized structure while $\hat{\mathbf{B}}_{s_i}$ is the strain-deformation matrix for the ith element defined as:

$$\hat{\mathbf{B}}_{s_i} = \begin{bmatrix} \hat{\mathbf{B}}(x_1) \\ \hat{\mathbf{B}}(x_2) \\ \vdots \\ \hat{\mathbf{B}}(x_{NIP}) \end{bmatrix} \tag{3.39}$$

In Eq. (3.37), $\mathbf{T} = \mathbf{T}_C \mathbf{T}_A$ is a matrix relating residual displacements in global coordinates to element end displacements in local coordinates, i.e. $\mathbf{q} = \mathbf{T}\mathbf{u}_r$, where $\mathbf{T}_A$ is the connectivity matrix while $\mathbf{T}_C$ is the following block diagonal matrix collecting coordinate transformation matrices for all elements:

$$\mathbf{T}_C = \begin{bmatrix} \mathbf{T}_{C_1} & 0 & \cdots & 0 \\ 0 & \mathbf{T}_{C_2} & \cdots & 0 \\ \vdots & \vdots & \ddots & \vdots \\ 0 & 0 & \cdots & \mathbf{T}_{C_{n_b}} \end{bmatrix} \tag{3.40}$$

where, for a 2D element in the x-y plane, $\mathbf{T}_{C_j}$ for $j = 1, ..., n_b$ reduces to the following transformation matrix:

$$\mathbf{T}_{C_j} = \begin{bmatrix} \mathbf{R}_T & & \\ & \mathbf{R}_T & \end{bmatrix}, \text{with } \mathbf{R}_T = \begin{bmatrix} \cos\theta & \sin\theta & 0 \\ -\sin\theta & \cos\theta & 0 \\ 0 & 0 & 1 \end{bmatrix} \tag{3.41}$$

with θ the rotation counter-clockwise about the z-axis. Similar transformation matrices can be defined for 3D structures considering rotations also about x and y-axes.

Under the assumption of elastic perfectly plastic (EPP) material behavior, an admissible self stress vector $\boldsymbol{\sigma}_s$, that collects the stresses in all fibers, due to a residual strain increment $\boldsymbol{\epsilon}_r - \boldsymbol{\epsilon}_0$ can be obtained through the following return mapping scheme:

$$\boldsymbol{\sigma}_s = \boldsymbol{\sigma}_E + \Delta\boldsymbol{\sigma} = \boldsymbol{\sigma}_E - \mathbf{E}\boldsymbol{\epsilon}_p \tag{3.42}$$

where $\mathbf{E}$ is the elastic matrix defined as the following block-diagonal matrix that contains $\mathbf{E}_f(x)$ of all sections:

$$\mathbf{E} = \begin{bmatrix} \mathbf{E}_f(x_1) & 0 & \cdots & 0 \\ 0 & \mathbf{E}_f(x_2) & \cdots & 0 \\ \vdots & \vdots & \ddots & \vdots \\ 0 & 0 & \cdots & \mathbf{E}_f(x_{NIP^* n_b}) \end{bmatrix} \tag{3.43}$$

$\boldsymbol{\sigma}_E = \boldsymbol{\sigma}_0 + \mathbf{E}\left(\boldsymbol{\epsilon}_r - \boldsymbol{\epsilon}_0\right)$ is the elastic predictor of $\boldsymbol{\sigma}_s$ with $\boldsymbol{\sigma}_0$ and $\boldsymbol{\epsilon}_0$ the initial stress and strain distribution while $\Delta\boldsymbol{\sigma} = -\mathbf{E}\boldsymbol{\epsilon}_p$ with $\boldsymbol{\epsilon}_p$ the plastic strain, i.e. plastic part of $\boldsymbol{\epsilon}_r$, governed by the associated flow rule:

$$\dot{\boldsymbol{\epsilon}}_p = \mathbf{N}\dot{\boldsymbol{\lambda}}, \qquad \dot{\boldsymbol{\lambda}} \geq \mathbf{0} \tag{3.44}$$

where $\dot{\boldsymbol{\lambda}}$ is the vector of plastic multipliers satisfying the following loading-unloading condition and consistency condition:

$$\boldsymbol{\varphi}^T\dot{\boldsymbol{\lambda}} = \dot{\boldsymbol{\varphi}}^T\dot{\boldsymbol{\lambda}} = 0 \tag{3.45}$$

Instead of solving $\boldsymbol{\sigma}_s$ directly through Eq. (3.42), an equivalent approach is to solve the following Haar-Kàrmàn condition that is based on solving the standard and strictly convex

quadratic programming problem (QPP):

$$\begin{aligned} &\min_{\Delta\boldsymbol{\sigma}} \frac{1}{2}\Delta\boldsymbol{\sigma}^T\mathbf{E}^{-1}\Delta\boldsymbol{\sigma} \\ &\text{subject to} \\ &\bar{\boldsymbol{\sigma}}^s = \max_{0\le t\le T} \mathbf{N}^T\boldsymbol{\sigma}_s^E(t) \\ &\boldsymbol{\phi}_s = s\bar{\boldsymbol{\sigma}}^s + \mathbf{N}^T\boldsymbol{\sigma}_s - \hat{\boldsymbol{\sigma}} \le \mathbf{0} \end{aligned} \tag{3.46}$$

where $\boldsymbol{\sigma}_s^E(t)$ consists the purely elastic fiber stress responses in $[0, T]$, which can be efficiently estimated by solving the dynamic equation of motion of the system in a modal framework with the fiber discretization described in Sections 3.4.1 and 3.4.2, while $\bar{\boldsymbol{\sigma}}^s$ is the maximum stress demand for each yield mode of each fiber of the system. The last condition of Eq. (3.46) ensures that the solutions in terms of $\boldsymbol{\sigma}_s(\mathbf{u}_r, s)$ satisfy the shakedown feasibility condition $\boldsymbol{\phi}_s \le \mathbf{0}$. To further satisfy the dynamic shakedown criterion, $\boldsymbol{\sigma}_s(\mathbf{u}_r, s)$ must also be self-equilibrated, which can be imposed in terms of the internal force vector, $\mathbf{S}(\mathbf{u}_r, s)$, as follows:

$$\mathbf{S}(\mathbf{u}_r, s) = \mathbf{T}^T\mathbf{D}_{sQ}\boldsymbol{\sigma}_s(\mathbf{u}_r, s) = \mathbf{0} \tag{3.47}$$

where $\mathbf{D}_{sQ}$ is the following block diagonal matrix collecting the matrices $\mathbf{D}_{sQ_i}$ transforming fiber stresses $\boldsymbol{\sigma}_s(\mathbf{u}_r, s)$ to element end forces $\mathbf{Q}$ for all n_b elements:

$$\mathbf{D}_{sQ} = \begin{bmatrix} \mathbf{D}_{sQ_1} & 0 & \cdots & 0 \\ 0 & \mathbf{D}_{sQ_2} & \cdots & 0 \\ \vdots & \vdots & \ddots & \vdots \\ 0 & 0 & \cdots & \mathbf{D}_{sQ_{n_b}} \end{bmatrix} \tag{3.48}$$

For each element, indexed with i, the transformation matrix $\mathbf{D}_{sQ_i}$ is defined through numerical integration as:

$$\mathbf{D}_{sQ_i} = \sum_{n=1}^{NIP} \frac{L_i}{2}\hat{\mathbf{B}}^T(x_n)\mathbf{l}^T(x_n)\mathbf{A}_f(x_n)w_n \tag{3.49}$$

By combining the self-equilibrated condition with the shakedown admissible stress state $\boldsymbol{\sigma}_s(\mathbf{u}_r, s)$, the dynamic shakedown problem can be written in the following form:

$$s_p = \max s : \exists \mathbf{u}_r : \mathbf{S}(\mathbf{u}_r, s) = \mathbf{0} \tag{3.50}$$

Eq. (3.50) is solved by an incremental iterative scheme that produces a series of admissible safe states $(s^{(k)}, \boldsymbol{\sigma}_s^{(k)}, \mathbf{u}_r^{(k)})$ that are self-equilibrated with monotonically non-decreasing $s^{(k)}$, eventually converging to the shakedown multiplier s_p when $s^{(k)} = s^{(k-1)}$.

It is worth mentioning that, in this formulation, the elastic matrix $\mathbf{E}$ is a simple diagonal matrix, i.e. the entries outside the main diagonal are all zero. Therefore, Eq. (3.46) that minimizes the objective function $\frac{1}{2}\Delta\boldsymbol{\sigma}^T\mathbf{E}^{-1}\Delta\boldsymbol{\sigma}$ can be decoupled and solved individually for each fiber. This particular characteristic greatly improves the scalability of the framework and facilitates the solution process that can be easily and efficiently applied to high-dimensional finite-element discretizations.

3.4.3.2 An iterative solution scheme

The dynamic shakedown problem described above can be solved through an iterative scheme, as discussed in Section 3.3. It is reformulated here for the fiber-based framework.

The iterative process starts from the elastic limit state ($s^{(1)} = s_e, \boldsymbol{\sigma}_s^{(1)} = \mathbf{0}, \mathbf{u}_r^{(1)} = \mathbf{0}$), where s_e is the maximum amount the external loads can be amplified before inelasticity will occur. Within each step k of the iterative process, the multiplier s and residual displacement field $\mathbf{u}_r$ are initialized through the following equations:

$$\begin{aligned} s_1 &= s^{(k-1)} + \beta(s^{(k-1)} - s^{(k-2)}) \\ \mathbf{u}_{r1} &= \mathbf{u}_r^{(k-1)} + \beta(\mathbf{u}_r^{(k-1)} - \mathbf{u}_r^{(k-2)}) \end{aligned} \tag{3.51}$$

with β being an appropriate scaling factor. To reach the self-equilibrated condition, the multiplier s and residual displacement field $\mathbf{u}_r$ are recursively updated, indexed with j,

through the following conditions:

$$\begin{cases} \mathbf{u}_{rj+1} = \mathbf{u}_{rj} + \dot{\mathbf{u}}_{rj} \\ s_{j+1} = s_j + \dot{s}_j \end{cases} \qquad \begin{cases} \mathbf{S}(\mathbf{u}_{rj+1}, s_{j+1}) = \mathbf{S}(\mathbf{u}_{rj}, s_j) + \mathbf{K}_j \dot{\mathbf{u}}_{rj} + \mathbf{y}_j \dot{s}_j = \mathbf{0} \\ \mathbf{y}_j^T \dot{\mathbf{u}}_{rj} = \mathbf{0} \end{cases} \tag{3.52}$$

where $\mathbf{S}(\mathbf{u}_{rj}, s_j)$ is estimated by Eq. (3.47) in which $\boldsymbol{\sigma}_s(\mathbf{u}_r, s)$ is solved through Eq. (3.46) while $\mathbf{K}_j$ and $\mathbf{y}_j$ are the initial tangent in $(\mathbf{u}_{rj}, s_j)$ of the nodal force $\mathbf{S}(\mathbf{u}_{rj}, s_j)$ given by

$$\begin{cases} \mathbf{K}_j = \left. \frac{\partial \mathbf{S}(\mathbf{u}_r, s)}{\partial \mathbf{u}_r} \right|_{(\mathbf{u}_{rj}, s_j)} \\ \mathbf{y}_j = \left. \frac{\partial \mathbf{S}(\mathbf{u}_r, s)}{\partial s} \right|_{(\mathbf{u}_{rj}, s_j)} \end{cases} \tag{3.53}$$

In particular, to improve the efficiency of the solution process, $\mathbf{K}_j$ can be taken as the elastic stiffness matrix of the system $\mathbf{K}$, defined at the start of the process through Eq. (3.28). In this way, the iterative process produces a sequence of monotonically decreasing $\mathbf{S}(\mathbf{u}_r, s)$ until the self-equilibrated condition is satisfied in each step k, therefore resulting in a series of self-equilibrated and admissible safe states $(s^{(k)}, \boldsymbol{\sigma}_s^{(k)}, \mathbf{u}_r^{(k)})$. The solution process is then terminated when reaching a multiplier of interest, e.g. $s = 1$, or through the convergence to the shakedown multiplier s_p.

3.4.4 A section-based model

The framework described in Section 3.4.3 provides solutions to the dynamic shakedown problem considering distributed plasticity in terms of fiber stress and strain. A limitation of this approach is that it requires linear elastic-perfectly plastic (EPP) material behavior for each fiber of the discretization. Hence, the fiber-based framework cannot be immediately applied to reinforced concrete structures due to the fact that concrete materials always exhibit a nonlinear constitutive relationship between stress and strain due to the lack of tensile strength. In other words, at the level of the fibers, concrete materials never exhibit linear elastic behavior. To circumvent this issue, it is here proposed to reformulate the

strain-driven solution process in terms of section forces, e.g. section axial forces and bending moments, along the element instead of fiber stresses. In this setting, the section forces are assumed to follow a linear EPP behavior, allowing the application of the strain-driven iterative scheme. Following this approach, only plasticity distributed along the element is taken into consideration while that within the section is assumed to instantaneously occur once an appropriate yield condition is satisfied. In this section, the necessary reformulations of the strain-driven dynamic shakedown framework for implementing the aforementioned section-based approach are presented in detail.

3.4.4.1 Problem formulation: section-level formulation

Following the strain-driven framework, the solution process commences from the elastic limit state with an increment in residual displacement $\mathbf{u}_r$ and load multiplier s. Rather than relating $\mathbf{u}_r$ to the fiber strains as in Section 3.4.3, it is referred to section residual deformations $\mathbf{d}_r$, i.e. axial strains and curvatures, of all sections of the element. The kinematic equation of Eq. (3.37) then becomes:

$$\mathbf{d}_r(\mathbf{u}_r) = \hat{\mathbf{B}}\mathbf{T}\mathbf{u}_r \tag{3.54}$$

Furthermore, the time-dependent self stress of Eq. (3.42) is expressed in terms of section forces $\mathbf{D}_s$, i.e. axial force and moments of all sections, as follows:

$$\begin{aligned} \mathbf{D}_s &= \mathbf{D}_E + \Delta\mathbf{D} = \mathbf{D}_E - \mathbf{k}_s\mathbf{d}_p \\ \mathbf{D}_E &= \mathbf{D}_0 + \mathbf{k}_s\left(\mathbf{d}_r - \mathbf{d}_0\right) \end{aligned} \tag{3.55}$$

where $\mathbf{k}_s$ is the following block-diagonal matrix that contains section stiffnesses, $\mathbf{k}_s(x)$, of all sections:

$$\mathbf{k}_s = \begin{bmatrix} \mathbf{k}_s(x_1) & 0 & \cdots & 0 \\ 0 & \mathbf{k}_s(x_2) & \cdots & 0 \\ \vdots & \vdots & \ddots & \vdots \\ 0 & 0 & \cdots & \mathbf{k}_s(x_{NIP^* n_b}) \end{bmatrix} \tag{3.56}$$

$\mathbf{D}_0$ and $\mathbf{d}_0$ are respectively vectors of the initial section forces and deformations while $\mathbf{d}_p$ is the plastic section deformation vector. The corresponding element end force vector $\mathbf{S}(\mathbf{u}_r, s)$ in global coordinates can be rewritten as:

$$\mathbf{S}(\mathbf{u}_r, s) = \mathbf{T}^T \mathbf{D}_{DQ} \mathbf{D}_s(\mathbf{u}_r, s) \tag{3.57}$$

where $\mathbf{D}_{DQ}$ is the following block diagonal matrix collecting the matrices $\mathbf{D}_{DQ_j}$ transforming the section forces $\mathbf{D}_s(\mathbf{u}_r, s)$ into element end forces $\mathbf{Q}$ for all elements:

$$\mathbf{D}_{DQ} = \begin{bmatrix} \mathbf{D}_{DQ_1} & 0 & \cdots & 0 \\ 0 & \mathbf{D}_{DQ_2} & \cdots & 0 \\ \vdots & \vdots & \ddots & \vdots \\ 0 & 0 & \cdots & \mathbf{D}_{DQ_{n_b}} \end{bmatrix} \tag{3.58}$$

For each element, the transformation matrix is once again defined through numerical integration as:

$$\mathbf{D}_{DQ_i} = \sum_{n=1}^{NIP} \frac{L_i}{2} \hat{\mathbf{B}}^T(x_n) w_n \tag{3.59}$$

In this context, the iterative process is carried out for estimating the inelastic deformation of the structural system. Within each step k of the process, the time-dependent generalized self stress, $\mathbf{D}_s$, is evaluated iteratively based on $\mathbf{u}_r$ and s until the self-equilibrated condition, $\mathbf{S}(\mathbf{u}_r, s) = \mathbf{0}$, is reached. The corresponding QPP problem of Eq. (3.46) for solving $\mathbf{D}_s$ is reformulated in terms of section forces as follows:

$$\begin{aligned} &\min_{\Delta \mathbf{D}} \frac{1}{2} \Delta \mathbf{D}^T \mathbf{k}_s^{-1} \Delta \mathbf{D} \\ &\text{subject to} \\ &\bar{\mathbf{D}}^s = \max_{0 \le t \le T} \mathbf{N}^T \mathbf{D}_s^E(t) \\ &\boldsymbol{\phi}_s = s\bar{\mathbf{D}}^s + \mathbf{N}^T \mathbf{D}_s - \mathbf{R} \le 0 \end{aligned} \tag{3.60}$$

where $\mathbf{D}_s^E(t)$ is the purely elastic section forces in $[0,T]$ that can be efficiently solved by modal analysis and the DB formulation of Section 3.4.2. The block diagonal matrix $\mathbf{N}$ now collects the unit external normals to the piecewise linearized yield surfaces of each section, as follows:

$$\mathbf{N} = \begin{bmatrix} \mathbf{N}_{s_1} & & & \\ & \mathbf{N}_{s_2} & & \\ & & \ddots & \\ & & & \mathbf{N}_{s_{n_s}} \end{bmatrix} \tag{3.61}$$

where $\mathbf{N}_{s_i}, i = 1, \cdots, n_s$ is the matrix containing external normal vectors $\mathbf{n}_k$ of the m linearized yield surfaces of the ith section with n_s being the total number of sections of the structure:

$$\mathbf{N}_{s_i} = \begin{bmatrix} \mathbf{n}_1 & \mathbf{n}_2 & \cdots & \mathbf{n}_m \end{bmatrix} \tag{3.62}$$

In Eq. (3.60), $\mathbf{R}$ defines the corresponding plastic resistances, defined as the distances from the origin to each linearized yield surface, of all sections and is given by:

$$\mathbf{R} = \begin{bmatrix} \mathbf{R}_{s_1} \\ \mathbf{R}_{s_2} \\ \vdots \\ \mathbf{R}_{s_{n_s}} \end{bmatrix} \tag{3.63}$$

where $\mathbf{R}_{s_i}, i = 1, \cdots, n_s$ is a $m \times 1$ plastic resistance vector for the ith section whose vector size depends on the number of linearized yield surfaces m.

3.4.4.2 An iterative solution scheme: section-level formulation

Within this context, the iterative solution scheme of Section 3.4.3.2 is once again adopted for solving the section-based dynamic shakedown problem. The internal force vector $\mathbf{S}(\mathbf{u}_{rj}, s_j)$ in Eq. (3.52) is now calculated by Eq. (3.57) with section force $\mathbf{D}_s(\mathbf{u}_r, s)$ solved through the QPP problem of Eq. (3.60). As such, the solution process produces a sequence of self-

equilibrated and admissible safe states $(s^{(k)}, \mathbf{D}_s^{(k)}, \mathbf{u}_r^{(k)})$ until reaching a multiplier of interest, e.g. unamplified load with $s = 1$, or convergence to the shakedown multiplier s_p.

3.5 Summary and Conclusions

The primary objective of the work outlined in this chapter was the development of an efficient framework for estimating the inelastic responses of multi-degree-of-freedom wind-excited building system. Both concentrated and distributed plasticity modeling environments were introduced. Considering the behaviors of different materials, and in particular the difficulty arising in treating concrete, two specific distributed models were developed based on fiber stresses and section forces, respectively. For the fiber-based framework, plasticity distributing over the section height is further taken into consideration.

CHAPTER IV

A Probabilistic Dynamic Shakedown Framework for Stochastic Excitations

4.1 Overview

The primary goals of the work outlined in this chapter are:

1. Development of a framework for the probabilistic generation of any number of wind load histories that captures not only the record-to-record variability in the dynamic wind loads, but also the physics behind any complex aerodynamic phenomenon, such as acrosswind wake-induced vortex shedding, captured in wind tunnel tests.

2. Development of a stochastic simulation framework for estimating the susceptibility to collapse of wind-excited structures within the setting of state-of-the-art probabilistic performance-based wind engineering frameworks of Chapter II and the dynamic shakedown models outlined in Chapter III.

In reaching the the first goal, a data-driven simulation model is developed based on spectral proper orthogonal decomposition (POD) (*Li and Kareem*, 1991, 1993, 1997; *Chen and Kareem*, 2005; *Peng et al.*, 2017). In particular, by allowing the frequency dependent spectral eigenvalues Λ_j and eigenvectors $\mathbf{\Psi}_j$ of the external wind loads to be estimated directly from classic wind tunnel data, a framework is outlined that can simulate dynamic

wind load traces that contain any building induced aerodynamics captured in wind tunnel tests. Once the eigenvalues Λ_j and eigenvectors $\mathbf{\Psi}_j$ of the external loads are known, any number of realizations of the external load histories can be obtained using a classic spectral representation algorithm based on the Fast Fourier Transform (*Deodatis*, 1996). Because only the first few eigenvalues/eigenvectors are generally necessary for accurately representing wind loads, the model is computationally extremely efficient allowing for the generation of probabilistically consistent wind loads of long duration in a matter of seconds. An alternative quasi-steady model is also outlined that can be used in cases when wind tunnel data is unavailable.

In reaching the second goal, the dynamic shakedown models outlined in the Chapter III are integrated with the above outlined stochastic wind load models within a stochastic simulation framework based on a Monte Carlo scheme. The efficiency with which any given stochastic wind load history can be analyzed ensures the computational feasibility of the scheme, while the possibility of estimating not only the state of shakedown for any given load history but also the deformations at shakedown enables a general definition of system-level collapse susceptibility.

4.2 Problem Setting

The system-level performance assessment of Eq. (2.4) requires estimation of the probability of collapse susceptibility, $P(C)$, of the structure. In general, a wind-excited structure can be identified as susceptible to collapse under two possible failure scenarios: (1) failure due to low cycle fatigue (acrosswind failure) or incremental plastic collapse (alongwind failure); and (2) failure due to excessive deformations, e.g. excessive residual displacements or hinge rotations. In order to estimate the probability associated with the first failure scenario, dynamic shakedown theory can be applied to define a limit state separating susceptibility to low cycle fatigue and/or incremental plastic collapse from a safe state, as presented in Chapter II. This method, however, does not provide any information on the plastic strains and

deformations of the structure, which are essential for estimating the second failure scenario as well as $P(DV > dv|NC)$.

To address this issue, a stochastic simulation scheme is outlined in this chapter based on the models detailed in Chapter III. In particular, the method is based on simulating a non-linear load deformation path (through the path-following iterative schemes of Chapter III) for each wind load history of interest. The efficiency with which solutions can be found for any given load history of long duration (hours) allows simulation methods to be directly used to estimate quantities such as $P(DV > dv|NC)$ and/or probabilities associated with exceeding strain limits in any inelastic response of interest.

4.3 The Proposed Framework

Sections 3.3 and 3.4 presented the solution schemes for evaluating the dynamic shakedown limit state and the associated plastic deformations and strains of the structure under a prescribed periodic and infinite duration load history. This solution method cannot be directly applied to wind storms due to their finite length. Also, even for a periodic and infinite duration wind load, the simulated and actual load paths will in general differ therefore limiting the usefulness of the plastic deformations and strains obtained from the solution scheme. However, under the conditions stated below, these limitations can be circumvented.

4.3.1 The artificial wind storm

A solution to the finiteness of real wind storms that has been recently proposed in *Tabbuso et al.* (2016) is to consider the wind storm of duration T indefinitely repeated, thereby creating a periodic and infinite excitation that meets the assumptions of dynamic shakedown theory considered in this work. This "artificial" wind storm is mathematically defined as:

$$\tilde{\mathbf{F}}(t + nT; \bar{v}_y, \alpha) = \mathbf{F}(t; \bar{v}_y, \alpha) \quad \text{for} \quad \begin{cases} n = 0, 1, ..., +\infty \\ t \in [0, T] \end{cases} \tag{4.1}$$

and is illustrated in Figure 4.1. In particular, it should be observed that no restrictions on the loads of the "actual" wind storm $\mathbf{F}(t;\bar{v}_y,\alpha)$ have been imposed in defining $\tilde{\mathbf{F}}(t+nT;\bar{v}_y,\alpha)$. Therefore, $\mathbf{F}(t;\bar{v}_y,\alpha)$ can be stationary or non-stationary which enables the consideration of both synoptic and non-synoptic wind events in the proposed framework. The basic idea in defining $\tilde{\mathbf{F}}$ is that now the shakedown models of Chapter III can be applied to estimate whether the state of shakedown occurs. If so, then the structure must necessarily be safe against incremental plastic collapse as well as low-cycle fatigue for the "actual" wind storm $\mathbf{F}(t;\bar{v}_y,\alpha)$. In other words, if the structure is safe for $\tilde{\mathbf{F}}$, it must be safe for $\mathbf{F}$.

4.3.2 The simulated load path

By using the iterative schemes of Chapter III , estimates of the plastic strains, $\boldsymbol{\epsilon}_p$, and deformations, $\mathbf{u}_r$, will also be available. As already mentioned, the general validity of these is unknown as the load path is simulated and will in general differ from the actual load path. However, under the following two conditions, the simulated load path will provide a good approximation of the actual load path:

1. The structure at $t=0$ has no plastic deformations, i.e. $\boldsymbol{\epsilon}_p = 0$.

2. The loads $\mathbf{F}(t;\bar{v}_y,\alpha)$ start at zero and end at zero, i.e. the wind storm is simulated over its entirety.

Indeed, if there are no previous plastic deformations, then $\boldsymbol{\epsilon}_p$ must be entirely produced during $\tilde{\mathbf{F}}$. Therefore, the simulated and actual load paths start from the same initial conditions. Also, because $\mathbf{F}$ is simulated over the entirety (i.e. from zero loads to zero loads), the structure will be in a steady state response regime from $t=0$. In other words, no initial transient phase exists that could produce plastic strains and deformations not considered in the simulated load path which is based on the assumption of a steady state response regime in T. Finally, it should be observed that, under these conditions, the actual load path must be essentially monotonic as any alternating plasticity occurring in any given period T would

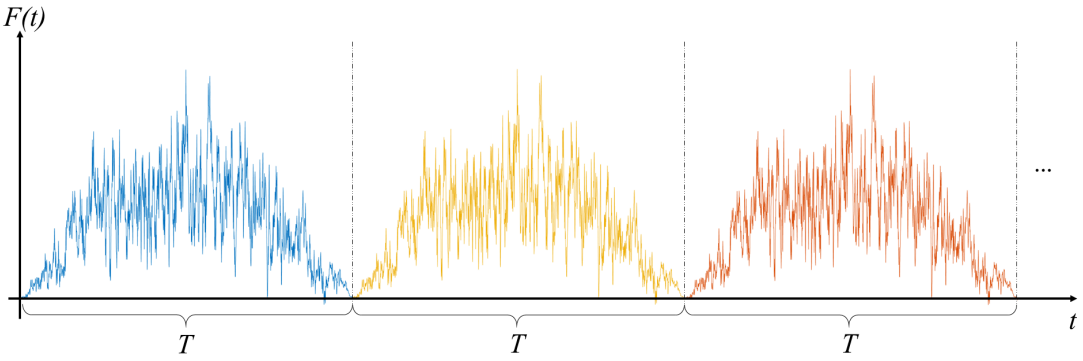

Figure 4.1: Illustration of a generic component of $\tilde{\mathbf{F}}$ for a wind storm of duration T.

be repeated indefinitely, therefore eliminating the possibility of shakedown. This behavior is reproduced by the simulated load path, which is also monotonic.

4.3.3 Remarks

Before closing this section, it should be observed that the plastic strains and deformations estimated by the proposed framework are an upper bound on the actual plastic strains and deformations, as the real wind storm has a duration of T while the estimated plastic strains and deformations are for $\tilde{\mathbf{F}}$ that has an infinite duration. This provides a safety factor against any differences between the actual and simulated load paths. Also, it should be observed that the need to simulate the wind loads from zero to zero does not pose any particular difficulty. Indeed, this condition is to ensure the absence of fictitious transient responses that would create artificial plastic strains and deformations. Therefore, any reasonable ramp-up/down can be used, including linear.

4.4 Stochastic Wind Load Models

4.4.1 Wind tunnel driven model

In order to study the record-to-record variability in the inelastic response of the system as well as characterize these responses probabilistically in a fully performance-based design framework such as that outlined in Chapter II, multiple wind load histories are required,

i.e. multiple realizations of $\mathbf{F}(t;\bar{v}_y,\alpha)$ are necessary. While multiple wind tunnel tests could be carried out, one for each $\mathbf{F}(t;\bar{v}_y,\alpha)$, this fast becomes prohibitive from a time and cost perspective, especially for frameworks based in Monte Carlo simulation where thousands of wind records are necessary. To overcome this, simulation models can be used, which allows any number of realizations of $\mathbf{F}(t;\bar{v}_y,\alpha)$ to be rapidly generated.

In general, $\mathbf{F}(t;\bar{v}_y,\alpha)$ may be modeled as a vector-valued stochastic process (*Chen and Kareem*, 2005). Classic models for simulating $\mathbf{F}$ are based on a quasi-steady assumption which, in general, will not hold for high-rise structures where complex aerodynamic phenomena, such as acrosswind wake-induced vortex shedding, can occur. To overcome this, a data-driven spectral proper orthogonal decomposition (POD) model is here considered for $\mathbf{F}$. In this approach, $\mathbf{F}$ is decomposed into N_l, with N_l the total dimension of $\mathbf{F}$, independent vector valued subprocesses and therefore as (*Li and Kareem*, 1991, 1993, 1997; *Chen and Kareem*, 2005; *Peng et al.*, 2017):

$$\mathbf{F}(t;\bar{v}_y,\alpha)=\sum_{j=1}^{N_l}\mathbf{F}_j(t;\bar{v}_y,\alpha) \tag{4.2}$$

with $\mathbf{F}_j(t)$ the jth subprocess of $\mathbf{F}(t)$ which can be given the following spectral representation:

$$\mathbf{F}_j(t;\bar{v}_y,\alpha)=\sum_{k=1}^{K}2|\mathbf{\Psi}_j(\omega_k;\alpha)|\sqrt{\Lambda_j(\omega_k;\bar{v}_y,\alpha)\Delta\omega}\times\cos(\omega_k t+\boldsymbol{\theta_j}(\omega_k)+\vartheta_{kj}) \tag{4.3}$$

where Λ_j is the jth frequency dependent eigenvalue of $\mathbf{F}$ with $\mathbf{\Psi}_j$ the corresponding frequency dependent eigenvector, $\Delta\omega$ is the frequency increment with a Nyquist (cutoff) frequency $K\Delta\omega/2$ with K the total number of discrete frequencies in the interval $[0,K\Delta\omega]$, $\omega_k=k\Delta\omega$, ϑ_{kj} are random variables with uniform distribution in $[0,2\pi]$, while $\boldsymbol{\theta}_j$ is a vector of complex angles with ith component given by:

$$\theta_{ji}(\omega_k)=\tan^{-1}\left\{\frac{\mathrm{Im}[\Psi_{ji}(\omega_k)]}{\mathrm{Re}[\Psi_{ji}(\omega_k)]}\right\} \tag{4.4}$$

where $\mathrm{Im}[\Psi_{ij}(\omega_k)]$ and $\mathrm{Re}[\Psi_{ij}(\omega_k)]$ are the imaginary and real parts of the ith component of the jth frequency dependent eigenvector of $\mathbf{F}$.

Once the eigenvalues Λ_j and eigenvectors $\mathbf{\Psi}_j$ of $\mathbf{F}$ are known, Eq. (4.2) can be used to simulate realizations of the vector-valued stochastic process $\mathbf{F}$ by simulating independent realizations of the subprocesses using a classic spectral representation algorithm based on the Fast Fourier Transform (*Deodatis*, 1996). Because the subprocesses can be generated independently, and only the first few eigenvalues/eigenvectors are generally necessary for accurately representing wind loads, Eq. (4.2) provides a computationally convenient representation of $\mathbf{F}$. In particular, in this work, Λ_j and $\mathbf{\Psi}_j$ are directly estimated from wind tunnel data therefore ensuring a full description of the complex aerodynamic response of the building under consideration.

4.4.2 Quasi-steady model

In alternative to the data-driven model of Section 4.4.1, $\mathbf{F}(t;\bar{v}_y,\alpha)$ can be modeled through a quasi-steady model. This will in general provide a good approximation of the alongwind loads but is unable to provide a general description of the acrosswind loads. Within this setting, the nth component of $\mathbf{F}(t;\bar{v}_y,\alpha)$ is described by the following relationship:

$$F_n(t;\bar{v}_y,\alpha) = \eta_n(\alpha)(\bar{v}_{z_n} + v_n(t))^2 \simeq \eta_n(\alpha)(\bar{v}_{z_n}^2 + 2\bar{v}_{z_n} v_n(t)), \quad n = 1, 2 \ldots, N \tag{4.5}$$

where N is the number of degrees of freedom of the system and $\bar{v}_{z_n}$ is the mean wind velocity at height z_n and related to $\bar{v}_y$ through the wind profile, $v_n(t)$ is the corresponding fluctuating component of the wind speed while η_n is a coefficient equal to $0.5\rho\bar{C}_n A_n$, in which ρ is the air density, $\bar{C}_n$ is a directional quasi-steady pressure coefficient and $A_n = h_n W$ is the influence area of the nth degree of freedom in the direction of the wind with W the influence width. To simulate the zero-mean fluctuating component over the height of the building, $v_n(t)$, a

target power spectral density (PSD) function must be considered. For example:

$$S_n(\omega) = \frac{1}{2}\frac{200}{2\pi}v_*^2\frac{z_n}{\bar{v}_{z_n}}\frac{1}{[1+50\frac{\omega z_n}{2\pi\bar{v}_{z_n}}]^{5/3}}, \quad n = 1, 2, \ldots, N \tag{4.6}$$

where v_* is the shear velocity of the flow represented by:

$$v_* = v_{10}\beta\frac{k_a}{\ln(\frac{10}{z_0})} \tag{4.7}$$

where $k_a = 0.4$ is the Von Kármán's constant while z_0 is the ground roughness height. The cross spectral density is given by:

$$S_{nk}(\omega) = \sqrt{S_n(\omega)S_k(\omega)}\gamma_{nk}(\omega), \quad n, k = 1, 2, \ldots, N, n \neq k \tag{4.8}$$

where γ_{nk} is the coherence function between $v_n(t)$ and $v_k(t)$ defined as

$$\gamma_{nk}(\Delta z, \omega) = \exp\left[-\frac{\omega}{2\pi}\frac{C_z\Delta z}{\frac{1}{2}(\bar{v}_1 + \bar{v}_2)}\right] \tag{4.9}$$

where $\bar{v}_1$ and $\bar{v}_2$ are the mean wind speeds at heights z_1 and z_2, respectively, $\Delta z = |z_1 - z_2|$ is the difference between two heights and C_z is a constant that can be set equal to 10 for design purposes.

The N-dimensional multivariate stochastic vector process $v(t)$ describing the fluctuating components of the wind is then simulated through the following series as $L \to \infty$:

$$v_n(t) = 2\sum_{m=1}^{N}\sum_{l=1}^{L}|H_{nm}(\omega_{ml})|\sqrt{\Delta\omega}cos[\,\omega_{ml}(t) - \theta_{nm}(\omega_{ml}) + \phi_{ml}], \quad n = 1, 2, \ldots, N \tag{4.10}$$

where ϕ_{ml} for $m = 1, 2, \cdots, N$ and $l = 1, 2, \cdots, L$ are sequences of independent random

phase angles uniformly distributed in $[0, 2\pi]$ while ω_{ml} is given by

$$\omega_{ml} = (l-1)\Delta\omega + \frac{m}{N}\Delta\omega, \quad l = 1, 2, \ldots, N \tag{4.11}$$

in which $\Delta\omega$ is the sampling frequency. $H_{nm}(\omega_{ml})$ is a typical element of the matrix $\mathbf{H}(\omega)$, defined through the following decomposition:

$$\mathbf{S}(\omega) = \mathbf{H}(\omega)\mathbf{H}^{T*}(\omega) \tag{4.12}$$

where $\mathbf{S}(\omega)$ is the cross spectral density matrix with diagonal components given by Eq. (4.6) and off-diagonal terms given by Eq. (4.8) and $(\cdot)^{T*}$ is the transpose of the complex conjugate.

In Eq. (4.10), $\theta_{nm}(\omega)$ is the complex angle that can be written in the following form if the off-diagonal elements $H_{nm}(\omega)$ of $\mathbf{H}(\omega)$ are written in the polar form:

$$\theta_{nm}(\omega) = \tan^{-1}\frac{\mathrm{Im}[H_{nm}(\omega)]}{\mathrm{Re}[H_{nm}(\omega)]} \tag{4.13}$$

where Im and Re are respectively the imaginary and real parts of the complex function. The period of the simulated forcing function is given by:

$$T = \frac{2\pi N}{\Delta\omega} = \frac{2\pi NL}{\omega_{up}} \tag{4.14}$$

where ω_{up} is the cut-off frequency.

4.5 The Monte Carlo Simulation Strategy

The stochastic wind load models outlined above allow the iterative solution schemes of Chapter III to be used to define a Monte Carlo simulation framework that can efficiently estimate system-level probability that a wind-excited structural system is susceptible to collapse whose inelasticity is idealized through the concentrated or distributed plasticity

models of Chapter III. The global safety of the structure, defined by the probabilities $P(C|\bar{v}_y)$ and $P(NC|\bar{v}_y) = 1 - P(C|\bar{v}_y)$, is determined by the dynamic shakedown multiplier, s_p, as well as any number of limit states placed on inelastic responses occurring at shakedown. With this in mind, the probability of collapse susceptibility of the structure can be estimated through the following expression:

$$P(C|\bar{v}_y, \alpha) = \frac{1}{N_s} \sum_{i=1}^{N_s} I_C^{(i)}(\bar{v}_y, \alpha) \tag{4.15}$$

where N_s is the total number of simulated wind events while $I_C^{(i)}$ is the following indicator function evaluated in $(\bar{v}_y, \alpha)$ as:

$$I_C^{(i)} = \begin{cases} 1 & \text{if} \quad (s_p^{(i)} < 1) \cup (\mathbf{u}_r^{(i)} \geq \tilde{\mathbf{u}}_r) \cup (\hat{\mathbf{u}}^{(i)} \geq \tilde{\hat{\mathbf{u}}}) \cup (\boldsymbol{\epsilon}_p^{(i)} \geq \tilde{\boldsymbol{\epsilon}}_p) \\ 0 & \text{if} \quad \text{otherwise} \end{cases} \tag{4.16}$$

where $s_p^{(i)}$, $\mathbf{u}_r^{(i)}$, $\hat{\mathbf{u}}^{(i)}$ and $\boldsymbol{\epsilon}_p^{(i)}$ are the ith sample of the shakedown multiplier, residual displacements, peak displacements, and plastic strains at shakedown, while $\tilde{\mathbf{u}}_r$, $\tilde{\hat{\mathbf{u}}}$ and $\tilde{\boldsymbol{\epsilon}}_p$ are user defined repairability limits set respectively on $\mathbf{u}_r$, $\hat{\mathbf{u}}$ and $\boldsymbol{\epsilon}_p$. In defining $I_C^{(i)}$ as above, susceptibility to collapse can be defined as:

1. the inability of the structure to reach the state of dynamic shakedown;

2. excessive residual $\mathbf{u}_r$ and/or peak $\hat{\mathbf{u}}$ displacements/drifts at shakedown;

3. excessive plastic deformations $\boldsymbol{\epsilon}_p$ at shakedown.

It is important to observe that any other limit state can be added to $I_C^{(i)}$ without computational consequences as the scheme is based on a Monte Carlo methods. Also, in evaluating $I_C^{(i)}$, the peak responses at shakedown $\hat{\mathbf{u}}$ are given by the sum of the peak elastic response $\hat{\mathbf{u}}_e$ and the residual response $\mathbf{u}_r$, i.e. as $\hat{\mathbf{u}} = \hat{\mathbf{u}}_e + \mathbf{u}_r$.

Similarly, the probability of the structure exiting an elastic regime can be simultaneously

estimated as:

$$P(s_e < 1) = \frac{1}{N_s} \sum_{i=1}^{N_s} I(s_e^{(i)}) \tag{4.17}$$

where $I(s_e^{(i)})$ is the following indicator function:

$$I(s_e^{(i)}) = \begin{cases} 1 \text{ if } s_e^{(i)} < 1 \\ 0 \text{ if } s_p^{(i)} \geq 1 \end{cases} \tag{4.18}$$

In addition to the above probabilities, the proposed framework can also provide probability distributions on the plastic strains (e.g. plastic hinge rotations) and deformations (e.g. residual displacements). Indeed, a Monte Carlo scheme provides, as a by-product, unbiased sets of samples of all responses occurring throughout the system. These can then be used to directly estimate distribution functions.

A flowchart of the proposed Monte Carlo scheme is shown in Figure 4.2. In particular, the step-by-step Monte Carlo algorithm is as follows:

1. Set the intensity of the wind storm of interest by selecting the mean wind speed $\bar{v}_y$ with a MRI of y years, the wind direction α, and total duration T.

2. Generate a realization of the wind loads $\mathbf{F}(t; \bar{v}_y, \alpha)$ through one of the stochastic wind load models of Section 4.4 after calibration to appropriate wind tunnel data.

3. Perform modal direct integration using the model outlined in Section 2.4.1.3.

4. Obtain a realization of $\mathbf{Q}^s(t)$ by extracting the elastic responses from Step 3.

5. Estimate realizations of the elastic and shakedown multipliers, s_e and s_p, by solving the linear programming problem of Eqs. (2.23) and (2.22). Check if the structure has remained elastic, i.e. $s_e \geq 1$, or is susceptible to collapse during the wind event, i.e. if $s_p < 1$.

6. If the structure remains elastic, i.e. $s_e \geq 1$, the plastic deformation is set to be zero as the structure remains elastic.

7. If the system is susceptible to collapse, i.e. if $s_p < 1$, the structure is identified as irreparable and no plastic deformation estimation is needed.

8. If the structure is deemed repairable, i.e. is not susceptible to collapse, and the structure experiences plasticity, i.e. $s_e < 1$ and $s_p \geq 1$, estimate residual displacements, $\mathbf{u}_r$, peak responses $\hat{\mathbf{u}}$, and total strains, $\boldsymbol{\epsilon}_p$, for the unamplified wind storm, i.e. $s = 1$, using the iterative methods of Chapter III and evaluate Eq. (4.16).

By repeating steps 2 to 8 for N_s samples of the wind loads, the safety of the system can be estimated probabilistically using Eq. (4.15). For structures that exit the elastic regime, plastic deformations due to the unamplified wind storms, i.e. $s = 1$, will also be evaluated, thereby providing an insight into the inelastic behavior of the system.

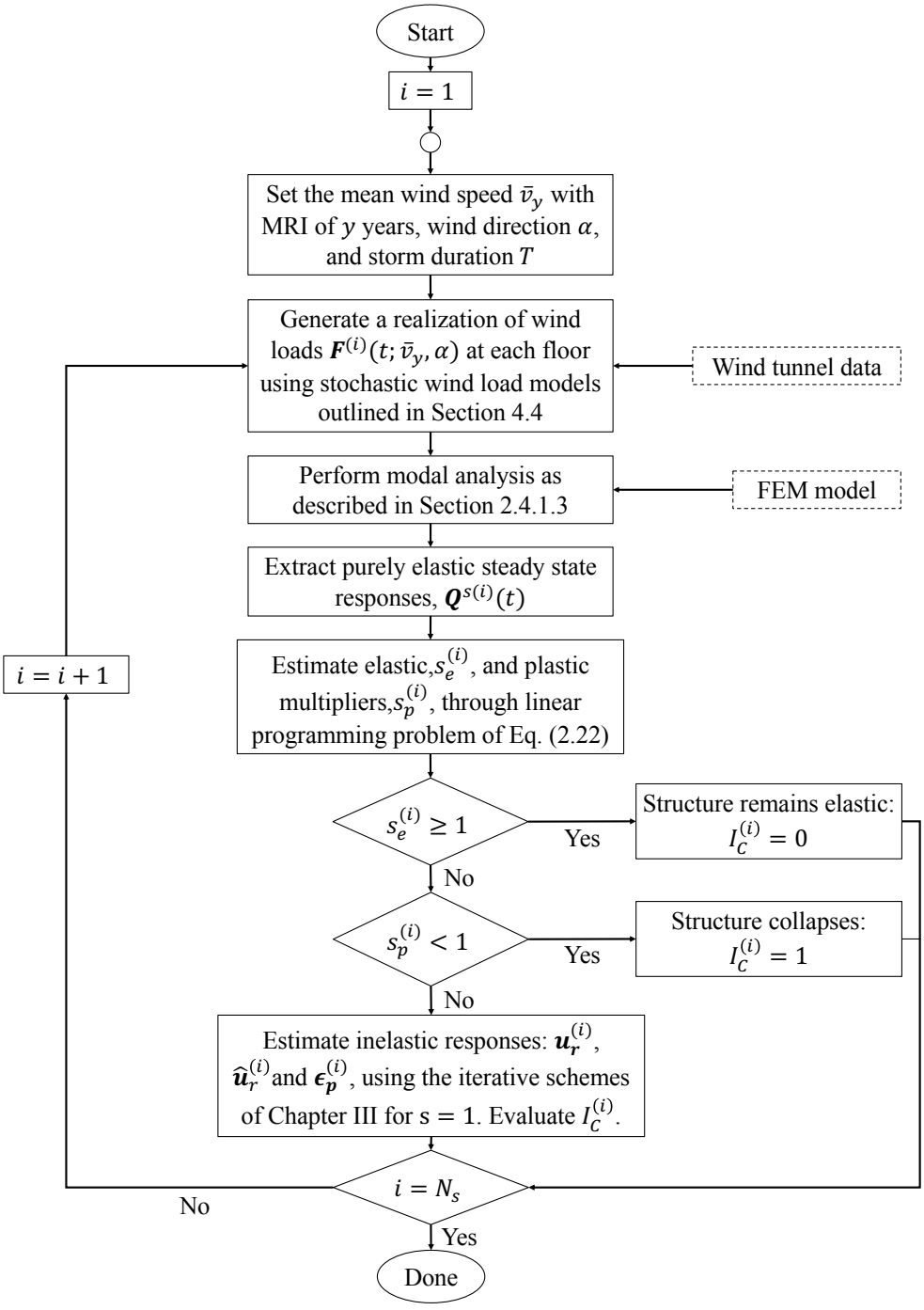

Figure 4.2: Flowchart of the overall simulation strategy.

4.6 Summary and Conclusions

The primary objective of the work outlined in this chapter was the development a general framework allowing the estimation of the probability associated with the susceptibility of the structure to system-level collapse based on the strain-based dynamic shakedown models presented in Chapter III. Contrary to the computationally intensive direct integration method that requires hours to analyze a structure under a single wind storm, the proposed model–which combines the classic solution method for dynamic shakedown with the iterative strain-based schemes outlined in Chapter III–can estimate the inelastic response for each wind storm in a matter of seconds therefore enabling the introduction of a stochastic simulation scheme based on robust Monte Carlo methods to be used to estimate the probabilities associated with exceeding inelastic system-level limit states modeling the susceptibility of the system to collapse.

CHAPTER V

Verification and Examples

5.1 Overview

The primary goals of the work carried out in this chapter are:

1. Verification of the proposed concentrated plasticity dynamic shakedown framework for plastic strains and deformations through comparison with results obtained from direct integration.

2. Validation of the simulated load path through a comprehensive statistical study involving a full range of wind directions.

3. Application and verification of the proposed dynamic shakedown framework for fiber elements considering distributed plasticity through comparison with results obtained from direct integration.

4. Illustration of the Monte Carlo scheme developed in Chapter IV on steel frames, modeled with both concentrated and distributed plasticity, subject to stochastic wind loads.

To achieve the first goal, alongwind and acrosswind loads histories were simulated for a 150 m steel frame using the model developed in Chapter IV. Wind tunnel data was used to calibrate the model. Direct integration of a fully non-linear OpenSees model was then

carried out and compared to the plastic strains and deformations estimated from the dynamic shakedown framework developed in Chapters III and IV. Near perfect correspondence between the two approaches was seen therefore verifying the proposed dynamic shakedown framework.

In reaching the second goal, non-linear responses at shakedown obtained through direct integration were compared with those obtained from the proposed strain-based dynamic shakedown framework. In particular, randomly selected wind load histories over a full range of wind directions, including alongwind, acrosswind and intermediate wind directions, were considered.

To achieve the third goal, a two-story two-bay frame subject to alongwind load histories was used to illustrate the potential of the proposed framework. Direct integration of a fiber element OpenSees steel model was carried out and compared to the plastic deformation estimated from the fiber-based dynamic shakedown framework developed in Chapters III. Near perfect correspondence between the two approaches was seen therefore verifying the proposed fiber-based dynamic shakedown framework. In addition, a framework based on section forces was also demonstrated on both steel and reinforced concrete frames subject to alongwind loads with predefined yield domains for each section. In this case, immediate comparison with direct integration is not available since there is no such element type available in OpenSees.

In reaching the fourth goal, the steel frames with concentrated and distributed plasticity developed for achieving the first and third goads of this chapter were analyzed while considering randomly generated wind storms within the Monte Carlo scheme of Chapter IV. To illustrate the versatility of the proposed framework, probability distributions for select inelastic responses were also estimated.

5.2 Verification of the Simulated Load Path

To illustrate the validity of the simulated load path of Section 4.3.2, this section focuses on the comparison of non-linear responses obtained for a 37 story wind-excited steel frame through direct integration to those obtained from the proposed incremental strain-based concentrated plasticity scheme. In particular, the finite element environment OpenSees (Open System for Earthquake Engineering Simulation) was used for carrying out the direct integration using the Newmark-Beta method.

5.2.1 Model description

The structure considered in this comparison is the 37-story six-span plane steel frame of Figure 5.1. The geometry consists of beam span lengths of 5 m and inter-story heights of 6 m at ground level and 4 m for all other floors. The overall height of the structure is 150 m. The columns are box members, while the beams are wide flange standard W24 sections. A summary of the section sizes is reported in Table 5.1. The dimensions of the box columns are defined by their center line diameters D. The thickness of the section, t, is set to $D/20$. The steel composing the frame is assumed to be elastic-perfectly plastic, and is therefore completely described by the yield stress σ_y and Young's modulus E_s, which were respectively taken as 355 MPa and 200 GPa. The mass of the structure was lumped at each floor and calculated as the sum of the element mass and carried mass derived from assuming a building density of 100 kg/m^3. The first two natural frequencies of the frame were respectively $f_1 = 0.1873$ Hz and $f_2 = 0.5340$ Hz. Rayleigh damping was considered, with damping ratios of the first two modes equal to 2.5%.

To evaluate the non-linear response of structure, rigid-perfectly plastic hinges were assumed at the extremes of all elements for a total of 962 possible hinges. In particular, in this case study, plastic hinges were purely moment based, neglecting axial load effects in both the beams and columns. The yield domains associated with plastic hinges were therefore defined by the ultimate moments of the sections, i.e. $M_u = \sigma_y Z$ with Z the plastic modulus

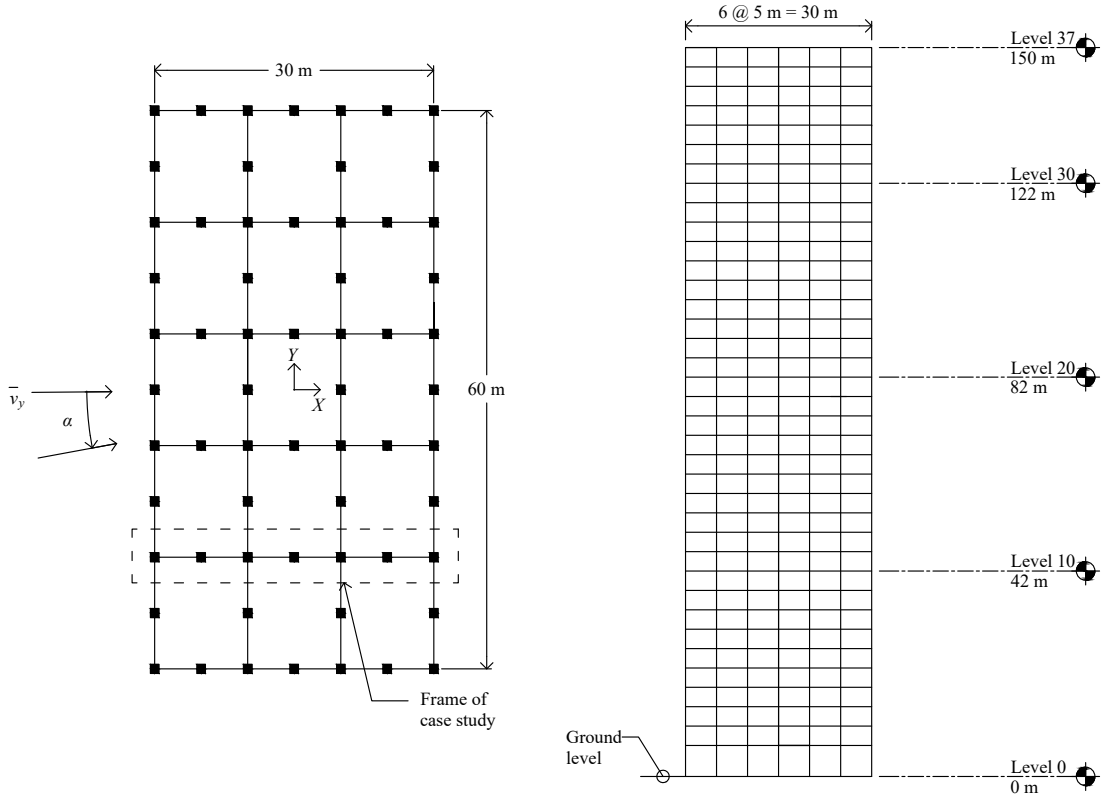

Figure 5.1: Schematic of the 37-story steel frame of the case study.

of the cross section.

To model the rigid-perfectly plastic hinges in OpenSees, TwoNodeLink elements of 1 cm length were placed at the two ends of each beam and column. The moment capacity of the hinges were defined as the ultimate moment strengths of the section while the rotational stiffnesses were calculated based on the stiffness that would be provided by a 1 cm segment of the original elastic beam/column element. This ensures that the elastic response of the hinges is, for all intents and purposes, the same as the corresponding elastic beam-column element. Similarly, the shear and axial stiffnesses were taken so as to correspond to a 1 cm segment of elastic beam/column element.

Table 5.1: Section sizes of the steel frame.

Level	Wide-flange Beams	Box Columns (cm)
1-10	W24 × 192	$D = 50$
11-20	W24 × 192	$D = 50$
21-30	W24 × 103	$D = 40$
31-37	W24 × 103	$D = 35$

5.2.2 Wind loads

The two wind directions $\alpha = 0°$ and $\alpha = 90°$, see Figure 5.1, were considered in the comparison of this section. These directions corresponded to alongwind and acrosswind loads respectively. To simulate wind load histories for these two directions, the stochastic wind load model of Section 4.4 was calibrated to wind tunnel data collected on a 1/300 rigid model of the building geometry shown in Figure 5.1. In particular, the data was part of the Tokyo Polytechnic University's (TPU) aerodynamic database (*Tokyo polytechnic university (TPU) Wind Pressure Database*, 2008) and was measured considering a sampling frequency of 1000 Hz and wind speed at the building top of 11 m/s. A total of 512 pressure taps were used for 32 s of recorded data. This data was integrated and scaled therefore defining X, Y and torsional loads at the center of mass of each floor. For the application here considered, 1/6 of the X direction loads were considered acting on the moment resisting frame. These loads were used to estimate the eigenvalues Λ_j and eigenvectors $\mathbf{\Psi}_j$ for the two wind directions of interest.

In calibrating Eq. (4.3), a sampling frequency of 2 Hz was considered for a cutoff frequency of 1 Hz. Five loading modes were considered for each wind direction. To ensure stability and accuracy when carrying out direct integration, the sampling frequency was increased through linear interpolation to 100 Hz. The mean wind speed at the building top was set to $\bar{v}_y = 52.5$ m/s, which corresponds to a MRI of $y = 700$ years for the Miami region of Florida. Due to the significant effort involved in performing direct integration, the total length of the wind storm was set to $T = 360$ s. The first and last minute of the loads were linearly ramped to ensure zero initial and final conditions. To fully capture the dynamic

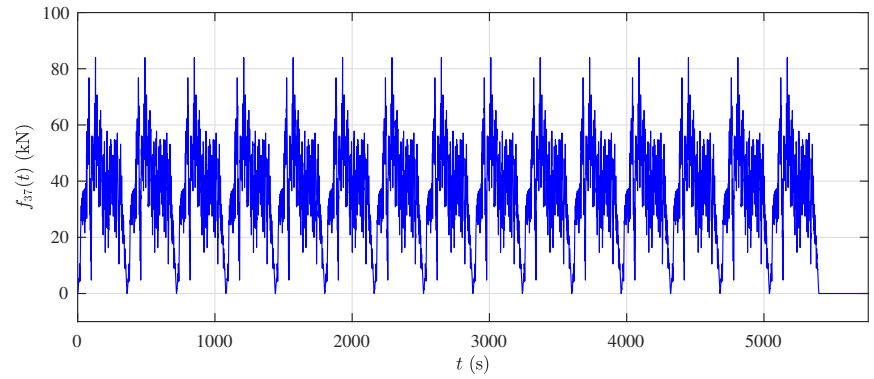

(a)

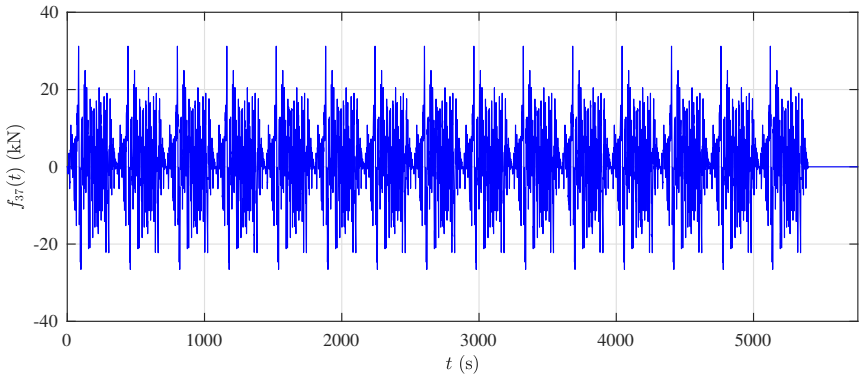

(b)

Figure 5.2: A realization of the top floor stochastic wind loads for: (a) alongwind direction, i.e. $\alpha = 0°$; (b) acrosswind direction, i.e. $\alpha = 90°$.

shakedown phenomena, the wind loads were repeated for 15 cycles before returning to zero for full cycle, as illustrated in Figure 5.2. This final unloading cycle allowed for the dynamic responses to completely damp out therefore enabling the direct estimation of the residual displacements and plastic rotations in the hinges. These quantities were directly compared to those obtained from the strain-based dynamic shakedown framework developed in Section 3.3.

5.2.3 Results

The comparison was carried out for four randomly generated wind loads acting in the alongwind and acrosswind directions, i.e. $\alpha = 0°$ and $\alpha = 90°$. Figure 5.3 reports the residual displacements for the four acrosswind and alongwind wind loads. As can be seen,

the residual displacements estimated through the proposed framework are almost identical to those obtained from direct integration in both the alongwind and acrosswind directions. Plastic strains, i.e. residual hinge rotations θ_r, for two samples are shown in Figures 5.4 and 5.5 with hinge locations shown in Figure 5.6. Once again, strong correspondence between the two approaches is seen. Figures 5.7 and 5.8 present the deformed shapes for a representative sample under acrosswind and alongwind loading where plastic hinge yielding occurred mostly in the first story and mid-height of the building. In particular, in these figures, plastic hinges were depicted by circles if only one hinge was present at the joint, while in the case of multiple hinges, e.g. hinges on more than one connecting beam or column, squares were used. It can be observed that under the assumptions outlined in Section 4.3, the proposed framework is capable of estimating the inelastic response in both the alongwind and acrosswind directions with high accuracy, proving that the simulated load path is quite comparable to the actual load path experienced by the structure.

To illustrate how the accumulation of plastic strain in the hinges is monotonically increasing, i.e. no alternating plasticity occurs during shakedown, the moment rotation histories of three representative plastic hinges are shown in Figure 5.9 for an alongwind sample, while Figure 5.10 shows the corresponding quantities for the acrosswind direction. In particular, the final residual moments and rotations are marked by squares. As can be seen, for shakedown to occur, plasticity increases monotonically for each cycle with, after several cycles of loading, an absence of further plastic accumulation as the structure begins to respond in a purely elastic manner, i.e. the state of shakedown has been reached.

5.3 Statistical Validation of the Load Path

A comprehensive statistical study was carried out considering the 37-story frame described in Section 5.2, and shown in Figure 5.1. The wind tunnel data informed stochastic wind model described in Section 5.2.2 was adopted for generating the wind load histories. To make the comparison, 200 randomly selected wind load histories were considered. Wind

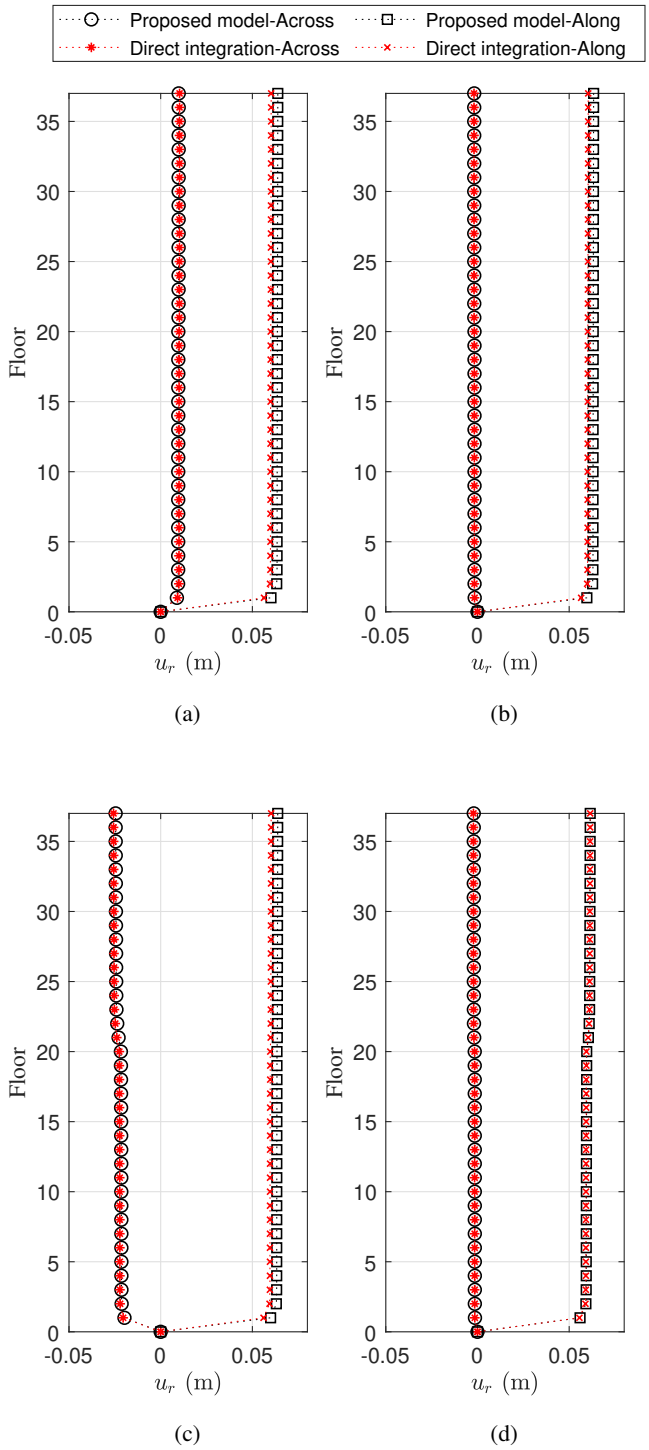

Figure 5.3: Comparison between the residual displacements evaluated through the proposed framework and direct integration for the four randomly generated wind load histories.

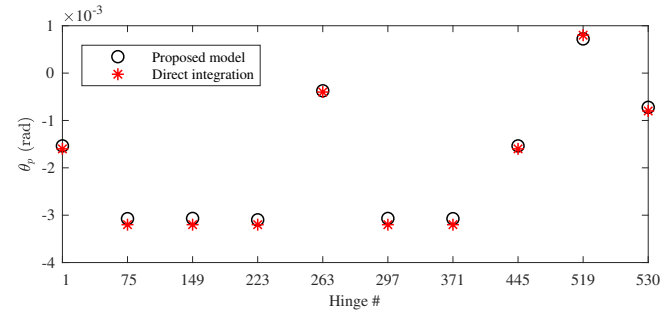

(a)

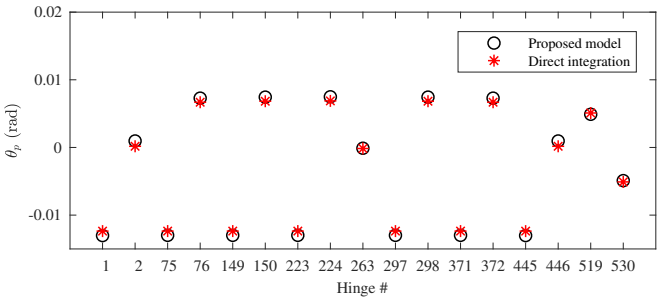

(b)

Figure 5.4: Residual hinge rotation, θ_r, for (a) acrosswind and (b) alongwind responses of representative sample 1.

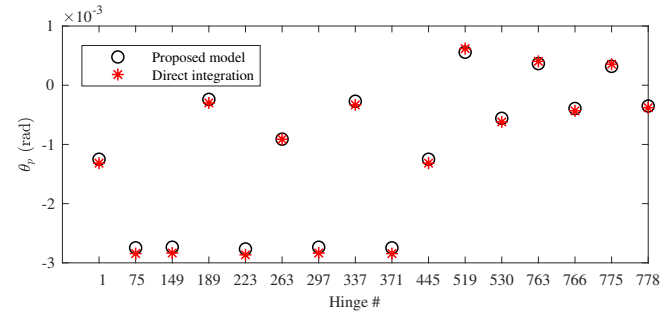

(a)

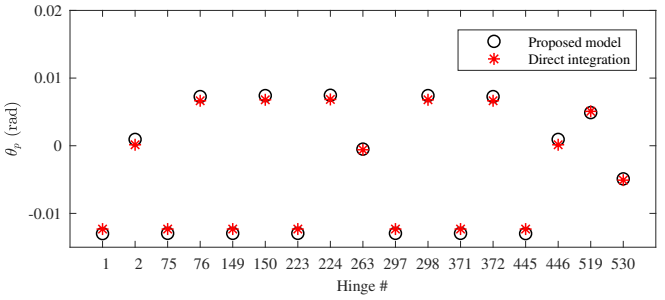

(b)

Figure 5.5: Residual hinge rotation, θ_r, for (a) acrosswind and (b) alongwind responses of representative sample 2.

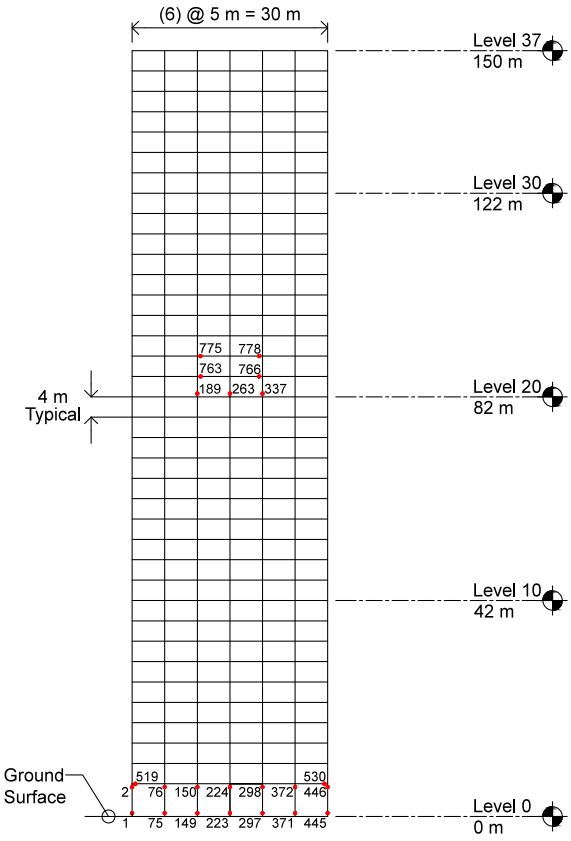

Figure 5.6: Plastic hinge locations.

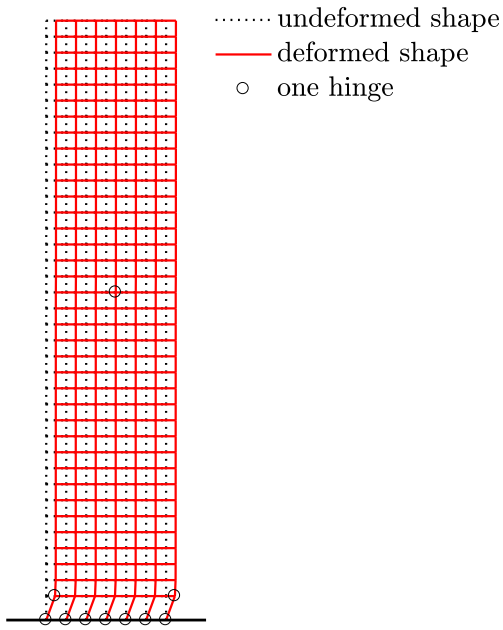

(a)

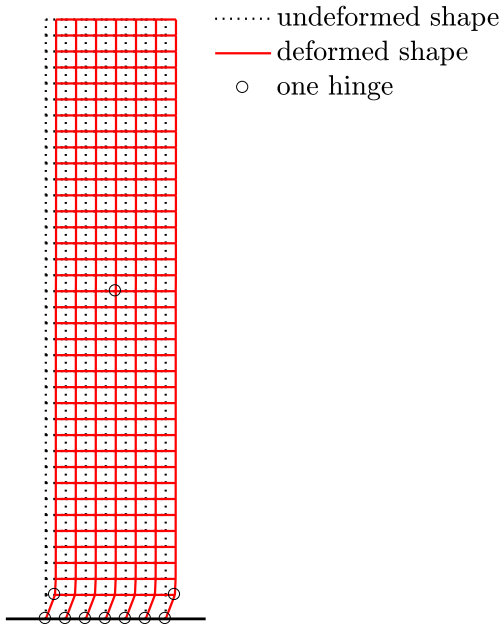

(b)

Figure 5.7: Deformed shape estimated from (a) strain-based dynamic shakedown and (b) direct integration for a representative acrosswind sample (deformed shape amplified by 250).

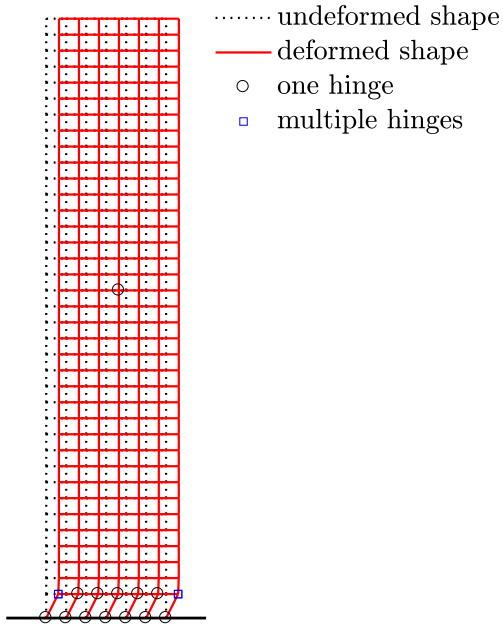

(a)

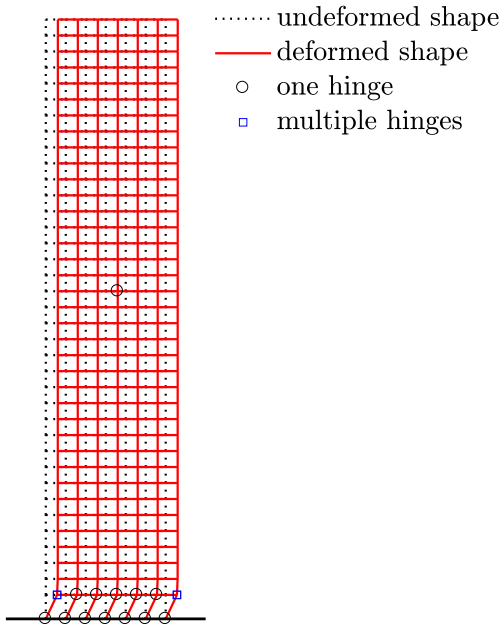

(b)

Figure 5.8: Deformed shape estimated from (a) strain-based dynamic shakedown and (b) direct integration for a representative alongwind sample (deformed shape amplified by 50).

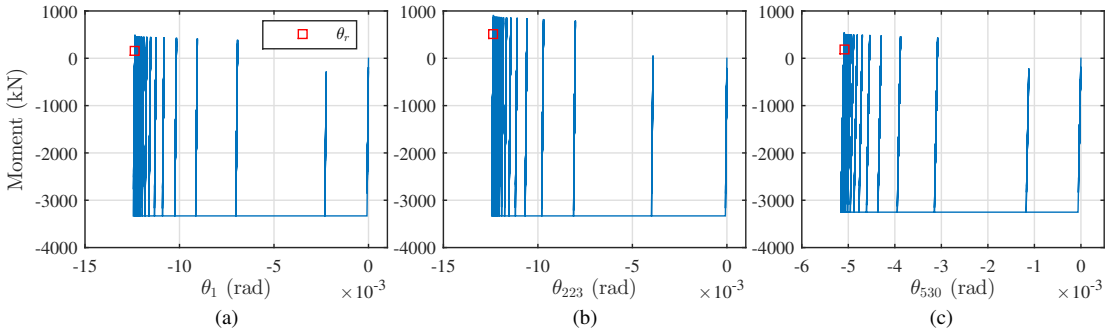

Figure 5.9: Moment rotation history for a representative alongwind sample at (a) Hinge 1 (b) Hinge 223 and (c) Hinge 530.

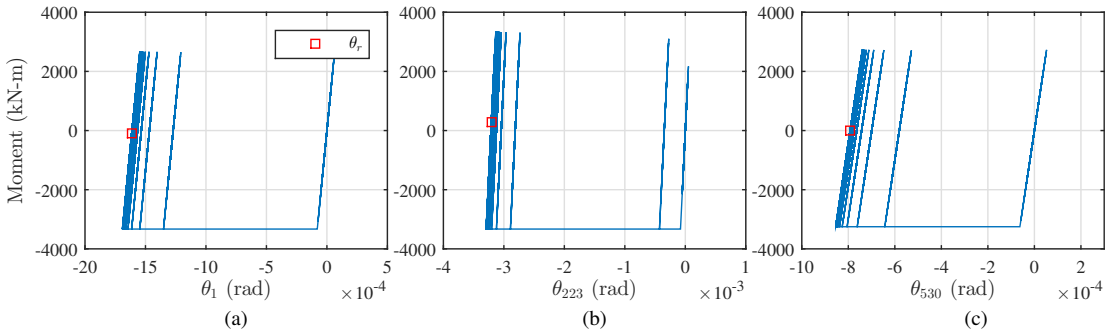

Figure 5.10: Moment rotation history for a representative acrosswind sample at (a) Hinge 1 (b) Hinge 223 and (c) Hinge 530.

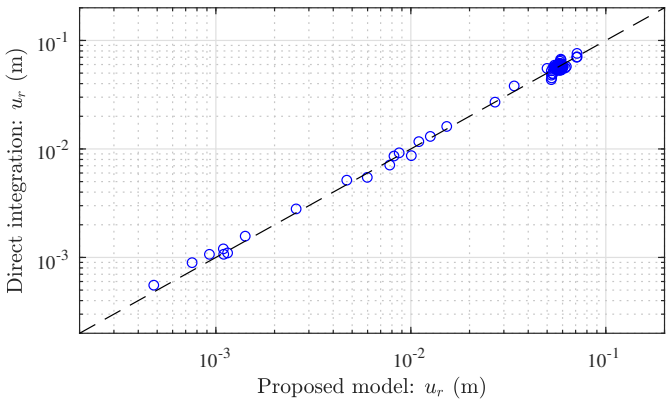

Figure 5.11: Comparison between residual displacements at the first floor for all 200 samples.

directions were selected from the set $\alpha \in \{0°, 10°, 20°, \ldots, 90°\}$ following a uniform distribution. Therefore, both alongwind and acrosswind directions were considered as well as intermediate wind directions.

For all 200 samples, the estimation of plastic deformations by the strain-based dynamic shakedown scheme was confirmed by the direct integration. To illustrate this, Figure 5.11 shows the comparison between all 200 residual displacements estimated from the strain-based dynamic shakedown scheme and direct integration for the first floor, where most of the plasticity occurred in this case. In addition, comparison for the plastic rotations of a representative hinge with plasticity occurring for all 200 samples (i.e. Hinge 1 as shown in Figure 5.6) is shown in Figure 5.12. As can be seen from these figures, there is strong correspondence between the results of the two methods. Indeed, a correlation coefficient greater than 0.99 existed in both cases. Similar results were seen for all other responses.

5.4 Verification of the Distributed Plasticity Model

In this section, both the fiber-based and section-based framework of Sections 3.4.3 and 3.4.4 are illustrated on a 2D two-story two-bay frame. In particular, due to the requirement of linear EPP materials in the fiber-based framework, only steel frame was used for illustration of this model, while the section-based framework was demonstrated on both steel and reinforced concrete structures. Direct integration of an OpenSees steel fiber model was car-

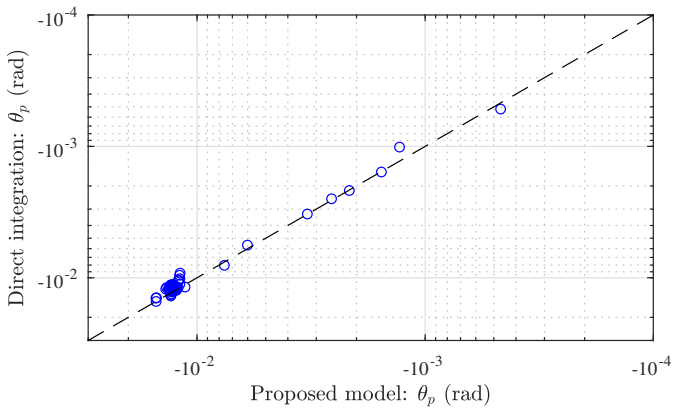

Figure 5.12: Comparison between plastic rotations at hinge 1 for all 200 samples.

ried out and compared to the responses estimated from the fiber-based dynamic shakedown framework. For the section-based framework, unfortunately, this same comparison cannot be achieved since there is no such element that defines the interaction diagram at each section along the member length in OpenSees. The general validity of the section-based framework, however, can be inferred from the results of Sections 5.2 and 5.3, where concentrated plasticity was assumed at the element ends with moment plastic hinges.

5.4.1 Steel frame

The first case study refers to the two-story two-bay frame shown in Figure 5.13. Rigid floor diaphragms were assumed at each story of the frame. The columns are box members, while the beams are wide flange standard W24 sections. A summary of the section sizes is reported in Table 5.2. The dimensions of the box columns are defined by their center line diameters D while the thickness of the section's flanges is set to $D/20$. The steel composing the frame is assumed to be elastic-perfectly plastic, and is therefore completely described by the yield stress σ_y and Young's modulus E_s, which were respectively taken as 345 MPa and 200 GPa. In addition to the element mass, a dead load of 160 kg/m^3 was considered at each floor. This was modeled through the point loads of Figure 5.13 while considering an influence width of 3.81 m. The first two natural frequencies of the frame were respectively $f_1 = 0.5146$ Hz and $f_2 = 1.2187$ Hz. Rayleigh damping was considered, with damping ratios

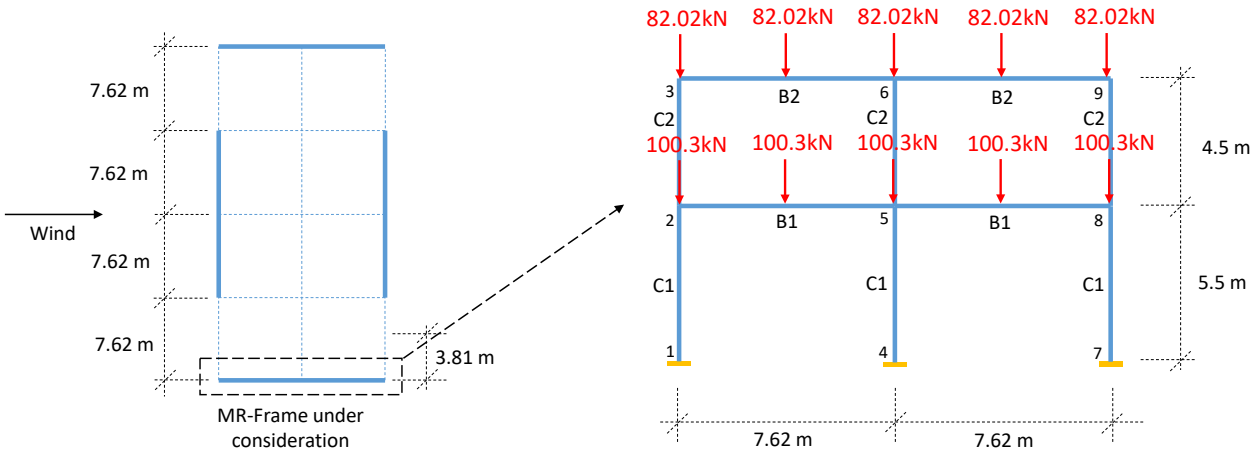

Figure 5.13: Two-story two-bay frame.

of the first two modes equal to 1.5%.

To model the distributed plasticity along the element, DB beam-column elements were considered with two elements for each member. Gauss-Legendre integration scheme was adopted with 5 integration points (control sections) along the element. External loads were defined by both static vertical point loads and the wind excitation, as shown in Figure 5.13. To define the stochastic wind loads, $\mathbf{F}(t;\bar{v}_y)$, acting on the structural system in $[0,T]$, and therefore $\tilde{\mathbf{F}}(t;\bar{v}_y)$ through Eq. (4.1), the quasi-steady model described in the Section 4.4.2 was adopted with linear ramp-up and -down at the beginning and end of the storm. The intensity of the wind event, $\bar{v}_y$, was described by the maximum mean hourly wind speed to occur at a height of interest $\bar{z}$, following the power law:

$$\bar{v}_y(\bar{z}) = \bar{b}\left(\frac{\bar{z}}{10}\right)^{\bar{\alpha}} v_y \tag{5.1}$$

where $\bar{\alpha} = 1/4.5$ and $\bar{b} = 0.45$ for Exposure B; v_y is the 3-s gust wind speed with MRI of y years at 10 m above ground. In simulating the wind load time histories, the quasi-steady model was calibrated assuming an influence width of 15.24 m for each floor. The pressure coefficient $\bar{C}_j$ was taken as 1.3 while the air density was taken as $\rho = 1.25$ kg/m^3. The affects of wind direction were accounted for through a directionality factor of 0.85. The building

Table 5.2: Section sizes of the steel frame.

Section type	B1	B2	C1	C2
Section size	W24 × 94	W24 × 68	$D = 0.27$ (m)	$D = 0.20$ (m)

was preliminary designed to meet a peak displacement limit at the building roof of $H/300$, with $H = 10$ m, under a 25 year MRI wind load, and elastic fiber response under a 700 year MRI wind load, i.e. a Risk Category II design.

In this case study, the mean wind speed at the building top was set to $\bar{v}_y = 34.0$ m/s, which approximately corresponds to a MRI of $y = 700$ years for the Miami region of Florida. Due to the significant effort involved in performing direct integration, the total length of the wind storm was set to $T = 600$ s with a sampling frequency of 100 Hz. The first and last two minutes of the loads were linearly ramped to ensure zero initial and final conditions and therefore, as outlined in Section 4.3.2, the validity of the simulated load path.

5.4.1.1 Fiber-based steel frame

To apply the fiber-based framework, each section of the steel frame is discretized into several fibers. Under uniaxial bending and plane section assumptions, fibers located at the same height of the section, i.e. same y coordinates, have the same stress-strain distribution. Therefore, each section considered in this case study was discretized vertically into 14 fibers (2 for both flanges and 10 for web), as shown in Figure 5.14, leading to a total of 1400 fibers for the frame.

In order to further compare the inelastic responses obtained from the proposed framework and those from direct integration, the steel frame was modeled in OpenSees using the DB element "dispBeamColumn" with 5-point Gauss-Legendre integration scheme. The nonlinear responses are integrated by the Newmark-Beta method with $\alpha = 0.5$ and $\beta = 0.25$ considering the limit load condition, i.e. external wind excitation multiplied by the shakedown multiplier s_p. To fully capture the dynamic shakedown phenomena, the wind loads were repeated for 15 cycles before returning to zero for a full cycle, as illustrated in Figure 5.15.

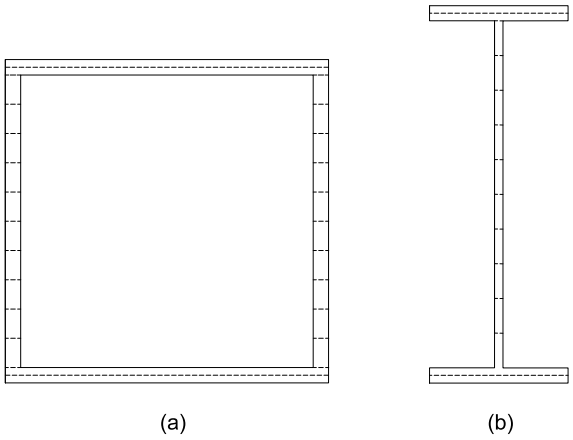

Figure 5.14: Fiber discretization of (a) box section and (b) W-shape section.

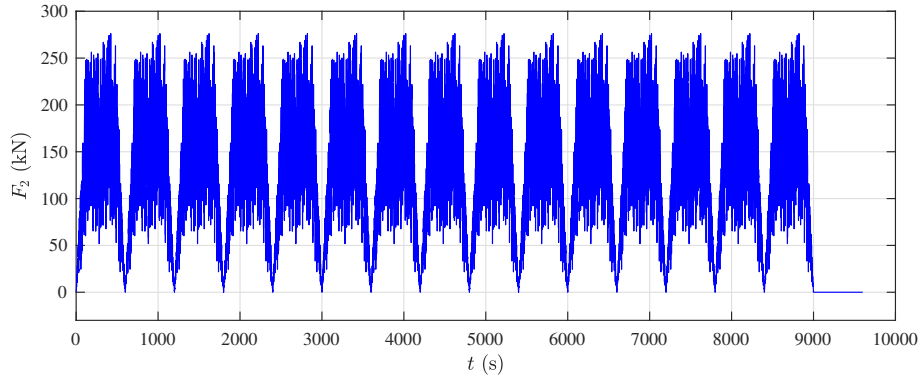

Figure 5.15: The top floor stochastic wind load.

This final unloading cycle allowed for the dynamic responses to completely damp out therefore enabling the direct estimation of the residual displacements and plasticity distributed along the element.

Given the set up described above, the fiber-based dynamic shakedown framework was applied yielding a shakedown multiplier of $s_p = 1.50$. Table 5.3 reports the corresponding residual displacements at shakedown estimated by both the proposed framework and direct integration, including horizontal displacements at the first and second floor, i.e. u_{r_1} and u_{r_2}, as well as the vertical displacements v_{r_i} and rotations ϕ_{r_i} at node i. The location of each node is shown in Figure 5.13. As can be seen from Table 5.3, responses obtained from both methods are almost identical. The time-independent self-stresses, i.e. fiber stresses $\boldsymbol{\sigma}(x)$, along the section height, y, obtained from the strain-driven framework are also compared

Table 5.3: Comparison between the residual displacements at shakedown obtained from the proposed fiber-based framework and direct integration.

Degree of freedom	u_{r_1} (m)	u_{r_2} (m)	v_{r_2} (m)	ϕ_{r_2} (rad)	v_{r_3} (m)	ϕ_{r_3} (rad)	v_{r_5} (m)
Proposed framework	0.00120	0.02599	-0.00048	-0.00092	-0.00088	-0.00129	-0.00088
Direct integration	0.00122	0.02621	-0.00048	-0.00093	-0.00088	-0.00130	-0.00088
Degree of freedom	ϕ_{r_5} (rad)	v_{r_6} (m)	ϕ_{r_6} (rad)	v_{r_8} (m)	ϕ_{r_8} (rad)	v_{r_9} (m)	ϕ_{r_9} (rad)
Proposed framework	0.00017	-0.00166	0.00019	-0.00049	0.00054	-0.00098	0.00092
Direct integration	0.00018	-0.00167	0.00020	-0.00049	0.00054	-0.00097	0.00092

with the direct integration results, as shown in Figure 5.16 for all sections belonging to Element 7. The location of the selected element on the frame is shown in Figure 5.17(a). Once again, the strain-driven framework has proved its ability to estimate inelastic responses with remarkable accuracy.

To illustrate the distributed plasticity, Figure 5.17(b) shows the fiber sections assumed along the length of Element 7, i.e. 5 integration points, where fibers experiencing inelasticity are filled in with red. In addition, plasticity distributed along section height can also be obtained from the fiber-based framework. It can be observed that the plasticity distributes through the second section along the member with more fibers plastified in Section 1 than in Section 2 as the bottom of a column usually experiences a larger bending moment than the top. The last three sections of the selected member, as shown in the figure, remain elastic during the excitation, therefore no plastic deformations occur.

5.4.1.2 Section-based steel frame

In addition to the fiber-based strain-driven framework, the same steel frame of Figure 5.13 was used to illustrate the application of section-based framework. Prior to carrying out the analysis, the yield domain associated with each section was identified first. The yield domain of Figure 2.6 is considered for a steel box section with $M_y = \sigma_y Z$ and $N_y = \sigma_y A$ being the moment and axial strength respectively, where A and Z are the area and the plastic section modulus of the relevant cross section (*Tabbuso et al.*, 2016). For a beam section, the yield domain is defined by bending strength $M_y = \sigma_y Z$ alone. A summary of the strengths

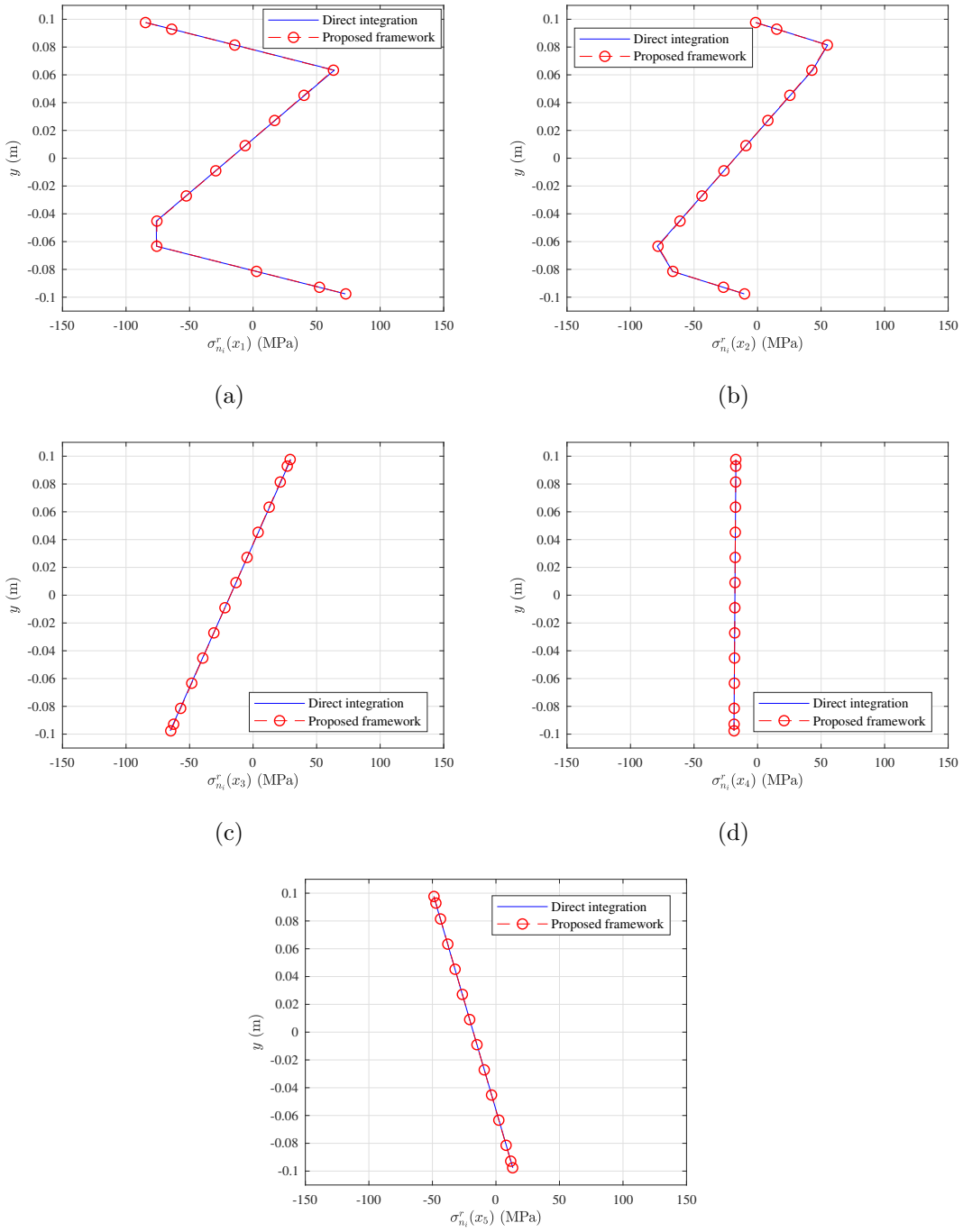

Figure 5.16: Comparison between the residual stresses obtained from the proposed framework and direct integration for Element 7: (a) Integration point 1; (b) Integration point 2; (c) Integration point 3; (d) Integration point 4 and (e) Integration point 5.

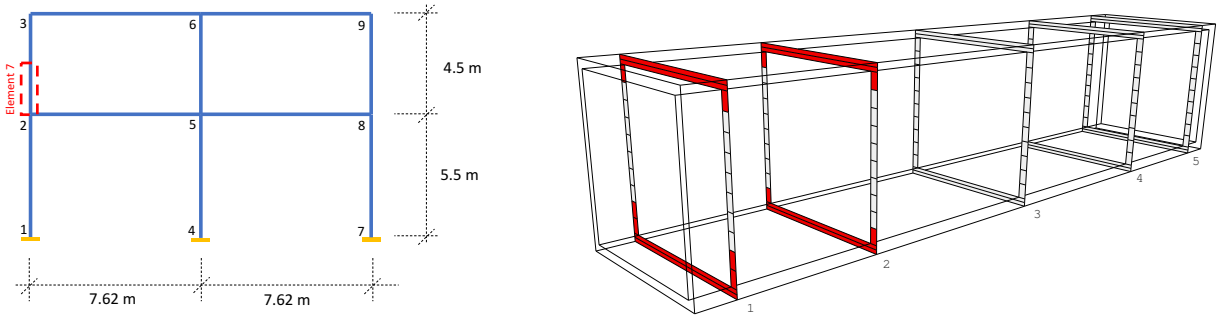

(a) (b)

Figure 5.17: (a) Element location; (b) Plasticity distributed along Element 7 of the steel frame obtained from the proposed framework.

Table 5.4: The axial and bending strengths for all sections of the steel frame.

Section Type	B1	B2	C1	C2
N_y (kN)	-	-	4904.2	2502.1
M_y (kN-m)	1435	999.9	490.9	178.9

of all sections is given in Table 5.4.

Given the set up described above, the section-based framework of Section 3.4.4 was applied yielding a shakedown multiplier of $s_p = 1.7252$, which is larger than the one estimated through the fiber-based framework. The reason behind this is due to the difference between the definition of the yield surface for the two methods. The yield surface for a section is defined as the ultimate strength that the entire cross section can reach in yielding, while that for a fiber-based framework is taken as yielding of any fiber of a section, which in general occurs at the extreme fibers and spreads over the height of the section. The shakedown residual displacements are reported in Table 5.5, which are also greater than the fiber-based results given the larger multiplier.

Figure 5.18 shows the plasticity distributed along Element 7 with 5 integration points along member length marked in dashed line. In this case, plasticity is identified by sections experiencing plastic deformations. The whole section is considered yielding at the same

Table 5.5: The shakedown residual displacements obtained from proposed section-based strain-driven framework of the steel frame under alongwind loads.

DOF	u_{r_1} (m)	u_{r_2} (m)	v_{r_2} (m)	ϕ_{r_2} (rad)	v_{r_3} (m)	ϕ_{r_3} (rad)	v_{r_5} (m)
Proposed framework	0.00226	0.18581	-0.00047	-0.00106	0.00081	-0.00138	-0.00082
DOF	ϕ_{r_5} (rad)	v_{r_6} (m)	ϕ_{r_6} (rad)	v_{r_8} (m)	ϕ_{r_8} (rad)	v_{r_9} (m)	ϕ_{r_9} (rad)
Proposed framework	0.00029	-0.00142	0.0003	-0.00047	0.00042	-0.0008	0.00085

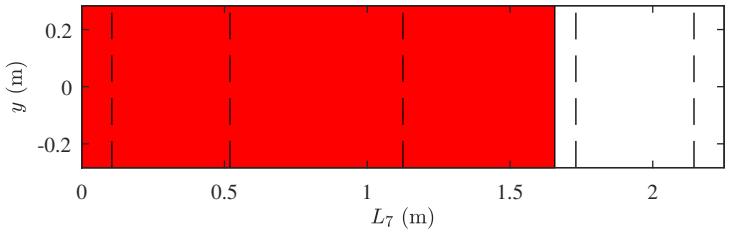

Figure 5.18: Plasticity distributed along Element 7 of the steel frame under alongwind loads obtained from the section-based framework.

time since there is no information about the fiber strains and plasticity distributed along section height. Based on the assumption of linear curvature and constant axial strain along the element from the interpolation function of Eq. (3.25), plastic deformations between integration points can also be evaluated. For Element 7, plasticity occurs from the bottom of the column to almost section 4. As compared to the fiber-based results, plasticity spreads more along the element in the section-based approach due to the different definition of the yield domain, therefore leading to larger residual displacements.

5.4.2 Reinforced concrete frame

The second case study refers to a reinforced concrete frame of the same geometry as Figure 5.13. All elements of the frame consist of rectangular reinforced concrete sections. A summary of the section sizes is reported in Figure 5.19. The yield stress of the concrete, f'_c, was taken as 6000 psi (41.37 MPa). Considering a concrete with a density of 145 lb/ft^3 (2322.7 kg/m^3), the modulus of elasticity can be defined as:

$$E_c = 57,000\sqrt{f'_c} \quad psi \tag{5.2}$$

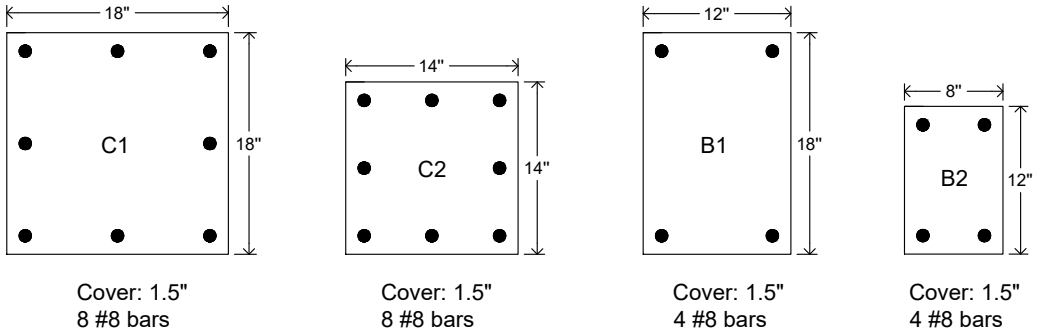

Figure 5.19: Section sizes composing the reinforced concrete frame.

Table 5.6: Summary of gravity loads.

	Live Loading	Superimposed Dead Loading
Level 1 and 2	70 psf	10 psf

The reinforcing steel is considered to have a yield stress of 60 ksi (413.7 MPa) and Young's modulus, E_s, of 29000 ksi (200 GPa).

External loads were defined by superimposed dead loads and live loads, summarized in Table 5.6, as well as the wind excitation. In addition to the mass of all elements and the framing system, which consists of 2-1/2 inches (0.0635 m) of normal-weight concrete over 3-inch (0.0762 m) ribbed steel decking (490 pounds per cubic foot (7849 kg/m^3)), additional lumped mass equal to the superimposed dead loads was applied at each floor. The first two natural frequencies of the frame were respectively $f_1 = 0.4251$ Hz and $f_2 = 1.4005$ Hz. A damping ratio of 2% was considered for the first two modes. The wind loads were simulated from the quasi-steady model with mean wind speed at the building top of 34.0 m/s in alongwind direction and sampling frequency of 100 Hz. The total duration of the external wind load was again limited to 10 minutes with the first and last two minutes linearly ramped.

In defining the finite element model, fiber sections with tangent modulus of E_c were used to model the elastic response of the frame. Each section of the frame was discretized into

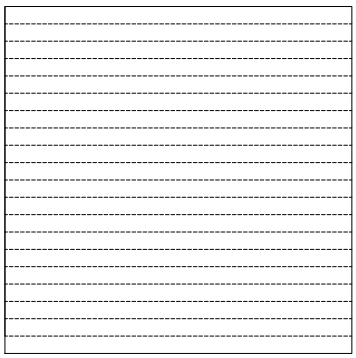

Figure 5.20: Fiber discretization of the rectangular elastic reinforced concrete section.

20 fibers in the y-direction, as illustrated in Figure 5.20, leading to a total of 2000 fibers. The section stiffness matrix $\mathbf{k}_s$ was then assembled from this fiber discretization through Eq. (3.18). To account for the reduction in stiffness after concrete cracking, the moment of inertia of a cracked section I_{cr} is generally used to compute the structural responses. In calculating I_{cr}, the concrete that is stressed in tension is assumed cracked, therefore effectively absent. The transformed section then consists of $n = E_s/E_c$ times the steel area in tension and $(n-1)$ times the steel area in compression. In the fiber element formulation, however, moment of inertia is not explicitly used in defining section stiffnesses $\mathbf{k}_s(x)$. Instead, a factor, I_r, relating the cracked and uncracked moment of inertia is applied to the bending related terms in section stiffness matrix, as follows;

$$I_r = \frac{I_{cr}}{I_g} \tag{5.3}$$

with I_g the moment of inertia of the gross concrete section.

To avoid the problem of concrete nonlinear behavior, section-based strain-driven framework was applied to model plasticity distributed along the DB beam-column elements with 5-point Gauss-Legendre integration scheme. Similar to the steel case, each member was broken into two elements for better accuracy.

In general, the yield domain of a reinforced concrete beam element is completely defined

by the bending capacity of the section M_n while a P-M interaction diagram has to be defined for the column considering the interaction between axial loads, P, and bending, M. The six characteristic points defining the interaction diagram are as follows (*Wight*, 2015):

1. the case of centric axial compression with a strain of 0.003;
2. the case of incipient cracking, in which the compressive failure of concrete is reached on one face while the other has zero strain;
3. the balanced condition, in which the compression failure of concrete is reached simultaneously with tensile yielding of steel bars at the tensile face;
4. the limiting tension-controlled condition, in which the compression failure of concrete is reached simultaneously with tensile strain of -0.005 in the reinforcement layer nearest to the tensile face;
5. the case of pure bending, $P = 0$;
6. the case of centric axial tension, in which a uniform tensile strain of $-\epsilon_y = 0.002$ is reached in the steel with the concrete cracked.

The piece-wise linear yield domains associated with the two column sections are shown in Figure 5.21. The yield domains for the beam sections B1 and B2, on the other hand, are defined by their bending strength M_n, as given in Table 5.7.

In this case, the dynamic shakedown framework yields a shakedown multiplier of $s_p = 1.6131$ with the corresponding shakedown residual displacements reported in Table 5.8. To illustrate how plasticity distributed along the element, Figure 5.22(b) shows plasticity along the first floor beam (Element 13). As can be seen, plasticity occurs from the left end of the beam to about one-half the distance between sections 3 and 4. Similar information can be obtained for all other elements.

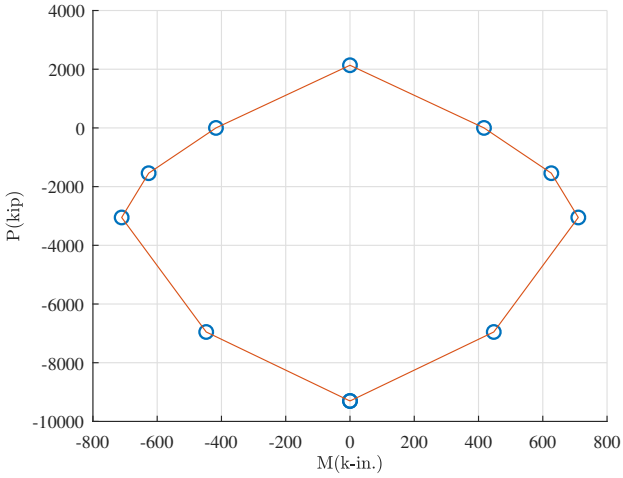

(a)

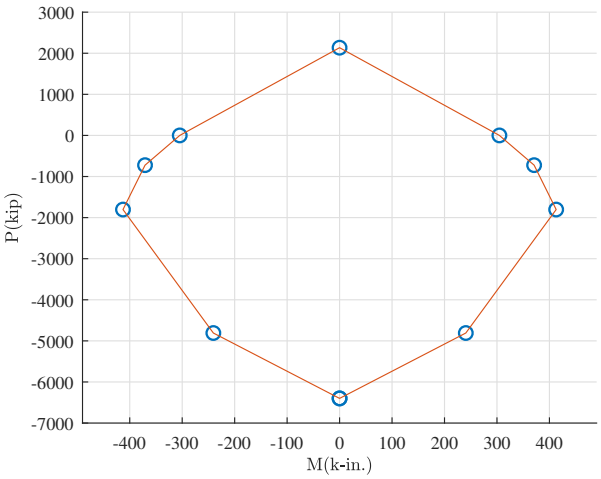

(b)

Figure 5.21: Piece-wise linear yield domains of: (a) Column C1; (b) Column C2.

Table 5.7: Bending strength for beam elements of the reinforced concrete frame.

RC Section type	B1	B2
M_n (kN-m)	211.15	127.10

Table 5.8: The shakedown residual displacements obtained from the proposed section-based strain-driven framework of the reinforced concrete frame under alongwind loads.

DOF	u_{r_1} (m)	u_{r_2} (m)	v_{r_2} (m)	ϕ_{r_2} (rad)	v_{r_3} (m)	ϕ_{r_3} (rad)	v_{r_5} (m)
Proposed framework	0.0434	0.0869	0.0005	-0.0121	0.0004	-0.0076	0.0012
DOF	ϕ_{r_5} (rad)	v_{r_6} (m)	ϕ_{r_6} (rad)	v_{r_8} (m)	ϕ_{r_8} (rad)	v_{r_9} (m)	ϕ_{r_9} (rad)
Proposed framework	-0.0122	0.0012	-0.0063	0.0007	-0.0121	0.0007	-0.0077

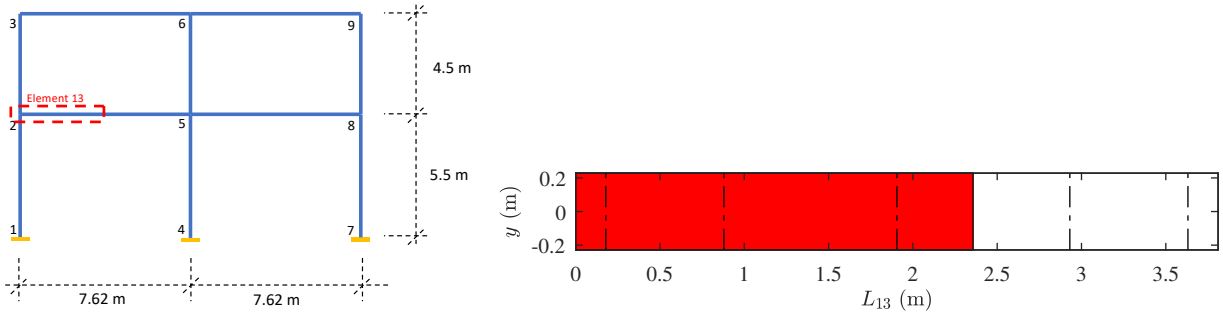

(a) (b)

Figure 5.22: (a) Element location; (b) Plasticity distributed along Element 13 of the reinforced concrete frame obtained from the section-based framework.

5.5 Example of the Monte Carlo Scheme

5.5.1 Concentrated plasticity example

5.5.1.1 Description

In this section, the probabilistic framework of Section 4.5 is illustrated on the steel frame of Figure 5.1. In addition to the horizontal loads, vertical dead loads due to the self weight of the elements as well as a super dead load of 23.5 kN/m were considered. For this application, the wind load histories were given a total length of $T = 3600$ s. A full range of wind directions were considered, namely α was varied between 0° and 90°, for mean wind speeds at the building top of $\bar{v}_y = 52.5$ m/s (approximately 700 year MRI for Miami) and $\bar{v}_y = 56.5$ m/s (approximately 1700 year MRI for Miami). The first five vibration modes with damping ratios of 2.5% were once again considered in estimating the dynamic steady state elastic response, $\mathbf{Q}^s(t)$, of the system. The following deformation limits were considered for describing the susceptibility to failure:

1. Residual drift ratio: $\tilde{u}_r/h_j = 0.5\%$

2. Peak interstory drift ratio: $\tilde{\hat{u}}/h_j = 2.5\%$

3. Plastic hinge rotation: $\tilde{\theta}_p = 0.01$ rad

where $\tilde{u}_r$ and $\tilde{\hat{u}}$ are the limits in terms of residual and peak horizontal floor displacements at shakedown, h_j is the height of the jth floor, while $\tilde{\theta}_p$ is the limit placed on the plastic hinge rotation. These limits were considered for all components of $\mathbf{u}_r$, $\hat{\mathbf{u}}$, and $\boldsymbol{\theta}_p$.

As described in Section 4.5, the classic solution method was first employed to identify whether the structure remained elastic or was susceptible to collapse due to non-shakedown. To estimate the plastic deformations for the non-collapse scenarios, the iterative algorithm of Section 3.3.2 was continued until a load multiplier of $s = 1$ (i.e. estimates of the plastic deformations and strains under the unamplified loads were considered).

5.5.1.2 Results

The analyses were carried out for α varying from $\alpha = 0°$ to $\alpha = 90°$ in 10 degree increments and for two wind intensities. For each wind direction and intensity, $N_s = 5000$ samples were considered in the Monte Carlo simulation. Table 5.10 reports the probabilities of collapse susceptibility for all wind directions and a wind intensity corresponding to a MRI of 700 years while Table 5.10 reports the analogous quantities for a wind intensity of MRI 1700 years. The governing failure probability for a MRI of 700 years is around 0.1. With 5000 simulations, the variance of the estimated failure probability is 1.8×10^{-5}, which is considered adequate for this case study. As can be seen from Figure 5.23, the alongwind ($\alpha = 0°$ in Figure 5.1) response of the structural system led to the highest total probabilities of collapse susceptibility. Having said this, in the acrosswind direction ($\alpha = 90°$), the structural system experienced a significant increase in failure probability, with respect to immediately adjacent wind directions, due to vortex shedding. From Tables 5.9 and 5.10, it can be seen that, in the alongwind direction, the structure was susceptible to inelastic collapse due to incapability to shakedown, excessive residual drift, and excessive plastic hinge rotations. In the acrosswind direction, on the other hand, failure for this structural system was due exclusively to an incapability to shakedown. For the intermediate wind directions,

it is interesting to observe how, for the deformation limits considered in this case study, susceptibility to collapse can easily be produced by excessive deformations. This illustrates the importance of estimating the plastic deformations and strains alongside the shakedown probability in order to fully characterize the collapse susceptibility of wind excited structural systems. Because the structural system considered in this work showed particular sensitivity to collapse susceptibility for alongwind and acrosswind actions (the wind directions $\alpha = 10^\circ$ and $\alpha = 20^\circ$ produce, for all intents and purposes, alongwind responses), the following discussion will focus on the wind directions of $\alpha = 0^\circ$ (alongwind) and $\alpha = 90^\circ$ (acrosswind).

As mentioned in Section 4.5, alongside the collapse susceptibility probabilities, the proposed framework also allows the probability distributions associated with peak/residual deformations and plastic strains at shakedown to be directly estimated. To illustrate this, Figures 5.24 and 5.25 report the exceedance probability distributions associated with the peak horizontal displacement responses given shakedown (SD) for the 1st, 20th and 37th floor in the alongwind and acrosswind directions. As can been seen, for low probabilities, significant deviation from the purely elastic peak responses can be observed. As mentioned in Section 4.2, this information is essential for the correct estimation of $P(DV > dv|NC, im)$ (i.e. losses given that the building is not susceptible to collapse (NC)). Exceedance probability distributions can also be estimated directly in terms of the residual deformations and plastic strains. As an example, Figure 5.26 reports the distributions associated with the residual displacements at select floors under 700-year alongwind loads. Figure 5.25, on the other hand, illustrates the exceedance probability distributions associated with plastic hinge rotations at two select hinges (see Figure 5.6) for 1700-year acrosswind loads. From Figure 5.25, it can be observed that for the structure considered in this case study, 57% of Hinge 263 responses, located at the 21st story, experienced plastic deformations while less than 40% of Hinge 223 responses experienced plastic deformations. Through the proposed framework, this kind of detailed information is made available for all 962 possible plastic hinge locations. Similarly, information such as that shown in Figure 5.26 is available for all the degrees of

Table 5.9: Inelastic collapse susceptibility performance for $\bar{v}_y$ with a MRI of 700 years

Wind direction, α	0°	10°	20°	30°	40°	50°	60°	70°	80°	90°
Non-shakedown collapse prob.	0.0718	0.0534	0.0040	0.0004	0	0	0	0	0	0.0034
Residual drift collapse prob.	0.0474	0.0194	0.0018	0.0002	0	0	0	0	0	0
Plastic hinge collapse prob.	0.0174	0.0098	0.0010	0	0	0	0	0	0	0
Peak drift collapse prob.	0	0	0	0	0	0	0	0	0	0
Total collapse prob.	0.137	0.0826	0.0068	0.0006	0	0	0	0	0	0.0034

Table 5.10: Inelastic collapse susceptibility performance for $\bar{v}_y$ with a MRI of 1700 years

Wind direction, α	0°	10°	20°	30°	40°	50°	60°	70°	80°	90°
Non-shakedown collapse prob.	0.9830	0.9914	0.6372	0.0364	0.0130	0.0064	0.0014	0.0004	0.0488	0.3690
Residual drift collapse prob.	0.0090	0.0022	0.0664	0.0130	0.0050	0.0026	0.0008	0	0.0014	0
Plastic hinge collapse prob.	0.0050	0.0028	0.0506	0.0074	0.0028	0.0020	0.0004	0	0.0018	0
Peak drift collapse prob.	0	0	0	0	0	0	0	0	0	0
Total collapse prob.	0.9970	0.9964	0.7542	0.0568	0.0208	0.0110	0.0003	0.0004	0.0520	0.3690

freedom of the system.

Finally, it should be observed that the proposed approach provided the solutions discussed above in a matter of hours. If a similar analysis was carried out by directly integrating the elastoplastic equations for each of the $N_s = 5000$ samples of the simulation, the estimated run time would be in the order of weeks.

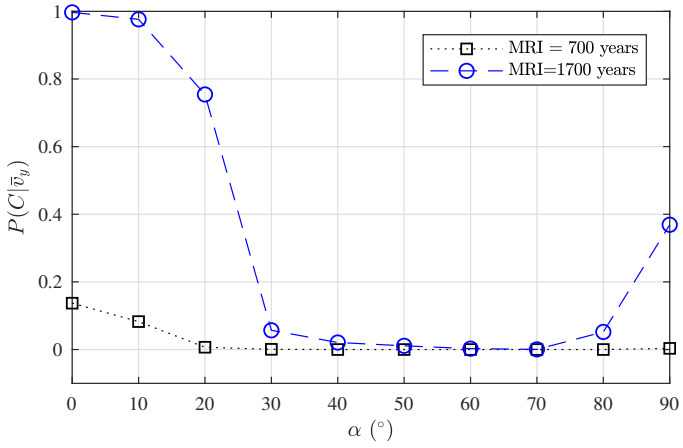

Figure 5.23: Variation of the total collapse probability with wind direction.

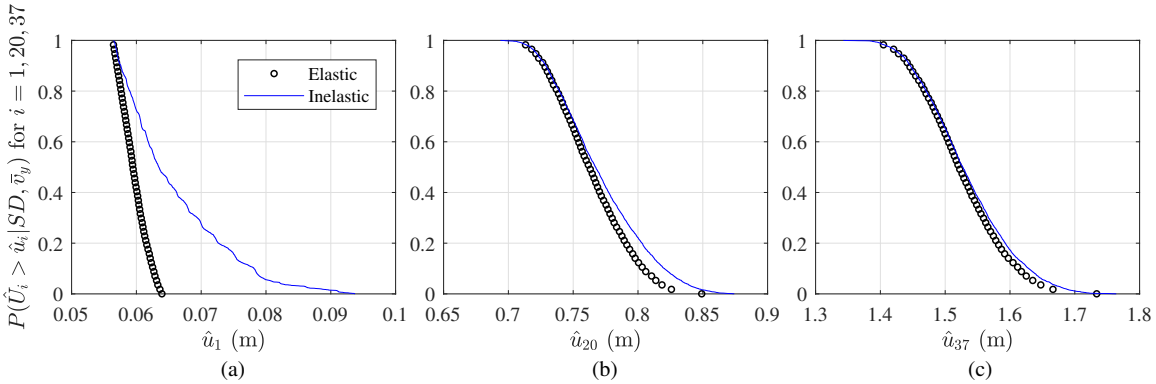

Figure 5.24: Probability of exceedance of the alongwind (MRI = 700 years) peak displacement responses at: (a) Floor 1; (b) Floor 20; and (c) Floor 37.

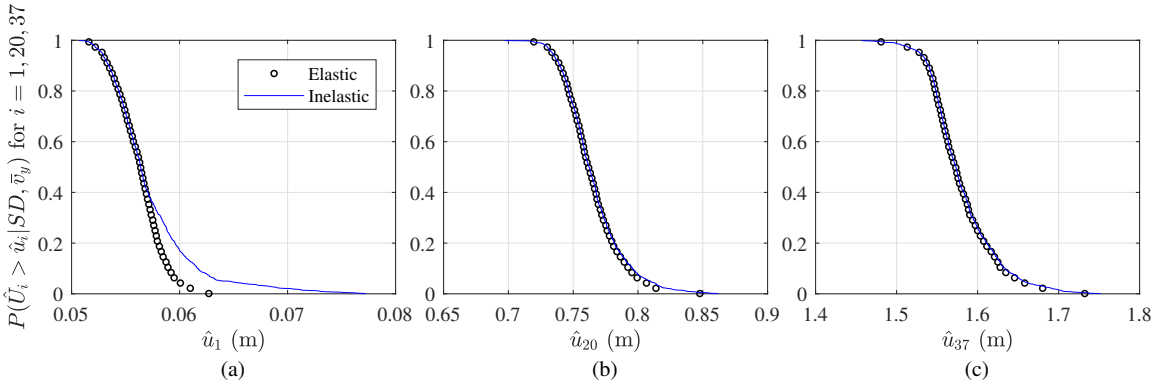

Figure 5.25: Probability of exceedance of the acrosswind (MRI = 1700 years) peak displacement responses at; (a) Floor 1; (b) Floor 20; and (c) Floor 37.

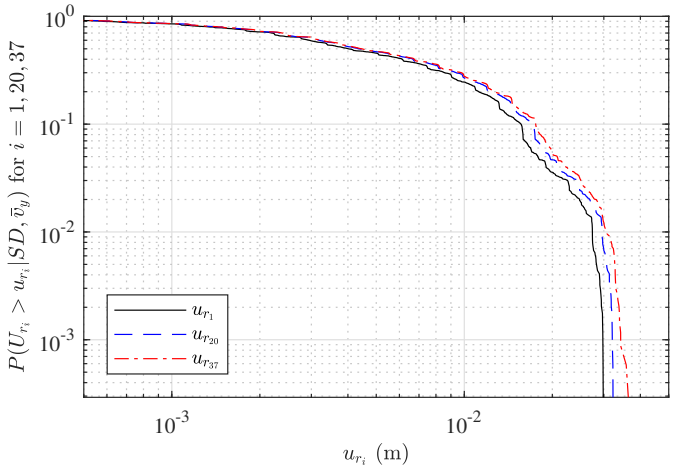

Figure 5.26: Probability of exceedance of the residual displacements at Floor 1, 20 and 37 in the alongwind direction with MRI = 700 years.

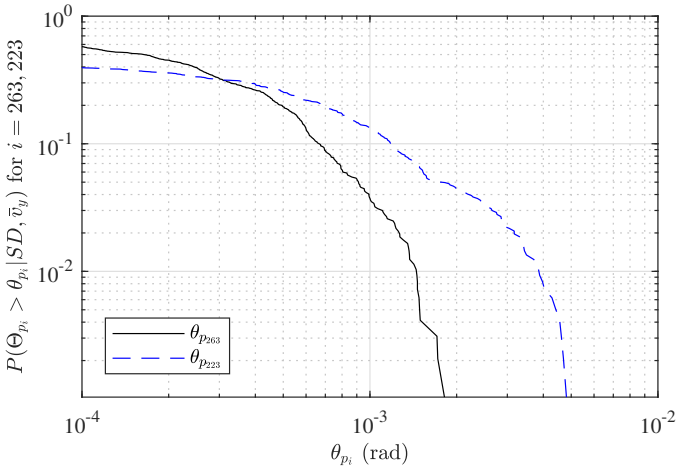

Figure 5.27: Probability of exceedance of the plastic hinge rotations for Hinge 263 and Hinge 223 in the acrosswind direction with MRI = 1700 years.

5.5.2 Distributed plasticity example

5.5.2.1 Description

In this section, the probabilistic framework of Section 4.5 is illustrated on the steel frame described in Section 5.4.1, as shown in Figure 5.13. The total duration of the wind storm was taken as $T = 3840$ s with linear ramp-up and -down over the first and last two minutes of the storm. Three intensity levels were considered, defined by wind speeds at the building top of $\bar{v}_y = 34.0$ m/s, 36.4 m/s and 38.0 m/s. These speeds corresponded to MRIs of 700, 1700 and 3000 years for Miami, FL. The following deformation limits were considered for describing failure:

1. Residual drift ratio: $\tilde{u}_r/h_j = 0.1\%$
2. Peak interstory drift ratio: $\tilde{\hat{u}}/h_j = 2.5\%$
3. Plastic fiber strain: $\tilde{\epsilon}^p_{n_i} = 0.01$

where $\tilde{\epsilon}^p_{n_i}$ is the limit placed on the plastic strain occurring in any of the fibers of the discretization. In defining these limits, it should be observed that any limiting values can be considered as can any response of interest, including relative deformations between the top and bottom of the columns to ensure stability requirements.

5.5.2.2 Results

In estimating the conditional probability of collapse susceptibility, $P(C|\bar{v}_y)$, through the estimator of Eq. (4.15), $N_s = 10000$ realizations of the stochastic wind loads were considered for each intensity level. The elastic failure probabilities, i.e. the probability that $s_e < 1$, for the three intensity levels were respectively 0.02, 0.59, and 0.99, while the inelastic failure probabilities (defined as the failure to reach the state of shakedown (failure scenario 1)) or exceedance of the inelastic response limits defined above (failure scenario 2)) were zero for the first two intensity levels (i.e. susceptibility to collapse occurred for no samples of the simulation) and 0.0017 for a MRI of 3000 years. In particular, all samples reached the state of shakedown. Susceptibility to collapse therefore occurred exclusively due to the occurrence of failure scenario 2. The large difference between the elastic and inelastic failure probabilities illustrates the significant reserves of strength of the structure after first yield. This reserve can be quantified through the ratio between the elastic and shakedown multipliers s_e/s_p. This ratio is illustrated in Figure 5.28 for the wind load histories associated with a MRI of 3000 years. In particular, the expected value of this ratio (i.e. the expected overstrength) is 1.65. This clearly illustrates how the state of shakedown, which provides safety against failure mechanisms associated with low cycle fatigue (i.e. alternating plasticity), ratcheting, or instantaneous plastic collapse, provides a large window of safe inelastic behavior. In this case study, the failure probability associated with the traditional first yield limit state is 0.02 for a MRI of 700 years. With 10000 samples, the variance of the estimated failure probability is 1.96×10^{-6}, which is deemed adequate for this example. With respect to the inelastic deformations at shakedown, it is interesting to observe that the probability of failure of the structure due to the exceedance of the limit states reported above was 0.0017 conditioned on a 3000 year wind speed. In particular, this was due exclusively to excessive residual deformations (i.e. no samples failed due to excessive peak drifts or plastic strains in the fibers).

The inelastic response samples generated from the resolution of the incremental dynamic

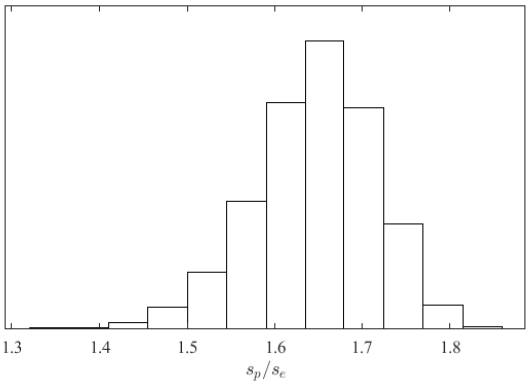

Figure 5.28: Histogram of the ratio between the elastic and shakedown multipliers for the wind records with MRI of 3000 years.

shakedown problem of Section 3.4.3 can be used to estimate the distribution functions associated with any parameter η of interest as:

$$F_\eta(\eta|\bar{v}_y) = F_\eta(\eta|\bar{v}_y, SD)P(SD|\bar{v}_y) \tag{5.4}$$

where $F_\eta(\eta|\bar{v}_y)$ is the cumulative distribution function (CDF) of η conditional on $\bar{v}_y$, $F_\eta(\eta|\bar{v}_y, SD)$ is the CDF of η conditional on both $\bar{v}_y$ and the occurrence of shakedown (SD), while $P(SD|\bar{v}_y)$ is the probability of shakedown given $\bar{v}_y$. In particular, $P(SD|\bar{v}_y)$ can be estimated as $P(s_p > 1|\bar{v}_y)$ while $F_\eta(\eta|\bar{v}_y, SD)$ can be directly estimated from the inelastic response samples. Within the context of Eq. (5.4), Figure 5.29 shows the exceedance distributions associated with the peak horizontal displacement responses at the building top for wind loads with MRIs of 1700 and 3000 years. It can be seen that, for low probabilities, there is a noticeable deviation from the elastic peak responses, especially under a 3000 MRI wind load. Figure 5.30 reports the exceedance distributions associated with the residual displacements occurring at the first and second floors for wind loads with MRIs of 1700 and 3000 years. As expected, larger residual displacements generally occur at the top floor. Figure 5.31(a) shows the exceedance distributions associated with the plastic strains for two selected fibers under a 3000 year MRI wind load. The location of the fibers is shown in

Figure 5.31(b). From Figure 5.31(a), it can be observed that there is a 94% chance that Fiber A will experience plastic strains for this wind intensity, while this is 92% for Fiber B.

In closing this section, it should be observed that this type of detailed information is available for all degrees of freedom and fibers of the discretization at a computational time that was over two orders of magnitude less than direct integration performed in OpenSees. This computational difference is expected to be even greater for larger systems subject to longer duration wind events.

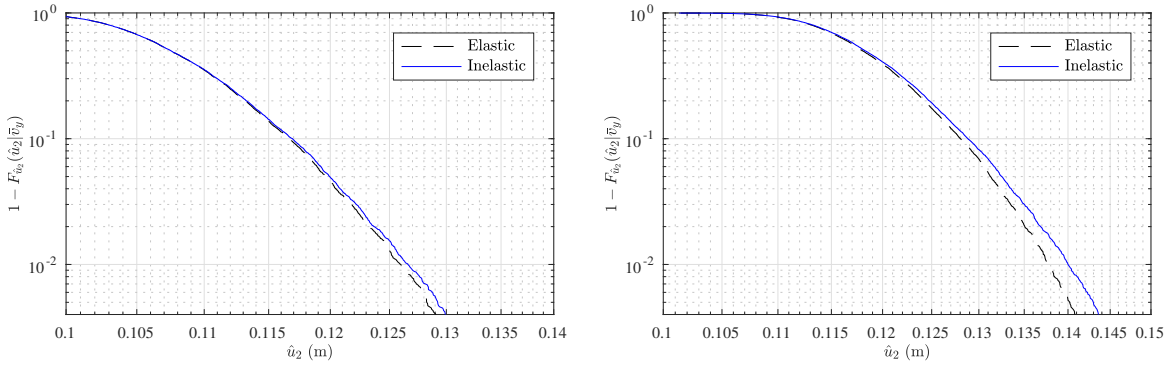

(a) (b)

Figure 5.29: Exceedance probabilities associated with peak displacement responses at the building top for: (a) MRI=1700 years; and (b) MRI=3000 years.

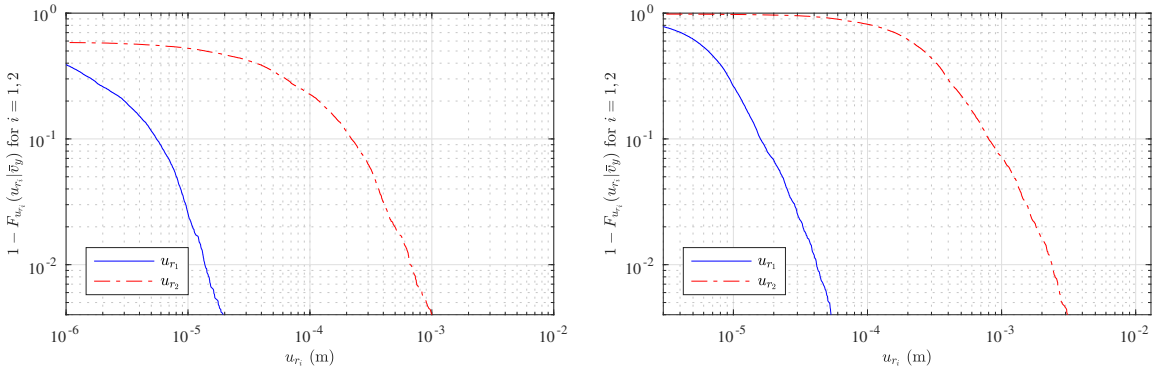

(a) (b)

Figure 5.30: Exceedance probabilities associated with residual displacement responses at floor 1 and 2 for: (a) MRI=1700 years; and (b) MRI=3000 years.

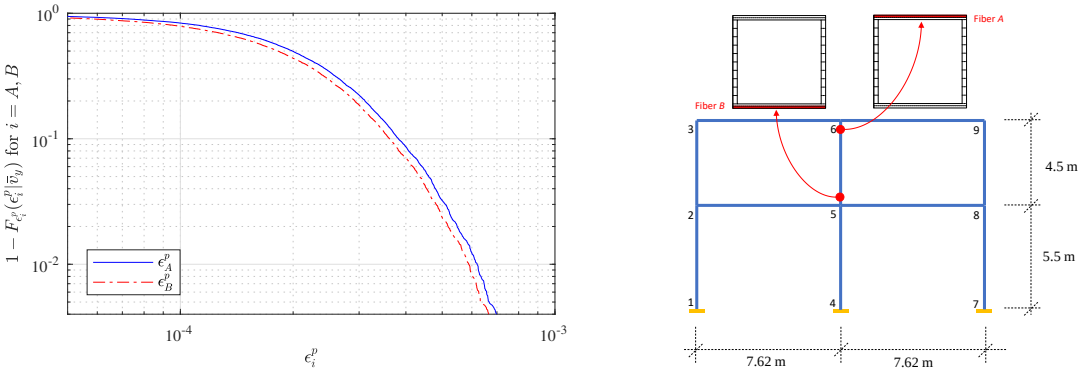

(a) (b)

Figure 5.31: (a) Probability of exceedance associated with the plastic strains of two selected fibers and wind loads with MRI = 3000 years; (b) location of the fibers.

5.6 Summary and Conclusions

The primary objective of the work outlined in this chapter was the validation of the framework outlined in Chapter IV. To this end, a suite of concrete and steel structures were developed and solved through both the approach of Chapter IV as well as through the implementation of direct integration methods. Near perfect correspondence between the proposed approach and direct integration provided an initial validation of the proposed concentrated and distributed shakedown models within the probabilistic setting of Chapter IV. Examples were also presented for the Monte Carlo simulation strategy of Section 4.5 while considering stochastic wind loads. The examples clearly illustrated both the efficiency of the proposed approach as well as the wide variety of probabilistic output parameters provided by the scheme.

CHAPTER VI

A Full Scale Case Study

6.1 Overview

In this chapter, a full scale three-dimensional case study is presented to illustrate the practicality of the proposed system-level collapse susceptibility framework. The primary goals of the work outlined in this chapter are:

1. Development and verification of a three-dimensional dynamic finite element model for the case study.

2. Application of the section-based distributed plasticity dynamic shakedown framework to the 3D model.

3. Inelastic performance assessment within the context of the system-level collapse susceptibility framework developed in Chapter IV.

In reaching the first goal, a three-dimensional finite element model of the Rainier Square Tower, provided by the engineering consultancy Magnusson Klemencic Associates (MKA), was developed in OpenSees. Displacement-based (DB) beam column elements were adopted with five integration points along each element. Walls were modeled by DB beam column elements. The width of the walls was modeled through rigid link elements connected to the axis of each wall element. Superimposed dead loads were considered in addition to the

self-weight of the elements and the weight of the framing system. The deformed shape of the structure was verified with unit loads in both global X- and Y-directions at the building top. For further application to dynamic analysis, the mode shapes and natural frequencies of the 3D tower were evaluated through modal analysis.

In reaching the second goal, the section-based dynamic shakedown framework of Chapter III was applied to the 3D tower. Prior to direct implementation, piecewise linear 3D yield surfaces were defined for all sections of the structure under consideration. In particular, for each reinforced concrete section, the yield domains were modeled through 26 flat surfaces that considered interaction between the axial force and biaxial bending, while, for steel sections, the yield surfaces suggested by the American Institute for Steel Construction (AISC) (*AISC 360-16*, 2016) were considered. Furthermore, the wind tunnel informed stochastic wind load model of Section 4.4.1, which is capable of capturing the record-to-record variability in the dynamic wind loads, was calibrated to building specific wind tunnel data for generating sets of synthetic wind records for the Rainier Square Tower. Dynamic shakedown analysis of the tower was then carried out considering wind loads of mean recurrence intervals (MRIs) of 300 and 700 years over a full range of wind directions, providing useful information on not only the safety but also the plastic reserves of the structure.

To achieve the third goal, stochastic wind loads were generated for wind directions selected from the set $\alpha \in \{10^\circ, 20^\circ, 30^\circ, \cdots, 360^\circ\}$ following a uniform distribution and a MRI of 300 years. The system-level collapse susceptibility framework developed in Chapter IV for providing a general description of collapse susceptibility, considering both non-shakedown and failure due to excessive deformations, was then adopted along with the section-based strain-driven dynamic shakedown framework to estimate the system-level collapse susceptibility probability of the 3D tower. In addition, probability distributions of residual displacements over the height of the tower were generated together with plastic deformations for all elements of the structure.

6.2 Numerical Model

In this chapter, the Rainier Square Tower designed by the engineering consultancy MKA was adopted for the full scale case study. A 3D finite element (FE) model of the Rainier Square Tower was first developed for dynamic analysis in OpenSees. In this section, this model will be described first. This will be followed by the verification of the model through static analyses considering unit loads at the building top, as well as dynamic analysis in the form of modal analysis.

6.2.1 Finite element model

Illustration of the Rainier Square Tower and the lateral load resisting system modeled in the case study are reported in Figure 6.1. The lateral load resisting system of the tower consists of a concrete core and an outrigger truss connected at floors 38-40 that engages six outrigger columns. The concrete core walls are connected by coupling beams at the floor levels, while the outrigger columns extend from the foundation to the outrigger truss. The concrete core system is composed of three cells from the foundation to Level 18, two cells from Level 18 to 40, and one cell from Level 40 to the roof. In addition, the walls of the concrete core system reduce in thickness along the height of the building at designated levels.

All the following analysis, i.e. shakedown analysis as well as dynamic response analysis, will consider the FEM model of the structure fixed at Level 1. Floor levels were taken to be at the coupling beam elevations as opposed to the indicated floor levels from the drawings (see Model Level Elevations in Appendix A). Each floor was considered to act as a rigid floor diaphragm for horizontal movements. Therefore, the floors could move freely in the X- and Y-directions and rotate about the Z-axis (indicated with u_X, u_Y and θ_Z respectively), giving the building a total of 177 degrees of freedom (The core roof acts as an additional floor level, giving the structure a total of 59 floors).

Materials with linear constitutive laws were assumed for both concrete and steel for elastic analysis. The material strengths considered are summarized in Table 6.1. The Young's

(a) (b)

Figure 6.1: Rainier Square Tower. (a) Architectural and structural system rendering of the building (*Hilburg*, 2018); (b) OpenSees finite element model.

modulus of the concrete, E_c, was calculated as follows:

$$E_c = 57,000\sqrt{f'_c} = 5098\ ksi \tag{6.1}$$

The shear modulus of the concrete was calculated using basic mechanics of materials as follows, with the assumption that the Poisson's ratio, ν, for the concrete was 0.15:

$$G_c = \frac{E_c}{2(1+\nu)} = 2216\ ksi \tag{6.2}$$

For the steel, the Young's modulus, E_s, and the shear modulus, G_s, were taken to be 29,000 ksi and 10,900 ksi, respectively. The modulus of elasticity used for the rigid material assigned to all rigid link connections, modeled as "twoNodeLink" elements, was taken to be 2.32×10^{10} ksi to guarantee a rigid behavior. Figure 6.2 reports the deformed shape of the 3D

Table 6.1: Summary of material properties.

Material	Strength
Structural steel (wide flange)	$F_y = 50$ ksi
Concrete (shear walls and mega-columns)	$f'_c = 8$ ksi
Reinforcing steel	$f_y = 60$ ksi

tower, illustrating that the rigid link elements (the brown elements in the red dashed oval) connecting the center lines of the shear walls to the coupling beam element (black element in the figure) were stiff enough to model the shear wall behavior.

To implement the distributed dynamic shakedown framework, the concrete core system was modeled using displacement-based (DB) beam-column elements with their local x-axis oriented in the vertical direction of the building. All elements were modeled with five integration points along their local x-axis and utilize a Gauss-Legendre integration scheme, as illustrated in Figure 6.3. To maintain continuity across all elements along the height of the building, adjacent wall elements were connected at each floor using two-node rigid link connections. The coupling beams, outrigger truss members, and outrigger columns were also modeled using DB beam-column elements with five integration points along their local x-axis, and utilizing Gauss-Legendre integration. All coupling beams were connected to adjacent wall elements using two node rigid link connections. See Appendix B for detailed element layout.

In addition to the mass of all elements and the framing system, which consists of 2-1/2 inches of normal-weight (145 pounds per cubic foot) concrete over 3-inch ribbed steel decking (490 pounds per cubic foot), additional lumped mass equal to the superimposed dead loads, summarized in Table 6.2, was applied at the mass node, taken to be located at the geometric center of each floor. Rigid floor diaphragms were then incorporated utilizing the Rigid Diaphragm multiple constraints function in OpenSees with the mass node assigned as the master node at each floor and all other nodes of the corresponding floor (outrigger column nodes included) assigned as slave nodes. The X- and Y-displacements of the slave nodes

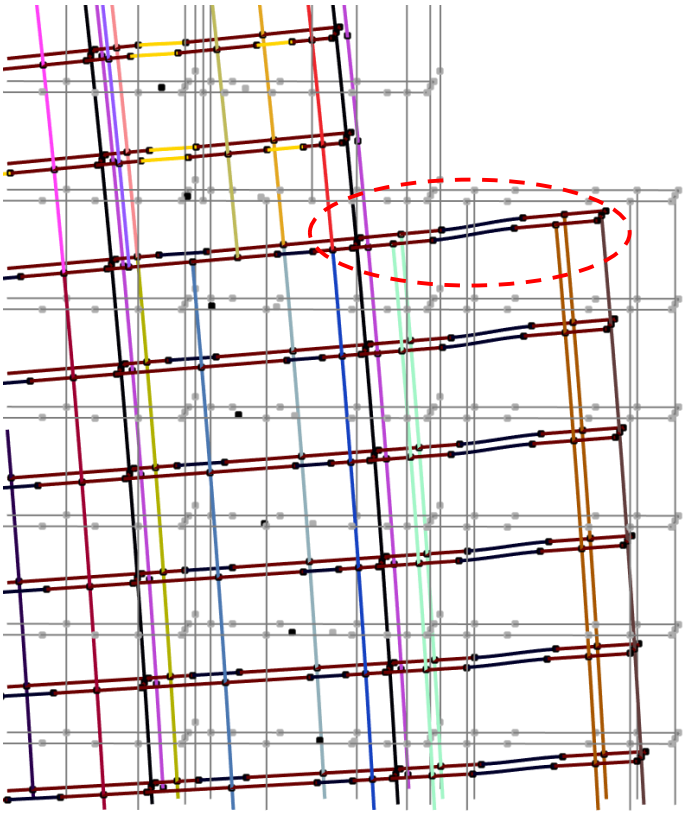

Figure 6.2: Illustration of the deformed shape with rigid link elements.

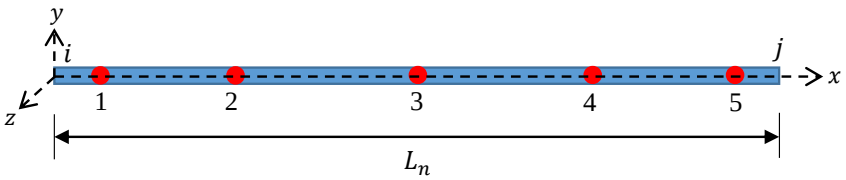

Figure 6.3: Location of the five integration points along a typical DB element.

Table 6.2: Summary of superimposed dead loading.

Use	Superimposed Dead Loading
Corridors and Stairs (within core)	15 psf
Level 2 to 38 and Level 59	10 psf
Level 39 to 58	30 psf
Level 60	25 psf

can then be defined in terms of the master node by the following kinematic relationship:

$$\begin{Bmatrix} u_{X1} \\ u_{Y1} \\ \vdots \\ u_{Xn_s} \\ u_{Yn_s} \end{Bmatrix} = \begin{bmatrix} 1 & 0 & -(Y_1 - Y_M) \\ 0 & 1 & (X_1 - X_M) \\ & \vdots & \\ 1 & 0 & -(Y_{n_s} - Y_M) \\ 0 & 1 & (X_{n_s} - X_M) \end{bmatrix} \begin{Bmatrix} u_{XM} \\ u_{XM} \\ \theta_{ZM} \end{Bmatrix} \tag{6.3}$$

where X_i, Y_i, X_M and Y_M are the X- and Y-coordinates of the slave nodes and master node while n_s is the number of slave nodes on the rigid diaphragm. This transformation was applied to the degrees of freedom of each floor.

6.2.2 Verification of the FE model

6.2.2.1 Static analysis

Before carrying out dynamic analysis, the 3D FE model was first verified with static loads at the building top. A unit load was applied to the master node of the top floor in both global X- and Y-directions. The structure deformed as expected under these loads, as shown in Figure 6.4 with amplification for illustration purpose.

In applying the dynamic shakedown approach, the structure under gravity loading, including self-weight of the structure and the superimposed dead load, is considered as the initial safe state, where the strain-driven iterative approach starts from, before applying the wind loads. Therefore, the initial generalized stress state as well as the initial displacements

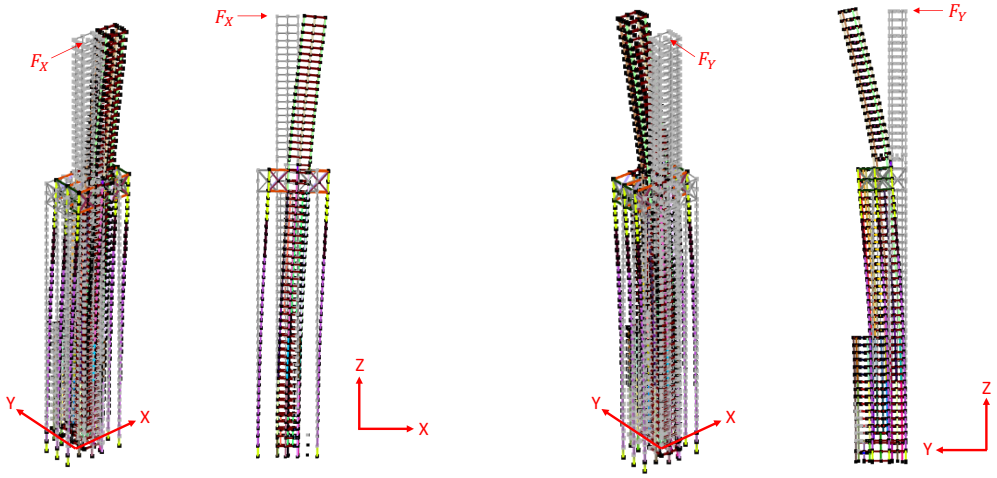

(a) (b)

Figure 6.4: Deformed shapes of the FE model subject to unit loads at the top floor in (a) X-direction and (b) Y-direction.

Table 6.3: Natural periods of the FEM model.

Mode	1^{st}	2^{nd}	3^{rd}	4^{th}	5^{th}
Period (s)	6.05	5.71	1.80	1.64	1.28

due to gravity loading have to be estimated through static analysis prior to the implementation of the dynamic shakedown framework.

6.2.2.2 Modal analysis

Given the set-up described in Section 6.2.1, modal analysis was carried out yielding the first five natural periods as provided in Table 6.3. The first two modes were respectively in global X- and Y-direction while the rotational mode about global Z-axis was the fifth mode, which could be due to an underestimation of the rotational mass at each floor. The mode shapes are shown in Figure 6.5.

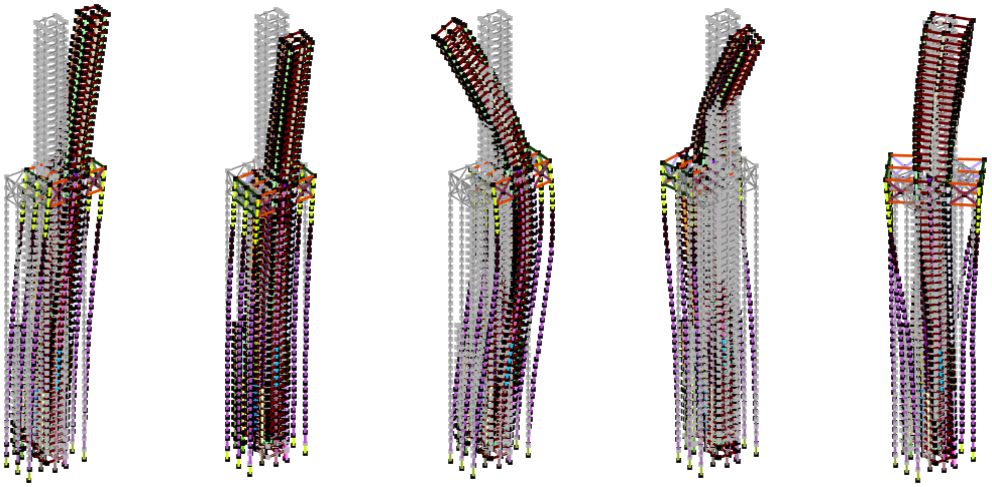

(a) 1^{st} (b) 2^{nd} (c) 3^{rd} (d) 4^{th} (e) 5^{th}

Figure 6.5: The first five mode shapes of the FEM model.

6.3 Dynamic Shakedown Analysis

In this section, the section-based distributed plasticity dynamic shakedown framework is applied to the 3D tower of Section 6.2. The 3D piecewise linear yield surfaces for all sections of the structure under consideration will be defined first, followed by the wind load model for generating wind tunnel informed synthetic wind records to be applied to the 3D structure.

6.3.1 Piecewise linearization of the yield surface

The implementation of the dynamic shakedown analysis requires the yield surfaces to be defined for each section along the beam-column elements of the structure under consideration. Assuming local y and z axes in the principal directions of the section, as illustrated in Figure 6.6, the yield surface is defined as the interaction domain between the axial load P and the biaxial bending M_y, M_z based on the following assumptions (*Wight*, 2015):

1. plane sections remain plane after deformation;

2. full strain compatibility exists between the steel reinforcements and the surrounding concrete;

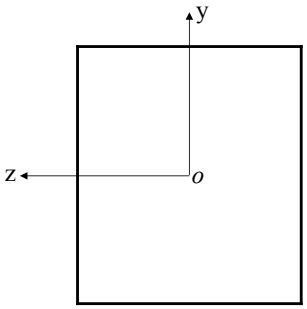

Figure 6.6: Reference system for a typical rectangular section.

3. elastic-perfectly plastic constitutive relation is assumed for both concrete (in compression) and reinforcing steel. Concrete is assumed to be a zero tension material;

4. shear and torsion failures are always prevented by the presence of appropriate transversal reinforcements.

In this section, piecewise linear three-dimensional yield surfaces will be defined for reinforced concrete wall and column sections, coupling beam sections, as well as steel beam sections.

6.3.1.1 Reinforced concrete wall and mega-column sections

Both mega-column and wall elements are designed to resist lateral wind or earthquake loads in addition to the gravity loads. Therefore, they are subjected to combined axial and biaxial bending loads. A multisurface piecewise linearization of the yield surface, as proposed in *Malena and Casciaro* (2008), is adopted as an approximate representation of the elastic domain of the section. Each surface is associated with a possible collapse mechanism of the section, defined by the following plastic strain vector:

$$\boldsymbol{\epsilon}_p = \left\{ \epsilon^p, \quad \chi_y^p, \quad \chi_z^p \right\}^T \tag{6.4}$$

where ϵ^p, χ_y^p and χ_z^p are respectively the plastic axial strain and curvatures about the local y- and z-axes of the section. The corresponding plastic resistance, R, can be determined

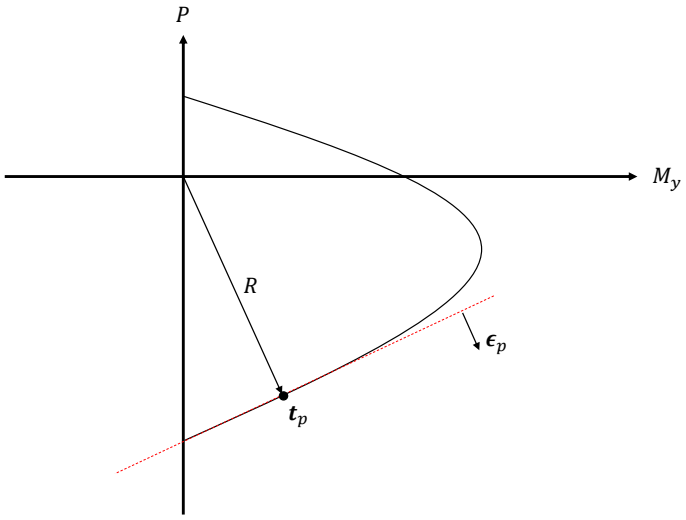

Figure 6.7: Linearized yield surface and the corresponding plastic resistance of a section.

through the following equation:

$$R = \max\{\boldsymbol{\epsilon}_p^T \mathbf{t} : \mathbf{t} \in \mathbb{E}\} \tag{6.5}$$

where $\mathbf{t} = \{P, M_y, M_z\}$ is the generalized stresses (i.e. section forces) of the section within the elastic domain $\mathbb{E}$. The failure stresses $\mathbf{t}_p$ associated with $\boldsymbol{\epsilon}_p$ can then be solved through the maximization of Eq. (6.5), as illustrated in Figure 6.7. In this work, since the full PMM yield surface was provided, the plastic resistance R, as well as the corresponding failure stresses $\mathbf{t}_p$ with respect to $\boldsymbol{\epsilon}_p$, can be conveniently estimated through the above equation by substituting $\mathbf{t}$ with all PMM points on the yield surface.

Considering both the precision and computational complexity, 26 flat surfaces are used for approximating the yield domain of the reinforced concrete column sections. The directions

for all surfaces, collected in $\mathbf{N} = [\mathbf{n}_1, \mathbf{n}_2, \cdots, \mathbf{n}_{26}]$, are given as:

$$\mathbf{N} = \begin{bmatrix} 1 & -1 & 0 & 0 & 0 & 0 & 1 & 1 & -1 & -1 & 1 & -1 & 1 & -1 \\ 0 & 0 & 1 & -1 & 0 & 0 & c_z & -c_z & c_z & -c_z & 0 & 0 & 0 & 0 \\ 0 & 0 & 0 & 0 & 1 & -1 & 0 & 0 & 0 & 0 & c_x & c_x & -c_x & -c_x \\ 0 & 0 & 0 & 0 & 1 & 1 & -1 & -1 & -1 & -1 & 1 & 1 \\ 1 & 1 & -1 & -1 & c_z & c_z & c_z & c_z & -c_z & -c_z & -c_z & -c_z \\ c_y & -c_y & c_y & -c_y & c & -c & c & -c & -c & c & c & -c \end{bmatrix} \tag{6.6}$$

where c_x, c_y and c_z are defined by limit stresses corresponding to principal directions through the following equations:

$$c_x = \frac{\|\mathbf{t}_{p_1} - \mathbf{t}_{p_2}\|}{\|\mathbf{t}_{p_5} - \mathbf{t}_{p_6}\|}, \qquad c_y = \frac{\|\mathbf{t}_{p_3} - \mathbf{t}_{p_4}\|}{\|\mathbf{t}_{p_5} - \mathbf{t}_{p_6}\|}, \qquad c_z = \frac{\|\mathbf{t}_{p_1} - \mathbf{t}_{p_2}\|}{\|\mathbf{t}_{p_3} - \mathbf{t}_{p_4}\|} \tag{6.7}$$

with $\mathbf{t}_{p_k}$ being the failure stresses corresponding to $\mathbf{n}_k$, while c is the average of c_x and c_z, i.e. $c = (c_x + c_z)/2$. Based on the normality condition, the direction of the k^{th} yield surface can be related to the plastic strain vector through $\mathbf{n}_k = \boldsymbol{\epsilon}_{p_k}$, therefore $\mathbf{t}_{p_k}$ can be easily solved through Eq. (6.5). In addition, it should be noted that this approximation provides an overestimate of the yield domain through external tangent linearization. The errors, however, have been shown to be relatively small and therefore acceptable for applications to concrete sections (*Malena and Casciaro*, 2008).

6.3.1.2 Reinforced concrete coupling beam sections

The axial loads P of the coupling beam elements are negligible due to the rigid diaphragm assumption, thereby allowing the definition of the yield surface to be completely governed by the interaction between the biaxial bending M_y and M_z. A yield domain of 8 flat surfaces, as shown in Figure 6.8, is therefore considered for a reinforced concrete beam with M_{py} and M_{pz} the moment strengths of the section with respect to bending around the y-axis and z-axis. In addition to these four points in the principal directions, the failure stresses at

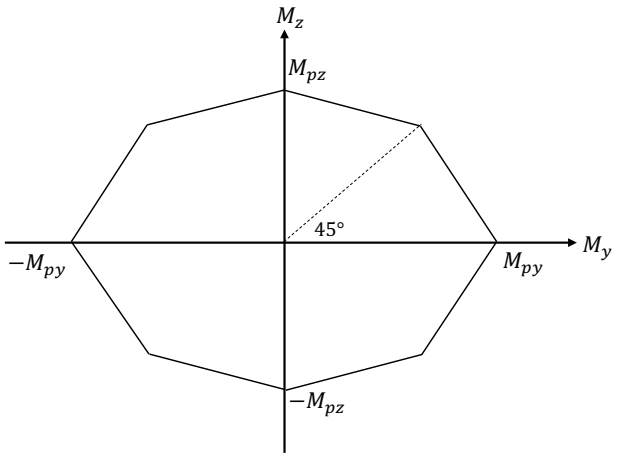

Figure 6.8: Piecewise linear failure domain of reinforced concrete coupling beams.

45°, 135°, 225° and 315° of Figure 6.8 can also be determined by interpolating the full PMM yield surface data with $P = 0$.

6.3.1.3 Steel beam sections

Similar to the coupling beam elements, the yield surfaces of steel beam sections are also defined by the interaction between the biaxial bending as the axial load effects are negligible. The AISC yield surface (*AISC 360-16*, 2016), as shown in Figure 6.9, is used in this work. The equation governing the interaction between the biaxial bending when the axial force $P = 0$ is:

$$\frac{|M_y|}{M_{py}} + \frac{|M_z|}{M_{pz}} = 1 \tag{6.8}$$

where the moment strengths M_{py} and M_{pz} of a steel section can be determined through

$$M_{py} = F_y Z_y, \quad M_{pz} = F_y Z_z \tag{6.9}$$

with Z_y and Z_z the plastic section moduli with respect to the y- and z-axes of the relevant cross section.

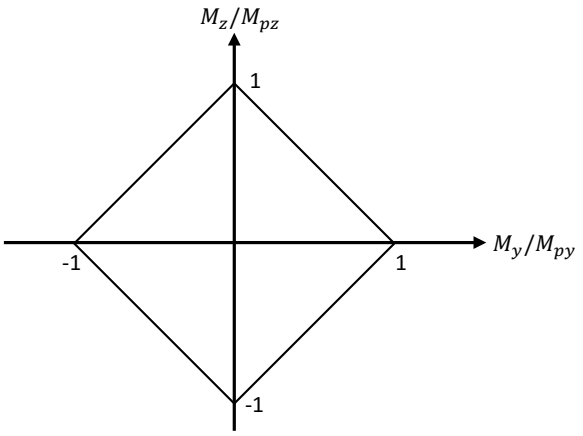

Figure 6.9: Piecewise linear failure domain for steel beams.

6.3.1.4 Elastic element assumption

To account for a few piers that are narrow and not pertinent to the global or local response of the structure, inelasticity is assumed not to occur in those elements, i.e. those elements are assumed elastic during the shakedown analysis. In addition, there are several small adjustment elements used during the modeling of the core walls that are used to connect the offset coupling beam to the actual floor level in the model (e.g. element #545 between Level 10 and 11 on Grid 3). These elements are also assumed elastic during shakedown analysis without compromising the accuracy of overall response of the structure. A list of DB elements that are considered elastic due to the aforementioned considerations is provided in Appendix A.

6.3.2 Stochastic wind loads

To enable Monte Carlo simulation for assessing failure probability, multiple realizations of the external aerodynamic loads $\mathbf{F}(t)$ are needed. For this application, the data-driven spectral proper orthogonal decomposition (POD) model of Section 4.4.1 is implemented. $\mathbf{F}(t)$ is therefore decomposed into N_l independent vector-valued subprocesses as follows (*Li*

and Kareem, 1991, 1993, 1997; *Chen and Kareem*, 2005; *Peng et al.*, 2017):

$$\mathbf{F}(t;\bar{v}_3,\alpha)=\sum_{j=1}^{N_l}\mathbf{F}_j(t;\bar{v}_b,\alpha) \tag{6.10}$$

where $\bar{v}_3$ is the 3-s gust basic wind speed at 33 ft (*ASCE 7-16*, 2016); $\bar{v}_b$ is the wind speed average over the total event duration (related to $\bar{v}_3$ through a deterministic transformation, as will be seen later); α is the wind angle measured from the true north, and $\mathbf{F}_j(t)$ is the jth vector-valued subprocess, which can be estimated through the following spectral representation:

$$\mathbf{F}_j(t;\bar{v}_3,\alpha)=\sum_{k=1}^{N_f}|\boldsymbol{\Psi}_j(\omega_k;\alpha)|\sqrt{2\Lambda_j(\omega_k;\bar{v}_3,\alpha)\Delta\omega_k}\times\cos(\omega_k t+\vartheta_{kj}+\boldsymbol{\theta_j}(\omega_k)) \tag{6.11}$$

where $\boldsymbol{\Psi}_j(\omega_k)$ and $\Lambda_j(\omega_k)$ are the jth frequency dependent eigenvector and eigenvalue of $\mathbf{F}(t)$, N_f is the total number of discrete frequencies considered in the interval $[0,N_f\Delta\omega_k]$ with $\Delta\omega_k$ representing the frequency increment that is related to the Nyquist (cutoff) frequency through $\omega_{\text{Nyquist}}=N_f\Delta\omega_k/2$, $\omega_k=k\Delta\omega_k$, ϑ_{kj} are independent and uniformly distributed random variables in $[0,2\pi]$, while $\boldsymbol{\theta}_j$ is a vector of complex angles with the ith component given by $\theta_{ji}(\omega_k)=\tan^{-1}(\text{Im}(\Psi_{ji}(\omega_k))/\text{Re}(\Psi_{ji}(\omega_k))$.

As discussed in Section 4.4.1 the eigenvalues and eigenvectors of $\mathbf{F}(t)$ used in Eq. (6.11) are to be estimated directly from the experimental loads obtained from the wind tunnel tests. In particular, $\Lambda_j(\omega_k)$ and $\boldsymbol{\Psi}_j(\omega_k)$ are related to the eigenvalues and eigenvectors of the scaled experimental wind tunnel load, $\mathbf{F}_w(\tilde{t})$, through the following relationships:

$$\Lambda_j(\omega_k;\bar{v}_3)=\left[\left(\frac{\bar{v}_{3600}}{\bar{v}_w}\right)^2\right]^2\left(\frac{\bar{v}_w}{\bar{v}_{3600}}\right)\Lambda_j^{(w)}(\tilde{\omega}_k) \tag{6.12}$$

$$\boldsymbol{\Psi}_j(\omega_k)=\boldsymbol{\Psi}_j^{(w)}(\tilde{\omega}_k) \tag{6.13}$$

where $\bar{v}_b=\bar{v}_{3600}$ is the mean hourly wind speed at a full-scale reference height that is related

to the basic wind speed $\bar{v}_3$ of interest through a transformation of Appendix A, $\bar{v}_w$ is the mean hourly wind speed at the reference height to which the wind tunnel loads $\mathbf{F}_w(\tilde{t})$ were scaled, $\omega_k = \frac{\bar{v}_{3600}}{\bar{v}_w}\tilde{\omega}_k$ with $\tilde{\omega}_k$ the kth frequency step at the wind tunnel reference speed, while $\Lambda_j^{(w)}(\tilde{\omega})$ and $\mathbf{\Psi}_j^{(w)}(\tilde{\omega})$ are eigenvalues and eigenvectors of $\mathbf{F}_w(\tilde{t})$ and are obtained from solving the following eigenvalue problem:

$$[\mathbf{S}_{\mathbf{F}_w}(\tilde{\omega}_k; \bar{v}_w, \alpha) - \Lambda^{(w)}(\tilde{\omega}_k; \bar{v}_w, \alpha)\mathbf{I}]\mathbf{\Psi}^{(w)}(\tilde{\omega}_k; \alpha) = 0 \tag{6.14}$$

where $\mathbf{S}_{\mathbf{F}_w}$ is the cross power spectral density of $\mathbf{F}_w(\tilde{t})$. It should be highlighted that, once $\Lambda_j^{(w)}(\tilde{\omega})$ and $\Psi_j^{(w)}(\tilde{\omega})$ are obtained through solving Eq. (6.14), they can be scaled to other wind speeds of interest simply through Eqs. (6.12)-(6.13). This scaling property, together with the POD scheme, which allows the subprocesses to be generated independently using only a few spectral modes, ensures the efficiency of the approach in generating the realizations of the stochastic wind loads process $\mathbf{F}(t)$. It should be observed that, the sampling frequency, $\tilde{\omega}$, associated with frequency points $\tilde{\omega}_k$, is related to the wind tunnel sampling frequency at model scale through $\tilde{\omega} = 2\pi\frac{\bar{v}_w s_{ws}}{\bar{v}_{ws} s_L}$ where $\bar{v}_{ws}$ is the wind speed at which the wind tunnel tests were carried out, s_L is the length scale factor of the full-scaled building to the rigid model, while s_{ws} is the sampling frequency used in the wind tunnel tests.

6.3.2.1 Wind tunnel data for Rainier Square Tower

In generating wind load histories, the stochastic wind load model of Section 6.3.2 was calibrated to wind tunnel datasets provided by Rowan Williams Davies & Irwin (RWDI). These data consisted in measurements made through the high-frequency base balance (HFBB) collected on a 1:400 rigid model of the Rainier Square Tower. In particular, the data was measured considering a sampling frequency of $s_{ws} = 300$ Hz for a total recorded duration of 118 s. Datasets associated with 36 wind directions ($\alpha = \{10°, 20°, ..., 350°, 360°\}$) were obtained, while the mean wind speeds, $\bar{v}_{ws}$, at a 60-inch height in the wind tunnel corre-

sponding to different angles can be found in Table A.1. These wind tunnel datasets were processed and scaled therefore defining horizontal force time series acting in the X and Y directions, $F_{X,j}(t)$ and $F_{Y,j}(t)$, and a torsional load time series, $M_{Z,j}(t)$, acting at the tower's reference center of coordinates (0 ft, -40 ft) at each floor. These full-scaled loading time histories were used in estimating the eigenvalues $\Lambda_j^{(w)}$ and eigenvectors $\mathbf{\Psi}_j^{(w)}$ of Eq. (6.14), which were related to Λ_j and $\mathbf{\Psi}_j$ of Eq. (6.11) through Eqs. (6.12)-(6.13). In calibrating Eq. (6.11), a sampling frequency of 2 Hz was considered for a cutoff frequency of 1 Hz. The first five POD spectral modes were considered in generating stochastic wind processes in this case study. The specific transformation scheme used in converting the basic wind speed $\bar{v}_3$ to the mean hourly wind speed $\bar{v}_{3600}$ is provided in Appendix A. An example of the scaled experimental dynamic wind loads and the corresponding simulated dynamic wind loads is presented in Figure 6.10. The effectiveness of the POD-based stochastic model in replicating correlation properties of experimental loads is illustrated through the autocorrelation and cross-correlation functions plotted in Figure 6.11 and Figure 6.12.

6.3.3 Shakedown analysis

6.3.3.1 Description

In this section, the section-based distributed plasticity dynamic shakedown framework is applied to the 3D tower with piecewise linear yield surfaces as defined in Section 6.3.1. The stochastic wind model of Section 6.3.2 was adopted for generating the wind loads at the reference point of each floor, which were then transferred to the master node of each level. Two intensity levels were considered with 3-s gust wind speeds $\bar{v}_3$ at 33 ft height of 91 and 96 mph, corresponding to MRI of 300 and 700 years respectively for Seattle. Wind load histories of total length of $T = 3600$ s were considered for all wind directions from 10° to 360° in 10° increments in order to provide a full description of the inelastic structural behavior of the system. In addition to the wind loads, gravity loads including the self-weight of the structure and the superimposed dead loads were considered in the analyses. To estimate the

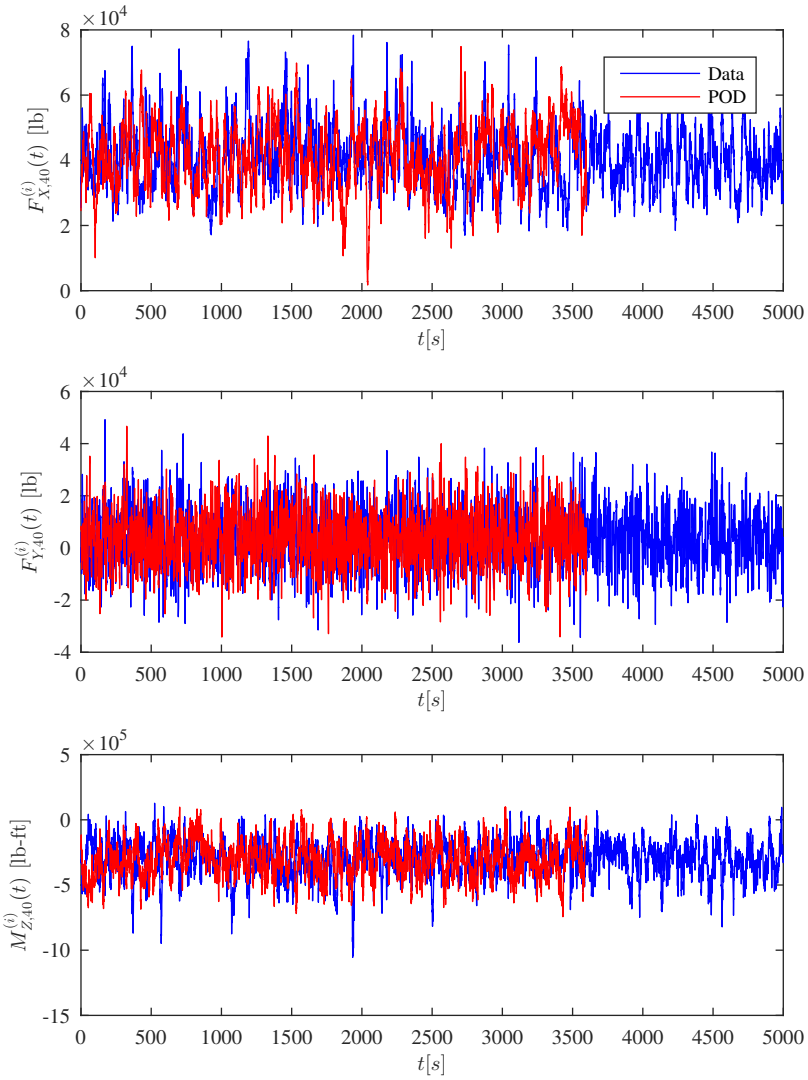

Figure 6.10: Experimental loads and a realization of the Level 40 stochastic wind loads for: $F_{X,40}(t)$, $F_{Y,40}(t)$, and $M_{Z,40}(t)$ associated with $\bar{v}_3 = 103$ mph and $\alpha = 330°$.

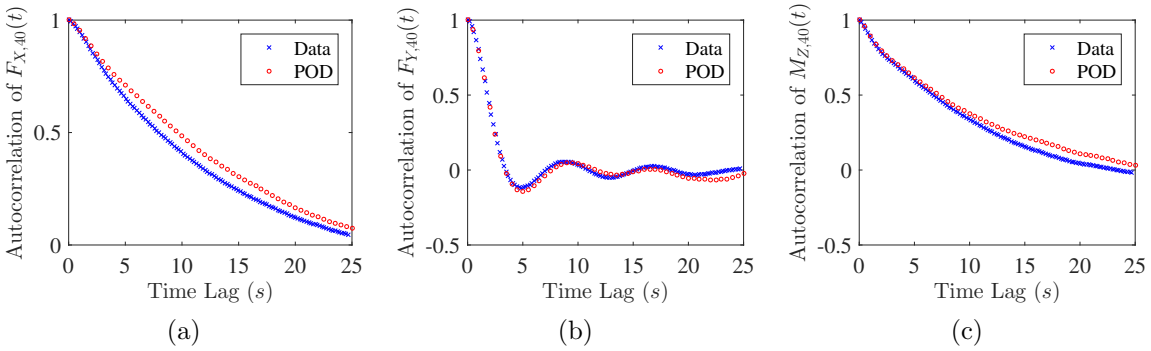

Figure 6.11: Autocorrelation of experimental loads and simulated wind loads associated with $\bar{v}_3 = 103$ mph and $\alpha = 330°$ for: (a) $F_{X,40}(t)$, (b) $F_{Y,40}(t)$, (c) $M_{Z,40}(t)$.

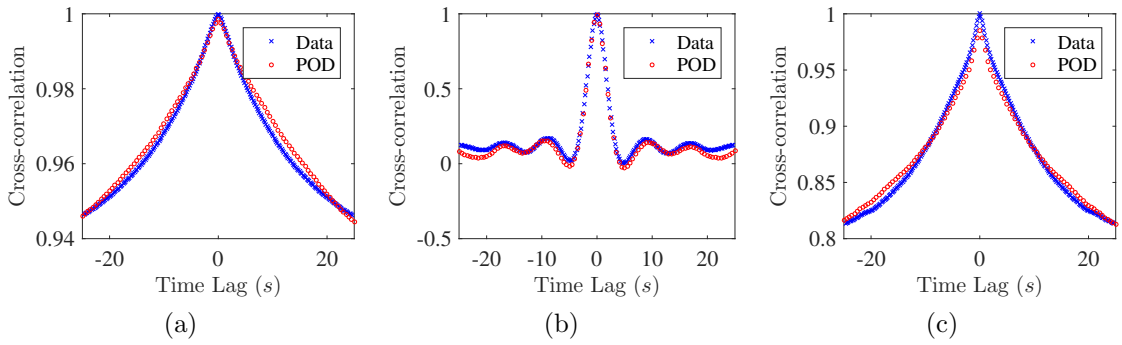

Figure 6.12: Cross-correlation of experimental loads and simulated wind loads associated with $\bar{v}_3 = 103$ mph and $\alpha = 330°$ between: (a) $F_{X,38}(t)$ and $F_{X,40}(t)$, (b) $F_{Y,38}(t)$ and $F_{Y,40}(t)$, (b) $M_{Z,38}(t)$ and $M_{Z,40}(t)$.

steady state elastic response of the system, the first five modes were considered in the modal analysis with damping ratios of 5%.

The linear programming (LP) solution method is first employed to identify whether the structure remains elastic or is susceptible to collapse due to non-shakedown by estimating the elastic, s_e, and plastic multiplier, s_p. This method allows a preliminary evaluation of the structure in just a few seconds. In particular, if $s_e \geq 1$, the structure will remain elastic under the windstorm with no occurrence of inelasticity. If $s_p \geq 1$, the structure will eventually shakedown under the wind loads and is therefore safe against plastic fatigue failure and/or incremental plastic collapse during the windstorm. In addition, elements where inelasticity occurs at shakedown are also identified.

6.3.3.2 Results

The analyses were carried out for $N_s = 10$ simulations in all wind directions, which is considered adequate for estimating the mean and standard deviation of all multipliers, and the two intensity levels mentioned above (i.e. 300 MRI and 700 MRI wind loads). Tables 6.4 and 6.5 report the mean and coefficient of variation (CV) of the elastic and plastic multipliers over all simulations for all directions respectively for the 300 and 700 MRI wind loads. It is worth noting how the multipliers vary from one direction to another, suggesting that the structure is more susceptible to wind excitation from certain wind directions. The structure is especially sensitive to wind loads coming from angles α between 190° and 280°. Indeed, for these directions, the elastic multipliers, s_e, are much smaller than those of other directions. It is of practical interest to observe that s_e can be interpreted as the fraction of external dynamic load that would be required to cause first yield somewhere in the structure. For example, for a wind direction of 250° and a 700 year MRI wind speed, Table 6.5 would suggest that on average 41% of the applied load would be enough to cause first yield somewhere in the system.

The plastic multipliers, s_p, on the other hand, are larger than 1 for all wind directions,

i.e. the structure will shakedown and be safe against low cycle fatigue, ratcheting and incremental plastic collapse. Furthermore, the plastic reserve of the system, which allows the structure to have some inelasticity while still remaining safe with respect to shakedown, can also be estimated by calculating the ratio between the plastic and elastic multipliers, i.e. s_p/s_e. As can be seen from Figure 6.13, the plastic reserve of the system has a mean value larger than 1.5 for most wind directions for both intensity levels, suggesting that the structure will still shakedown even under wind loads that are multiplied by 1.5 in intensity. For those critical wind directions, the plastic reserves are even higher with a maximum ratio of 5.1.

In addition, elements where inelasticity occurs at shakedown, i.e. $s = s_p$, can also be identified through the LP solution method. An average of 44 elements (among the 1359 DB elements of the entire structure) experienced inelasticity over all wind directions and both intensity levels. Figure 6.14 shows the number of inelastic elements for one of the 10 simulations for each intensity level and all wind directions. In particular, most of the inelastic elements for wind loads associated with the critical wind directions are coupling beam elements, which also govern the elastic limit of the structure. A list of all inelastic elements with tags for a representative case of both intensity levels is provided in Appendix A.

It should be observed that this preliminary analysis based on the LP shakedown approach can provide the information above in just a few seconds for each simulation, and is therefore suitable for a rapid preliminary evaluation of the safety and identification of the most critical elements of the structure.

6.4 System-level Susceptibility to Collapse

In this section, the probabilistic framework for assessing the susceptibility to system-level collapse was adopted for the probabilistic collapse susceptibility evaluation of the Rainier Square Tower. The uncertainties considered in this simulation-based framework will be first

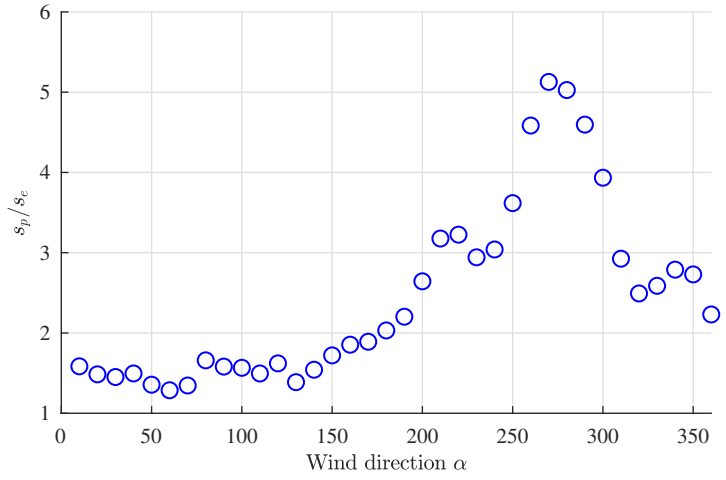

(a)

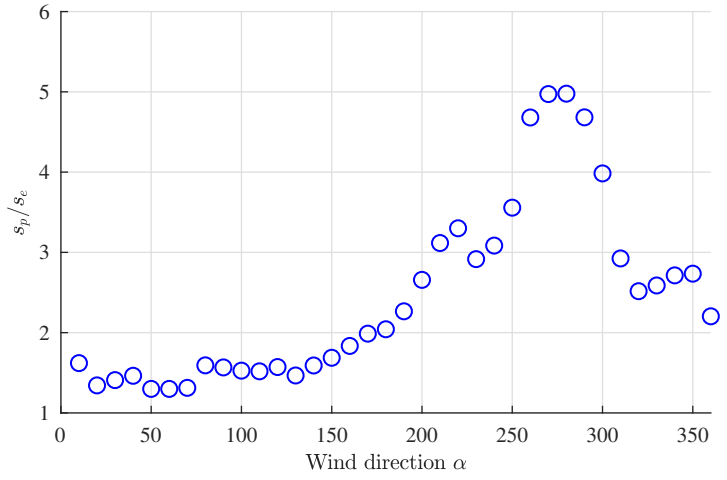

(b)

Figure 6.13: Mean values of the ratios s_p/s_e for all wind directions under (a) 300 MRI wind loads and (b) 700 MRI wind loads.

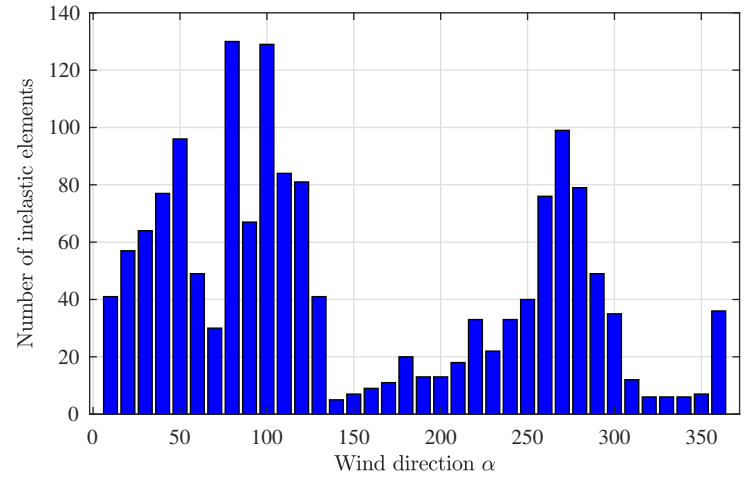

(a)

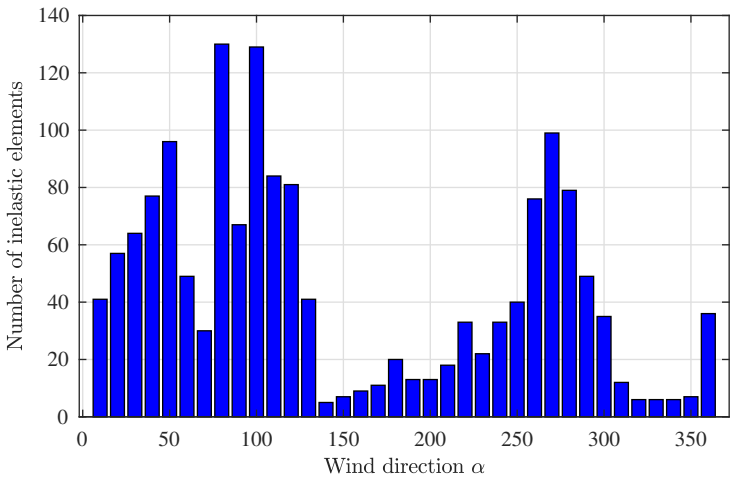

(b)

Figure 6.14: Number of inelastic elements for all wind directions of a representative simulation and for (a) 300 MRI wind loads and (b) 700 MRI wind loads.

Table 6.4: Mean and coefficient of variation (CV) of the elastic and plastic multipliers for all wind directions under wind loads of 300 MRI.

Direction (°)		10	20	30	40	50	60	70	80
s_e	mean	2.2139	3.2968	3.2192	3.3957	2.7409	2.4369	2.3323	2.0777
	CV	0.0994	0.0367	0.0321	0.0424	0.0667	0.0576	0.0534	0.0558
s_p	mean	3.4889	4.8877	4.6715	5.0696	3.7115	3.1306	3.1324	3.4390
	CV	0.0514	0.0434	0.0504	0.0483	0.0739	0.0493	0.0585	0.0528
Direction (°)		90	100	110	120	130	140	150	160
s_e	mean	2.0316	2.2214	2.2333	2.0267	1.8113	1.2170	0.8018	0.7454
	CV	0.0287	0.0375	0.0451	0.0925	0.0669	0.1100	0.0650	0.0904
s_p	mean	3.2114	3.4794	3.3347	3.2622	2.5031	1.8682	1.3751	1.3776
	CV	0.0498	0.0512	0.0404	0.0707	0.0522	0.0765	0.0602	0.0638
Direction (°)		170	180	190	200	210	220	230	240
s_e	mean	0.8569	0.8982	0.8228	0.6091	0.5241	0.4835	0.5601	0.5351
	CV	0.0796	0.0794	0.0856	0.0815	0.0705	0.0488	0.0510	0.0643
s_p	mean	1.6174	1.8207	1.8098	1.6076	1.6633	1.5579	1.6481	1.6218
	CV	0.0703	0.0759	0.0787	0.0669	0.0647	0.0549	0.0684	0.0335
Direction (°)		250	260	270	280	290	300	310	320
s_e	mean	0.4544	0.4959	0.5762	0.6538	0.8855	1.1657	0.9573	0.7320
	CV	0.0557	0.0414	0.0202	0.0413	0.0426	0.0339	0.0676	0.1040
s_p	mean	1.6406	2.2735	2.9550	3.2868	4.0674	4.5843	2.8005	1.8180
	CV	0.0520	0.0672	0.0507	0.0581	0.0459	0.0389	0.0715	0.0823
Direction (°)		330	340	350	360				
s_e	mean	0.6480	0.7025	1.0093	1.3495				
	CV	0.0324	0.0703	0.0802	0.1071				
s_p	mean	1.6756	1.9584	2.7495	3.0003				
	CV	0.0421	0.0717	0.0570	0.0850				

discussed.

6.4.1 Uncertainties in the probabilistic framework

To set up the Monte Carlo simulation, it is first convenient to define all uncertainties in both the structural system and the external loads. For the external wind loads, record-to-record variability, wind directions and intensities are generally taken as random variables. The wind model of Section 6.3.2 models the record-to-record variability in the dynamic wind loads, therefore the wind load histories will be different even with the same wind direction and intensity for each realization. To further take into account the wind directionality, a joint probability distribution of wind direction and intensity can be adopted. In this work,

Table 6.5: Mean and coefficient of variation (CV) of the elastic and plastic multipliers for all wind directions under wind loads of 700 MRI.

Direction (°)		10	20	30	40	50	60	70	80
s_e	mean	1.8442	3.0273	2.8507	2.9492	2.4924	2.1077	2.0567	1.8871
	CV	0.1067	0.0340	0.0422	0.0496	0.0268	0.0779	0.0526	0.0373
s_p	mean	2.9642	4.0645	4.0139	4.3150	3.2384	2.6539	2.6967	3.0028
	CV	0.0725	0.0536	0.0591	0.0738	0.0521	0.0332	0.0848	0.0386
Direction (°)		90	100	110	120	130	140	150	160
s_e	mean	1.7912	1.9240	2.0153	1.7269	1.5965	0.9956	0.7053	0.6524
	CV	0.0479	0.0691	0.0427	0.0534	0.0924	0.1114	0.1064	0.1128
s_p	mean	2.8011	2.9285	3.0542	2.7088	2.3315	1.5762	1.1818	1.1915
	CV	0.0544	0.0624	0.0658	0.0737	0.0734	0.0700	0.0722	0.0780
Direction (°)		170	180	190	200	210	220	230	240
s_e	mean	0.7406	0.8172	0.6608	0.5191	0.4483	0.4176	0.4859	0.4813
	CV	0.0900	0.0730	0.0665	0.0497	0.0786	0.0722	0.0504	0.0463
s_p	mean	1.4708	1.6631	1.4940	1.3793	1.3917	1.3741	1.4150	1.4836
	CV	0.0881	0.0487	0.0441	0.0505	0.0326	0.0558	0.0442	0.0415
Direction (°)		250	260	270	280	290	300	310	320
s_e	mean	0.4146	0.4477	0.4920	0.5892	0.8078	1.0346	0.8453	0.6250
	CV	0.0439	0.0343	0.0493	0.0241	0.0384	0.0362	0.0698	0.0672
s_p	mean	1.4740	2.0933	2.4487	2.9327	3.7826	4.1193	2.4703	1.5741
	CV	0.0495	0.0337	0.0776	0.0458	0.0609	0.0398	0.0616	0.0893
Direction (°)		330	340	350	360				
s_e	mean	0.5468	0.6022	0.8695	1.2175				
	CV	0.1022	0.0406	0.0566	0.1057				
s_p	mean	1.3869	1.6339	2.3732	2.6646				
	CV	0.1017	0.0508	0.0332	0.0576				

however, this site specific information is not available, therefore a non-directional wind speed is considered for all directions. To be consistent with ASCE 7-16 procedures (*ASCE 7-16*, 2016), the same 3-s gust wind speed at 33 ft $\bar{v}_3$, i.e. the basic wind speed, is considered for all wind directions with directionality effects modeled as reported in Appendix A. Wind direction is then selected from the set $\alpha = \{10°, 20°, ..., 350°, 360°\}$ following a uniform distribution. The intensity of the wind is kept as constant in this work, therefore providing estimates of probabilities on the susceptibility to collapse that are conditional on a given intensity level (i.e. conditional on wind speeds of prescribed MRIs). The case in which $\bar{v}_3$ is taken as a random variable, therefore providing estimates of non-conditional failure probabilities, will be considered in Chapter VII together with uncertainties in the structural

system properties, e.g. stiffness and damping, and material strengths (e.g. f'_c, f_y). Indeed, the consideration of these additional uncertainties adds some complexity to the problem as a new set of yield domains for all sections must be generated for each new simulation which, if carried out directly, would increase simulation time. In addition, for concrete structures, the dependency between the material strength and the stiffness of the system (changes of E_c due to f'_c) should also be carefully examined before direct application. It should be observed that, consistent with previous studies, E_c and f'_c are considered constant throughout the structure, i.e. variability in E_c and f'_c from element to element is not considered.

6.4.2 Calibration of the probabilistic framework

A general description of collapse susceptibility, considering both non-shakedown and failure due to excessive plastic deformations, was defined for estimating the conditional susceptibility to collapse probability $P(C|\bar{v}_3)$ as follows:

1. the inability of the structure to reach the state of dynamic shakedown;
2. peak interstory drift $\hat{\mathbf{u}} \geq h/100$;
3. permanent set $\mathbf{u}_r \geq h/500$;

where h is the interstory height of the structure, $\mathbf{u}_r$ is the vector of residual interstory drifts, while $\hat{\mathbf{u}}$ are the peak interstory drifts at shakedown given by:

$$\hat{\mathbf{u}} = \max_{0 \leq t \leq T} [|\mathbf{u}(t) + \mathbf{u}_r|] \tag{6.15}$$

with $\mathbf{u}(t)$ the purely elastic interstory drift response at shakedown.

Wind loads of total length $T = 3600$ s with directions randomly selected from $\{10°, 20°, \cdots, 350°, 360°\}$ were simulated for a wind speed $\bar{v}_3$ of 91 mph (corresponding to a MRI of 300 years) using the wind load model of Section 6.3.2. The structure subjected to gravity loading was once again considered as the initial safe state. Similarly to Section 6.3.3, the first

five modes with damping ratios of 5% were considered in the modal analysis for estimating steady state elastic responses. The LP solution method was adopted to quickly identify whether the structure remains elastic or is susceptible to collapse due to non-shakedown. Then, for the non-collapse susceptible scenarios, the strain-driven framework is applied to estimate the residual displacements and plastic deformations until a load multiplier of $s = 1$ is reached (i.e. estimates of the plastic deformations for unamplified loads are achieved). The system-level collapse susceptibility probability can then be estimated considering the above outlined failure criteria.

In addition, because the framework is based on Monte Carlo simulation, direct estimation of the probability distributions of the residual displacements, plastic deformations (in terms of axial strain and curvatures) at each integration point of each element, as well as peak responses of the inelastic system, is possible. For example, the probability of the residual displacements U_r exceeding a threshold u_r under wind loads of intensity $\bar{v}_3$ is simply estimated as:

$$P(U_r > u_r, \text{SD}|\bar{v}_3) = P(U_r > u_r|\text{SD}, \bar{v}_3)P(\text{SD}|\bar{v}_3) \tag{6.16}$$

where $P(U_r > u_r|\text{SD}, \bar{v}_3)$ is the conditional exceedance probability given shakedown (SD) occurs under wind loads of intensity $\bar{v}_3$, while $P(\text{SD}|\bar{v}_3)$ is the probability that shakedown occurs under a wind load of intensity $\bar{v}_3$, i.e. $P(\text{SD}|\bar{v}_3) = P(s_p \geq 1|\bar{v}_3)$. Equivalent expressions hold for all other response parameters of interest, e.g. plastic deformations and peak responses at any degree of freedom (DOF) of the system.

6.4.3 Results

The analysis was carried out for $N_s = 5000$ simulations. Under 300 MRI wind loads, 46.9% of samples remained elastic while none of the 5000 samples showed susceptibility to collapse, as summarized in Table 6.6. For the probability that the structure does not remain elastic, i.e. $P(s_e < 1)$, 5000 samples results in a variance of 5×10^{-5} for $P(s_e < 1)$, which is considered adequate for this case study. The deformation limits on the peak interstory drift

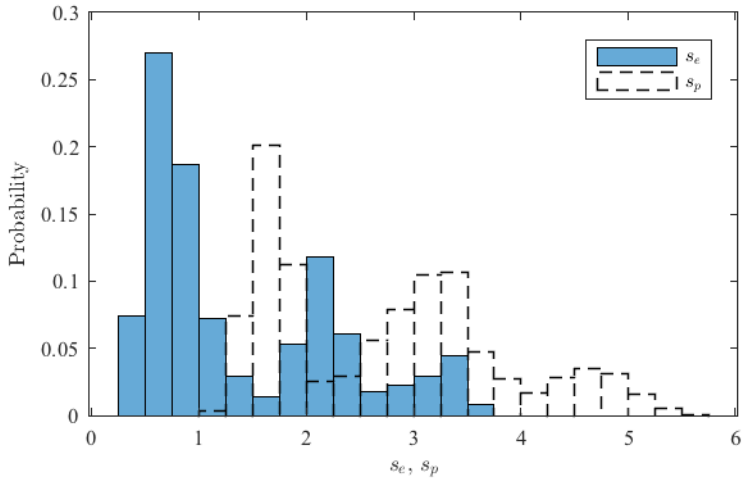

Figure 6.15: Histogram of elastic, s_e, and plastic, s_p, multipliers over all simulations.

Table 6.6: Probability of remaining elastic $P(E|\bar{v}_3)$ and of collapse susceptibility $P(C|\bar{v}_3)$ under 300 MRI wind loads.

	$P(E\|\bar{v}_3)$	$P(C\|\bar{v}_3)$
Probability	46.9%	0%

and permanent set were never exceeded. This can be explained by the fact that most of the inelastic elements were coupling beams, which cannot cause large residual deformations in the structure. Figure 6.15 reports the histograms of both the elastic, s_e, and plastic, s_p, multipliers over all simulations. The mean values for the elastic and plastic multipliers are respectively 1.38 and 2.73. It can be observed that less than 50% of the samples remained elastic (i.e. $s_e \geq 1$) under the 300 MRI wind loads. However, owing to the plastic reserve of the system, all of them could reach the state of dynamic shakedown (i.e. $s_p \geq 1$), and therefore achieve a safe state against plastic collapse.

As mentioned in the previous section, this framework provides not only the system-level collapse susceptibility probability but also the probability distributions of plastic deformations and residual displacements, which are useful for estimating the non-collapse performance. Figures 6.16 to 6.18 respectively report the exceedance probability distributions associated with the residual displacements in the global X- and Y-directions and rotations about

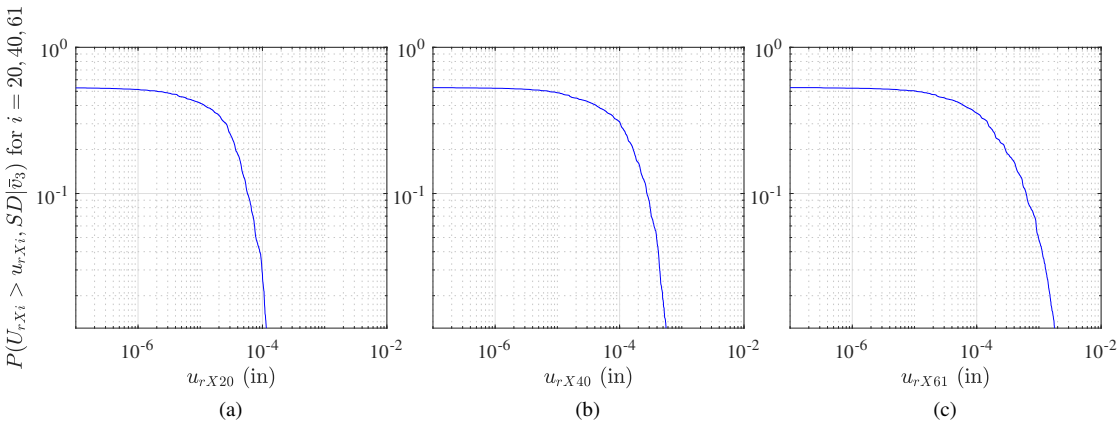

Figure 6.16: Exceedance probability of residual displacements at the master nodes in the global X-direction at (a) Level 20; (b) Level 40; (c) Core roof.

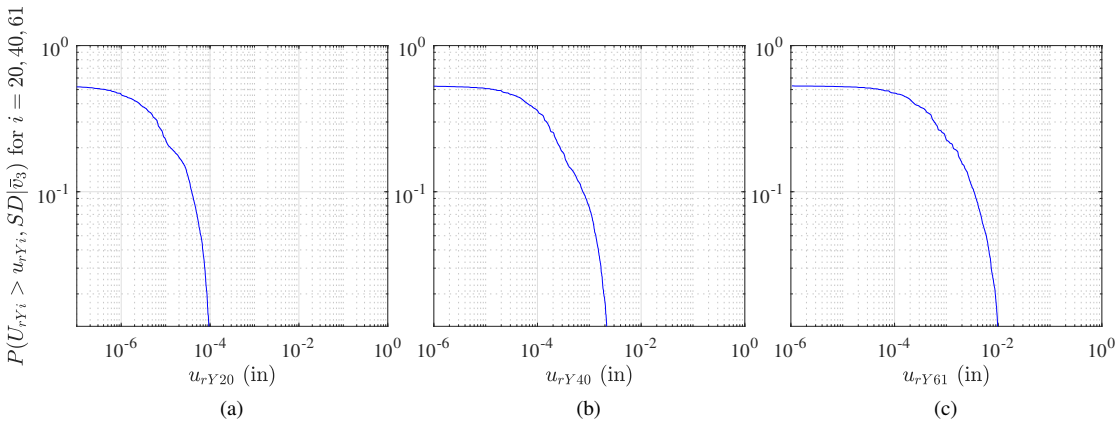

Figure 6.17: Exceedance probability of the residual displacements at the master nodes in the global Y-direction at (a) Level 20; (b) Level 40; (c) Core roof.

the Z-axis at shakedown for Level 20, Level 40 and Core roof (indicated with $i = 20, 40, 61$). The response at the master node of each floor was chosen for representation. It can be seen that residual displacements in the Y-direction are larger than those in the X-direction, even though both are within the deformation limits. To determine the responses at any other point of the rigid floor diaphragm, the transformation of Eq. (6.3) can be used.

Furthermore, exceedance probabilities can also be estimated for plastic deformations, in terms of plastic axial strain and curvatures about local y- and z-axes, at each section along the DB elements. To illustrate this, Figures 6.19 and 6.20 show the exceedance probability distributions associated with the plastic curvatures about the strong axis of the section, χ_{pz},

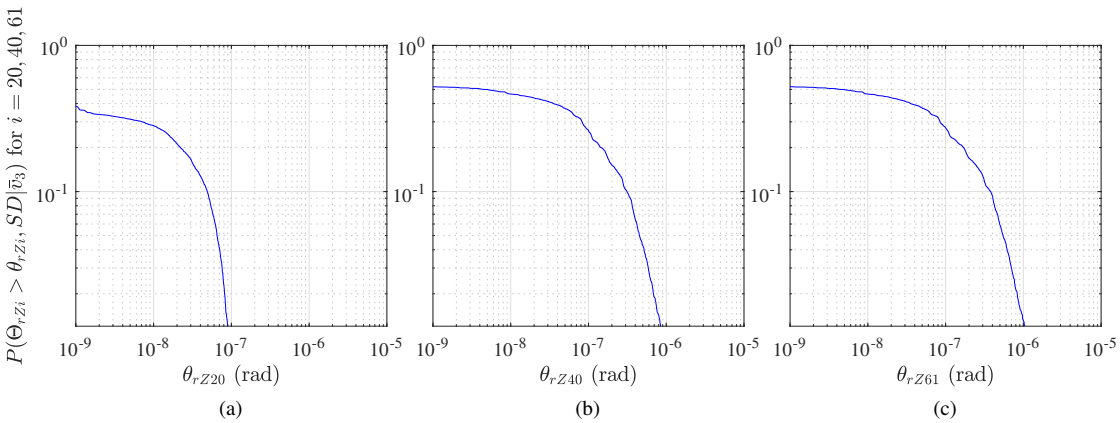

Figure 6.18: Exceedance probability of the residual rotations around the global Z-axis at the master nodes of (a) Level 20; (b) Level 40; (c) Core roof.

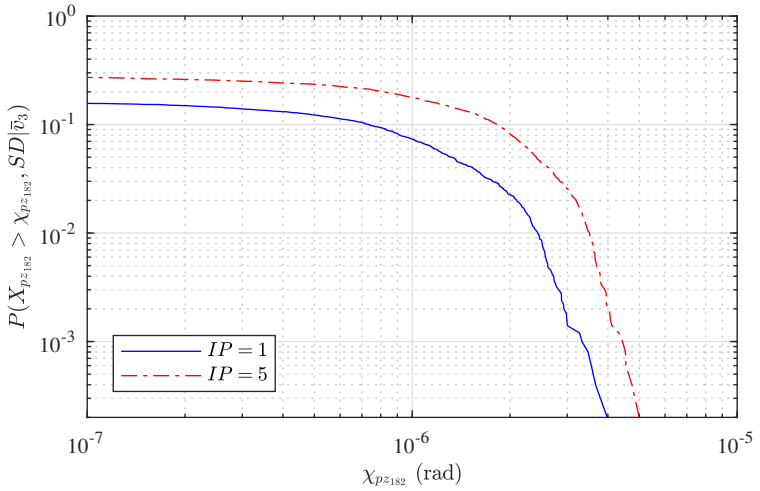

Figure 6.19: Exceedance probabilities of plastic curvatures at integration points 1 and 5 of element #182.

for two representative coupling beam elements. Element #182 and #1929 (located on Grid D, Level 4 and 38) were chosen as they were the most critical elements over all simulations, i.e. the most likely elements to have inelasticity. In particular, for a beam element, the maximum moment response often occurs at the ends of the element, therefore integration points (IPs) 1 and 5, as illustrated in Figure 6.3, were selected for representation.

To illustrate the distributed plasticity, a sample with plastic multiplier s_p close to 1 was chosen. Figure 6.21 shows the plastic curvature χ_{pz} distributed along Element #182 together with the locations of the five integration points marked in dashed line. Based on

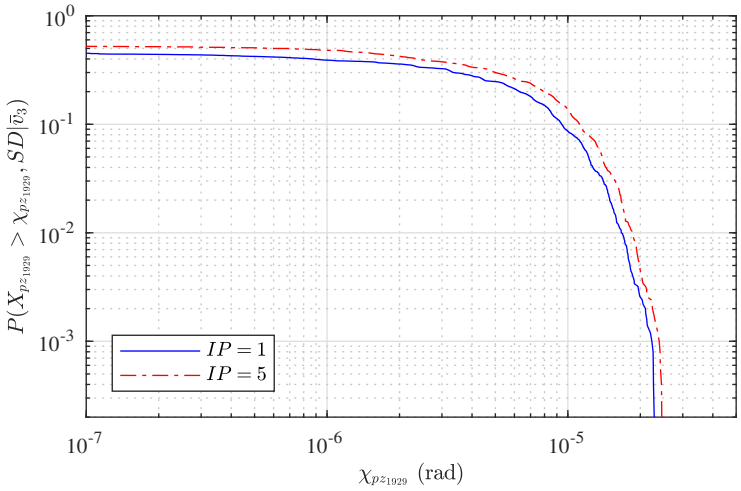

Figure 6.20: Exceedance probabilities of plastic curvatures at integration points 1 and 5 of element #1929.

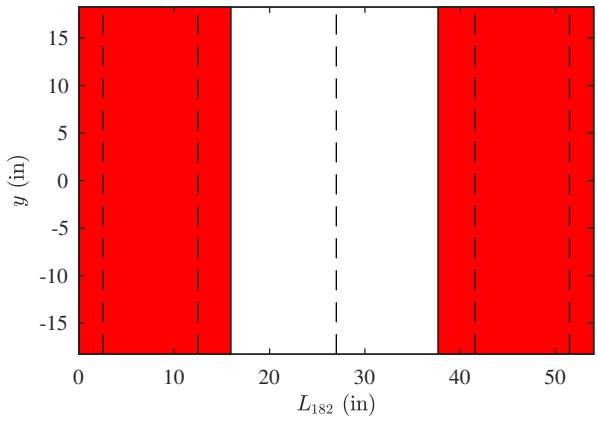

Figure 6.21: Plasticity distributed along Element #182 of the structure for a representative sample.

the assumption of linear curvature and constant axial strain along the element from the interpolation function of a DB element, plastic deformations between integration points can also be evaluated. For the selected element, plasticity (colored in red) occurred from the two ends of the element to around half the distance to the midpoint of the element. The residual displacements at shakedown, in terms of u_{rX}, u_{rY} and θ_{rZ} at the mass node on each floor, of this selected sample are also presented in Figure 6.22.

Finally, it should be noted that the simulation-based approach provided the solutions discussed above in less than 72 hours while running the analysis on a typical dual processor

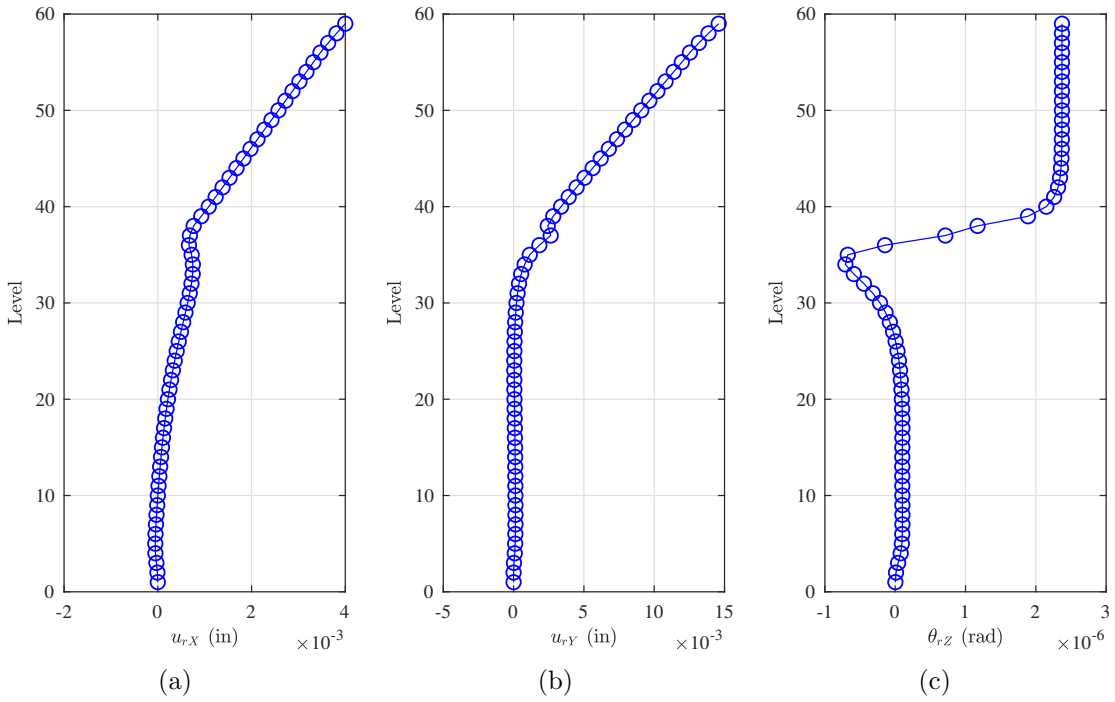

Figure 6.22: Residual displacements in the (a) X-direction; (b) Y-direction and (c) residual rotation about the Z-axis for a representative sample.

desktop machine. If a similar analysis was carried out by direct integration for each of the $N_s = 5000$ windstorms of duration $T = 3600$ s considered in the simulation, the estimated run time would be in the order of months.

6.5 Summary and Conclusions

The primary objective of the work outlined in this chapter was the application of the proposed probabilistic system-level collapse susceptibility estimation framework based on the strain-driven dynamic shakedown algorithm to a full scale 3D model, i.e. the Rainier Square Tower. In particular, considering the zero tension nature of concrete, the section-based distributed plasticity framework was adopted for the shakedown analysis. Contrary to methods based on direct integration (that would require days to analyze a structure of this scale under a single windstorm of one hour duration), it was seen that the dynamic shakedown approach was capable of estimating the inelastic responses at shakedown for each windstorm

in a matter of minutes. By simulating over a suite of windstorms, the framework enabled the rapid identification of the critical wind directions as well as the elements experiencing inelasticity. With respect to the Rainier Square Tower as designed, collapse susceptibility was due exclusively to non-shakedown (i.e. deformation limits were not exceeded), as most of the critical elements experiencing inelasticity were coupling beams therefore leading to small residual deformations. Due to the significant difference between the elastic and plastic multipliers, on average the ratio between the elastic and plastic multipliers was over 1.5, the structure is safe against plastic collapse even though the probability of remaining elastic is less than 50 %, conditional on 300-year wind loads.

CHAPTER VII

Extension to Uncertain System and Reliability Analysis

7.1 Overview

The primary goals of the work outlined in this chapter are:

1. Identification and modeling of a range of uncertainties that are consistent with code development requirements.

2. Development of a reliability assessment framework considering both component- and system-level failure limit states.

3. Illustration of the proposed reliability assessment framework on both a simple frame and the full scale archetype building of Chapter VI.

In reaching the first goal, a full range of uncertainties affecting the structural system were identified in addition to those in the external loads described in Section 6.4.1. In particular, material properties, including yield strengths and elastic moduli of both the concrete and steel, were taken as random variables together with the damping capacity of the structure. As a result, the yield domain, i.e. the resistance, of each section of each member was considered uncertain. For the external loads, uncertainties in dead and live loads were considered in

addition to the wind loads. In modeling uncertainties in the wind excitations, randomness in wind speeds, wind directions, and wind loading trace were considered.

To achieve the second goal, a reliability assessment framework was developed based on the probabilistic dynamic shakedown framework outlined in Chapter IV. In particular, a system-level failure limit state defined in terms of both non-shakedown and failure due to excessive deformations was adopted for estimating the system-level reliability while considering the uncertainties described in the first goal. In addition, failure limit states defined as the occurrence of inelasticity in any given component, i.e. classic component-based limit states, were considered together with system-level failure modeled as the elastic failure of any component in the system, i.e. system-level collapse susceptibility in terms of classic component limit states. Furthermore, to reduce the computational efforts associated with carrying out the reliability analysis using direct Monte Carlo simulation, a conditional simulation strategy is proposed based on partitioning the wind hazard curve.

In reaching the third goal, the proposed reliability assessment framework was illustrated on a simple 2D frame as well as the archetype structure represented by the Rainier Square Tower of Chapter VI. Reliability indexes associated with the three failure limit states defined in the second goal were estimated to provide insight into the differences in reliability if damage is allowed at ultimate load levels.

7.2 Code Development Consistent Uncertainties

As discussed in Section 6.4.1, uncertainties in both structural system and external loads have to be identified for estimating the reliability of a structure. In order to compare with the target reliability provided in ASCE 7-16 (*ASCE 7-16*, 2016), all random variables considered in the analysis were carefully chosen so as to be compliant with those considered in the derivation of load factors stipulated in design codes. In particular, in this section, uncertainties in the structural system, gravity loads, and wind loads will be discussed.

7.2.1 Uncertainties in the structural system

Uncertainties in the structural system are considered in terms of both material and structural properties. In particular, the following parameters are taken as basic random variables:

1. Material properties: concrete compressive strength f'_c; reinforcing steel yield strength f_y; structural steel yield strength F_y; and Young's modulus of steel E_s.

2. Structural properties: modal damping ratios ξ.

As a consequence of the uncertainties outlined above, the Young's modulus of the concrete, defined as $E_c = 57,000\sqrt{f'_c}$ (psi), is also a random variable due to its dependence on the concrete compressive strength. Detailed statistical information for each random variable will be presented in Section 7.4 for each case study.

By taking material strengths as random, the yield domain, i.e. the resistance, of each section of any given member also becomes random. Within the setting stochastic simulation, this implies the need to generate yield domains for each realization of the material strengths.

7.2.2 Uncertainties in gravity and wind loads

7.2.2.1 Gravity loads

To carry out the reliability analysis, uncertainties in the gravity loads, including dead and live loads, should also be taken into account in addition to those in the wind loads. The dead loads and live loads are respectively taken as normal and gamma random variables with mean and coefficient of variation (COV) summarized in Table 7.1. In particular, "arbitrary point-in-time" live load, denoted as L_{apt}, are considered in reliability analysis.

7.2.2.2 Wind loads

In generating dynamic wind loads, the overall intensity is traditionally modeled through the site specific mean wind speed, v_H, at a height of interest H (e.g. building height).

Table 7.1: Properties of the random variables used in modeling the gravity and wind loads.

	Mean	COV	Distribution	Reference
D	$1.05D_n$ [a]	0.1	Normal	*Ellingwood et al.* (1982); *Zhang et al.* (2014)
L_{apt}	$0.24L_n$ [a]	0.6	Gamma	*Ellingwood et al.* (1982); *Zhang et al.* (2014)
w_1	1.0	[b]	Normal	*Sadek et al.* (2004)
w_2	1.0	0.05	Normal	*Bashor et al.* (2005a)
w_3	1.0	0.05	Normal	*Bashor et al.* (2005a)

[a] D_n, L_n: Nominal dead load and live load
[b] Depends on the record length.

In general, v_H is a random variable which can be related to available meteorological data, v, collected at a meteorological height H_{met} at a nearby weather station characterized by a roughness length z_{01}. In this work, the probabilistic model of Eq. (2.6) is adopted to account for the inevitable uncertainties in transforming limited data from the meteorological site to the building site. In addition to the site-specific wind speed, wind direction must also be considered as a random variable.

Given a realization of wind speed v_H and direction α, the stochastic wind load models of Section 4.4 can be adopted to simulate the stochastic wind loads, which takes into account the record-to-record variability. If the wind tunnel driven model of Section 4.4.1 is used, uncertainties associated with the use of wind tunnels should be further considered. In particular, three uncertain parameters are introduced, indicated respectively as w_1, w_2 and w_3 in Table 7.1. In particular, w_1 models the sampling errors due to the finite length of the wind tunnel record, w_2 accounts for the uncertainty due to the use of scale models, while w_3 accounts for the presence of observational errors. Through the mathematical derivation outlined in Appendix C, the aforementioned uncertain parameters can be directly applied to the simulated full scale wind loads as:

$$\tilde{\mathbf{F}}(t; v_H, \alpha) = w_1 w_2 w_3 \mathbf{F}(t; v_H, \alpha) \tag{7.1}$$

where $\mathbf{F}(t; v_H, \alpha)$ are the wind loads generated without considering wind tunnel uncertainties.

7.3 Reliability assessment Framework

7.3.1 Reliability analysis

In current performance-based design procedures, the structural and non-structural components are designed to provide a reliability consistent with the target reliabilities stipulated in the design code (*ASCE 7-16*, 2016). In general, the reliability, in terms of the "reliability index", β, can be evaluated through the first-order reliability method (FORM), as follows:

$$\beta = \Phi^{-1}(1 - P_f) \tag{7.2}$$

where P_f is the failure probability associated with a predefined failure limit state, which can be theoretically evaluated through the Monte Carlo framework described in Section 4.5 by simulating over a full range of wind speeds v_H and wind directions α. The probability of collapse susceptibility of the system can then be estimated through:

$$P(C) = P_f = \iint P(C|v_H, \alpha) \cdot |dG(\alpha|v_H)| \cdot |dG(v_H)| \tag{7.3}$$

where $P(C|v_H, \alpha)$ is the conditional probability of collapse susceptibility determined through Eq. (4.15), $G(\alpha|v_H)$ is the complimentary cumulative distribution function (CCDF) of α given v_H, while $G(v_H)$ is the CCDF of v_H.

To define the indicator function of Eq. (4.16) for evaluating the failure probability, the failure limit state of interest needs to be identified. Currently, the majority of the existing design methods are based on component-level strength limit states, indicated as "LS1" in this work, evaluated through elastic analysis. The behavior of the structural system is therefore expressed in terms of a set of structural and non-structural members instead of the entire system. To explicitly express the system behavior and investigate the possibility of designing wind excited structures with controlled inelasticity, potentially leading to the design of more economic structures, a reliability assessment framework considering not only

the traditional limit state but a system-level inelastic limit state is proposed based on the dynamic shakedown framework of Chapter IV. In particular, reliabilities are estimated for the following three limit states of interest:

1. LS1: component-level yield limit state (traditional limit state used in current design);
2. LS2: system-level yield limit state;
3. LS3: system-level inelastic limit state (defined as in the proposed dynamic shakedown framework).

The reliability associated with the first limit state, denoted as $\beta_c^{(LS1)}$, is defined by the most critical element, i.e. the element with lowest reliability index in the system. To estimate system reliabilities associated with the second and third limit states, denoted respectively as $\beta_s^{(LS2)}$ and $\beta_s^{(LS3)}$, the system-level collapse susceptibility framework proposed in Section 4.5 is applied. In particular, for the second limit state, failure occurs if any of the components of the structure yields. This limit state can be rapidly identified by calculating the elastic multiplier s_e, i.e. the maximum amount the external loads can be multiplied before any inelasticity would occur, through the linear programming problem outlined in Section 2.4.2.1. The corresponding failure probability is therefore defined as $P_f = P(s_e < 1)$. This limit state probability will be strictly greater than or at least equal to the component limit state probability (against yield), therefore with a lower reliability, since it is defined as the probability of the union of all the failure events for all the elements of the structure.

The third limit state is as defined in Section 4.5. Safety is therefore defined at a system-level as the achievement of the state of dynamic shakedown. This limit state fundamentally differs from those considered in current design practice as it allows yielding to occur anywhere in the structure as long as shakedown is achieved. In general, and as outlined in Section 4.5, this limit state is augmented through the addition of any number of component level limit states on responses such as peak inelastic responses at shakedown and residual deformations.

7.3.2 Simulation strategy

To solve the failure probability associated with each limit state through the integral of Eq. (7.3), the Monte Carlo based approach, as presented in Section 4.5, would fast become computationally unfeasible due to the need to repeatedly update the stiffness matrix as well as the yield domains of each section/fiber for each simulation point. This is especially true when the reliability index of interest are associated with small failure probabilities, i.e. are in the tail of the distributions, therefore requiring very large sample sizes if reasonable accuracy is to be achieved.

To overcome the aforementioned difficulty, the stochastic simulation scheme recently proposed in *Ouyang and Spence* (2019) is adapted in this work for defining an efficient reliability assessment framework. In particular, this is based on approximating the outer integral of Eq. (7.3) by first splitting the sample space of v_H into a set of N_w mutually exclusive and collectively exhaustive events $E_{v_{H,k}}$ for $k = 1, \cdots N_w$, leading to the following expression:

$$P(C) = P_f = \sum_{k=1}^{N_w} \left[\int P(C|E_{v_{H,k}}, \alpha) \cdot |dG(\alpha|E_{v_{H,k}})| \right] P(E_{v_{H,k}}) \tag{7.4}$$

where $E_{v_{H,k}}$ is the kth event defined as $v_H \in [v_{H,k}^L, v_{H,k}^U)$ with $v_{H,k}^L$ and $v_{H,k}^U$ respectively the lower and upper bound wind speed of the kth event, $G(\alpha|E_{v_{H,k}})$ is the conditional CCDF of α given $E_{v_{H,k}}$ while $P(E_{v_{H,k}})$ is the probability of $E_{v_{H,k}}$ that can be directly estimated from the CCDF of v_H. Since wind pressure, and therefore wind force, is closely related to the squared of wind speed, the hazard curve is divided into N_w intervals of equal squared wind velocity difference. In this work, the lower bound wind speed of the first event is taken as zero while the last event is unbounded to ensure the collectively exhaustive nature of the partition. To define each interval, the lower bound of the last event is chosen as the wind speed corresponding to an exceedance probability of interest, e.g. $P(V_H > v_H) = 0.005$ for a 50-year observation period. This scheme is illustrated in Figure 7.1 for $N_w = 8$ and the

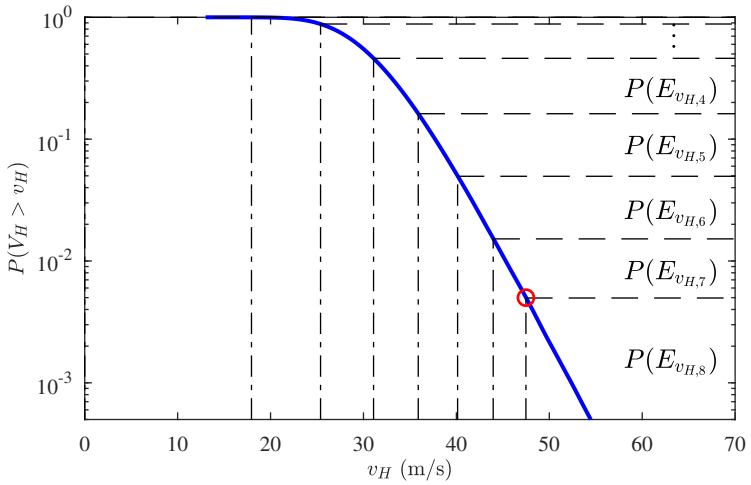

Figure 7.1: Illustration of the wind speed discretization.

wind speed discretization that will be considered in the case study of Section 7.4.2.

Within this context, the problem of Eq. (7.4) becomes one of estimating, for N_w wind speed partitions, the conditional probability of collapse susceptibility $P(C|E_{v_{H,k}})$, i.e. the term in square brackets, through the Monte Carlo scheme presented in Section 4.5. In particular, for each event, wind speeds are generating from the hazard curve between the identified lower and upper bounds. The overall simulation algorithm used to estimate the reliability of the system through the strategy outlined above is summarized in the flowchart of Figure 7.2. Methods for determining the variance of the estimate of the failure probability calculated through the conditional simulation scheme outlined above would require further investigation.

7.4 Case Study

In this section, the reliability assessment framework presented in Section 7.3 is illustrated on a simple 2D frame example as well as the full scale archetype building of Chapter VI.

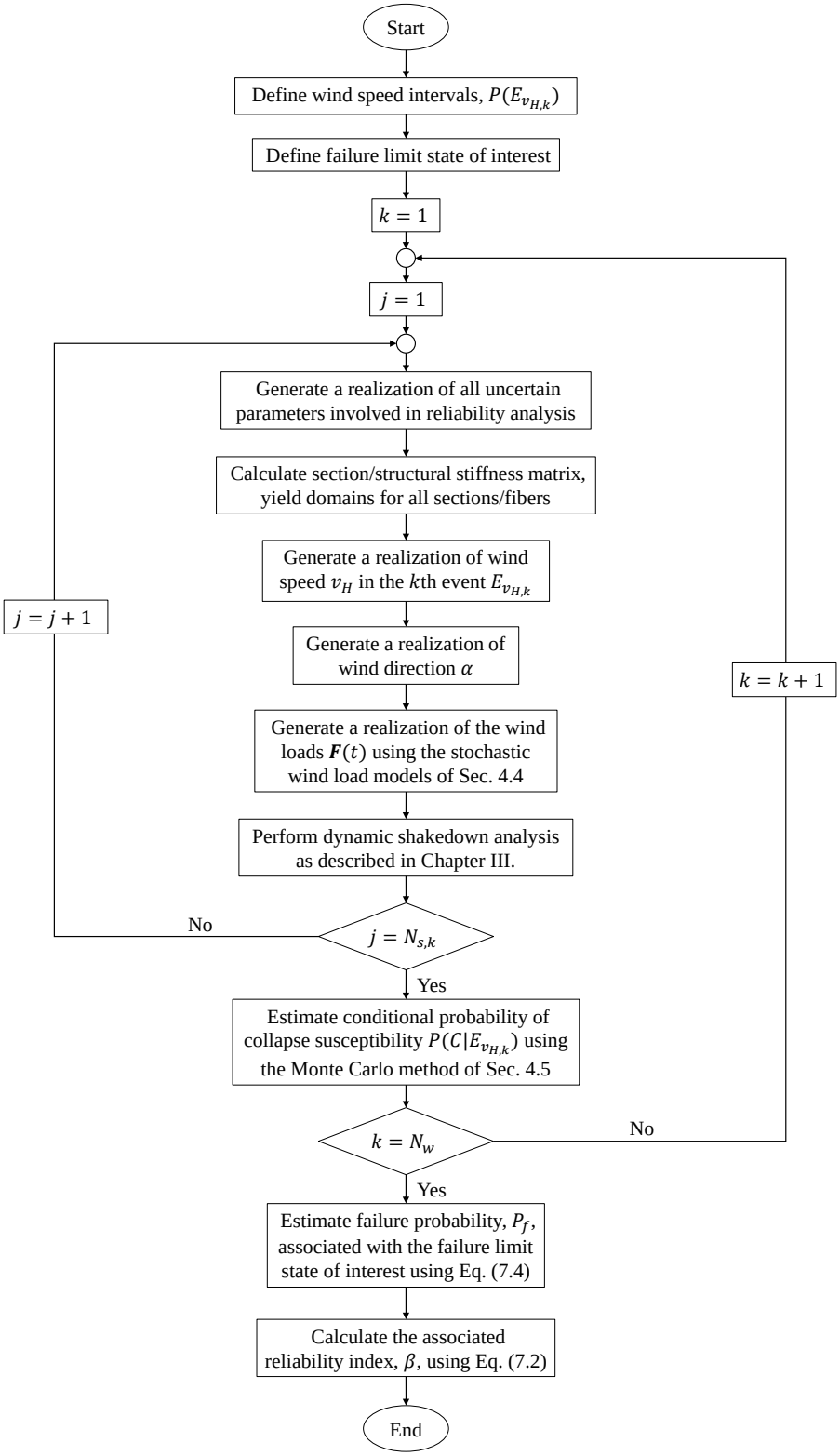

Figure 7.2: Flowchart of the proposed reliability assessment framework.

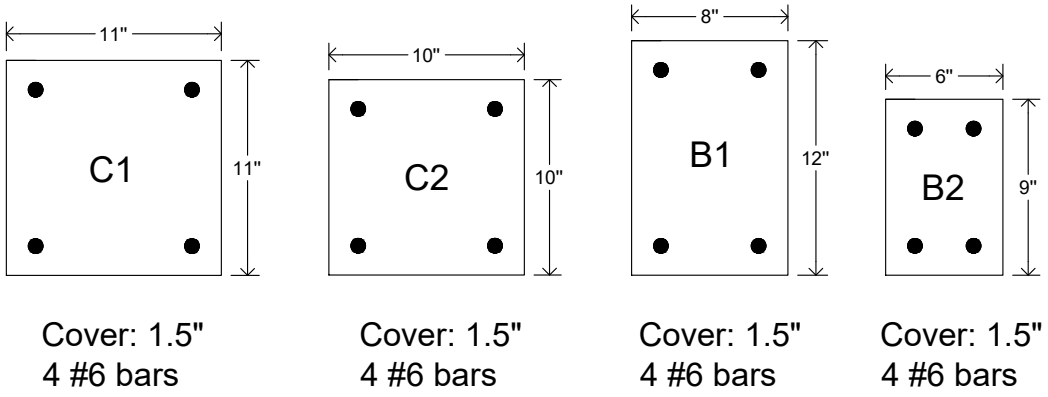

Figure 7.3: Section sizes composing the simple 2D frame.

Table 7.2: Description of random variables in the structural system for the simple 2D frame.

	Nominal	$\frac{\text{Mean}}{\text{Nominal}}$	COV	Distribution	Reference
f'_c	6 (ksi)	1.15	0.125	Normal	*Nowak and Collins* (2013)
f_y	60 (ksi)	1.13	0.03	Normal	*Nowak and Collins* (2013)
E_s	29000 (ksi)	1	0.04	Lognormal	*Bartlett et al.* (2003); *Zhang et al.* (2014)
ξ	2%	1	0.4	Lognormal	*Healey et al.* (1980)

COV: coefficient of variation

7.4.1 Simple 2D frame

7.4.1.1 Description

The first case study refers to a 2D reinforced concrete frame of the same geometry as Figure 5.13. A summary of the section sizes for all elements of the frame is reported in Figure 7.3. Superimposed dead loads and live loads (nominal values provided in Table 5.6) are considered in addition to the wind excitation. As described in Section 5.4.2, a lumped mass equal to the superimposed dead loads was applied on each floor in addition to the mass of all elements and framing system. Considering nominal material strengths, as given in Table. 7.2, the first two natural frequencies of the frame were respectively $f_1 = 0.1939$ Hz and $f_2 = 0.6198$ Hz.

To carry out the reliability analysis, parameters discussed in Section 7.2 were taken as random variables. The statistical information for the uncertainties in the structural

system is summarized in Table 7.2. For each simulation, linearized yield domains for all sections, as discussed in Section 5.4.2, are generated for a realization of material strengths. In addition to the uncertainties in the structural system, uncertainties in external loads were also considered.

In applying Eq. (2.6) to the wind analysis of the 2D frame, available wind data with a record length of 27 years, in terms of annual maximum 3-s gust wind speed at 33 ft height, i.e. $v = v_3$ with $\tau = 3$ s and $H_{met} = 33$ ft, collected at Miami International Airport was used. The roughness length z_{01} was taken as 0.1 ft (0.03 m), i.e. open terrain conditions were considered at the meteorological station. Considering sampling errors generated by the limited amount of available climatological data, this wind speed, v_3, was assigned a Type I distribution with mean value of 53.15 mph and standard deviation 10.47 mph calculated from the wind data. The site of the building was characterized by a roughness length $z_0 = 9.8$ ft (3 m) while the averaging time of interest was one hour ($T = 3600$ s). The mean value of E_3 was taken as 0.6623 for averaging times τ and T considered in this case study.

For evaluating the reliability of the system, the frame limit state is defined by combined gravity and wind loads, $D + L_{apt} + W_{50}$, where W_{50} is the dynamic wind loads calibrated to the largest wind speed to occur within a period of 50 years (the service lifetime of the structure). Within this context, the wind speed subdivisions are defined in terms of the 50-year mean hourly wind speed at building top, v_H. The lower bound of the last interval was taken as the wind speed corresponding to an annual probability of failure of 3.0×10^{-5} for a Risk Category II building. The corresponding hazard curve with $N_w = 8$ subdivisions is shown in Figure 7.4.

Given a realization of the wind speed v_H, the stochastic wind loads $\mathbf{F}(t)$ were simulated using the quasi-steady model of Section 4.4.2. The mean wind speed at height z_n was related to the wind speed at building top, v_H, through the following equation:

$$\bar{v}_{z_n} = v_H \frac{\ln(z_n/z_0)}{\ln(H/z_0)} \tag{7.5}$$

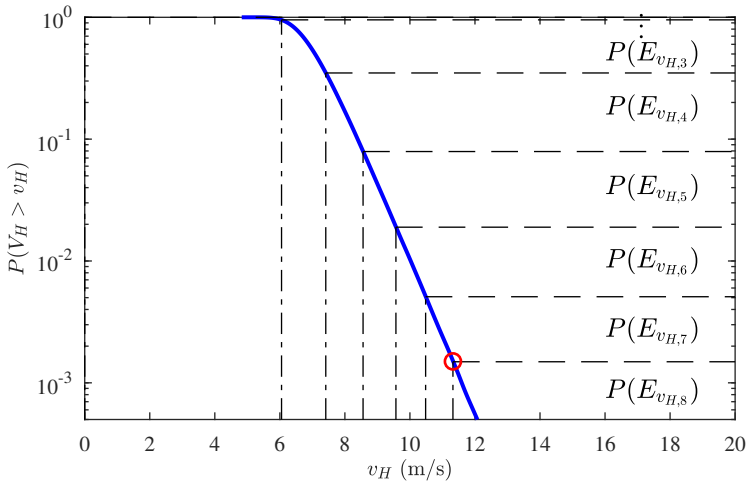

Figure 7.4: Wind speed discretization for the simple 2D frame.

An influence width of 50 ft (15.24 m) was assumed for each floor. The pressure coefficient $\bar{C}_j$ was taken as 1.3 while the air density was taken as $\rho = 1.25$ kg/m^3. To account for wind directionality, a factor of 0.85 was considered for the simulated wind loads.

Given the set up described above, reliability indexes for the three limit states, as discussed in Section 7.3.1, were evaluated through the simulation scheme of Section 7.3.2. In particular, the following inelastic system-level limit state was considered for LS3:

1. the inability of the structure to reach the state of dynamic shakedown;

2. peak interstory drift $\hat{\mathbf{u}}/h_j \geq 1.25\%$;

3. permanent set $\mathbf{u}_r/h_j \geq 0.2\%$;

7.4.1.2 Results

The analysis, as outlined in Section 7.3.2, was carried out considering $N_{s,k} = 1000$ for each interval (therefore a total of 8000 samples). For the 50-year design life considered in this work, 99.9% of samples remained elastic while 0.007% were susceptible to collapse due to non-shakedown, i.e. $s_p < 1$. The reliability indexes for LS1, LS2 and LS3 defined in Section 7.3.1 are summarized in Table 7.3 for combined gravity and wind loads. Table 7.3 also reports the reliability indexes for three additional limit states, LS3a, LS3b and LS3c.

In particular, for LS3a failure is defined as the failure to reach the state of shakedown, for LS3b failure is defined as the peak interstory drift ratio exceeding 1.25% anywhere over the height of the structure, while for LS3c failure is defined as residual drift ratio exceeding 0.2% anywhere over the height of the structure. To estimate the reliability indexes associated with LS3b and LS3c, the following expression can be used:

$$P_f^{(LS3b/LS3c)} = P(R > \tilde{r}) = P(R > \tilde{r}|SD)P(SD) \tag{7.6}$$

where R is the response of interest (i.e. largest peak/residual drift occurring anywhere over the height of the structure), $\tilde{r}$ is the limit of interest (i.e. h/100 for peak drift and h/500 for residual drift), $P(R > \tilde{r}|SD)$ is the probability of R exceeding the limit $\tilde{r}$ conditional on shakedown, while $P(SD)$ is the probability of shakedown. In particular, $P(R > \tilde{r}|SD)$ can be estimated from the samples of each interval as:

$$P(R > \tilde{r}|SD) = \sum_{k=1}^{N_w} P(R > \tilde{r}|E_{v_{H,k}}, SD)P(E_{v_{H,k}}) \tag{7.7}$$

To estimate the reliability indexes, $P_f^{(LS3b/LS3c)}$ can then be substituted into Eq. (7.2).

The component reliability, $\beta_c^{(LS1)}$, was 3.10 for the most critical element, which is higher than the target reliability of 3.0 stipulated in ASCE 7-16 for a Risk Category II building. The reliability index associated with the system-level first yield limit state, LS2, was estimated to be $\beta_s^{(LS2)} = 3.10$. In this example, $\beta_c^{(LS1)} = \beta_s^{(LS2)}$ since the structure fails exclusively due to the failure of a single common element, i.e. Element 3, the middle column at the first floor. With respect to the system-level inelastic limit state, the reliability index was estimated to be $\beta_s^{(LS3)} = 3.31$.

From Table 7.3, it can be seen that $\beta_s^{(LS3b)} = \beta_s^{(LS3)}$ while $\beta_s^{(LS3a)}$ and $\beta_s^{(LS3c)}$ were larger than the reliability index associated with LS3, indicating how, in this case, the reliability of the structure associated with the inelastic failure limit state was governed by excessive peak drift. It is interesting to observe that from a pure shakedown perspective, the reliability index

Table 7.3: Reliability indexes for three different limit states of the 2D frame.

Limit state	LS1	LS2	LS3	LS3a	LS3b	LS3c
Description	First component yield	First system yield	Non-shakedown or $\hat{\mathbf{u}}/h_j \geq 1.25\%$ or $\mathbf{u}_r/h_j \geq 0.2\%$	Non-shakedown	$\hat{\mathbf{u}}/h_j \geq 1.25\%$	$\mathbf{u}_r/h_j \geq 0.2\%$
Reliability index	3.10	3.10	3.31	3.81	3.31	3.68

is 3.81 (i.e. $\beta_s^{(LS3a)} = 3.81$) that well exceeds Risk category IV and illustrates the significant inelastic reserve of the structural system. Indeed, if the limit on peak drift was relax, Risk Category IV reliability could be achieved. Notwithstanding this, by considering the inelastic limit state, the structure originally designed to satisfy a Risk Category II reliability using a traditional reliability approach can reach the target reliability for a Risk Category III building.

7.4.2 Full scale 3D model: The Rainier Square Tower

In this section, the reliability assessment framework outlined in Section 7.3 was adopted for the reliability evaluation of the Rainier Square Tower described in Chapter VI.

7.4.2.1 Uncertain parameters

Uncertainties in the structural system

To model the uncertainties in the structural system, parameters outlined in Section 7.2.1 are considered as random variables. The statistical information and nominal values adopted for the Rainier Square Tower are summarized in Table 7.4. Methods for efficiently generating yield domains for each realization of the uncertainties are presented as follows.

Uncertainty propagation: steel beams

The linearized yield surfaces associated with sections of steel beams are completely governed by the moment strengths M_{py} and M_{pz} of the section. Therefore, the propagation of uncertainty from the material properties to the yield domain can be directly evaluated

Table 7.4: Description of random variables in the structural system for the Rainier Square Tower.

	Nominal	$\frac{\text{Mean}}{\text{Nominal}}$	COV	Distribution	Reference
f'_c	8 (ksi)	1.1	0.11	Normal	*Nowak and Collins* (2013)
f_y	60 (ksi)	1.13	0.03	Normal	*Nowak and Collins* (2013)
F_y	50 (ksi)	1.1	0.06	Lognormal	*Bartlett et al.* (2003); *Zhang et al.* (2014)
E_s	29000 (ksi)	1	0.04	Lognormal	*Bartlett et al.* (2003); *Zhang et al.* (2014)
ξ	2%	1	0.4	Lognormal	*Healey et al.* (1980)

COV: coefficient of variation

through:

$$M_{py} = F_y Z_y, \quad M_{pz} = F_y Z_z \tag{7.8}$$

with Z_y and Z_z the plastic section moduli with respect to the $y-$ and $z-$axes of the cross section.

Uncertainty propagation: RC elements

In the case of reinforced concrete sections, however, the propagation of uncertainty from the material properties to the 3D yield domains is more complex due to a lack of explicit relationships between material properties and the linearized 3D yield surfaces. To overcome this issue, surrogate models are used as proxies of yield surfaces that are treated as arbitrary black-box functions of the material properties. For example, consider the plastic resistances, R_s for $s = 1, ..., 26$, associated with the 26 planes of the general linearization scheme for 3D yield domains of concrete sections outlined in Section 6.3.1. In general, these are functions of both the strength of the concrete and reinforcing steel, i.e. $R_s = g_s(f'_c, f_y)$. Similarly, the components of the normal vectors defining the orientation of the 26 planes are also functions of f'_c and f_y, i.e. $n_{s,i} = g_n(f'_c, f_y)$ with $i = x, y, z$. Within this context, it is of interest to construct metamodels of how $g_s(f'_c, f_y)$ and $n_{s,i} = g_n(f'_c, f_y)$ vary over the space of f'_c and f_y. Among various available metamodeling approaches (*Forrester et al.*, 2008), ordinary Kriging (*Echard et al.*, 2011) is adopted in this work due to its versatility in representing different typologies of functions.

Kriging metamodel Given a set of n observed responses of g (i.e. plastic resistance or component of the normal vector of one of the planes defining the linearization) collected in the vector $\mathbf{y} = \{g(f_c'^{(1)}, f_y^{(1)}), \cdots, g(f_c'^{(n)}, f_y^{(n)})\}^T$, the Kriging prediction of g at $\{f_c', f_y\}$ is expressed as:

$$\hat{g}(f_c', f_y) = \hat{\mu} + \mathbf{\Psi}^T(f_c', f_y)\mathbf{R}^{-1}(\mathbf{y} - \mathbf{1}\hat{\mu}) \tag{7.9}$$

where $\hat{\mu}$ is the maximum likelihood estimator of the mean of the random field defined by considering $\mathbf{y}$ the realizations of a Gaussian process, $\mathbf{\Psi}$ is a vector of basis functions with the ith term defined as

$$\Psi_i(f_c', f_y) = \mathrm{Corr}[g(f_c'^{(i)}, f_y^{(i)}), g(f_c', f_y)] \tag{7.10}$$

with Corr an appropriate correlation function, while $\mathbf{R}^{-1}(\mathbf{y} - \mathbf{1}\hat{\mu})$ are the weights assigned to each basis function with $\mathbf{R}$ the correlation matrix associated with the correlation function Corr. To define $\mathbf{\Psi}$ and $\mathbf{R}$, the following exponential correlation function was used:

$$\mathrm{Corr}[g(f_c'^{(i)}, f_y^{(i)}), g(f_c'^{(j)}, f_y^{(j)})] = \exp\left(-\sum_{k=1}^{l} [\theta_k^{(f_c')} |f_{c_k}'^{(i)} - f_{c_k}'^{(j)}|^{p_k{}^{(f_c')}} + \theta_k^{(f_y)} |f_{y_k}^{(i)} - f_{y_k}^{(j)}|^{p_k{}^{(f_y)}}] \right) \tag{7.11}$$

where $\theta_k^{(f_c')}$, $\theta_k^{(f_y)}$, $p_k{}^{(f_c')}$ and $p_k{}^{(f_y)}$ are the parameters defining the Kriging model. In particular, here a square exponential model is considered, i.e. $p_k{}^{(f_c')} = p_k{}^{(f_y)} = 2$. Based on this formulation, the maximum likelihood estimates of the mean value can then be derived as

$$\hat{\mu} = \frac{\mathbf{1}^T \mathbf{R}^{(-1)} \mathbf{y}}{\mathbf{1}^T \mathbf{R}^{(-1)} \mathbf{1}} \tag{7.12}$$

where $\mathbf{1}$ is a $n \times 1$ column vector of ones.

The first step towards calibrating the Kriging model g is the identification of the sampling space. For unbounded random variables, the upper and lower bounds of the sampling space can be defined in such a way that the confidence region spans a space sufficiently large

Table 7.5: Bounds of sampling space.

Variable	Lower bound	Upper bound
f'_c	5.95 ksi	11.80 ksi
f_y	61.70 ksi	73.90 ksi

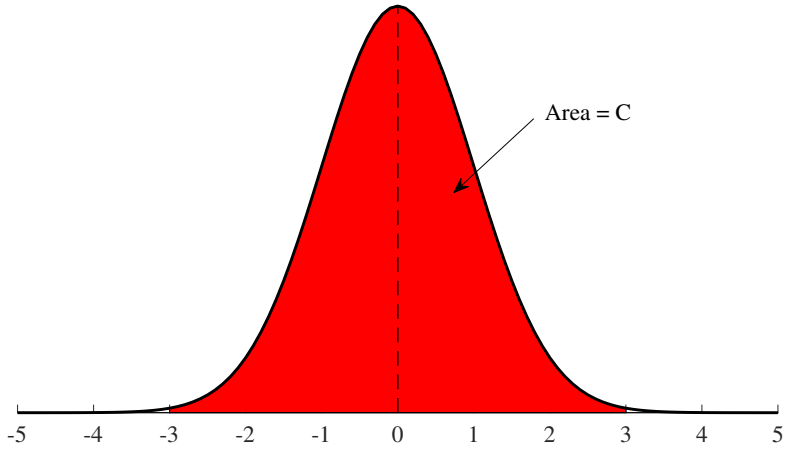

Figure 7.5: Illustration of the confidence interval of a Gaussian variable.

to contain with high probability (e.g. 99-99.9%) all realizations of the random variable (*Moustapha et al.*, 2016). In the application that follows, a confidence interval of $C = 0.9973$ is selected for each random variable, which corresponds to $\mu + 3\sigma$ for a Gaussian variable, as illustrated in Figure 7.5. The upper and lower bounds for f'_c and f_y are summarized in Table 7.5 with mean and standard deviation defined in Table 7.4.

The second step is the choice of sampling points within the sampling space in which to calibrate the model, i.e. the choice of support points, within the identified space of f'_c and f_y, in which to evaluate the vector $\boldsymbol{y}$. To reduce the bias error of the metamodel, sampling plans that attempt to evenly fill the space are generally favored. In this work, a 20-point sampling plan was created based on optimal Latin hypercube sampling (*D.Morris and Mitchell*, 1995), ensuring the optimal space-filling properties of the sample points, as illustrated in Figure 7.6.

Based on the 3D yield domains evaluated at the sampling points (provided by MKA), i.e. the observed responses $\mathbf{y}$, Kriging models were created for the plastic resistances, R_s

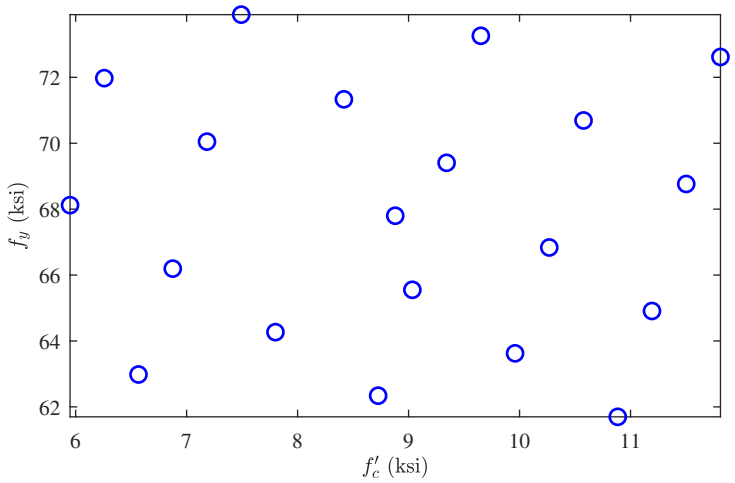

Figure 7.6: A 20-point sampling plan for Kriging model calibration.

Table 7.6: Nominal values for gravity loads of the Rainier Square Tower.

Use	Superimposed Dead Loading (D_n)	Live Loading (L_n)
Corridors and Stairs (within core)	15 psf	100 psf
Level 2 to 37	10 psf	70 psf
Level 38 and Level 59	10 psf	125 psf
Level 39 to 58	30 psf	40 psf
Level 60	25 psf	20 psf

for $s = 1, ..., 26$, and components of the normal vectors of the planes defining the linearized yield surfaces of all reinforced concrete sections. The calibrated models were then used to rapidly update the 3D yield domains for each realization of f'_c and f_y considered in evaluating through stochastic simulation the reliability of the structure.

Uncertainties in gravity and wind loads

Gravity loads As outlined in Section 7.2.2.1, the gravity loads were taken as random variables with nominal values summarized in Table 7.6.

Wind loads As outlined in Section 7.2.2.2, in applying Eq. (2.6) to the wind analysis of the Rainier Tower site, available wind data with a record length of 46 years, in terms of annual maximum 3-s gust wind speed at 33 ft height collected at Seattle Tacoma International Airport was used. This wind speed was taken as a Type I random variable with mean

and standard deviation of 57.7 mph and 8.08 mph respectively from the wind data. The roughness length z_{01} was taken as 0.1 ft (0.03 m). The site of the building was characterized by a roughness length $z_0 = 9.8$ ft (3 m) while the averaging time of interest was one hour ($T = 3600$ s). The mean value of E_3 was once again taken as 0.6623.

In addition to the site-specific wind speed, wind direction must also be considered. In this example, due to the lack of site specific information on the joint probability distribution of wind speed and direction, wind directionality was modeled by reducing the non-directional wind speed, v_H, in function of wind direction, α, through the following expression:

$$\tilde{v}_H(\alpha) = \mathrm{K}_R(\alpha)\mathrm{K}_D(\alpha)v_H \tag{7.13}$$

where K_R is a reduction factor while K_D is a directionality factor. Appropriate values for K_R and K_D for Seattle were provided by Rowan Williams Davies & Irwin (RWDI). To use the model of Eq. (7.13) in a stochastic simulation, the wind direction α can be taken as a uniform distribution in $[0°, 360°]$. The values used for K_R and K_D are summarized in Appendix A.

Given a realization of wind speed $\tilde{v}_H$ and direction α, the wind tunnel driven wind load model of Section 6.3.2 was adopted to simulate the stochastic wind loads, which takes into account the record-to-record variability. To further consider the uncertainties associated with the use of wind tunnels, Eq. (7.1) was adopted for the simulated full scale wind loads. For a record length greater than 1 hour at full scale, w_1 was taken to have a coefficient of variation (COV) of 0.075.

7.4.2.2 Design target for the structure

In order to achieve a target reliability stipulated in ASCE 7-16, several adjustments were made to the design of Rainier Square Tower supplied by MKA. In particular, target reliabilities for structural members and connections are provided in Table 1.3-1 of ASCE

Table 7.7: List of redesigned coupling beams.

Element ID	90	182	212	1800	1929	1974	1994	1998	2012	2016	2058	2067
Substituted ID	1949	1974	1606	1647	559	86	508	2047	1364	1953	2078	2087

7-16 (*ASCE 7-16*, 2016) and were developed for common limit states, such as yielding in tension members, formation of plastic hinges, or column buckling and connection fracture for a nominal service period of 50 years. For a Risk Category III structure, the target component reliability is 3.25 for failure that is not sudden and does not lead to widespread progression of damage, a classification deemed appropriate for the members of the structural system of Rainier Square Tower. Here, this reliability target is taken as the system-level reliability target. The goal is to therefore re-size select members of the structure such that the system reliability $\beta_s^{(LS3)}$, estimated through the proposed dynamic shakedown framework (and therefore with respect to a system-level inelastic limit state), achieves a Risk Category III target reliability. To this end, the structure was preliminary redesigned to have an expected elastic response under dynamic wind loads calibrated to a 300 MRI wind speed. Wind direction was modeled as in Eq. (7.13) while all material properties were set to their nominal values. Based on this analyses, the most critical elements resulted to be the coupling beams. To achieve satisfactory performance, the most critical (i.e. most under-designed) coupling beam elements were redesigned by substituting the under-deigned element with one of greater capacity. For simplicity, the new elements were chosen from sections already used in the structure. The IDs of the redesigned coupling beams is reported in Table 7.7 together with the IDs identifying the coupling beams used in redesigning the member.

7.4.2.3 Reliability analysis

The reliability for the adjusted structure of Section 7.4.2.2 was determined through the first-order reliability method (FORM) while considering the three failure limit states outlined in Section 7.3.1. In particular, the following inelastic system-level limit state was considered for LS3:

1. the inability of the structure to reach the state of dynamic shakedown;

2. peak interstory drift $\hat{\mathbf{u}} \geq h/100$;

3. permanent set $\mathbf{u}_r \geq h/500$;

where h is the interstory height of the structure, $\mathbf{u}_r$ is the vector of residual interstory drifts, while $\hat{\mathbf{u}}$ are the peak interstory drifts at shakedown given by:

$$\hat{\mathbf{u}} = \max_{0 \leq t \leq T} [|\mathbf{u}(t) + \mathbf{u}_r|] \tag{7.14}$$

with $\mathbf{u}(t)$ the purely elastic interstory drift response at shakedown.

In evaluating reliability, the loads were combined over a nominal lifespan of 50 years. Therefore, the wind speed subdivisions were once again defined in terms of the 50-year mean hourly wind speed at building top in order to apply the simulation strategy of Section 7.3.2. The corresponding hazard curve is shown in Figure 7.1.

7.4.2.4 Results

To evaluate P_f, and therefore the reliability indexes with respect to the limit states outlined in Section 7.3.1 through Eq. (7.2), the simulation scheme of Section 7.3.2 was implemented while considering $N_{s,k} = 1000$ and the uncertainties outlined above. Figure 7.7 reports the probability density function of the plastic reserves of the system in terms of s_p/s_e. As can be seen, plastic reserve between 1.5 and 2 are most likely to occur. In interpreting the ratio s_p/s_e, it should be kept in mind that larger ratios indicate greater potential for force redistribution and therefore safe inelastic behavior. To further illustrate the relation between wind directions and plastic reserves of the system, Figure 7.8 shows the mean value of s_p/s_e for each direction. For wind loads coming from directions that would cause acrosswind response to the structure, i.e. close to $\alpha = \{60°, 150°, 240°, 330°\}$, the structure would seem to have less capacity to shakedown, therefore resulting in a smaller ratio between the plastic and elastic multipliers.

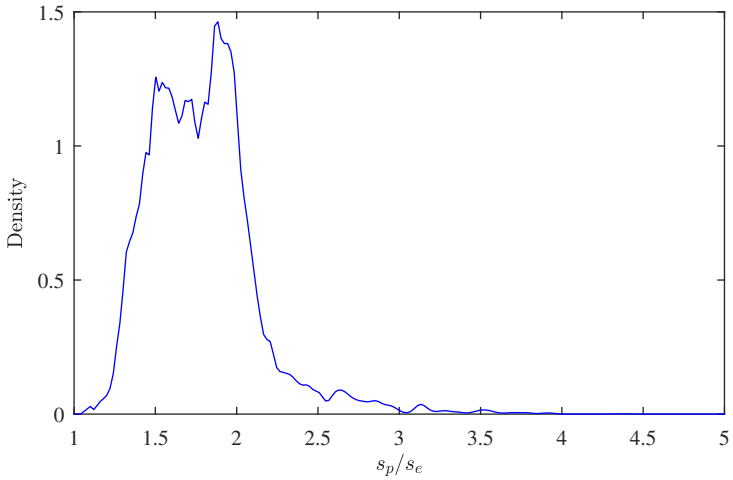

Figure 7.7: Probability density function of plastic reserve of the system, s_p/s_e, over all simulations.

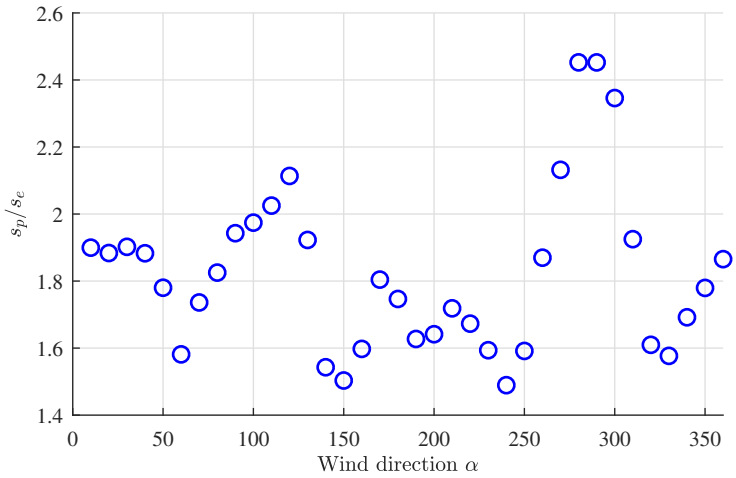

Figure 7.8: Mean values of the ratios, s_p/s_e, for all wind directions.

Table 7.8: Reliability indexes for three different limit states of the Rainier Square Tower.

Limit state	LS1	LS2	LS3	LS3a	LS3b	LS3c
Description	First component yield	First system yield	Non-shakedown or $\hat{\mathbf{u}}/h_j \geq 1.25\%$ or $\mathbf{u}_r/h_j \geq 0.2\%$	Non-shakedown	$\hat{\mathbf{u}}/h_j \geq 1.25\%$	$\mathbf{u}_r/h_j \geq 0.2\%$
Reliability index	2.99	2.81	3.29	3.30	4.26	7.88

Table 7.9: Elements with reliability indexes lower than the target reliability stipulated in ASCE 7-16.

Element ID	90	156	212	238	273	305	722	1193	1244
Reliability index $\beta_c^{(LS1)}$	3.23	3.03	3.04	3.03	3.04	3.17	3.15	3.22	3.18
Element ID	1295	1346	1397	1448	1728	1953	1998	2003	2012
Reliability index $\beta_c^{(LS1)}$	3.18	3.19	3.21	3.23	3.24	3.13	2.99	3.22	3.02

For the 50-year design life considered in this work, 99.76% of samples remained elastic while 0.05% collapsed due to non-shakedown. The reliability indexes for LS1, LS2 and LS3 defined in Section 7.3.1 are summarized in Table 7.8 for combined gravity and wind loads. Table 7.8 also reports the reliability indexes for three additional limit states, LS3a, LSb and LS3c. In particular, as before, for LS3a failure is defined as not reaching shakedown, for LS3b failure is defined as the peak interstory drift exceeding $h/100$ anywhere over the height of the structure while for LS3c failure is defined as residual drift exceeding $h/500$ anywhere over the height of the structure.

The component reliability, $\beta_c^{(LS1)}$, associated with LS1 is 2.99 for the most critical element of the structure, which is lower than the target β of 3.25 for a Risk Category III building. Table 7.9 reports the most critical elements that have reliability indexes smaller than the target reliability. It can be observed that most elements correspond to coupling beams. The reliability index associated with the system-level first yield limit state, LS2, was estimated to be $\beta_s^{(LS2)} = 2.81$. As expected, the reliability index of this limit state was lower than the component-reliability index since the structure is considered failed if any one of the elements fail. Indeed, the limit case of $\beta_s^{(LS2)} = \beta_c^{(LS1)}$ occurs when the structure fails exclusively due to the failure of a single common element, as for the simple 2D frame example. For this case study, however, the component for which failure occurs depends, among other things, on the direction of the wind event. Referring to Table 1.3-1 of ASCE 7-16 (reported in Figure 7.9 for convenience), this system reliability index $\beta_s^{(LS2)}$ only exceeds the target reliability for a Risk Category I building. This is consistent with how, apart from the coupling elements of Table 7.7, all elements were initially designed (as supplied by MKA) for a 300-year windstorm.

Table 1.3-1 Target Reliability (Annual Probability of Failure, P_F) and Associated Reliability Indices (β)[1] for Load Conditions That Do Not Include Earthquake, Tsunami, or Extraordinary Events[2]

	Risk Category			
Basis	**I**	**II**	**III**	**IV**
Failure that is not sudden and does not lead to widespread progression of damage	$P_F = 1.25 \times 10^{-4}$/yr $\beta = 2.5$	$P_F = 3.0 \times 10^{-5}$/yr $\beta = 3.0$	$P_F = 1.25 \times 10^{-5}$/yr $\beta = 3.25$	$P_F = 5.0 \times 10^{-6}$/yr $\beta = 3.5$
Failure that is either sudden or leads to widespread progression of damage	$P_F = 3.0 \times 10^{-5}$/yr $\beta = 3.0$	$P_F = 5.0 \times 10^{-6}$/yr $\beta = 3.5$	$P_F = 2.0 \times 10^{-6}$/yr $\beta = 3.75$	$P_F = 7.0 \times 10^{-7}$/yr $\beta = 4.0$
Failure that is sudden and results in widespread progression of damage	$P_F = 5.0 \times 10^{-6}$/yr $\beta = 3.5$	$P_F = 7.0 \times 10^{-7}$/yr $\beta = 4.0$	$P_F = 2.5 \times 10^{-7}$/yr $\beta = 4.25$	$P_F = 1.0 \times 10^{-7}$/yr $\beta = 4.5$

[1]The target reliability indices are provided for a 50-year reference period, and the probabilities of failure have been annualized. The equations presented in Section 2.3.6 are based on reliability indices for 50 years because the load combination requirements in Section 2.3.2 are based on the maximum loads for the 50-year reference period.
[2]Commentary to Section 2.5 includes references to publications that describe the historic development of these target reliabilities.

Figure 7.9: Target reliability stipulated in ASCE 7-16 (*ASCE 7-16*, 2016).

This behavior is also seen in Tables 6.4 and 6.5 through the mean values of s_e that, for certain wind directions, assume values significantly smaller than one. With respect to the system-level inelastic limit state, the reliability index was estimated to be $\beta_s^{(LS3)} = 3.29$. In particular, as can be seen in Table 7.8, failure occurs mostly due to non-shakedown. As compared with the system reliability considering first member yield, i.e. $\beta_s^{(LS2)}$, the reliability of the system increased from 2.81 to 3.29. From Table 7.8 it is interesting to observe that $\beta_s^{(LS3b)}$ and $\beta_s^{(LS3c)}$ well exceeded the reliability index associated with LS3, i.e. $\beta_s^{(LS3)} = 3.29$, indicating how the system was not susceptible to failure due to excessive peak or residual drifts.

The results of this section clearly illustrate the advantage of allowing controlled inelasticity in order to increase the reliability of the system. Indeed, by comparing $\beta_s^{(LS3)}$ with $\beta_c^{(LS1)}$, i.e. classic component reliability, it can been seen that a system designed to satisfy a Risk Category II using traditional approaches can achieve a Risk Category III classification by adopting the inelastic system-level limit state proposed in this research and outlined in Section 7.3.

In addition, Table 7.10 reports the elements experiencing inelasticity for representative samples of the Monte Carlo simulation for which LS3 was not satisfied, i.e. the structure was susceptible to collapse. It is interesting to observe how the number of elements experiencing

Table 7.10: Number of inelastic elements for the 3 samples of the Monte Carlo simulation for which Limit State 3 was not satisfied.

Sample	1	2	3
Elastic multiplier s_e	0.6566	0.5419	0.6458
Plastic multiplier s_p	0.7502	0.8495	0.9030
# of Inelastic elements	147	126	65

damage reached as high as 147 and involved both coupling beams and wall elements.

7.5 Summary and Conclusions

This chapter outlined a system-level reliability assessment framework for evaluating the reliability of systems with respect to three different limit states, including component yield, system-level first yield, and system-level inelastic failure due to non-shakedown and/or excessive plastic deformation, all within the context of a carefully selected range of uncertainties that are consistent with modern code development. In particular, by housing the framework within a conditional simulation model, efficient evaluation of reliabilities associated with small failure probabilities was achieved.

Two case studies were presented to illustrate the applicability of the proposed framework, from which it can be seen that structures design to satisfy classic component-level reliability targets can achieve a higher Risk Category classification at system-level by considering as a limit state the achievement of dynamic shakedown without excessive residual/peak inelastic drifts. This significant increase in the reliability of the system clearly illustrates the potential of designing wind-excited structures to have controlled inelasticity at ultimate load levels.

CHAPTER VIII

Rapid Uncertainty Quantification for Non-linear and Stochastic Wind Excited Structures: A Metamodeling Approach

8.1 Overview

This chapter presents an alternative approach for estimating the dynamic responses of non-linear wind excited structures based on metamodeling techniques. Methods will be introduced that can handle both stochastic excitations as well as system uncertainty. A case study consisting in a 40-story moment resisting frame subject to multivariate stochastic wind excitation and an array of non-linear viscous dampers is presented to illustrate the potential of the scheme.

8.2 Literature Review

In the design of building systems against natural hazards, performance-based design (PBD), as outlined in Chapter II, has grown in popularity over the past years owing to the advantages that an approach of this kind can offer in terms of both the reliability and cost (*Spence and Kareem*, 2014b; *Bernardini et al.*, 2015; *Tabbuso et al.*, 2016). In order to apply such an approach, particular attention must be devoted to understanding and modeling the

behavior of the system over a full range of hazard levels, i.e. from serviceability to possible collapse. From a computational standpoint, it is the estimation of the extreme responses that often becomes computationally challenging, as nonlinear dynamic systems generally have to be considered. This computational challenge becomes particularly noteworthy in the case of modern probabilisitc PBD where uncertainty must be propagated through the system for estimating performance (*Ciampoli et al.*, 2011b; *Petrini and Ciampoli*, 2012; *Caracoglia*, 2014; *Cui and Caracoglia*, 2015; *Bernardini et al.*, 2015; *Cui and Caracoglia*, 2017).

In addition to the dynamic shakedown framework proposed in the previous Chapters, an alternative approach for overcoming these difficulties, which has recently gained significant interest, is that offered by metamodeling. The basic idea in this approach is to define a metamodel (also known as a surrogate model) of the original system that is computationally efficient to evaluate. This allows any uncertainty to be easily propagated through the system using methods such as Monte Carlo simulation. In general, to calibrate the metamodel, a training process must be carried out that entails running the original computationally burdensome model in a limited number of carefully chosen points. Recently, researches have been focused on developing metamodeling approaches for describing the stochastic response of uncertain non-linear systems driven by stochastic excitation (*Spiridonakos and Chatzi*, 2015; *Mai et al.*, 2016). Of particular interest to this work is a recently proposed numerical approach based on combining polynomial chaos (PC) expansions and non-linear autoregressive with exogenous input (NARX) models (*Spiridonakos and Chatzi*, 2015; *Mai et al.*, 2016). In this approach, NARX models are used to capture the dynamic behavior of the system, while polynomial chaos expansions (PCEs) are adopted to treat the uncertainties in the system properties. The resulting metamodel has been seen to be effective in accurately reproducing the response of several earthquake engineering applications involving stochastic excitation (*Spiridonakos and Chatzi*, 2015; *Mai et al.*, 2016). Current limitations of the approach lie in difficulties associated with identifying appropriate NARX models in the case of multi-degree-of-freedom systems (*Mai*, 2016), and in its single-input single-output

structure. This last is particular limiting in the case of wind excited structures due to the inherently multivariate nature of external wind loads.

8.3 Problem Definition

The general class of non-linear systems of interest can be cast, for an N-degree-of-freedom system, in the following form:

$$\mathbf{M}\ddot{\mathbf{u}}(t) + \mathbf{C}\dot{\mathbf{u}}(t) + \mathbf{K}\mathbf{u}(t) + \mathbf{F}_{\text{nl}}(t; \mathbf{u}, \dot{\mathbf{u}}) = \mathbf{F}(t; \bar{v}) \tag{8.1}$$

where: $\dot{\mathbf{u}}(t)$, $\ddot{\mathbf{u}}(t)$ and $\mathbf{u}$ are the $N \times 1$ velocity, acceleration and displacement response vectors; $\mathbf{M}$, $\mathbf{C}$ and $\mathbf{K}$ are the $N \times N$ mass, damping and linear stiffness matrices of the system; $\mathbf{F}(t)$ is a $N \times 1$ external vector of multivariate stochastic wind excitation; $\bar{v}$ is the mean wind speed to which $\mathbf{F}(t)$ is calibrated; and $\mathbf{F}_{\text{nl}}(t)$ is a $N \times 1$ vector of non-linear restoring forces that depend on the system response. In the following, it will be assumed that the matrices $\mathbf{M}$, $\mathbf{C}$ and $\mathbf{K}$ are constant in time, while the forcing functions $\mathbf{F}(t)$ are considered to be a general stochastic representation of wind loads occurring during a wind event of duration T.

To propagate uncertainty through Eq. (8.1) in the presence of system uncertainties, e.g. uncertainties in the damping and stiffness, as well as general stochastic loads, simulation methods are generally required. This is especially true if performance of a system is to be characterized within modern performance-based wind engineering frameworks, where performance is assessed in terms of correlated sample sets of peak responses occurring in $[0, T]$ (*Ciampoli et al.*, 2011b; *Petrini and Ciampoli*, 2012; *Caracoglia*, 2014; *Cui and Caracoglia*, 2015; *Bernardini et al.*, 2015; *Cui and Caracoglia*, 2017). This chapter is focused on developing a metamodeling approach for efficiently propagating uncertainty through the non-linear system of Eq. (8.1) within a stochastic simulation environment.

8.4 The Proposed Approach

8.4.1 Reduced order model

Because of the structure of Eq. (8.1), i.e. existence of a time independent elastic stiffness $\mathbf{K}$, a straightforward approach to defining a reduced order model for the non-linear $N \times N$ system of Eq. (8.1) is to carry out modal analysis on the left-hand side of the following system (*Eman et al.*, 2000; *Pradlwarter et al.*, 2003; *Schenk et al.*, 2004; *Jensen and Catalan*, 2007; *Valdebenito and Schuëller*, 2011; *Beck et al.*, 2014; *Mitseas et al.*, 2016):

$$\mathbf{M}\ddot{\mathbf{u}}(t) + \mathbf{C}\dot{\mathbf{u}}(t) + \mathbf{K}\mathbf{u}(t) = \mathbf{F}(t;\bar{v}) - \mathbf{F}_{\text{nl}}(t;\mathbf{u},\dot{\mathbf{u}}) \tag{8.2}$$

According to this approach, the dynamic response of the system can be estimated through the following set of non-linear equations (*Eman et al.*, 2000; *Pradlwarter et al.*, 2003; *Schenk et al.*, 2004; *Jensen and Catalan*, 2007):

$$\begin{aligned} M_m\ddot{y}_m(t) + 2M_m\omega_m\zeta_m\dot{y}_m(t) + M_m\omega_m^2 y_m(t) &= \Phi_m^T\left[\mathbf{F}(t;\bar{v}) - \mathbf{F}_{\text{nl}}(t;\mathbf{u},\dot{\mathbf{u}})\right] \\ &= Q_m(t;\bar{v}) + \Phi_m^T\mathbf{F}_{\text{nl}}(t;\mathbf{u},\dot{\mathbf{u}}), \\ m &= 1,...,N_m \leq N \end{aligned} \tag{8.3}$$

where; $\ddot{y}_m$, $\dot{y}_m$ and y_m are the generalized responses of the system; M_m, ω_m, ζ_m and Φ_m are respectively the mth generalized mass, natural circular frequency, damping ratio and mode shape associated with the left-hand side of Eq. (8.2); while $Q_m(t)$ is the generalized forcing function. In general, the damping ratio, ζ_m, can be directly assigned, while M_m and ω_m can be estimated as:

$$\begin{aligned} M_m &= \Phi_m^T\mathbf{M}\Phi_m \\ \omega_m^2 &= \frac{1}{M_m}\Phi_m^T\mathbf{K}\Phi_m \end{aligned} \tag{8.4}$$

where the mode shapes are estimated from solving a standard eigenvalue/eigenvector problem in terms of $\mathbf{M}$ and $\mathbf{K}$. Once the generalized responses are known, the responses in physical coordinates can be estimated through the transformation:

$$\begin{aligned} \mathbf{u}(t) &= \mathbf{\Phi}_{N_m}\mathbf{y}_{N_m}(t) \\ \dot{\mathbf{u}}(t) &= \mathbf{\Phi}_{N_m}\dot{\mathbf{y}}_{N_m}(t) \\ \ddot{\mathbf{u}}(t) &= \mathbf{\Phi}_{N_m}\ddot{\mathbf{y}}_{N_m}(t) \end{aligned} \tag{8.5}$$

where $\mathbf{\Phi}_{N_m}$ is the modal matrix collecting the first $N_m \leq N$ modes while $\mathbf{y}_{N_m}$, $\dot{\mathbf{y}}_{N_m}$ and $\ddot{\mathbf{y}}_{N_m}$ are the generalized response vectors collecting the responses of the first N_m generalized coordinates.

The advantage of the non-linear system of Eq. (8.3) is that, in general, only the first few modes are necessary to accurately predict the response of the system, i.e. N_m can be taken such that $N_m \ll N$. This has been illustrated in a number of applications involving structures subject to stochastic seismic excitations and governed by non-linear equations of the type shown in Eq. (8.1) (*Eman et al.*, 2000; *Pradlwarter et al.*, 2003; *Schenk et al.*, 2004; *Jensen and Catalan*, 2007). In practice, through the reduction of this section, the state of the non-linear system is governed by the reduced set of variables, $\{\mathbf{y}_{N_m}(t), \dot{\mathbf{y}}_{N_m}(t), \ddot{\mathbf{y}}_{N_m}(t)\}$ as opposed to $\{\mathbf{u}(t), \dot{\mathbf{u}}(t), \ddot{\mathbf{u}}(t)\}$.

Notwithstanding the order reduction, as outlined in *Jensen and Catalan* (2007), the system of Eq. (8.3) still requires to be solved simultaneously through an appropriate step-by-step integration scheme, such as the Newmark constant acceleration method (*Jensen and Catalan*, 2007) or fast non-linear analysis (*Wilson*, 2002). In cases where uncertainty is to be propagated through the system using approaches such as Monte Carlo simulation, this can fast become computationally cumbersome. To overcome this, the possibility of using appropriate metamodeling schemes for rapidly propagating uncertainty through the reduced system of Eq. (8.3) will be investigated.

8.4.1.1 Uncertainty modeling

The reduced system of Eq. (8.3) provides a convenient setting for modeling uncertainties in the system parameters, e.g. damping and stiffness. Indeed, there are a number of studies that have been carried out that characterize the uncertainty in the modal quantities, i.e. ω_m and ζ_m, of wind excited systems (*Diniz et al.*, 2004b; *Diniz and Simiu*, 2005; *Bashor et al.*, 2005b; *Bernardini et al.*, 2015). Therefore, once the reduced system is defined, uncertainty can be modeled directly at the level of the natural frequencies and damping ratios of the reduced system through assigning appropriate probability distributions. In alternative, a direct approach can also be taken, in which the uncertainties are modeled at the level of $\mathbf{K}$ and $\mathbf{M}$. In this case, the modal matrix, $\mathbf{\Phi}_{N_m}$, becomes uncertain and requires evaluation for each realization of the uncertainties affecting $\mathbf{K}$ and $\mathbf{M}$. However, because this only requires the evaluation of a standard eigenvalue/eigenvector problem, it does not represent a significant computational challenge. Together with these uncertainties, in general, uncertainties characterizing the intensity of the stochastic excitation, e.g. the wind speed $\bar{v}$, as well as the properties of the non-linear components generating the restoring forces $\mathbf{F}_{\text{nl}}$, will require modeling. These additional sources of uncertainty can be incorporated, without difficulty, in the reduced order model directly at the level of the non-linear components and stochastic wind load model. In the following, all uncertainties associated with the elastic system parameters, external excitation model and non-linear components will be collected in the uncertain vector $\mathbf{X}$.

8.4.2 A metamodel-based solution scheme

Recently, a metamodeling approach has been proposed for efficiently simulating the response of uncertain non-linear systems excited by stochastic loads (*Spiridonakos and Chatzi*, 2015; *Mai et al.*, 2016). The approach has been seen to be particularly well suited for single-input single-output low dimensional non-linear systems subject to stochastic excitation, e.g. earthquake loads (*Mai et al.*, 2016). With this mind, it is interesting to observe that, in-

dependently of whether the original stochastic excitation is multivariate or not, each generalized coordinate of the reduced system of Eq. (8.3) can be treated as a single-input (Q_m) single-output (y_m, $\dot{y}_m$, or $\ddot{y}_m$ depending on the variable of interest) system. Within this context, consider representing the input output relationship of the mth generalized coordinate through the following NARX model (where the dependency on the mth coordinate is not explicitly shown for clarity of presentation) (*Billings*, 2013):

$$\begin{aligned} y(t_j) &= G(\mathbf{z}(t_j)) + \epsilon(t_j) \\ &= G(Q(t_j), ...Q(t_{j-n_Q}), y(t_{j-1}), ...y(t_{j-n_y})) + \epsilon_t \end{aligned} \tag{8.6}$$

where: $y(t_j)$, $Q(t_j)$, and $\epsilon(t_j)$ are the system output, input, and noise sequences at discrete time step t_j, respectively; n_y and n_Q are the maximum lags for the system output and input; $G(\cdot)$ is the underlying nonlinear approximator to be identified; $\mathbf{z}(t_j)$ is the regression vector collecting the system outputs and inputs at time step t_j; while ϵ_t is a normal random variable with zero mean and standard deviation $\sigma_\epsilon(t_j)$ (i.e. $\epsilon_t \sim N(0, \sigma_\epsilon^2(t_j))$) representing the residual error of the NARX model. Equation (8.6) above can then be expressed in a commonly used linear-in-the-parameters form:

$$y(t_j) = \sum_{i=1}^{n_g} \vartheta_i \, g_i(\mathbf{z}(t_j)) + \epsilon_t \tag{8.7}$$

in which n_g is the number of potential model terms $g_i(\mathbf{z}(t_j))$ that are functions of the regression vector, $\mathbf{z}(t_j)$, while ϑ_i are the corresponding parameters of the NARX model. In general, the identification of the NARX model consists in firstly selecting the correct model structure (i.e. selecting the NARX terms $g_i(\mathbf{z}(t))$ of the model), and secondly estimating the model parameters, ϑ_i, from the system inputs and outputs. To this end, several approaches have been proposed for identifing the simplest model that can appropriately represent the underlying dynamics of non-linear systems (*Billings*, 2013; *Billings and Wei*, 2008; *Chen and Ni*, 2011; *Wei and Billings*, 2008).

Once calibrated, the NARX model of Eq. (8.7) is capable of capturing the time evolution of the system in the time interval $[0, T]$, i.e. given a realization of the generalized force, $Q(t_j)$ with $t_j = 0, \Delta t, 2\Delta t, ..., N_T \Delta t$ with N_T the total number of discrete time steps of duration Δt in $[0, T]$, Eq. (8.7) can be used to estimate the output discrete time series $y(t_j)$. In particular, models of this type can be constructed not only for the displacement responses, but also for the velocities, $\dot{y}(t_j)$, and accelerations, $\ddot{y}(t_j)$. What the NARX models cannot capture are the effects of uncertainties in the system parameters, i.e. the uncertainties collected in $\mathbf{X}$ and discussed in Section 8.4.1.1. A recently proposed approach for capturing this type of system uncertainty, and that will be followed here, is to consider the parameters, ϑ_i, of the NARX model as deterministic functions of the system uncertainties. In particular, this functional relationship can be estimated through a truncated PCE:

$$\vartheta_i(\mathbf{X}) = \sum_{l=1}^{n_\psi} \vartheta_{i,l} \psi_l(\mathbf{X}) + \epsilon_i \tag{8.8}$$

where $\mathbf{X}$ is the vector collecting all the system uncertainties, ϵ_i is the truncation error, $\psi_l(\mathbf{X})$ for $l = 1, \cdots, n_\psi$ are multivariate orthonormal polynomials associated with $\mathbf{X}$, while $\vartheta_{i,l}$ for $i = 1, \cdots, n_g$ and $l = 1 \cdots, n_\psi$ are the associated deterministic polynomial chaos coefficients.

By combining the truncated PCE representation of the coefficients with the NARX model of Eq. (8.7), the following PC-NARX metamodel of the input output relationship of the generalized coordinates of the reduced model of Section 8.4.1 is obtained:

$$y(t_j, \mathbf{X}) = \sum_{i=1}^{n_g} \sum_{l=1}^{n_\psi} \vartheta_{i,l} \psi_l(\mathbf{X})\, g_i(\mathbf{z}(t_j)) + \epsilon(t_j, \mathbf{X}) \tag{8.9}$$

with $\epsilon(t_j, \mathbf{X})$ designating the total error due to the truncation of the PCE and the noise of the NARX model. To calibrate Eq. (8.9), procedures are required for selecting the NARX terms $g_i(\mathbf{z}(t_j))$ as well as calibrating the PCEs of the model parameters, ϑ_i. The next section will outline models to this end.

8.4.2.1 Non-intrusive metamodel calibration

A non-intrusive approach to calibrating metamodels of the type shown in Eq. (8.9) has been recently proposed in *Mai et al.* (2016). In particular, this approach is based on selecting the NARX terms, i.e. model structure, through a least angle regression (LARS) algorithm, while estimating the corresponding coefficients through the optimization of the one-step-ahead prediction error (PE). This approach has been seen to provide good accuracy in reproducing the response of non-linear dynamic systems subject to short duration stochastic excitation, e.g. seismic loads. However, wind excitation has a much longer duration of sustained loading which can easily lead to a serious error accumulation problem, i.e. small prediction errors accumulating to larger ones due to the model output feedback. In extreme situations, the model can become unstable (i.e. predictions that tend to infinity), even if the model still possesses very good one-step ahead prediction performance.

In this work, the approach suggested in *Mai et al.* (2016) for refining the selection of the parameters of the NARX model will be investigated as a means to avoid the error accumulation problem encountered in using the PE-based LARS algorithm for calibrating the PC-NARX model of Eq. (8.9). To this end, consider an experimental design consisting in K realizations of the generalized forces, $Q_k(t_j)$ for $k = 1, ...K$, and realizations of the system uncertainties, $\mathbf{x}_k$ for $k = 1, ...K$. By following the PE-based LARS algorithm outlined in *Mai et al.* (2016), an appropriate model structure can be identified. This process provides an initial estimate of the NARX parameters for each of the K experiments through a PE criterion. Based on these values, the response to $Q_k(t_j)$ can be simulated as:

$$\hat{y}_k(t_j; \mathbf{x}_k) = \sum_{i=1}^{n_g} \vartheta_{ki}(\mathbf{x}_k)\, g_i(\hat{\mathbf{z}}_k(t_j)) \tag{8.10}$$

where $\hat{\mathbf{z}}_k(t_j) = (Q_k(t_j), \cdots, Q_k(t_{j-n_Q}), \hat{y}_s(t_{j-1}), \cdots, \hat{y}_s(t_{j-n_y}))^T$, while ϑ_{ki} are the calibrated parameters of the NARX model for the kth experiment.

The difference between the simulated response, $\hat{y}_k(t)$, and the actual response, $y_k(t)$,

in $[0, T]$, can now be minimized in terms of the vector of NARX model parameters, $\hat{\boldsymbol{\vartheta}}_k = \{\vartheta_{k1}, ..., \vartheta_{kn_g}\}^T$, through the following simulation error (SE) criterion:

$$\hat{\boldsymbol{\vartheta}}_k(\mathbf{x}_k) = \underset{\hat{\boldsymbol{\vartheta}}_k}{\operatorname{argmin}} \left\{ \sum_{j=1}^{N_T} \left(y(t_j; \mathbf{x}_k, \hat{\boldsymbol{\vartheta}}_k) - \hat{y}_k(t_j; \mathbf{x}_k, \hat{\boldsymbol{\vartheta}}_k) \right)^2 \right\} \tag{8.11}$$

By solving this optimization problem, refined estimates for the NARX parameters are obtained. In particular, this optimization problem can be solved by any appropriate nonlinear optimization technique. In this work, the Nelder-Mead simplex algorithm (*Lagarias et al.*, 1998) is adopted. The execution time depends on how close the initial guess is to the optimal value of the NARX parameters and the number of NARX parameters, i.e. design variables, and is therefore relatively insensitive to the total duration of the excitation. In particular, the parameters obtained through the PE-based LARS algorithm outlined in *Mai et al.* (2016) have been seen to provide a good starting point for solving the optimization problem of Eq. (8.11).

After identifying the refined NARX parameters, they can be expanded onto an appropriate PC basis, with corresponding deterministic coefficients, through the LARS-based procedure outlined in *Mai et al.* (2016), therefore leading to a fully calibrated PC-NARX model. In particular, it should be observed that the calibration process outlined here is non-intrusive, as it only requires the input and output of the reduced coordinate.

8.4.3 Overall procedure

The overall procedure for defining the metamodel of order N_m for the system outlined in Eq. (8.1) subject to multivariate stochastic wind loads of duration T can be summarized as follows:

1. Generate a set of K realizations of the uncertain vector $\mathbf{X}$, with associated realizations of the mulitvariate forcing functions $\mathbf{F}(t_j)$ of time step Δt and total duration T, through a space filling sampling procedure such as Latin hypercube sampling.

2. Identify the elastic modal properties of the non-linear system of Eq. (8.1) by carrying out an eigenvalue/eigenvector analysis in terms of $\mathbf{M}$ and $\mathbf{K}$ for each realization of $\mathbf{X}$.

3. Use the mode shape vectors $\mathbf{\Phi}_{N_m}$ of order N_m to generate K realizations of the generalized stochastic forcing functions $\mathbf{Q}_{N_m}(t_j) = \mathbf{\Phi}_{N_m}^T \mathbf{F}(t_j)$.

4. Solve the reduced order system of Eq. (8.1) through a direct integration approach for each realization of $\mathbf{X}$ and $\mathbf{Q}_{N_m}(t_j)$, therefore generating K realizations of the reduced states $\{\mathbf{y}_{N_m}(t_j), \dot{\mathbf{y}}_{j\,N_m}(t), \ddot{\mathbf{y}}_{j\,N_m}(t)\}$.

5. From the K discrete input/output sets of the N_m reduced coordinates, calibrate PC-NARX metamodels using the procedures outlined in Sec. 8.4.2.

Once the metamodels of order N_m are calibrated, stochastic responses in physical coordinates can be generated by simply generating samples of $\mathbf{X}$ and $\mathbf{F}(t)$, estimating the corresponding samples $\mathbf{y}_{N_m}(t)$ in the reduced space, and using the transformation of Eq. (8.5) to estimate stochastic responses in physical coordinates. In particular, if the responses of interest are velocities and/or accelerations, PC-NARX models can be calibrated to these input/outputs.

8.5 Case Study

In this section, a multi-degree-of-freedom building structure equipped with an array of non-linear response mitigation devices, and excited by multivariate stochastic wind forces, is presented to illustrate the proposed metamodeling approach.

8.5.1 General description of the structure

The following results and discussion will refer to the 40-story steel frame shown in Figure 8.1. The geometry of the frame is described by four 6.1 m bays and by inter-story heights, h_j, of 6.1 m at ground level and 3.8 m for all other floors. The overall height of the structure, H,

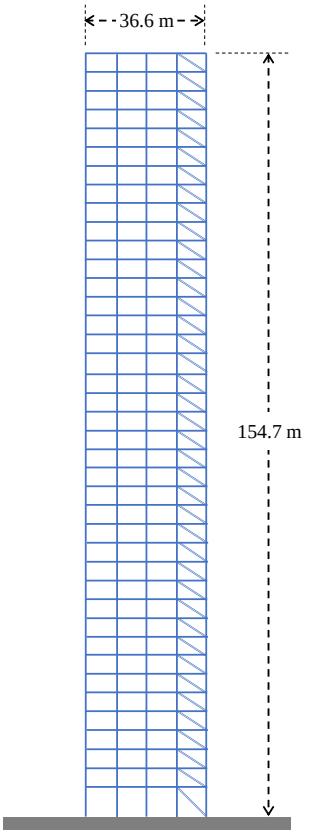

Figure 8.1: Schematic of the 40-story steel frame considered in the case study.

is 154.7 m, while the influence width W of the frame is considered to be 36.6 m. In particular, the columns were considered as square box sections while the beams were assigned standard AISC (American Institute for Steel Construction) wide flange sections. Table 1 reports the specific section sizes used in designing the structure. The mass was considered lumped at each floor with expected value calculated as the sum of the element mass and carried mass. The carried mass at each floor was taken as $M = q_0 L/g$, where g is the gravitational acceleration, $q_0 = 11.96 h_j$ kN/m is a uniformly distributed dead load, while h_j and L are the height and length of each floor. In this example, uncertainties were considered directly at the level of the stiffness, $\mathbf{K}$, and mass, $\mathbf{M}$, matrices. In particular, uncertainty in $\mathbf{K}$ was modeled by taking the Young's modulus of the material as a lognormal random variable with mean 210 GPa and standard deviation 15 GPa. To model the uncertainty in the mass, $\mathbf{M}$ was multiplied by a lognormal random variable with mean of 1 kg and standard deviation of

0.05 kg. To model uncertainty in the damping, the damping ratios were taken as dependent lognormal random variables with mean 0.015 and standard deviation 0.005.

As illustrated in Figure 8.1, response mitigation devices are diagonally mounted between each floor. In particular, these take the form of fluid viscous dampers (*Symans and Constantinou*, 1998) leading to the following nonlinear restoring forces:

$$\mathbf{F}_{\text{nl}}(t;\dot{\mathbf{u}}) = \begin{Bmatrix} c_1 \text{sgn}(v_{r_1})|v_{r_1}(\dot{u}_1(t))|^\alpha \\ \vdots \\ c_1 \text{sgn}(v_{r_{10}})|v_{r_{10}}(\dot{u}_{10}(t),\dot{u}_9(t))|^\alpha \\ c_2 \text{sgn}(v_{r_{11}})|v_{r_{11}}(\dot{u}_{11}(t),\dot{u}_{10}(t))|^\alpha \\ \vdots \\ c_2 \text{sgn}(v_{r_{20}})|v_{r_{20}}(\dot{u}_{20}(t),\dot{u}_{19}(t))|^\alpha \\ c_3 \text{sgn}(v_{r_{21}})|v_{r_{21}}(\dot{u}_{21}(t),\dot{u}_{20}(t))|^\alpha \\ \vdots \\ c_3 \text{sgn}(v_{r_{30}})|v_{r_{30}}(\dot{u}_{30}(t),\dot{u}_{29}(t))|^\alpha \\ c_4 \text{sgn}(v_{r_{31}})|v_{r_{31}}(\dot{u}_{31}(t),\dot{u}_{30}(t))|^\alpha \\ \vdots \\ c_4 \text{sgn}(v_{r_{40}})|v_{r_{40}}(\dot{u}_{40}(t),\dot{u}_{39}(t))|^\alpha \end{Bmatrix} \tag{8.12}$$

where v_{r_j} is the relative velocity between the ends of the damper at floor j, c_1, c_2, c_3, and c_4 are uncertain damping coefficients with uniform distribution in $[0, 100]$ N-s/m, while $\alpha = 0.38$ is the damping exponent. In total, for this problem, the uncertain vector $\mathbf{X}$ has eight components.

8.5.2 Stochastic wind force model

The multivariate stochastic wind loads, $\mathbf{F}(t)$, acting at each floor of the frame of Figure 8.1 are modeled in this work through a quasi-steady model based on a spectral representation of the multivariate wind speed field acting over the height of the frame. The overall intensity

Table 8.1: Section sizes of the steel frame.

Level range	Wide-flange Beams	Box columns	
		Interior (cm)	Exterior (cm)
1-10	W36 × 282	56 × 56	51 × 51
		$t = 7.6$	$t = 6.4$
11-20	W36 × 194	51 × 51	51 × 51
		$t = 5.0$	$t = 5.0$
21-30	W33 × 169	46 × 46	46 × 46
		$t = 2.5$	$t = 2.5$
31-40	W27 × 84	46 × 46	46 × 46
		$t = 1.9$	$t = 1.9$

t = wall thickness

of the stochastic wind loads is defined in terms of the mean hourly wind speed $\bar{v}$ to occur at a meteorological station of height H_{met} and roughness length z_{01}. This is related to the mean hourly wind speed over the height of the building, z, through the following transformation (*Spence and Kareem*, 2014b):

$$\bar{v}_z(z_0) = 0.8065 \left(\frac{z_0}{z_{01}}\right)^{0.0706} \frac{\ln[\frac{z}{z_0}]}{\ln[\frac{H_{met}}{z_{01}}]} \bar{v}(H_{met}, z_{01}) \tag{8.13}$$

where z_0 is the roughness length at the site of interest. In particular, in this case study, the wind speed $\bar{v}$ of Eq. (8.13), was taken as a Type II distribution with mean 30 m/s and standard deviation 3.5 m/s. A roughness length of $z_{01} = 0.05$ m and a meteorological height of $H_{met} = 10$ m were considered for $\bar{v}$. The roughness length at the site of the structure, z_0, was taken to be 0.02 m.

From Eq. (8.13), the jth component of $\mathbf{F}(t)$ (i.e. wind loads acting at height z_j), can be estimated through the quasi steady model outlined in Section 4.4.2. In particular, a storm duration of $T = 900$ s with sampling frequency of 100 Hz was considered with a quasi-steady pressure coefficient $\bar{C}_n$ of 1.3. In this case, each realization of $\mathbf{F}(t)$ entails the generation of a total of 81920 independent and uniformly distributed random numbers in $[0, 2\pi]$.

8.5.3 Results

8.5.3.1 Calibration

The first three natural circular frequencies of the frame were in the range of $\omega_1 \approx 1.5$ rad/s, $\omega_2 \approx 4$ rad/s, and $\omega_3 \approx 7$ rad/s. Due to how wind does not, for all intents and purposes, have energy above 2π rad/s, the first three generalized coordinates were considered sufficient in defining the dimension of the reduced model, i.e. $N_m = 3$. In defining the metamodel of the displacement responses of the reduced system, i.e. $y_m(t)$ for $m = 1, 2, 3$, a full NARX model was chosen as the following polynomial function:

$$g_i(t_j) = y_1^{l_1}(t_{j-n_y}) Q_1^{l_2}(t_{j-n_Q}) \tag{8.14}$$

with $l_1 + l_2 \leq 3$, $0 \leq l_1 \leq 3$, $0 \leq l_2 \leq 1$, $n_y = 1, 2$ and $n_Q = 0, 1, 2$, therefore leading to 10 candidate terms including the constant term. To identify the most appropriate NARX model, an experimental design consisting in $K = 200$ simulations were carried out with input random variables, i.e. $\mathbf{X}$, generated by Latin hypercube sampling. From the LARS procedure of *Mai et al.* (2016), four terms were selected, namely the constant term, $Q_m(t_j)$, $y_m(t_{j-1})$, and $y_m(t_{j-2})$. After implementing the output error procedure of Section 8.4.2.1, the mean relative error (as defined in *Mai et al.* (2016)) over all 200 simulations was $\bar{\epsilon} = 0.017$. In representing the NARX coefficients through PCEs, adaptive expansions were considered with maximum interaction rank of 2 and truncation parameter of 1. Figure 8.2(a) shows, for one of 200 calibration points, the comparison between the reconstructed and reference displacement response (estimated through the fast non-linear analysis scheme reported in *Wilson* (2002)) of the structure at the top floor. As can be seen, the metamodel captures the response evolution remarkably well. In particular, Figure 8.2(b) shows the evolution of the error induced by the NARX model, while Figure 8.2(c) reports the evolution of the overall error induced by the NARX and PC approximations. As can be seen, the overall error is not only small, but also stable with time, i.e. no error accumulation is seen, notwithstanding the

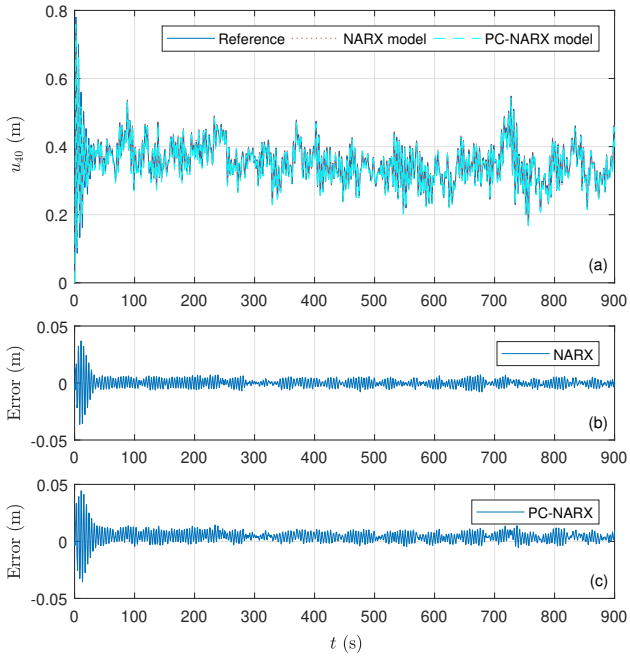

Figure 8.2: Comparison for a point of the calibration set between the reconstructed and reference top floor displacement response: (a) Evolution of the response in $[0, T]$; (b) Error evolution due to NARX approximation; (c) Overall error evolution due to NARX and PC approximations.

long prediction horizon. This illustrates the effectiveness of the simulation error refinement scheme of Section 8.4.2.1.

8.5.3.2 Simulation results

To investigate the simulation performance of the metamodel, a validation set consisting in 200 randomly generated samples of $\mathbf{X}$, with associated samples of $\mathbf{F}(t)$, were generated. Reference solutions were estimated for each sample using once again the fast non-linear analysis scheme. The calibrated metamodel was then run for each sample and the predictive capability of the metamodel was investigated. Figure 8.3 shows a typical result with respect to the simulation of the coordinates of the reduced model. As can been seen, very good correspondence between the reference solutions and the reduced coordinates of the metamodel is achieved. Figure 8.4(a) reports the comparison between the reference solution and the

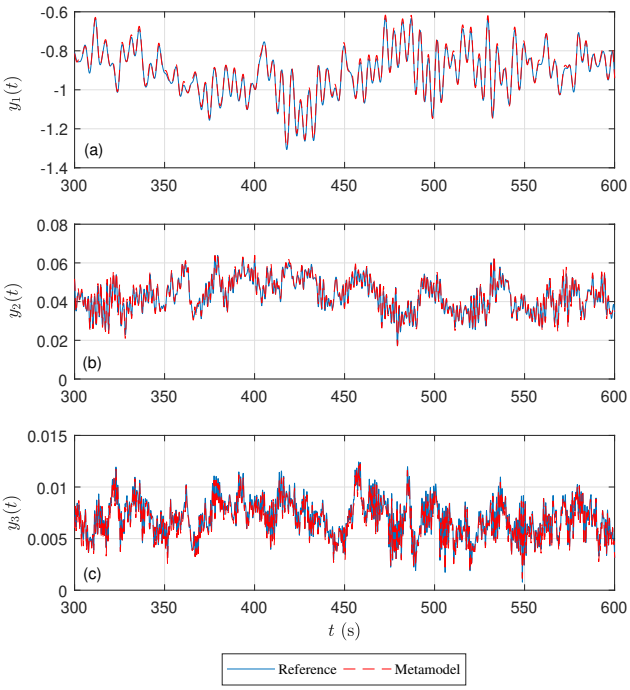

Figure 8.3: Comparison between the simulated and reference displacement responses of the reduced system for a representative sample: (a) First generalized coordinate; (b) Second generalized coordinate; (c) Third generalized coordinate.

metamodel in physical coordinates, and in particular the top floor displacement response. As can be seen, very good correspondence is achieved. Figure 8.4(b) shows the evolution of the difference between the reference and simulated responses, from which the stability of the prediction can be seen. Similar results were seen for all simulations in the validation set. Figure 8.5 illustrates the typical non-linear response seen in the dampers over the duration of the event.

To illustrate the predictive capability of the metamodel over all samples, Figure 8.6 reports the comparison between the 200 reference and simulated maximum absolute responses at the top floor of the structure. As can be seen, there is strong correspondence between the reference and simulated responses with a correlation coefficient of 0.97. The strong correspondence between the responses allows for the direct estimation of quantities such as the exceedance probabilities associated with the peak absolute response of the system in $[0, T]$, as illustrated in Figure 8.7.

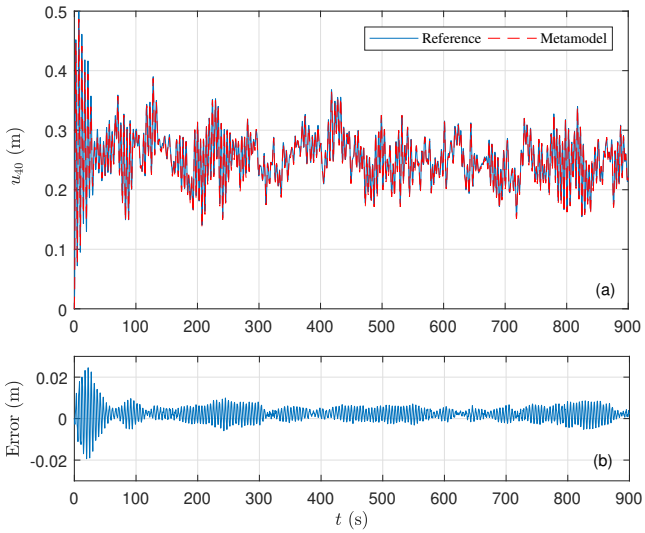

Figure 8.4: Comparison between the simulated and reference displacement responses at the top floor of the structure: (a) Evolution of the response in $[0, T]$; (b) Overall error evolution.

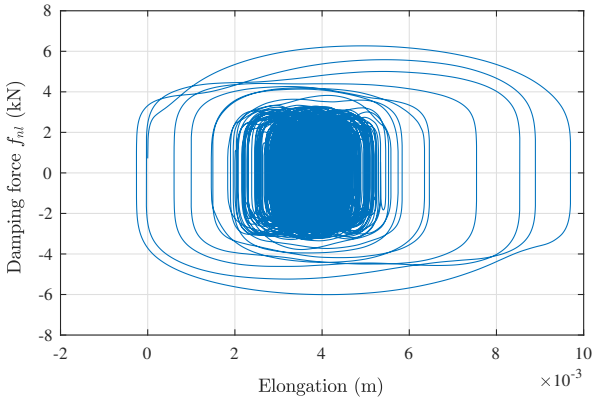

Figure 8.5: Typical hysteretic response of the top floor damper.

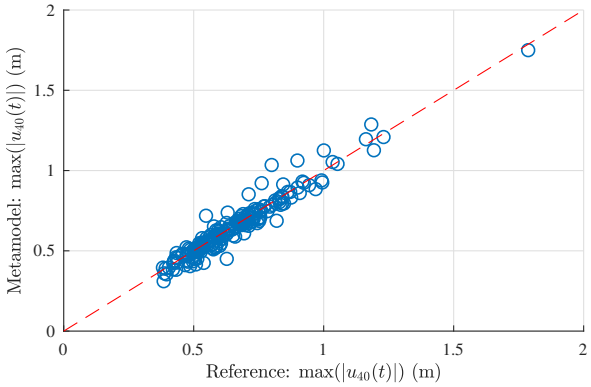

Figure 8.6: Comparison between the reference and simulated peak absolute responses in $[0, T]$ at the top floor of the structure.

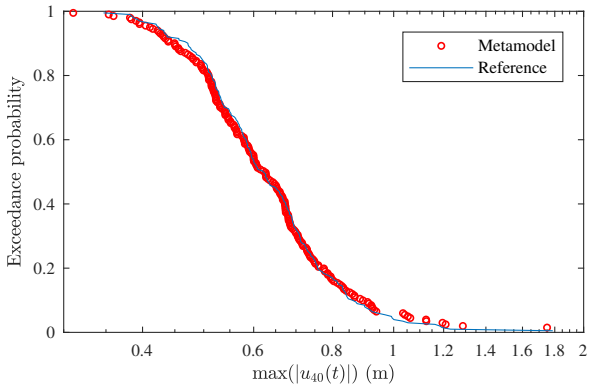

Figure 8.7: Comparison between the exceedance probabilities of the top floor response estimated from the reference and simulated data.

8.5.3.3 Discussion

The capability of the proposed metamodeling approach to accurately propagate uncertainty through the class of multi-degree-of-freedom non-linear systems outlined in Section 8.3 was illustrated in this section through the example structure of Figure 8.1. If it is observed that, once calibrated, the generation of the response time histories through the metamodel was around two orders of magnitude faster than the fast non-linear scheme used to estimate the reference solutions, the potential of the approach becomes clear. This is especially true if it is kept in mind that the fast non-linear scheme outlined in *Wilson* (2002) is an approach specialized for rapid resolution of the class of non-linear systems investigated in this work. By observing how the reduction scheme of Section 8.4.1 can be applied to systems involving a wide variety of non-linear component behaviors, e.g. *Eman et al.* (2000); *Pradlwarter et al.* (2003); *Schenk et al.* (2004); *Jensen and Catalan* (2007), and how the PC-NARX metamodeling approach has been seen to accurately reproduce the behavior of single-degree-of-freedom systems (i.e. generalized coordinates of this work) involving similar types of non-linearities (*Mai et al.*, 2016), the applicability of the proposed combined approach for rapid uncertainty propagation through a wide variety of large-scale non-linear dynamic systems subject to stochastic excitation would seem possible.

8.6 Summary and Conclusions

The feasibility of combining metamodeling techniques with model order reduction schemes as a means to define metamodeling approaches for the rapid propagation of uncertainty through multi-degree-of-freedom nonlinear and stochastic wind excited dynamic systems was investigated in this chapter. To this end, a scheme was outlined based on combining a recently introduced metamodeling approach for non-linear stochastic systems with a modal-based order reduction framework. In choosing the potential terms of the metamodel, general knowledge of the non-linear system can be used. Because of the strong capability

of the metamodeling approach of replicating the time evolution of a wide class of single-degree-of-freedom dynamic systems, coupled with the applicability of the reduction scheme to an equally wide class of non-linear multi-degree-of-freedom systems, the approach has the potential to be applied to a number of problems of practical interest. In particular, the possibility to calibrate the metamodel for the resolution of the reduced system in a non-intrusive mode (i.e. using only input/output) ensures the applicability to systems for which only the classic elastic modal properties are known.

To demonstrate the applicability of the approach, uncertainty was propagated through a 40-story moment resisting frame equipped with an array of non-linear viscous dampers and subject to stochastic multivariate wind loads. The proposed approach was seen not only to be capable of accurately reproducing the dynamic response of the system, but also to be nearly two orders of magnitude faster than existing specialized direct integration approaches.

CHAPTER IX

Summary and Conclusions

9.1 Summary

This dissertation presented a performance-based design framework for the integrated collapse and non-collapse assessment of wind excited buildings. A new generation of computational tools was introduced for the system-level inelastic performance assessment. Probabilistic collapse susceptibility and reliability assessment frameworks are also developed for a system-level inelastic failure limit state. More details regarding these specific areas are summarized below.

9.1.1 Performance-based design framework for wind excited structures

A probabilistic PBWE framework is presented for multistory wind excited buildings that rigorously integrates estimates of both collapse and non-collapse losses. Models are developed for estimating performances in terms of system-level losses, such as repair cost and downtime. The theory of dynamic shakedown is used as an efficient means for describing the post yield behavior of structural systems subject to long duration dynamic wind loads and therefore the collapse susceptibility of the main wind-force resisting system. The practicality and potential of the proposed framework is illustrated on a full scale case study.

9.1.2 Inelastic behavior of uncertain wind excited structures

A class of path-following algorithms is developed to rapidly estimate the state of dynamic shakedown together with a full range of inelastic responses at shakedown. The models were developed within the setting of concentrated plasticity as well as distributed plasticity. In particular, with respect to distributed plasticity, models were introduced for estimating inelasticity at both the level of an individual fiber and the level of the member cross-section. To validate the models, a suite of example reinforced concrete and steel structures were considered with concentrated and distributed plasticity. Dynamic and inelastic responses estimated from the proposed approach were compared with those estimated from direct integration.

An alternative approach based on combining model order reduction and metamodeling techniques was also presented for propagating uncertainty through a class of multi-degree-of-freedom non-linear dynamic systems. A case study consisting in a 40-story moment resisting frame subject to multivariate stochastic wind excitation and an array of non-linear viscous dampers is presented to illustrate the potential of the scheme.

9.1.3 Probabilistic collapse susceptibility and reliability assessment framework

The successful development of the models for efficiently estimating inelastic responses of wind excited systems enabled the introduction of a new system-level limit state, defined as the achievement of the state of dynamic shakedown together with the satisfaction of an arbitrary number of local limit states written in terms of inelastic responses at shakedown, against which to assess the adequate performance of a wind excited system experiencing inelasticity. Importantly, due to the nature of dynamic shakedown, this limit state inherently ensures safety against collapse mechanisms involving ratcheting in the alongwind direction, and low-cycle fatigue in the acrosswind direction. The computational efficiency with which the proposed algorithms can assess the limit state for any given wind load history enabled the introduction of a stochastic simulation schemes for rapid probabilistic evaluation of the limit

state while considering a full range of uncertainties, including record-to-record variability in the load histories. These developments allowed for the straightforward estimation of the reliability of the system against inelastic failure described through the aforementioned limit state, therefore opening the door to the design of wind excited systems with controlled inelasticity at ultimate load levels.

9.2 Conclusions

Major findings and contributions from this research are as follows.

9.2.1 Performance-based design framework for wind excited structures

- A general PBD framework is developed to account for both non-collapse and collapse performance for wind excited structures. While it is foreseen that the framework would first see application in the design and analysis of special structures, it is believed that the lessons learned from applying this type of framework will ultimately change design procedures associated normal buildings.

- System-level performance expressed in terms of repair costs and downtime enables straightforward interpretation by decision-makers of diverse technical backgrounds.

- The theory of dynamic shakedown is adopted as an efficient means for describing collapse susceptibility due to low cycle fatigue/ratcheting/instantaneous plastic collapse for wind excited structures.

- The proposed framework is capable of systematically estimating not only the integrated system-level collapse and non-collapse losses, but also the deaggregated non-collapse losses.

- The efficiency of the proposed framework and its systematic estimation of both structural and non-structural damage would be of significant and immediate interest to the

designers of wind excited building systems.

9.2.2 Inelastic behavior of uncertain wind excited structures

- An efficient strain-driven dynamic shakedown approach is introduced for characterizing the inelastic response of wind-excited systems considering concentrated and distributed plasticity.

- The inelastic response modeled through fiber-based distributed plasticity enables a rational and straightforward modeling of the non-linear material behavior of the structure.

- The development of the section-based model, which overcomes the requirement of elastic-perfectly plastic (EPP) material behavior of the fiber-based approach, enables direct application to modeling distributed plasticity of reinforced concrete structures.

- The near perfect correspondence between the inelastic responses obtained through the proposed approach and direct integration provides verification of the accuracy of the strain-driven procedures.

- The strain-driven dynamic shakedown framework can estimate the inelastic response at shakedown around two orders of magnitude faster than direct integration approaches.

- The alternative approach based on combining metamodeling techniques and model order reduction schemes is able to propagate uncertainty through non-linear systems and accurately predict the non-linear responses around two orders of magnitude faster than direct integration.

9.2.3 Probabilistic collapse susceptibility and reliability assessment framework

- A system-level collapse susceptibility estimation framework was developed with a general description of failure considering both global and local limit states.

- By simulating over a suite of windstorms, the proposed framework is well-suited for identifying critical windstorms for which full step-by-step non-linear analysis could be carried out, therefore providing an exhaustive picture of the inelastic performance of a given wind excited structure.

- A simulation method based on conditional simulation is presented together with the reliability assessment framework, enabling efficient estimation of reliability indexes associated with component yield, system-level yield and system-level inelastic limit states.

- By considering a system-level inelastic limit state, a building can achieve a higher Risk Category than the traditional component-level yield limit state. This illustrates the potential of designing wind-excited structures to have controlled inelasticity at ultimate load levels.

9.3 Future Work

Future directions of this work would entail the development of additional theoretical models for describing a general class of non-linear components, such as non-linear hysteretic dissipation devices, or components specifically designed to experience continued inelasticity (i.e. buckling-restrained braces), that could be integrated with the path-following strain-driven dynamic shakedown algorithms of Chapter III. This would enable a hybrid approach to inelastic performance where certain elements are designed to shakedown during the windstorm, while other elements are designed to dissipate energy through controlled but continuous inelasticity. Such developments would result in greater controlled excursion into the inelastic response regime, therefore further enhancing the already extremely promising results presented in Chapter VII. To guarantee the accuracy of predictions at such high levels of inelasticity, the framework would require the incorporation of procedures that model the effects of large displacements and therefore P-Delta effects. In addition, the development of

a comprehensive user-friendly interface would enable the straightforward use of the models outlined in this work, as well as any future developments, by a wide range of design professionals of diverse backgrounds. This would unleash the full potential of allowing inelasticity at the ultimate load level in the design of wind excited structural systems.

With respect to the data-driven approach for estimating non-linear dynamic responses, in addition to the schemes of Chapter VIII where concentrated non-linearity is considered, models can be developed that can account for wider class of non-linearity, including distributed inelasticity, through the introduction of more general reduction schemes based, for example, on model space proper orthogonal decomposition. For capturing system uncertainty, other types of surrogate models, e.g. Kriging models, neural networks, Volterra-series, etc., should be investigated. Developments of these kinds have the potential to lead to a class of metamodel schemes that are capable of treating general high-dimensional non-linear systems subject to a wide variety of stochastic excitation.

APPENDICES

APPENDIX A

Additional Information: Chapter VI

Model level elevations

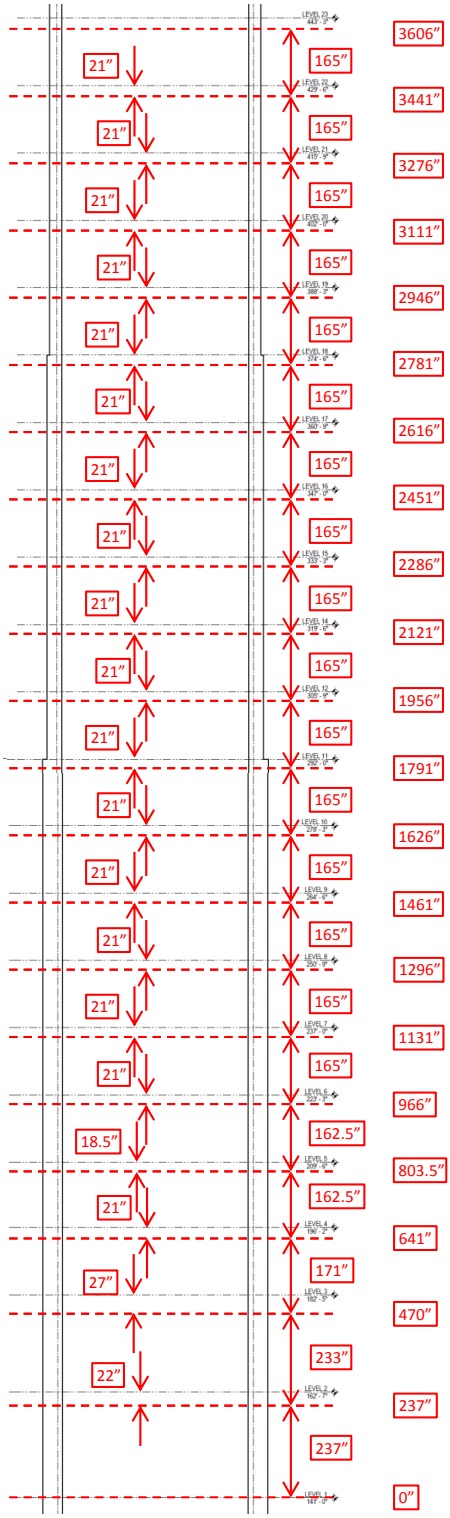

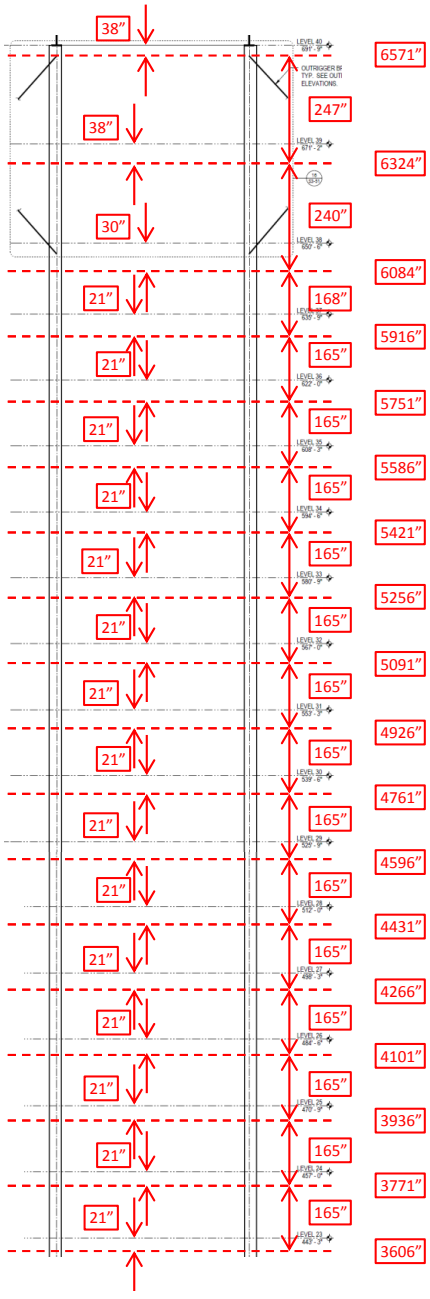

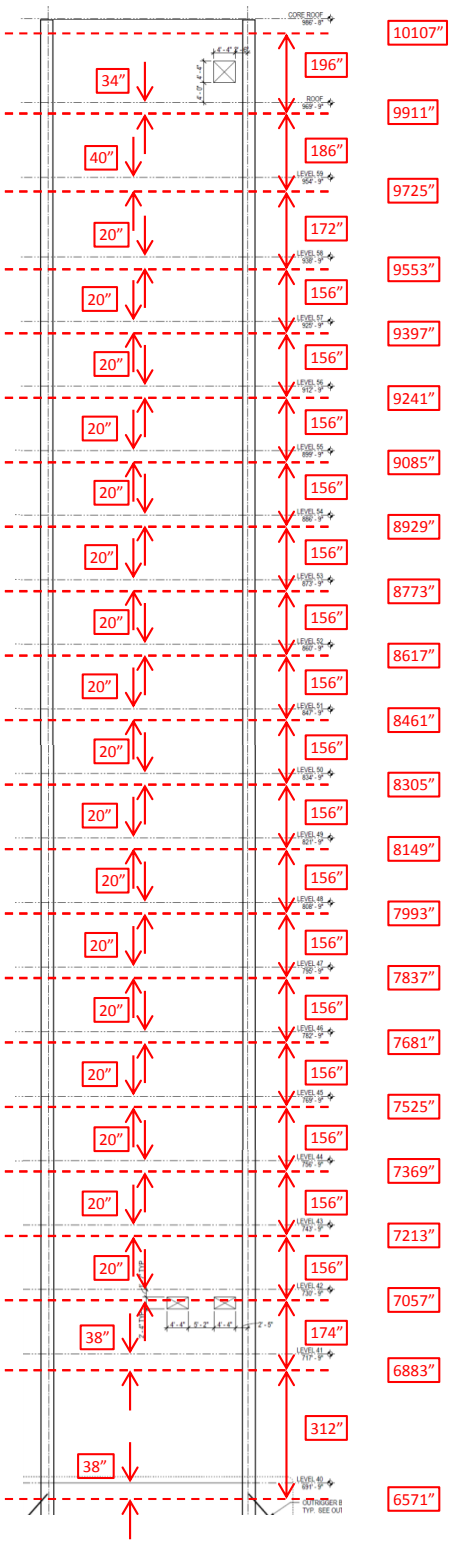
10107″
196″
34″
9911″
186″
40″
9725″
172″
20″
9553″
156″
20″
9397″
156″
20″
9241″
156″
20″
9085″
156″
20″
8929″
156″
20″
8773″
156″
20″
8617″
156″
20″
8461″
156″
20″
8305″
156″
20″
8149″
156″
20″
7993″
156″
20″
7837″
156″
20″
7681″
156″
20″
7525″
156″
20″
7369″
156″
20″
7213″
156″
20″
7057″
174″
38″
6883″
312″
38″
6571″

Elements assumed elastic in shakedown analysis

7	600	1123	1633
56	601	1124	1634
57	655	1173	1683
69	656	1174	1684
131	657	1175	1685
132	711	1224	1734
133	712	1225	1735
143	713	1226	1736
196	767	1275	1785
197	768	1276	1786
198	769	1277	1787
252	823	1326	1836
253	824	1327	1837
254	825	1328	1838
319	879	1377	1887
320	880	1378	1888
321	881	1379	1889
375	935	1428	1937
376	936	1429	1938
377	937	1430	1944
431	978	1479	1946
432	979	1480	1982
433	980	1481	1983
487	1021	1530	1989
488	1022	1531	1991
489	1023	1532	2027
543	1064	1581	
544	1065	1582	
545	1066	1583	
599	1122	1632	

Wind speed transformation scheme

In converting the 3-s gust basic wind speed $\bar{v}_3$ at 33-ft height to the mean hourly wind speed $\bar{v}_{3600}$ at 2000-ft reference height, this work adopts the following transformation scheme:

$$\bar{v}_{3600} = \left(\frac{600}{10}\right)^{0.14} \left(\frac{\bar{v}_3}{1.525}\right) \mathrm{K}_R \mathrm{K}_D \tag{A.1}$$

where $\bar{v}_{3600}$ and $\bar{v}_3$ are in mph while the reduction factor K_R and the directionality factor K_D are provided in Table A.1.

Table A.1: Values of $\bar{v}_w$, K_R, and K_D for different wind directions.

$\alpha(^\circ)$	$\bar{v}_{ws}$(ft/s)	$\mathrm{K_R}$	$\mathrm{K_D}$	$\alpha(^\circ)$	$\bar{v}_{ws}$(ft/s)	$\mathrm{K_R}$	$\mathrm{K_D}$
10	20.2	0.976	0.78	190	20.5	0.992	1.00
20	20.3	0.986	0.69	200	20.4	1.015	1.00
30	20.3	0.986	0.69	210	20.0	0.986	0.99
40	20.2	0.984	0.65	220	20.0	0.986	0.97
50	20.2	0.995	0.70	230	20.0	0.986	0.97
60	20.2	0.995	0.76	240	19.9	0.986	0.97
70	20.3	0.985	0.80	250	19.9	0.989	0.97
80	20.5	0.985	0.81	260	20.4	0.989	0.94
90	20.6	0.999	0.82	270	20.3	0.989	0.87
100	21.0	0.999	0.82	280	20.3	0.989	0.80
110	20.9	0.985	0.82	290	20.3	0.989	0.72
120	20.7	0.995	0.82	300	20.0	0.955	0.69
130	20.4	0.995	0.82	310	19.8	1.006	0.74
140	20.3	1.001	0.88	320	19.8	1.006	0.77
150	20.2	0.988	0.96	330	20.1	1.006	0.78
160	20.2	0.988	1.00	340	20.2	1.006	0.78
170	20.2	0.981	1.00	350	20.0	0.976	0.78
180	20.4	0.992	1.00	360	20.1	0.970	0.78

Inelastic elements for a representative sample

Wind load of 300 MRI

MRI	300
$\tilde{v}_3$ (*mph*)	91

Coupling beams

Direction												
10		20		30			40					
51	772	4	597	1929	10	883	1639	51	540	1077		
52	939	51	604	2012	52	939	1690	52	541	1116		
53	1014	52	660	2058	128	982	1741	53	548	1129		
128	1019	53	716	2067	140	1014	1792	128	554	1133		
129	1025	128	772	2071	193	1019	1800	129	604	1137		
193	1057	129	820		194	1025	1929	193	610	1164		
194	1062	193	876		201	1057	1994	194	660	1180		
249	1072	194	933		250	1062	2012	201	666	1184		
250	1244	249	939		262	1072	2058	212	716	1231		
316	1295	250	976		317	1077	2067	249	721	1235		
317	1346	262	982		324	1116	2218	250	722	1282		
372	1397	316	1014		373	1129	2227	262	772	1333		
373	1929	317	1019		380	1133		316	778	1384		
428	2012	324	1025		429	1137		317	820	1435		
429	2067	372	1057		436	1164		324	828	1486		
484		373	1062		485	1180		372	876	1537		
485		380	1072		492	1184		373	933	1588		
492		428	1116		540	1231		380	939	1639		
540		429	1120		541	1235		428	976	1800		
541		436	1129		548	1282		429	982	1929		
548		484	1171		604	1333		436	1014	1994		
597		485	1180		660	1384		442	1019	2003		
604		492	1231		716	1435		484	1025	2012		
653		540	1282		722	1486		485	1057	2058		
660		541	1333		772	1537		492	1062	2067		
716		548	1800		828	1588		498	1072			

Direction													
50				60		70		80					
15	436	939	1397	15	541	128	1994	10	386	778	1077	1619	
16	441	982	1435	16	548	373	2012	15	429	820	1116	1639	
51	442	987	1448	51	554	380	2058	16	436	827	1129	1670	
52	485	1014	1486	52	604	429	2067	52	441	828	1133	1690	
73	492	1019	1499	74	609	436		64	442	833	1137	1741	
74	497	1025	1537	75	610	485		73	485	844	1164	1792	
75	498	1030	1550	90	660	492		75	492	865	1180	1800	
128	540	1057	1588	128	666	548		90	497	870	1184	1843	
147	541	1062	1601	147	716	604		128	498	876	1193	1929	
193	548	1072	1759	194	722	660		140	548	883	1231	1994	
194	553	1077	1800	206	778	716		147	553	900	1235	2003	
206	554	1129	1929	212	923	772		194	554	923	1244	2012	
207	604	1133	1958	250	1025	939		201	604	928	1282	2029	
250	609	1137	1994	267	1077	982		206	609	933	1286	2053	
262	610	1142	2003	268	1193	1014		207	610	939	1295	2058	
267	660	1180	2012	317	1244	1019		212	641	944	1333	2067	
268	665	1184	2058	329	1295	1025		250	660	971	1337	2073	
317	666	1193	2067	330	1346	1057		262	665	982	1346	2093	
324	716	1231		373	1397	1062		267	666	987	1384	2113	
329	721	1235		385	1448	1072		268	715	1014	1388	2218	
330	722	1244		386	1499	1077		324	716	1019	1435	2227	
373	772	1282		429	1550	1129		329	721	1025	1486	2238	
380	778	1295		442	2012	1180		330	722	1030	1517	2247	
385	828	1333		485		1231		373	771	1057	1537	2318	
386	865	1346		492		1800		380	772	1062	1568	2327	
429	923	1384		498		1929		385	777	1072	1588	2347	

Direction											
90			100					110			
16	828	1435	10	497	939	1346	1874	15	553	1129	1929
140	833	1486	15	498	944	1384	1885	16	554	1133	1958
201	865	1537	16	548	982	1388	1929	73	604	1142	1994
262	883	1588	73	553	987	1397	1958	74	609	1180	2003
268	923	1639	74	554	1014	1435	1974	75	610	1184	2058
324	939	1690	75	604	1025	1439	1994	90	660	1193	2067
330	982	1741	90	609	1030	1448	2003	147	665	1231	
380	987	1800	140	610	1057	1486	2012	206	666	1235	
386	1014	1929	147	641	1072	1499	2029	207	716	1244	
436	1025	1994	201	660	1077	1517	2053	212	721	1282	
442	1030	2003	206	665	1129	1537	2055	262	722	1286	
492	1057	2012	207	666	1133	1550	2058	267	772	1295	
498	1072	2058	212	716	1137	1568	2067	268	777	1333	
548	1077	2067	262	721	1142	1588	2075	324	778	1346	
554	1129	2218	267	722	1164	1601	2093	329	833	1384	
604	1133		268	771	1180	1619	2095	330	865	1397	
609	1137		324	772	1184	1639	2113	380	923	1435	
610	1164		329	777	1193	1652	2115	385	939	1448	
660	1180		330	778	1231	1670	2135	386	944	1486	
665	1184		380	809	1235	1690	2155	436	982	1499	
666	1231		385	828	1244	1721	2218	441	987	1517	
716	1235		386	833	1282	1741	2227	442	1014	1550	
721	1282		436	865	1286	1759	2238	492	1025	1568	
722	1286		441	883	1295	1783	2247	497	1030	1601	
772	1333		442	923	1333	1792	2318	498	1072	1652	
778	1384		492	928	1337	1800		548	1077	1800	

Direction												
120			130		140	150	160	170	180	190	200	210
15	660	1235	15	1129	182	90	90	90	90	90	90	90
16	665	1244	16	1133	212	182	182	182	182	182	182	182
73	666	1282	74	1193	1800	212	212	212	212	212	212	212
74	716	1286	90	1244	1929	1800	1800	273	273	273	1800	305
75	721	1295	147	1295	2012	1929	1929	722	610	722	1929	900
90	722	1333	206	1346		1994	1994	1800	666	778	1953	1677
147	772	1346	212	1397		2012	1998	1929	722	1800	1974	1728
206	777	1397	267	1448			2012	1994	778	1929	1994	1800
207	778	1448	268	1499			2016	1998	1193	1974	1998	1881
212	833	1499	330	1929				2012	1244	1994	2012	1929
267	865	1517	386	1994				2016	1295	1998	2016	1953
268	923	1550	442	2003					1346	2012	2058	1974
329	939	1568	498	2012					1397	2016	2067	1994
330	944	1601	548	2067					1448			1998
385	982	1619	554						1800			2012
386	987	1652	604						1929			2016
441	1025	1703	610						1994			2058
442	1030	1759	660						1998			2067
492	1072	1800	666						2012			
497	1077	1929	716						2016			
498	1129	1958	722									
548	1133	1994	778									
553	1142	2003	923									
554	1180	2012	939									
604	1184	2058	1025									
609	1193	2067	1072									
610	1231	2075	1077									

Direction									
220		230	240		250		260		
90	1974	90	90	1998	90	1800	1	1371	1994
156	1994	156	156	2003	156	1881	156	1397	1998
182	1998	182	182	2012	182	1929	182	1422	2003
212	2012	212	212	2016	212	1953	212	1448	2012
238	2016	273	273	2058	238	1958	238	1473	2016
305	2067	1320	1193	2067	273	1974	305	1499	2026
1142		1371	1244		305	1994	361	1517	2028
1193		1422	1295		844	1998	417	1524	2050
1244		1473	1320		870	2003	473	1550	2052
1295		1524	1346		900	2012	641	1568	2058
1320		1575	1371		928	2016	788	1575	2067
1346		1626	1397		1193	2058	814	1601	2070
1371		1677	1422		1244	2067	844	1619	2072
1397		1728	1448		1295		865	1626	2090
1422		1800	1473		1320		870	1652	2092
1448		1929	1499		1346		900	1670	2110
1473		1974	1524		1371		923	1677	2112
1499		1994	1550		1397		928	1703	2130
1524		1998	1575		1422		934	1728	2150
1550		2012	1626		1448		977	1754	2218
1575		2016	1677		1473		1014	1800	2227
1601		2067	1728		1499		1020	1881	2238
1626			1800		1524		1142	1929	
1677			1929		1575		1193	1953	
1728			1958		1626		1244	1958	
1800			1974		1677		1295	1971	
1929			1994		1728		1346	1974	

Direction											
270				280			290		300		310
1	870	1601	2050	1	934	1929	1	1652	182	1994	182
48	878	1619	2052	48	974	1953	182	1670	238	1998	373
49	900	1626	2058	49	977	1958	190	1703	305	2003	1244
51	923	1652	2067	51	1014	1974	238	1754	361	2016	1295
126	928	1670	2070	126	1020	1988	305	1800	865	2067	1346
156	931	1677	2072	182	1049	1994	361	1881	923	2070	1800
182	934	1703	2090	190	1090	1998	641	1929	928	2090	1929
190	971	1721	2092	238	1142	2003	844	1953	1142	2110	1974
212	974	1728	2110	246	1193	2012	865	1958	1193		1994
238	977	1754	2112	305	1244	2016	870	1974	1244		1998
246	1014	1800	2130	313	1295	2026	900	1994	1295		2012
305	1020	1881	2150	361	1346	2050	923	1998	1346		2016
313	1049	1929	2170	369	1397	2052	928	2003	1397		
361	1063	1953	2218	417	1448	2058	1090	2012	1448		
369	1090	1958	2227	425	1499	2067	1142	2016	1499		
417	1121	1971	2238	473	1517	2070	1193	2050	1517		
425	1142	1974	2247	641	1550	2090	1244	2058	1550		
473	1193	1977	2318	788	1568	2092	1295	2067	1568		
529	1244	1988		809	1601	2110	1346	2070	1601		
641	1295	1994		814	1619	2112	1397	2090	1619		
732	1346	1998		844	1652	2130	1448	2110	1652		
758	1397	2003		865	1670	2150	1499	2150	1703		
788	1448	2012		870	1703	2218	1517		1754		
809	1499	2016		900	1721	2227	1550		1800		
814	1517	2022		923	1754	2238	1568		1929		
844	1550	2026		928	1800		1601		1958		
865	1568	2028		931	1881		1619		1974		

Direction					
320	330	340	350	360	
182	182	182	182	51	1397
1800	1800	1800	1800	52	1448
1929	1929	1929	1929	53	1499
1974	1974	1974	1974	128	1550
1994	1994	1994	1994	129	1929
2016	2016	2016	2003	193	1974
			2016	194	1994
				249	2003
				250	2012
				316	
				317	
				372	
				373	
				428	
				429	
				484	
				485	
				540	
				541	
				597	
				653	
				1019	
				1062	
				1193	
				1244	
				1295	
				1346	

Wind load of 700 MRI

MRI	700
$\vec{v}_3$ (*mph*)	96

Coupling beams

Direction												
10			20			30			40			
4	604	1397	51	1929	10	660	1282	10	554	1077		
51	653	1435	52	2012	52	666	1333	16	604	1116		
52	660	1448	128	2058	64	716	1384	52	609	1129		
53	716	1486	193	2067	128	721	1435	128	610	1133		
128	772	1499	194		140	722	1486	140	660	1137		
129	828	1537	250		193	772	1537	193	665	1164		
193	933	1550	317		194	778	1588	194	666	1180		
194	939	1588	373		201	828	1639	201	716	1184		
249	976	1800	429		250	883	1690	250	721	1231		
250	982	1929	485		262	900	1741	262	722	1235		
262	1014	2012	492		317	939	1792	268	772	1282		
316	1019	2058	540		324	982	1800	317	778	1286		
317	1025	2067	541		373	1014	1929	324	820	1333		
324	1057		548		380	1019	1994	330	828	1384		
372	1062		604		429	1025	2003	373	865	1435		
373	1072		660		436	1057	2012	380	876	1486		
380	1116		716		442	1062	2058	386	923	1537		
428	1129		772		484	1072	2067	429	939	1588		
429	1180		939		485	1077	2218	436	982	1639		
436	1193		982		492	1116	2227	442	987	1690		
484	1231		1019		498	1129		484	1014	1800		
485	1244		1025		540	1133		485	1019	1929		
492	1282		1057		541	1137		492	1025	1994		
540	1295		1062		548	1164		498	1030	2003		
541	1333		1072		554	1180		540	1057	2012		
548	1346		1129		604	1184		541	1062	2058		
597	1384		1800		610	1231		548	1072	2067		

Direction												
50		60		70				80				
15	722	52	1346	15	386	833	1295	10	484	900	1333	
16	772	90	1397	16	429	865	1333	15	485	923	1384	
128	778	128	1929	51	436	923	1346	16	492	933	1435	
147	923	194	1994	52	441	939	1384	52	498	939	1486	
206	939	212	2012	73	442	982	1397	64	540	976	1537	
262	982	373		75	485	987	1435	128	541	982	1588	
268	1014	429		90	492	1014	1486	129	548	987	1639	
324	1025	442		128	497	1019	1517	140	554	1014	1690	
330	1057	485		140	498	1025	1537	193	604	1019	1741	
373	1072	492		147	540	1030	1568	194	609	1025	1792	
380	1077	498		193	541	1057	1588	201	610	1057	1800	
386	1129	548		194	548	1062	1639	206	641	1062	1929	
429	1133	554		201	553	1072	1690	250	660	1072	1994	
436	1180	604		206	554	1077	1800	262	665	1077	2003	
442	1231	610		207	604	1116	1929	268	666	1116	2012	
492	1282	660		212	609	1129	1994	316	716	1129	2053	
498	1333	666		250	610	1133	2003	317	721	1133	2058	
548	1384	716		262	660	1137	2012	324	722	1137	2067	
554	1800	722		267	665	1164	2058	330	764	1164	2093	
604	1929	778		268	666	1180	2067	372	771	1171	2218	
609	1994	939		317	716	1184		373	772	1180	2227	
610	2003	1019		324	721	1193		380	778	1184		
660	2012	1025		329	722	1231		386	820	1222		
665	2058	1072		330	772	1235		428	828	1231		
666	2067	1077		373	777	1244		429	865	1235		
716		1244		380	778	1282		436	876	1273		
721		1295		385	828	1286		442	883	1282		

Direction									
90				100					
15	553	1057	1568	10	497	900	1295	1800	2338
16	554	1072	1588	15	498	923	1333	1843	2347
73	604	1077	1619	16	548	928	1337	1874	2367
74	609	1129	1639	64	553	939	1346	1885	
75	610	1133	1670	73	554	944	1384	1929	
90	660	1137	1690	74	604	971	1388	1958	
140	665	1164	1800	75	609	982	1397	1974	
147	666	1180	1929	90	610	987	1435	1994	
201	716	1184	1958	140	641	1014	1439	2003	
206	721	1193	1994	147	660	1025	1448	2029	
207	722	1231	2003	201	665	1030	1486	2053	
262	772	1235	2012	206	666	1057	1490	2055	
267	777	1244	2058	207	715	1072	1499	2058	
268	778	1282	2067	212	716	1077	1517	2067	
324	828	1286	2075	262	721	1129	1537	2073	
329	833	1295		267	722	1133	1550	2075	
330	865	1333		268	771	1137	1568	2093	
380	883	1337		324	772	1142	1588	2095	
385	923	1346		329	777	1164	1601	2113	
386	939	1384		330	778	1180	1619	2115	
436	944	1397		380	809	1184	1639	2155	
441	982	1435		385	827	1193	1670	2218	
442	987	1448		386	828	1231	1690	2227	
492	1014	1486		436	833	1235	1741	2238	
497	1019	1499		441	865	1244	1759	2247	
498	1025	1517		442	870	1282	1783	2318	
548	1030	1537		492	883	1286	1792	2327	

Direction												
110					120				130	140	150	160
15	548	1057	1517	2075	15	660	1235	2095	90	182	182	90
16	553	1072	1537	2093	16	665	1244	2115	212	1800	212	182
73	554	1077	1550	2095	73	666	1286		442	1929	1800	212
74	604	1129	1568	2115	74	716	1295		498	1994	1929	1800
75	609	1133	1588	2135	75	721	1346		554	2012	1994	1929
90	610	1137	1601	2155	90	722	1397		610		2012	1994
140	660	1142	1619	2218	147	772	1448		666			1998
147	665	1164	1639	2227	206	777	1499		722			2012
201	666	1180	1652		207	778	1517		778			2016
206	716	1184	1670		212	833	1550		1077			
207	721	1193	1690		267	865	1568		1133			
212	722	1231	1703		268	923	1601		1929			
262	772	1235	1741		329	939	1619		1994			
267	777	1244	1754		330	944	1652		2012			
268	778	1282	1759		385	982	1703					
324	828	1286	1800		386	987	1759					
329	833	1295	1810		441	1025	1800					
330	865	1333	1874		442	1030	1874					
380	883	1337	1885		492	1072	1929					
385	923	1346	1929		497	1077	1958					
386	939	1384	1958		498	1129	1994					
436	944	1388	1974		548	1133	2003					
441	982	1397	1994		553	1142	2012					
442	987	1435	2003		554	1180	2055					
492	1014	1448	2055		604	1184	2058					
497	1025	1486	2058		609	1193	2067					
498	1030	1499	2067		610	1231	2075					

Direction												
170	180	190	200	210	220	230	240	250		260		
90	90	90	90	90	90	90	90	90	1974	90	1473	2052
156	156	182	182	182	182	156	156	156	1994	156	1499	2058
182	182	212	212	212	212	182	182	182	1998	182	1517	2067
212	212	1800	1800	238	238	212	212	212	2003	212	1524	2070
273	273	1929	1929	305	305	238	900	238	2012	238	1550	2090
610	442	1974	1974	1800	1728	273	1677	273	2016	305	1568	2092
666	498	1994	1994	1929	1800	305	1728	305	2058	361	1575	2110
722	554	1998	1998	1974	1929	900	1800	844	2067	417	1601	2130
778	610	2012	2012	1994	1974	1320	1929	870		641	1619	2150
1244	666	2016	2016	1998	1994	1371	1953	900		788	1626	2218
1295	722			2012	1998	1422	1974	928		814	1652	
1346	778			2016	2012	1473	1994	1193		844	1670	
1800	1142			2067	2016	1524	1998	1244		865	1677	
1929	1193				2067	1575	2003	1295		870	1703	
1994	1244					1626	2012	1346		900	1728	
1998	1295					1677	2016	1397		923	1754	
2012	1346					1728	2058	1448		928	1800	
2016	1397					1800		1499		1014	1881	
	1448					1881		1550		1142	1929	
	1499					1929		1575		1193	1953	
	1550					1953		1626		1244	1958	
	1601					1974		1677		1295	1974	
	1800					1994		1728		1320	1994	
	1929					1998		1800		1346	1998	
	1994					2012		1881		1371	2003	
	1998					2016		1929		1397	2012	
	2012					2058		1953		1422	2016	
	2016					2067		1958		1448	2050	

Direction													
270				280				290				300	
1	971	1874	2238	1	923	1703	2090	1	934	1929		51	1994
48	974	1881	2318	48	928	1721	2092	48	974	1953		182	1998
49	977	1929	2338	49	931	1728	2110	49	977	1958		238	2003
126	1014	1953		51	934	1754	2112	51	1014	1974		305	2012
182	1020	1958		126	971	1800	2130	126	1049	1994		865	2016
190	1049	1971		156	974	1805	2150	182	1090	1998		923	2050
212	1090	1974		182	977	1874	2170	190	1142	2003		928	2058
238	1142	1988		190	1014	1881	2218	191	1193	2012		1142	2067
246	1193	1994		212	1020	1929	2227	238	1244	2016		1193	2070
305	1244	1998		238	1049	1953	2238	246	1295	2022		1244	2090
313	1295	2003		246	1090	1958	2318	283	1346	2026		1295	2110
361	1346	2012		305	1121	1971	2338	305	1397	2050		1346	
369	1397	2016		313	1142	1974		313	1448	2052		1397	
417	1448	2026		361	1193	1988		361	1499	2058		1448	
473	1499	2050		369	1244	1994		369	1517	2067		1499	
529	1517	2052		417	1295	1998		417	1550	2070		1517	
641	1550	2058		425	1346	2003		425	1568	2090		1550	
788	1568	2067		473	1397	2012		641	1601	2092		1568	
809	1601	2070		529	1448	2016		788	1619	2110		1601	
814	1619	2090		641	1499	2022		809	1652	2112		1619	
844	1652	2092		758	1517	2026		814	1670	2130		1652	
865	1670	2110		788	1550	2028		844	1703	2150		1703	
870	1703	2112		809	1568	2050		865	1721	2170		1754	
900	1721	2130		814	1601	2052		870	1754	2218		1800	
923	1728	2150		844	1619	2058		900	1800	2227		1929	
928	1754	2170		865	1652	2067		923	1805	2238		1953	
931	1800	2218		870	1670	2070		928	1874			1958	
934	1805	2227		900	1677	2072		931	1881			1974	

Direction					
310	320	330	340	350	360
182	182	182	182	182	51
1800	1800	1800	1800	1193	52
1929	1929	1929	1929	1244	53
1974	1974	1974	1974	1295	128
1994	1994	1994	1994	1346	129
2016	2012	2016	2016	1397	193
	2016			1448	194
				1800	249
				1929	250
				1974	317
				1994	373
				2003	429
				2016	485
					492
					541
					548
					604
					660
					1019
					1057
					1244
					1295
					1346
					1929
					1974
					1994
					2012

APPENDIX B

Element Layout: FEM Model of the Rainier Square Tower

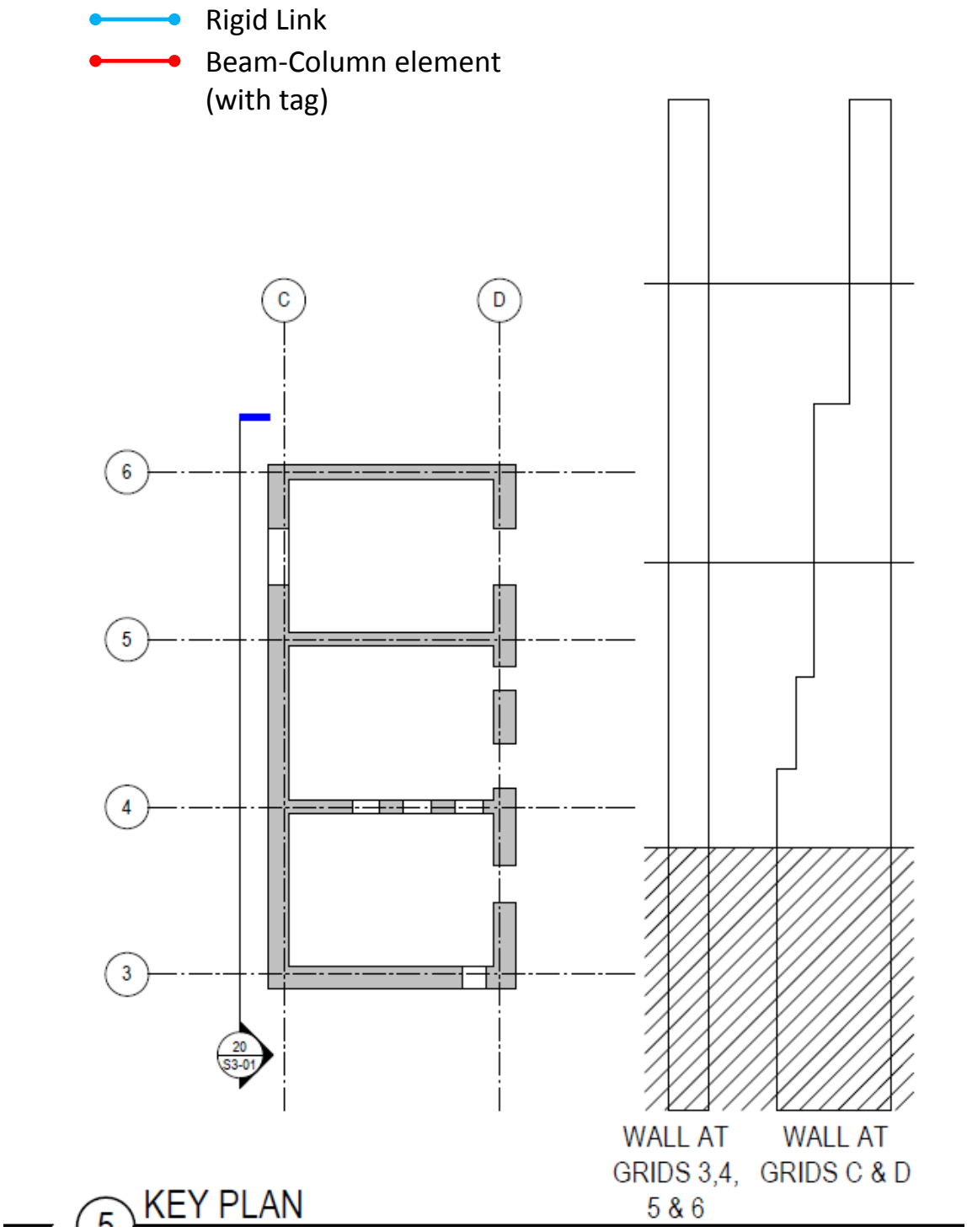
Rigid Link
Beam-Column element
(with tag)
C
D
6
5
4
3
20
S3-01
WALL AT
GRIDS 3,4,
5 & 6
WALL AT
GRIDS C & D
5
KEY PLAN

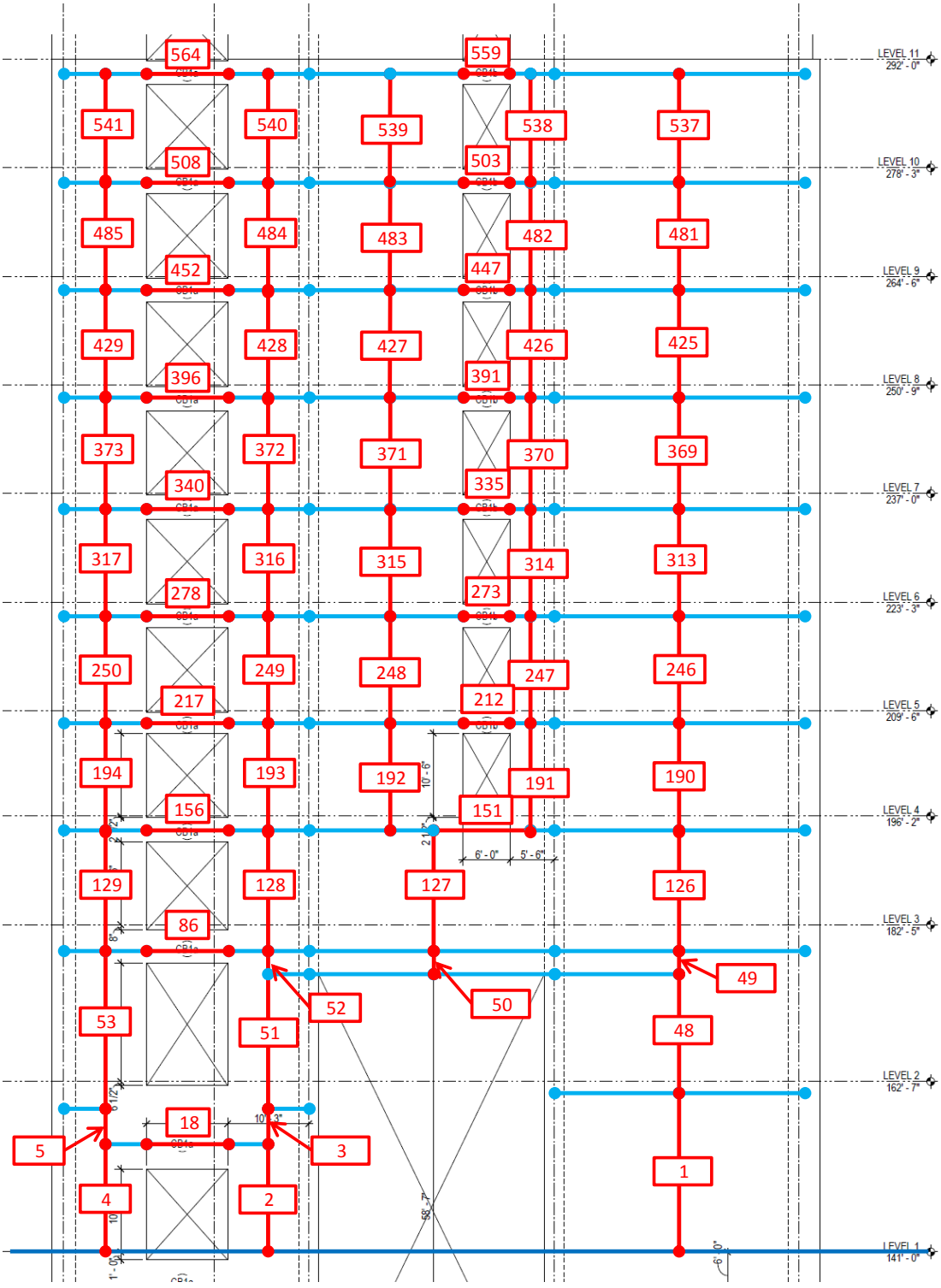
564
559
541
540
539
538
537
508
503
485
484
483
482
481
452
447
429
428
427
426
425
396
391
373
372
371
370
369
340
335
317
316
315
314
313
278
273
250
249
248
247
246
217
212
194
193
192
191
190
156
151
129
128
127
126
86
53
51
52
50
49
48
18
5
3
4
2
1
LEVEL 11
292' - 0"
LEVEL 10
278' - 3"
LEVEL 9
264' - 6"
LEVEL 8
250' - 9"
LEVEL 7
237' - 0"
LEVEL 6
223' - 3"
LEVEL 5
209' - 6"
LEVEL 4
196' - 2"
LEVEL 3
182' - 5"
LEVEL 2
162' - 7"
LEVEL 1
141' - 0"

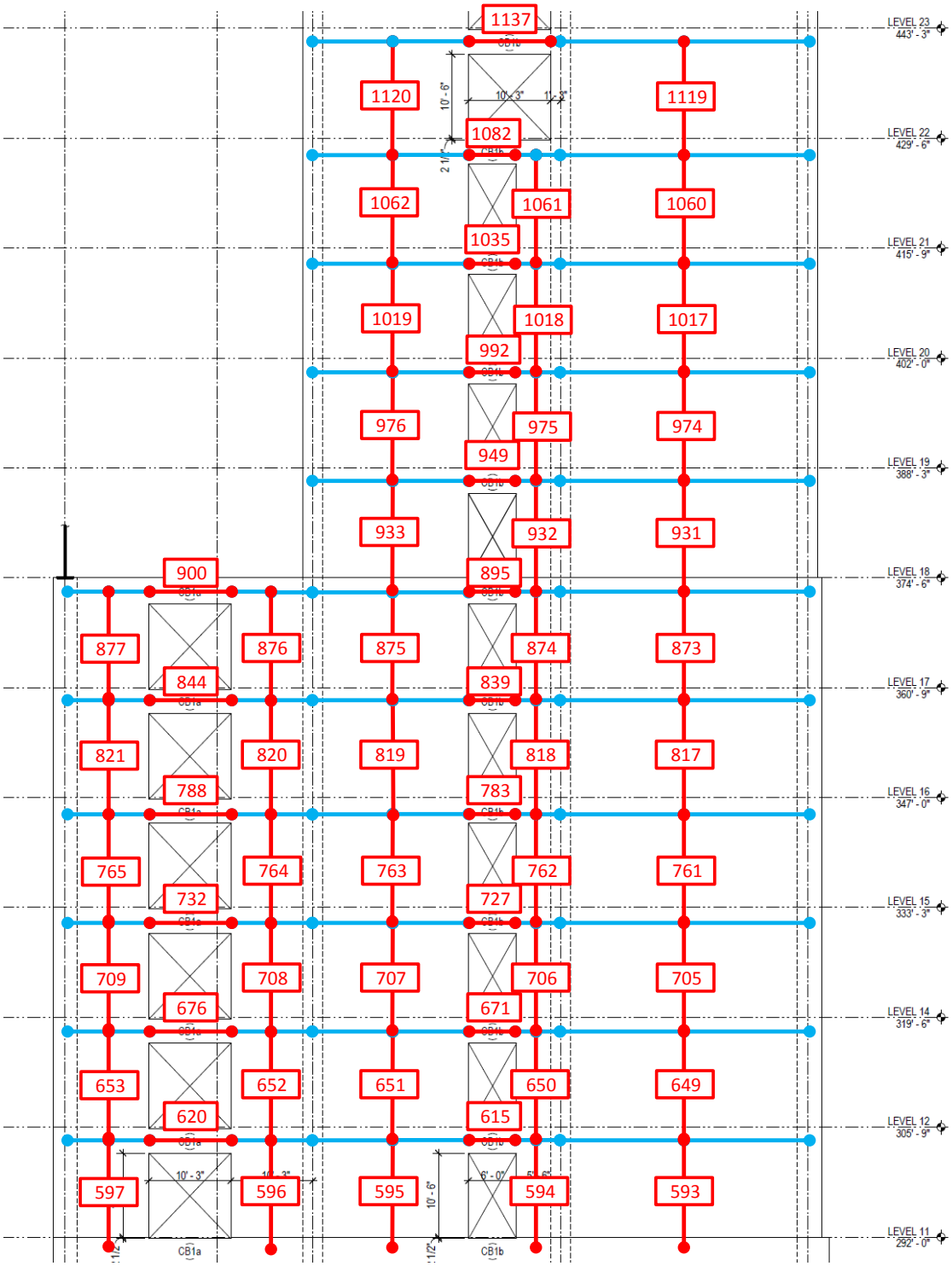
1137
1120
1119
1082
1062
1061
1060
1035
1019
1018
1017
992
976
975
974
949
933
932
931
900
895
877
876
875
874
873
844
839
821
820
819
818
817
788
783
765
764
763
762
761
732
727
709
708
707
706
705
676
671
653
652
651
650
649
620
615
597
596
595
594
593
LEVEL 23
443' - 3"
LEVEL 22
429' - 6"
LEVEL 21
415' - 9"
LEVEL 20
402' - 0"
LEVEL 19
388' - 3"
LEVEL 18
374' - 6"
LEVEL 17
360' - 9"
LEVEL 16
347' - 0"
LEVEL 15
333' - 3"
LEVEL 14
319' - 6"
LEVEL 12
305' - 9"
LEVEL 11
292' - 0"
10' - 6"
10' - 3"
6' - 0"
CB1a
CB1b

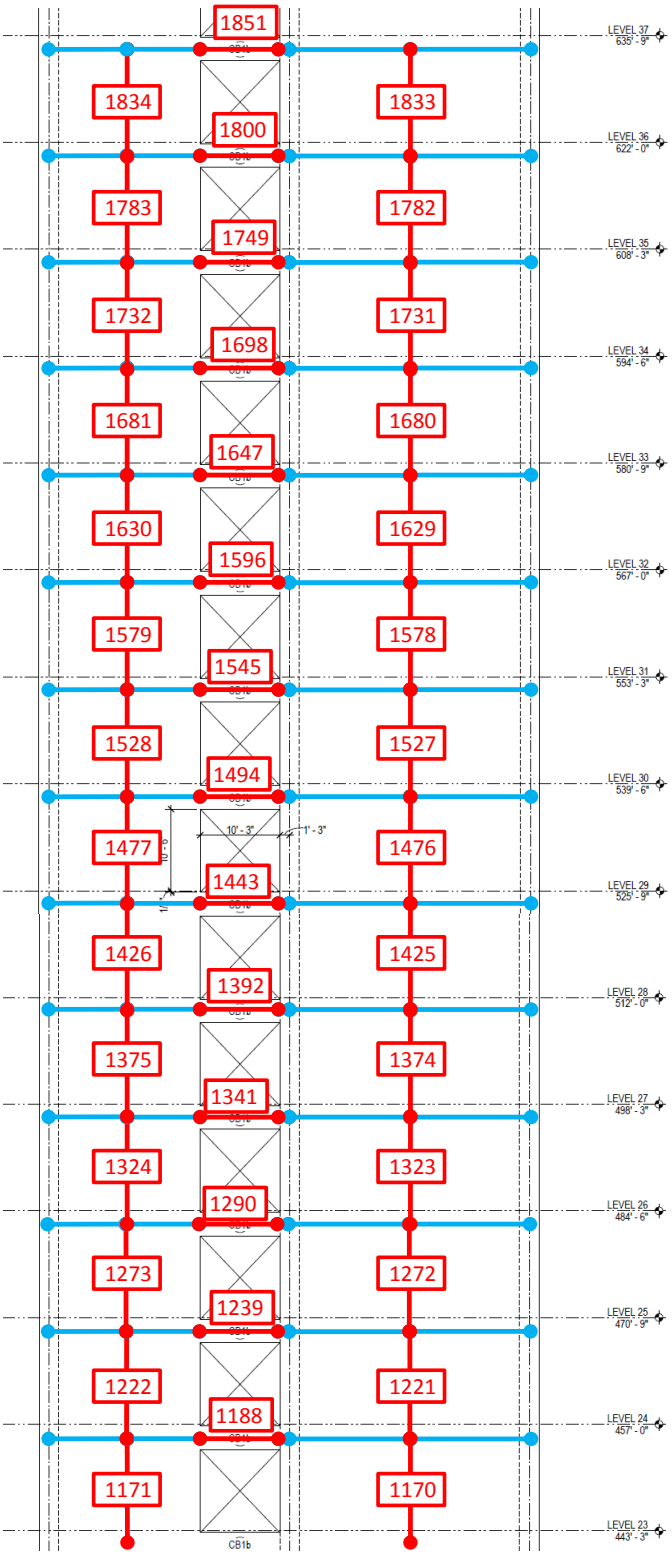
1851
1834
1833
1800
1783
1782
1749
1732
1731
1698
1681
1680
1647
1630
1629
1596
1579
1578
1545
1528
1527
1494
1477
1476
1443
1426
1425
1392
1375
1374
1341
1324
1323
1290
1273
1272
1239
1222
1221
1188
1171
1170
LEVEL 37
635' - 9"
LEVEL 36
622' - 0"
LEVEL 35
608' - 3"
LEVEL 34
594' - 6"
LEVEL 33
580' - 9"
LEVEL 32
567' - 0"
LEVEL 31
553' - 3"
LEVEL 30
539' - 6"
LEVEL 29
525' - 9"
LEVEL 28
512' - 0"
LEVEL 27
498' - 3"
LEVEL 26
484' - 6"
LEVEL 25
470' - 9"
LEVEL 24
457' - 0"
LEVEL 23
443' - 3"
10' - 3"
1' - 3"
10' - 6"
CB1b

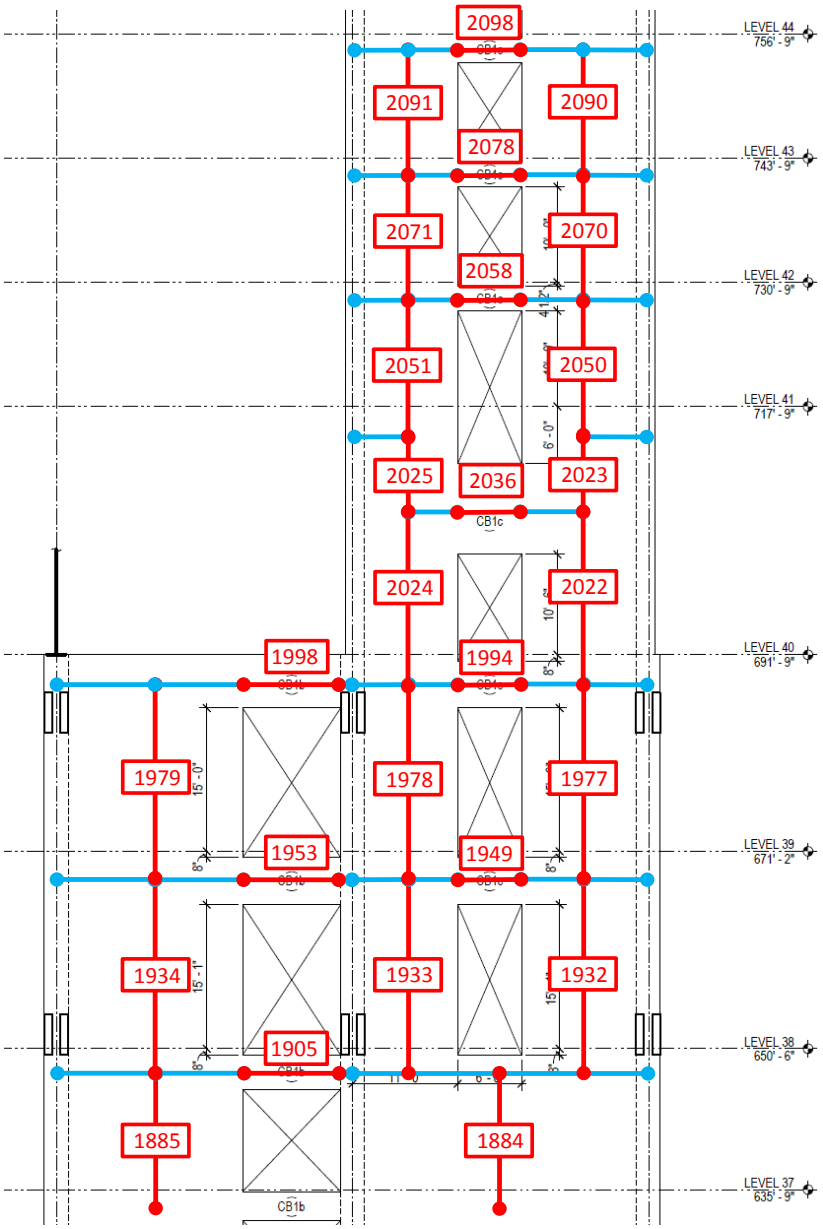
2098
2091
2090
2078
2071
2070
2058
2051
2050
2025
2036
2023
2024
2022
1998
1994
1979
1978
1977
1953
1949
1934
1933
1932
1905
1885
1884
LEVEL 44
756' - 9"
LEVEL 43
743' - 9"
LEVEL 42
730' - 9"
LEVEL 41
717' - 9"
LEVEL 40
691' - 9"
LEVEL 39
671' - 2"
LEVEL 38
650' - 6"
LEVEL 37
635' - 9"
CB1c
CB1b

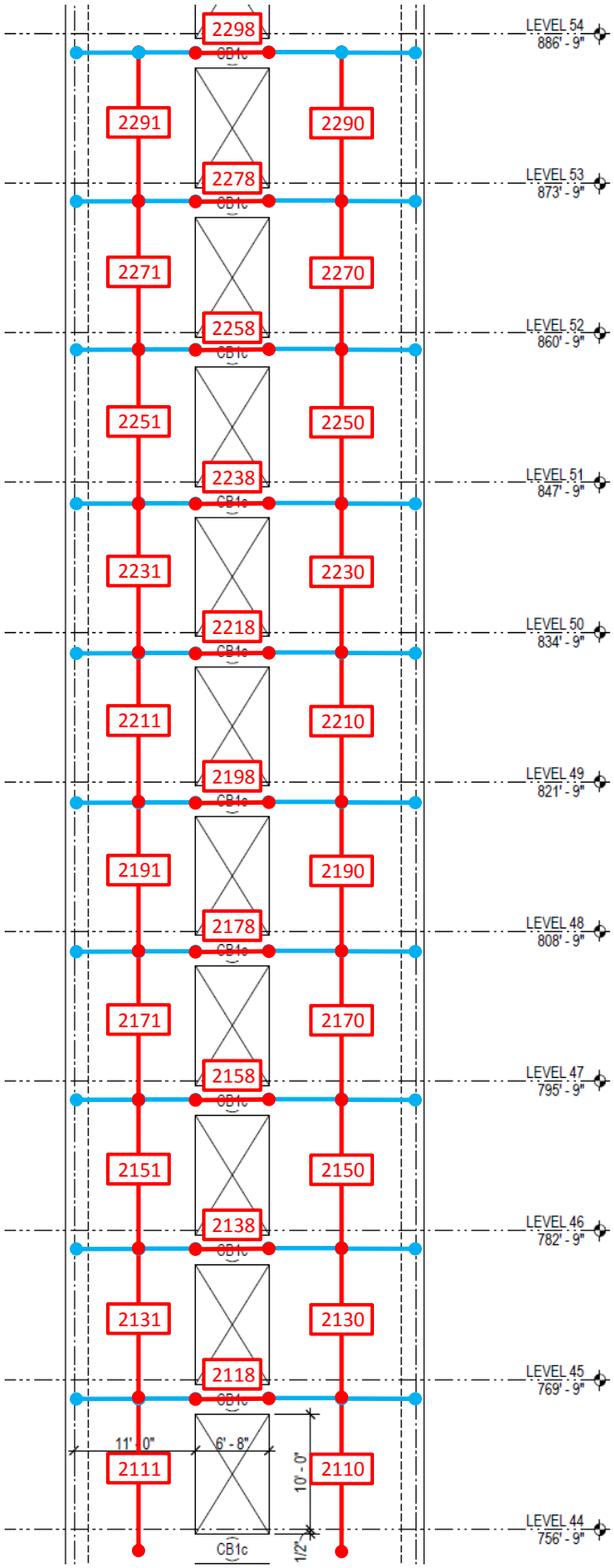
2298
CB1c
2291
2290
2278
CB1c
2271
2270
2258
CB1c
2251
2250
2238
CB1c
2231
2230
2218
CB1c
2211
2210
2198
CB1c
2191
2190
2178
CB1c
2171
2170
2158
CB1c
2151
2150
2138
CB1c
2131
2130
2118
CB1c
11' - 0"
6' - 8"
10' - 0"
2111
2110
CB1c
1/2"
LEVEL 54
886' - 9"
LEVEL 53
873' - 9"
LEVEL 52
860' - 9"
LEVEL 51
847' - 9"
LEVEL 50
834' - 9"
LEVEL 49
821' - 9"
LEVEL 48
808' - 9"
LEVEL 47
795' - 9"
LEVEL 46
782' - 9"
LEVEL 45
769' - 9"
LEVEL 44
756' - 9"

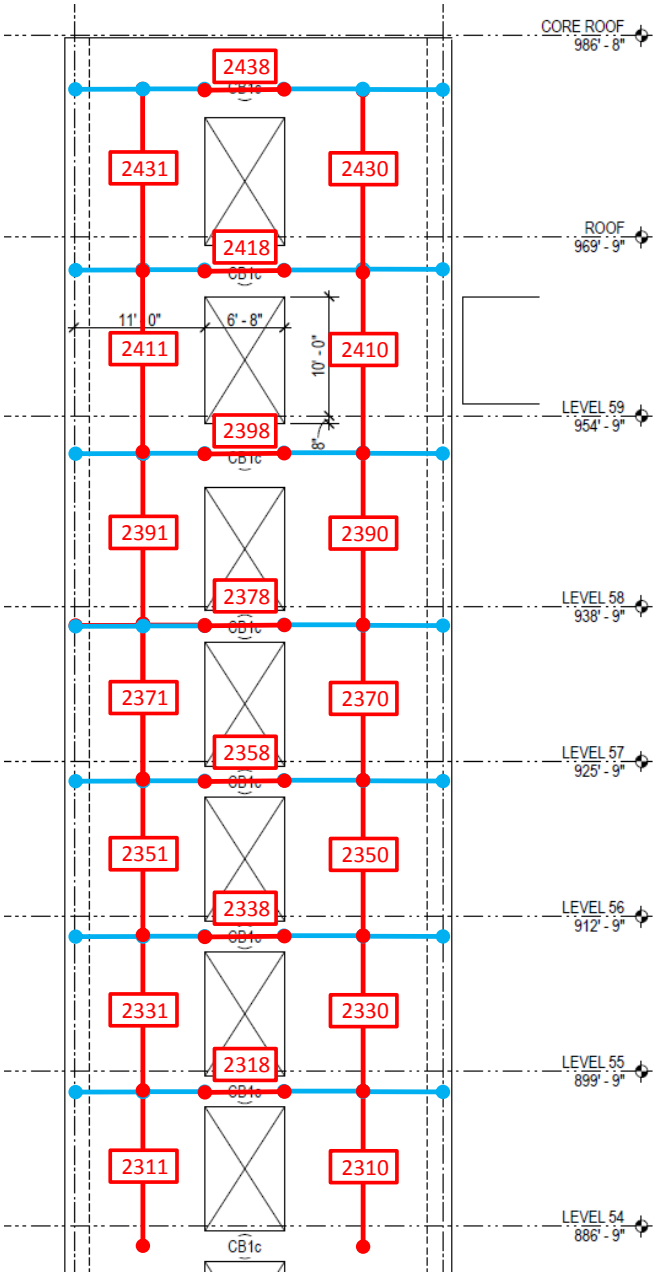
CORE ROOF
986' - 8"
ROOF
969' - 9"
LEVEL 59
954' - 9"
LEVEL 58
938' - 9"
LEVEL 57
925' - 9"
LEVEL 56
912' - 9"
LEVEL 55
899' - 9"
LEVEL 54
886' - 9"
2438
2431
2430
2418
11' - 0"
6' - 8"
10' - 0"
2411
2410
2398
8"
2391
2390
2378
2371
2370
2358
2351
2350
2338
2331
2330
2318
2311
2310
CB1c

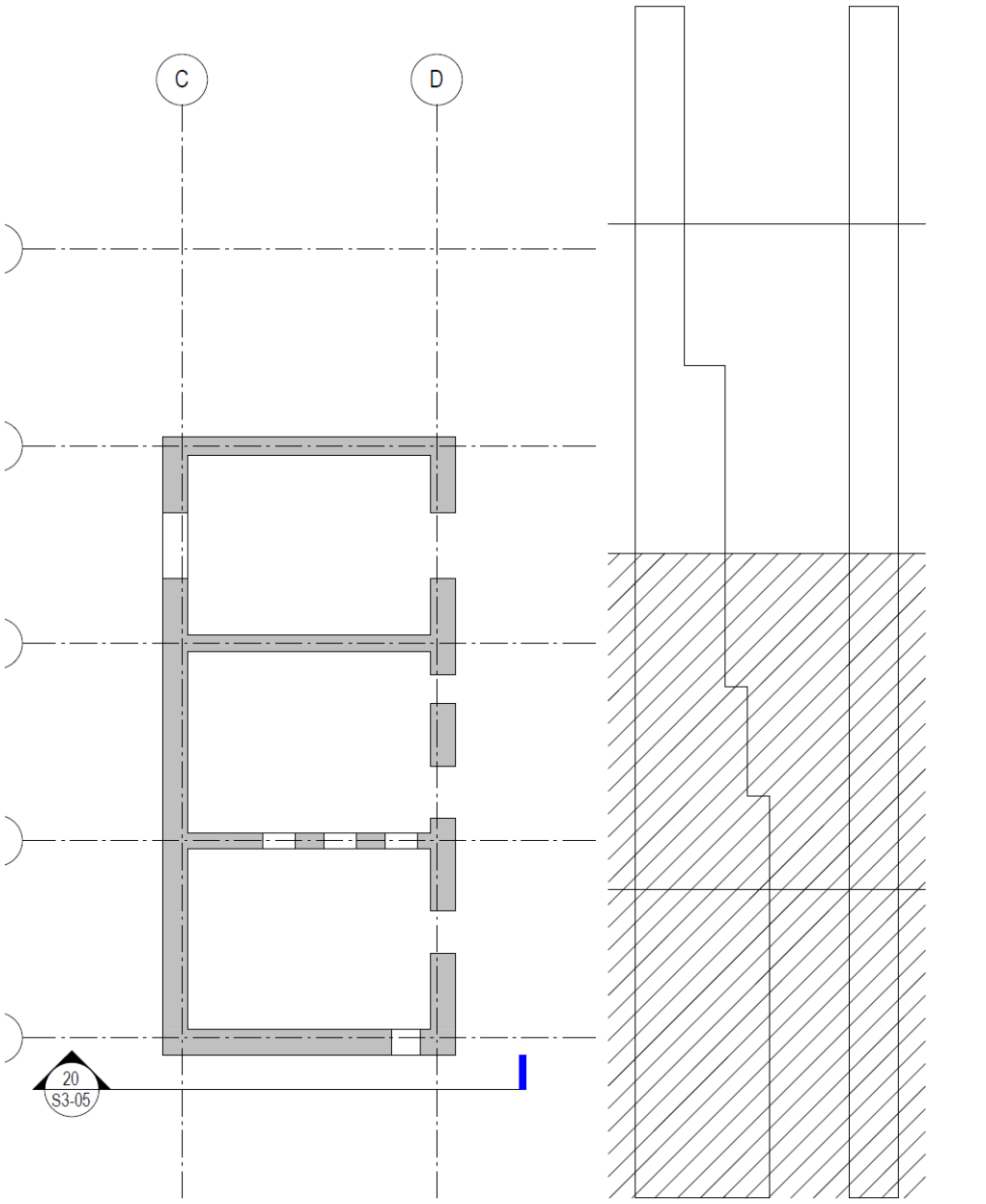

KEY PLAN

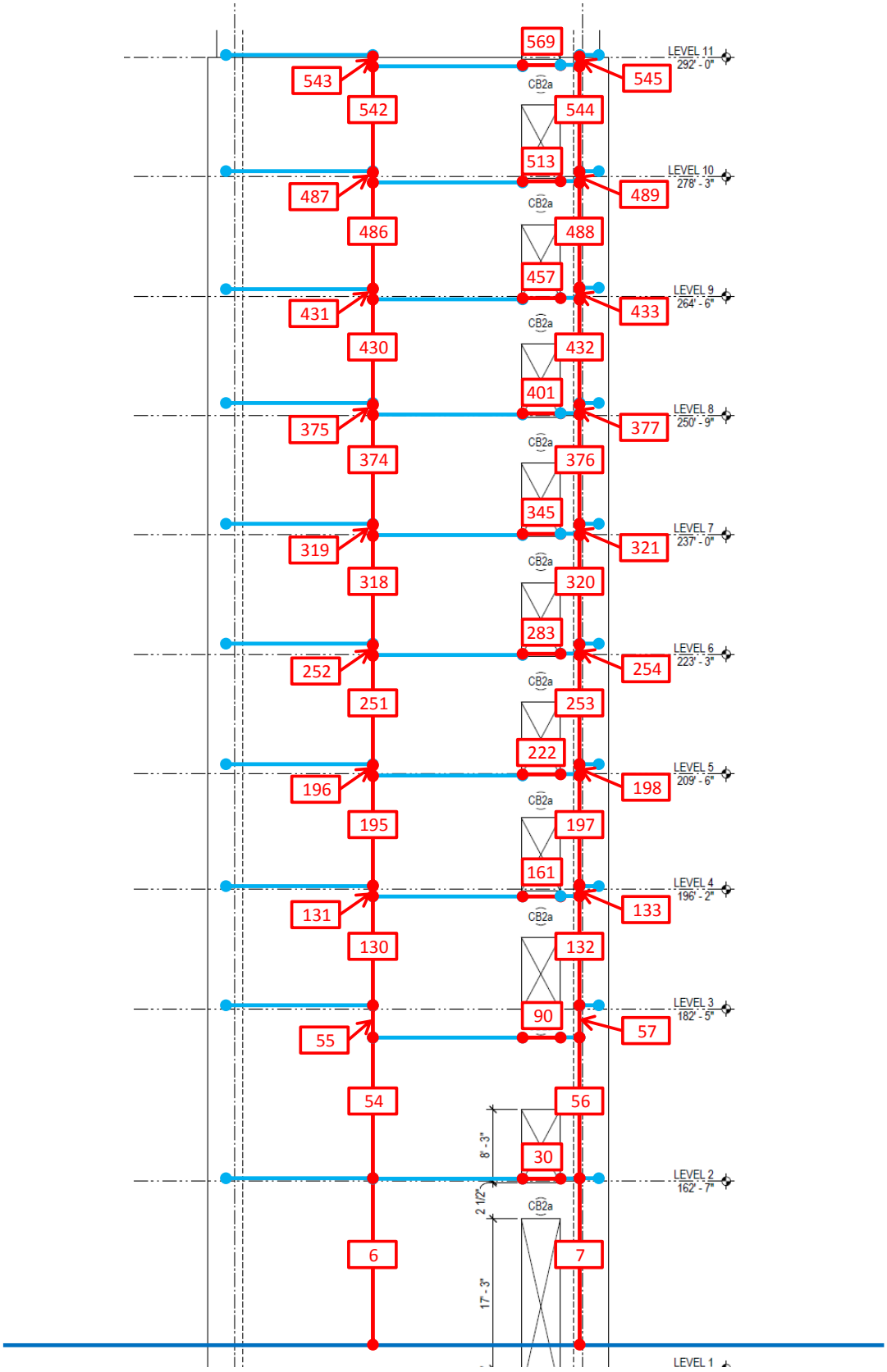
569
543
545
542
544
513
487
489
486
488
457
431
433
430
432
401
375
377
374
376
345
319
321
318
320
283
252
254
251
253
222
196
198
195
197
161
131
133
130
132
90
55
57
54
56
30
6
7
LEVEL 11
292' - 0"
LEVEL 10
278' - 3"
LEVEL 9
264' - 6"
LEVEL 8
250' - 9"
LEVEL 7
237' - 0"
LEVEL 6
223' - 3"
LEVEL 5
209' - 6"
LEVEL 4
196' - 2"
LEVEL 3
182' - 5"
LEVEL 2
162' - 7"
LEVEL 1
CB2a
8' - 3"
2 1/2"
17' - 3"

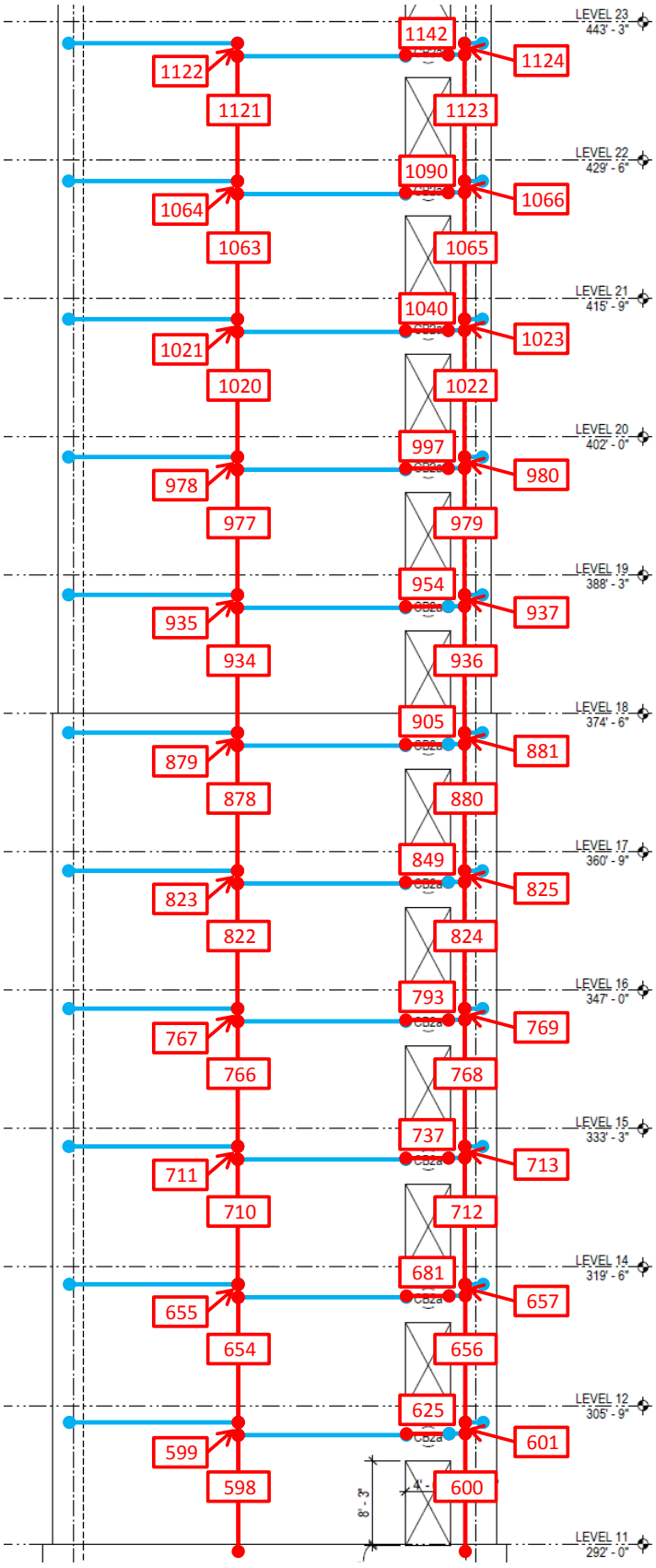
LEVEL 23
443' - 3"
LEVEL 22
429' - 6"
LEVEL 21
415' - 9"
LEVEL 20
402' - 0"
LEVEL 19
388' - 3"
LEVEL 18
374' - 6"
LEVEL 17
360' - 9"
LEVEL 16
347' - 0"
LEVEL 15
333' - 3"
LEVEL 14
319' - 6"
LEVEL 12
305' - 9"
LEVEL 11
292' - 0"
1142
1124
1122
1121
1123
1090
1066
1064
1063
1065
1040
1023
1021
1020
1022
997
980
978
977
979
954
937
935
934
936
905
881
879
878
880
849
825
823
822
824
793
769
767
766
768
737
713
711
710
712
681
657
655
654
656
625
601
599
598
600
8' - 3"
4' -

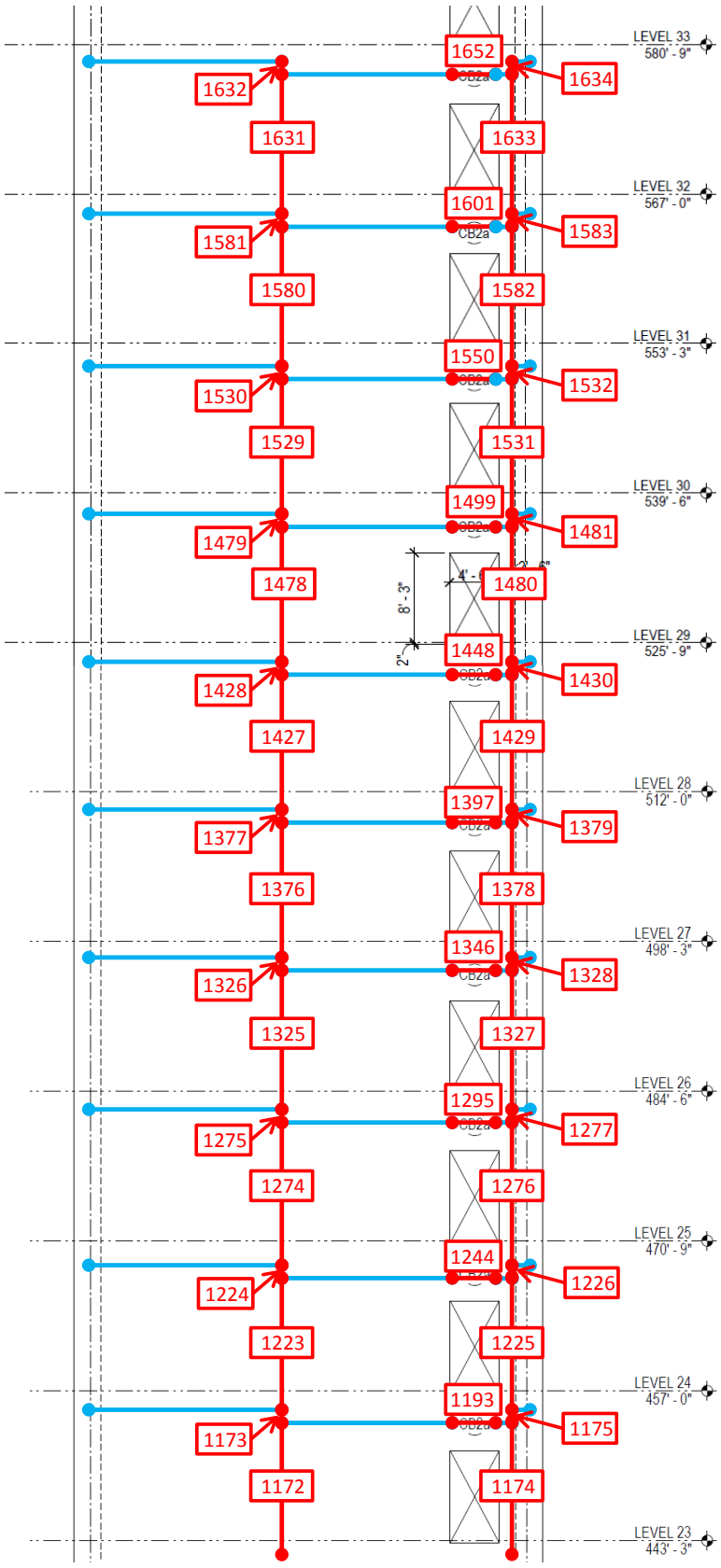
LEVEL 33
580' - 9"
LEVEL 32
567' - 0"
LEVEL 31
553' - 3"
LEVEL 30
539' - 6"
LEVEL 29
525' - 9"
LEVEL 28
512' - 0"
LEVEL 27
498' - 3"
LEVEL 26
484' - 6"
LEVEL 25
470' - 9"
LEVEL 24
457' - 0"
LEVEL 23
443' - 3"
1652
1634
1632
1631
1633
1601
1583
1581
1580
1582
1550
1532
1530
1529
1531
1499
1481
1479
1478
1480
8' - 3"
2"
1448
1430
1428
1427
1429
1397
1379
1377
1376
1378
1346
1328
1326
1325
1327
1295
1277
1275
1274
1276
1244
1226
1224
1223
1225
1193
1175
1173
1172
1174

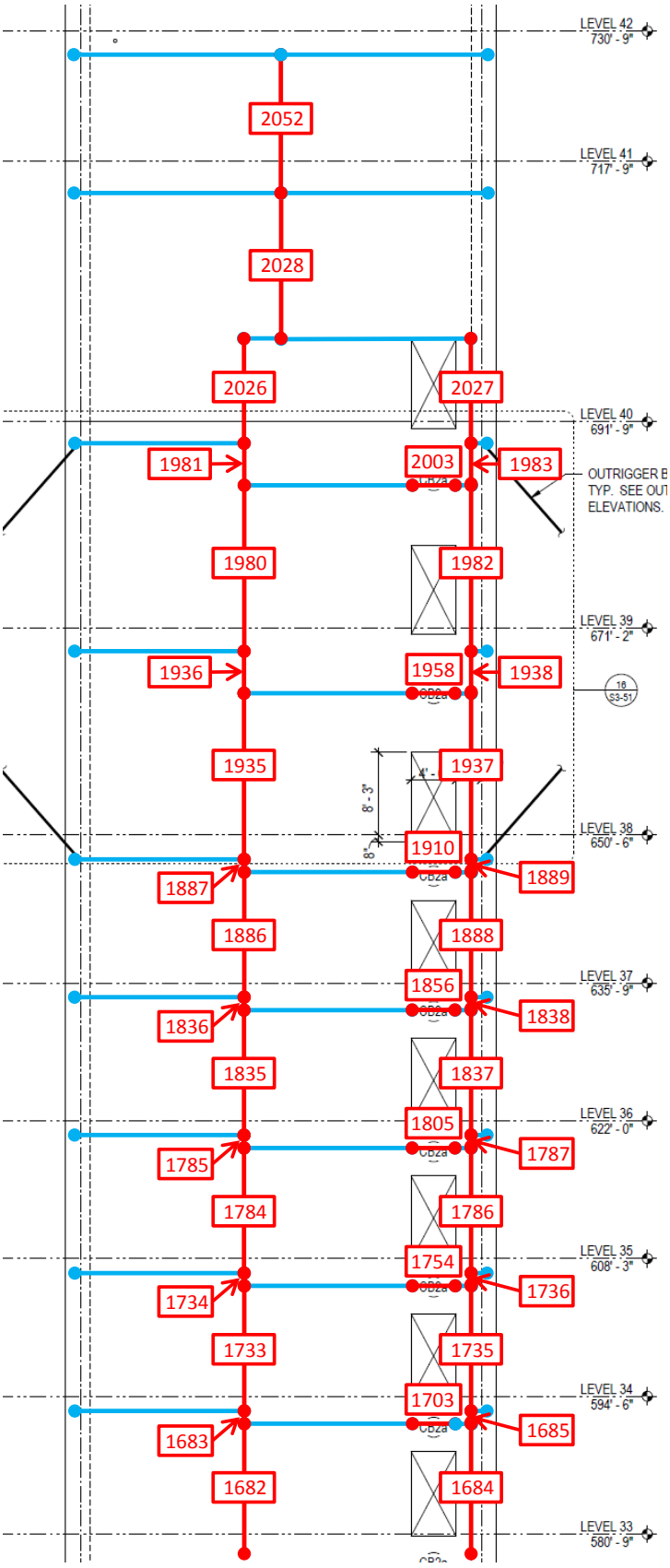
LEVEL 42
730' - 9"
2052
LEVEL 41
717' - 9"
2028
2026
2027
LEVEL 40
691' - 9"
1981
2003
1983
OUTRIGGER B
TYP. SEE OUT
ELEVATIONS.
1980
1982
LEVEL 39
671' - 2"
1936
1958
1938
16
S3-51
1935
1937
8' - 3"
4' -
8"
LEVEL 38
650' - 6"
1910
1887
1889
1886
1888
1856
LEVEL 37
635' - 9"
1836
1838
1835
1837
1805
LEVEL 36
622' - 0"
1785
1787
1784
1786
1754
LEVEL 35
608' - 3"
1734
1736
1733
1735
1703
LEVEL 34
594' - 6"
1683
1685
1682
1684
LEVEL 33
580' - 9"

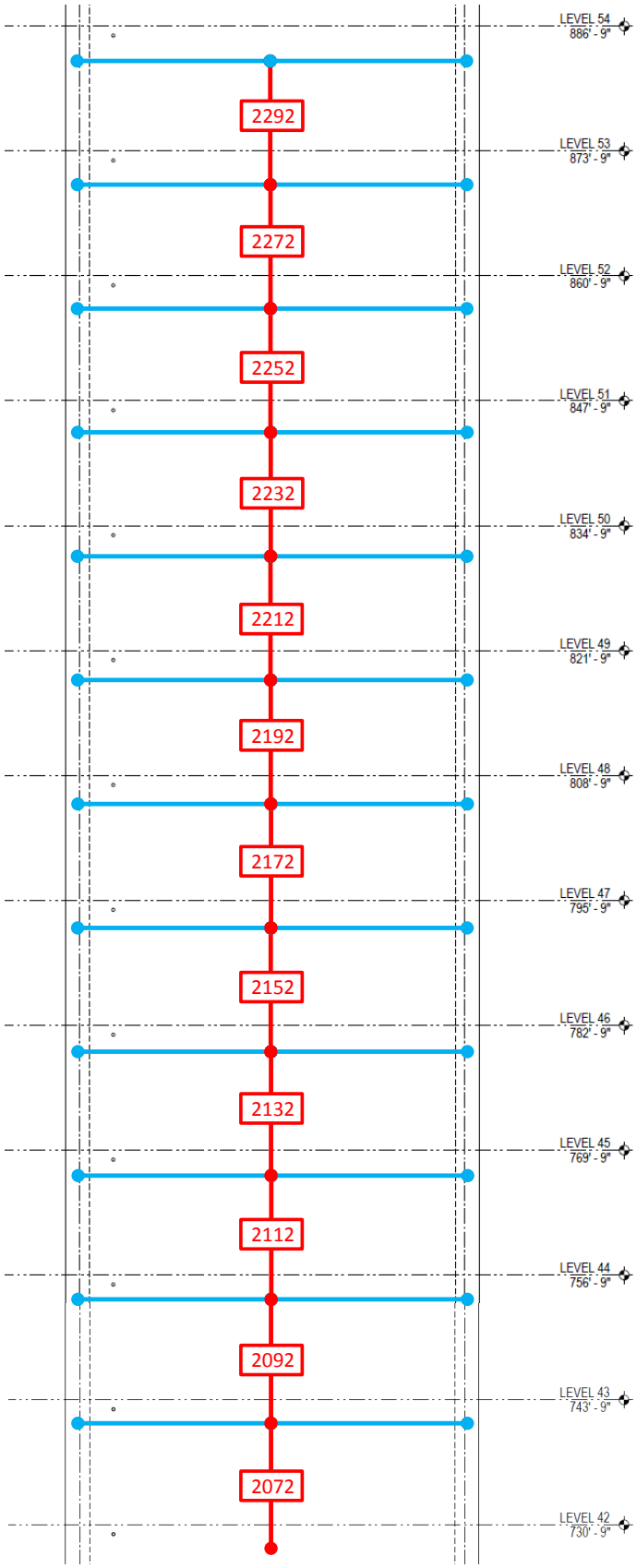
LEVEL 54
886' - 9"
2292
LEVEL 53
873' - 9"
2272
LEVEL 52
860' - 9"
2252
LEVEL 51
847' - 9"
2232
LEVEL 50
834' - 9"
2212
LEVEL 49
821' - 9"
2192
LEVEL 48
808' - 9"
2172
LEVEL 47
795' - 9"
2152
LEVEL 46
782' - 9"
2132
LEVEL 45
769' - 9"
2112
LEVEL 44
756' - 9"
2092
LEVEL 43
743' - 9"
2072
LEVEL 42
730' - 9"

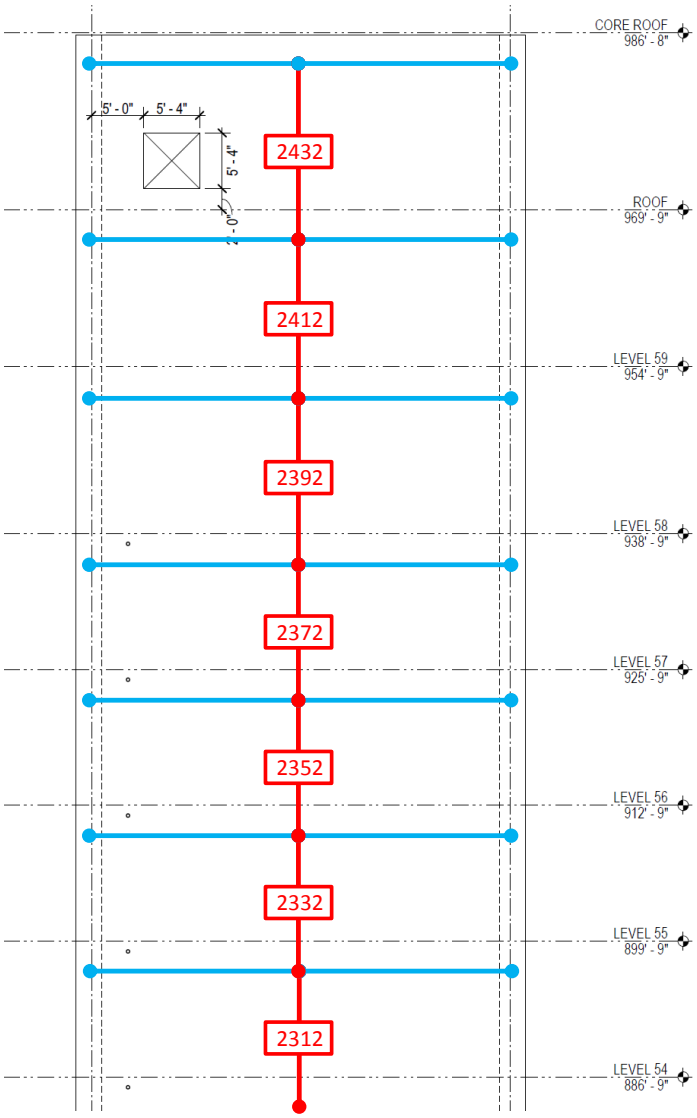
CORE ROOF
986' - 8"
5' - 0"
5' - 4"
5' - 4"
2' - 0"
2432
ROOF
969' - 9"
2412
LEVEL 59
954' - 9"
2392
LEVEL 58
938' - 9"
2372
LEVEL 57
925' - 9"
2352
LEVEL 56
912' - 9"
2332
LEVEL 55
899' - 9"
2312
LEVEL 54
886' - 9"

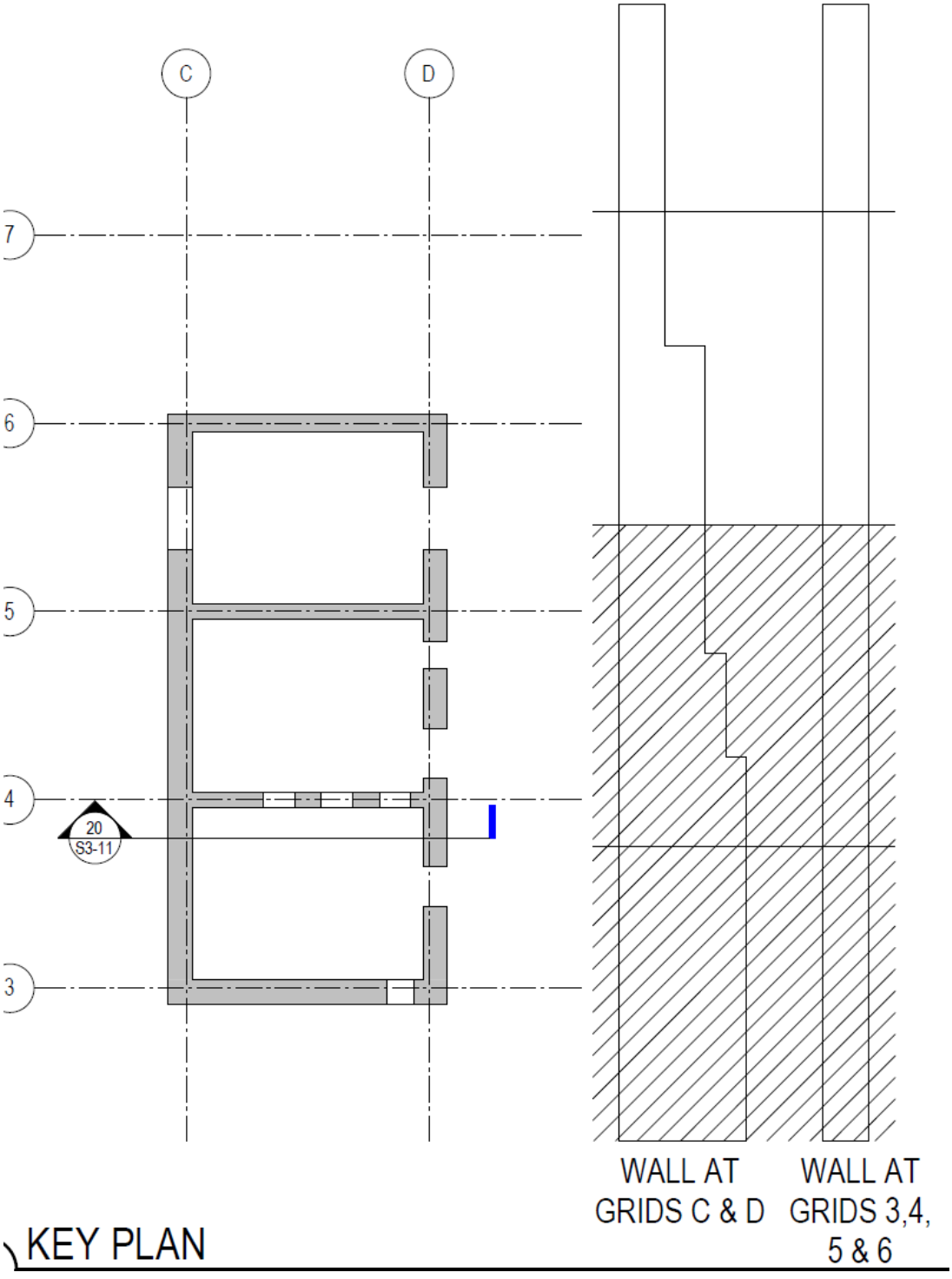

KEY PLAN

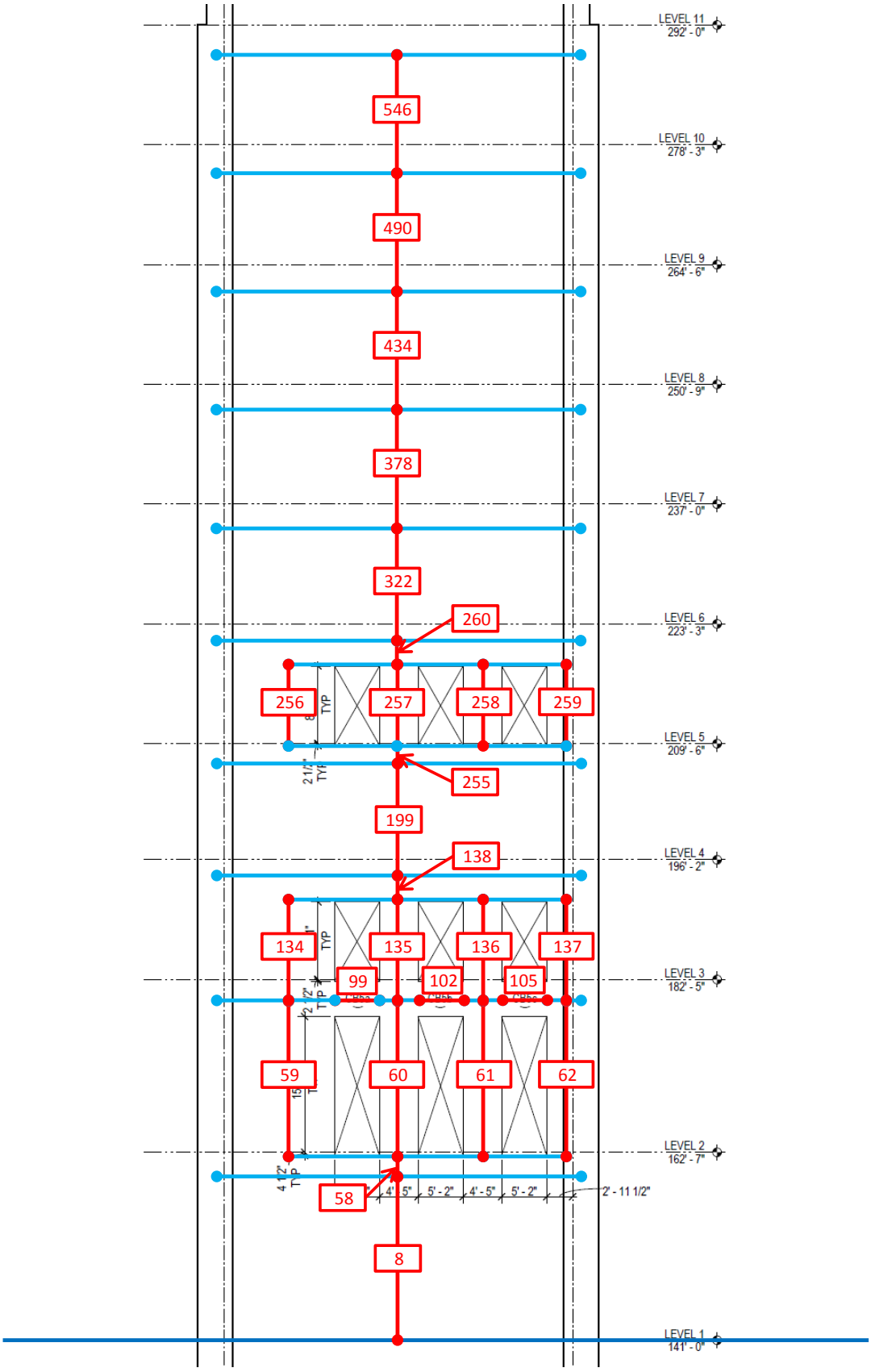
LEVEL 11
292' - 0"
546
LEVEL 10
278' - 3"
490
LEVEL 9
264' - 6"
434
LEVEL 8
250' - 9"
378
LEVEL 7
237' - 0"
322
LEVEL 6
223' - 3"
260
256
257
258
259
8" TYP.
21/2" TYP.
LEVEL 5
209' - 6"
255
199
LEVEL 4
196' - 2"
138
134
135
136
137
8" TYP.
LEVEL 3
182' - 5"
99
102
105
21/2" TYP.
59
60
61
62
15" TYP.
LEVEL 2
162' - 7"
41/2" TYP.
58
4' - 5"
5' - 2"
4' - 5"
5' - 2"
2' - 11 1/2"
8
LEVEL 1
141' - 0"

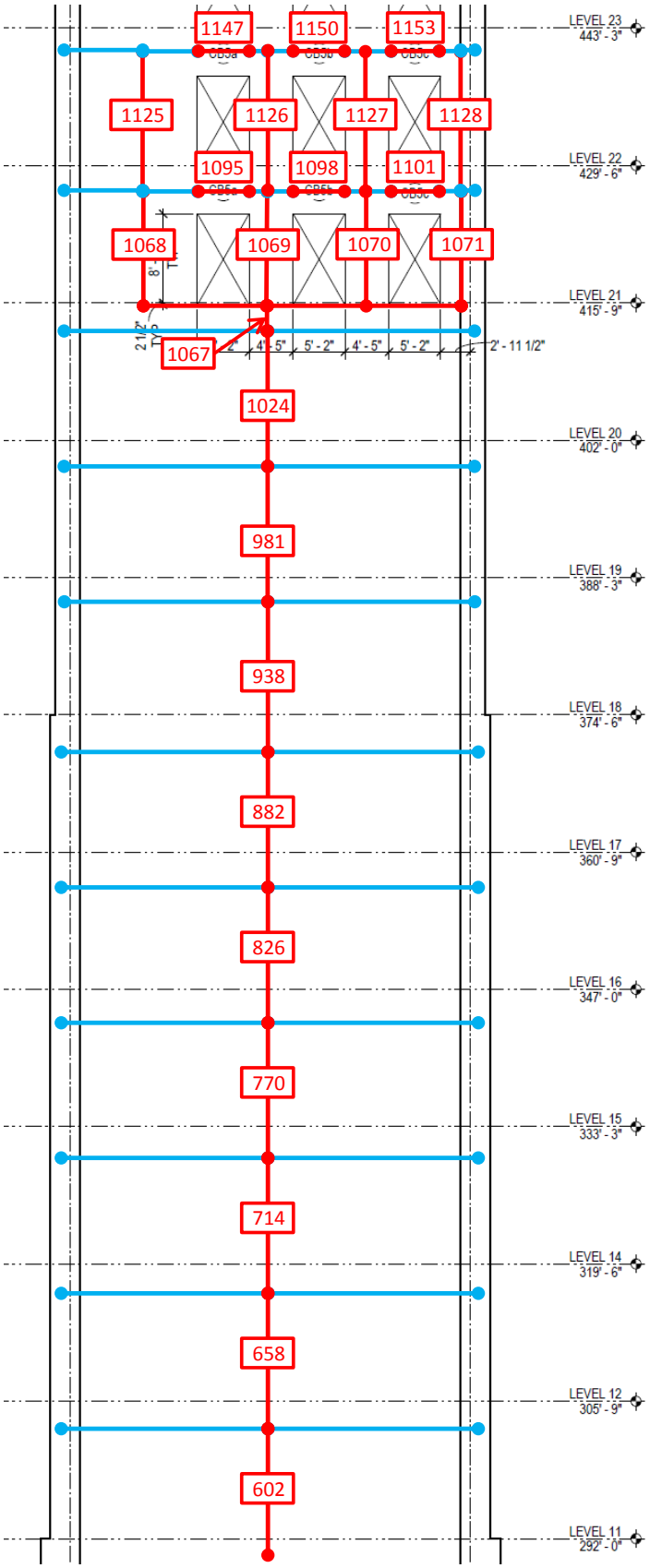
1147
1150
1153
1125
1126
1127
1128
1095
1098
1101
1068
1069
1070
1071
1067
1024
981
938
882
826
770
714
658
602
LEVEL 23
443' - 3"
LEVEL 22
429' - 6"
LEVEL 21
415' - 9"
LEVEL 20
402' - 0"
LEVEL 19
388' - 3"
LEVEL 18
374' - 6"
LEVEL 17
360' - 9"
LEVEL 16
347' - 0"
LEVEL 15
333' - 3"
LEVEL 14
319' - 6"
LEVEL 12
305' - 9"
LEVEL 11
292' - 0"
2' - 11 1/2"

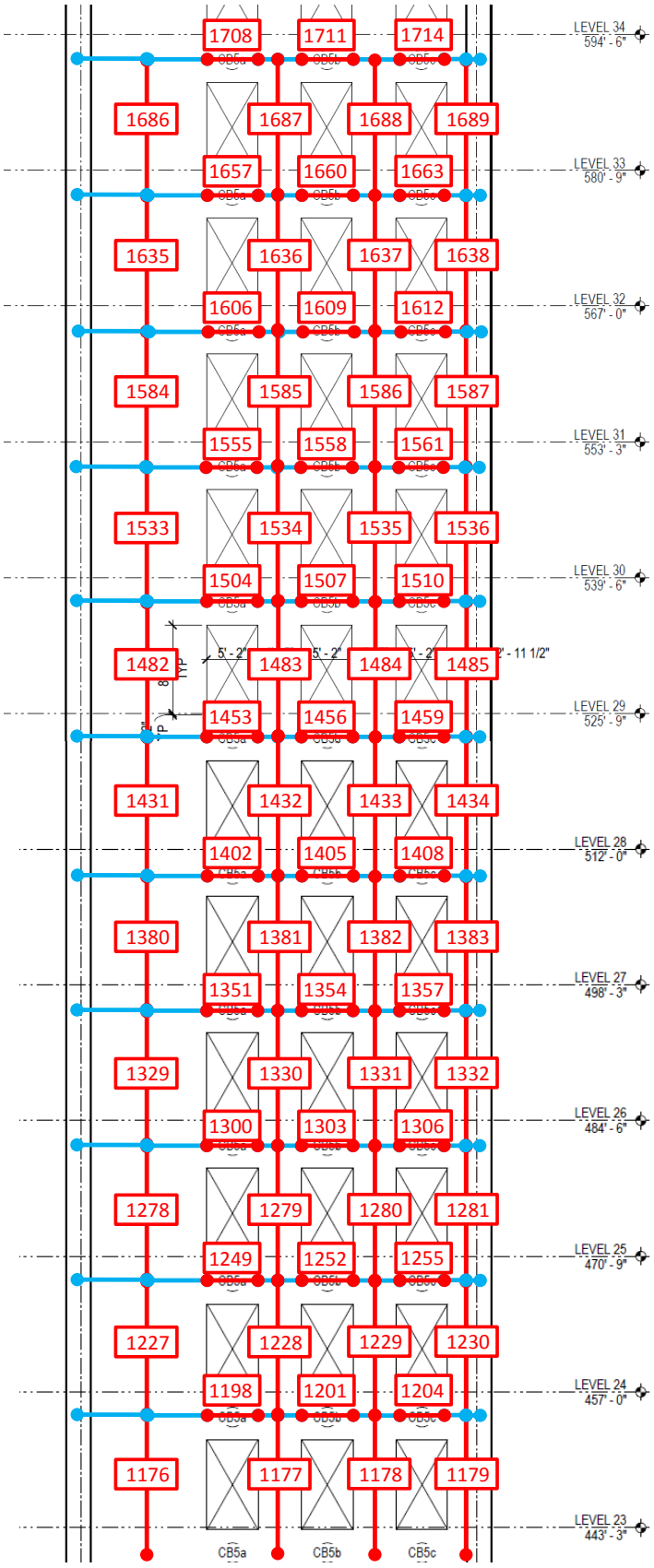
1708
1711
1714
1686
1687
1688
1689
1657
1660
1663
1635
1636
1637
1638
1606
1609
1612
1584
1585
1586
1587
1555
1558
1561
1533
1534
1535
1536
1504
1507
1510
1482
1483
1484
1485
1453
1456
1459
1431
1432
1433
1434
1402
1405
1408
1380
1381
1382
1383
1351
1354
1357
1329
1330
1331
1332
1300
1303
1306
1278
1279
1280
1281
1249
1252
1255
1227
1228
1229
1230
1198
1201
1204
1176
1177
1178
1179
LEVEL 34
594' - 6"
LEVEL 33
580' - 9"
LEVEL 32
567' - 0"
LEVEL 31
553' - 3"
LEVEL 30
539' - 6"
LEVEL 29
525' - 9"
LEVEL 28
512' - 0"
LEVEL 27
498' - 3"
LEVEL 26
484' - 6"
LEVEL 25
470' - 9"
LEVEL 24
457' - 0"
LEVEL 23
443' - 3"
CB5a
CB5b
CB5c

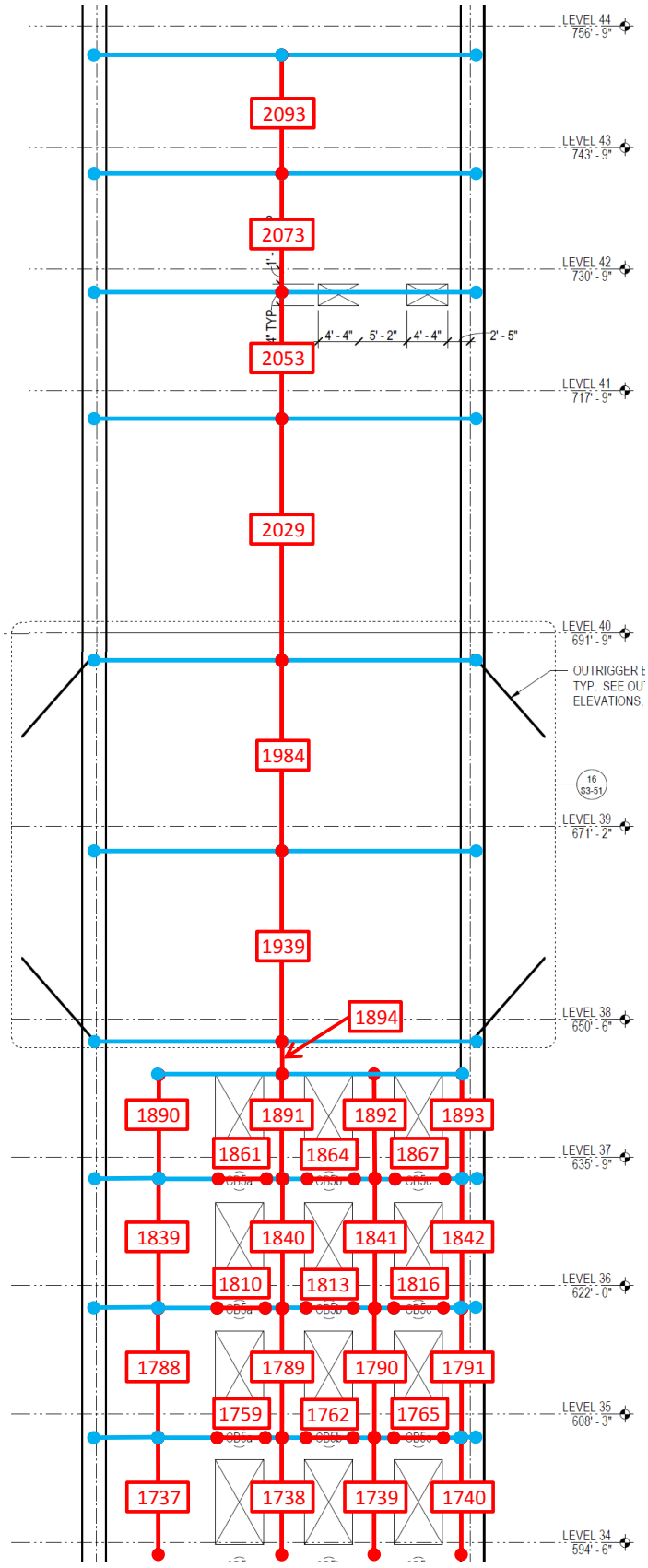
LEVEL 44
756' - 9"
2093
LEVEL 43
743' - 9"
2073
LEVEL 42
730' - 9"
4' - 4"
5' - 2"
4' - 4"
2' - 5"
2053
LEVEL 41
717' - 9"
2029
LEVEL 40
691' - 9"
OUTRIGGER B
TYP. SEE OU
ELEVATIONS.
1984
16
S3-51
LEVEL 39
671' - 2"
1939
LEVEL 38
650' - 6"
1894
1890
1891
1892
1893
1861
1864
1867
LEVEL 37
635' - 9"
1839
1840
1841
1842
1810
1813
1816
LEVEL 36
622' - 0"
1788
1789
1790
1791
1759
1762
1765
LEVEL 35
608' - 3"
1737
1738
1739
1740
LEVEL 34
594' - 6"

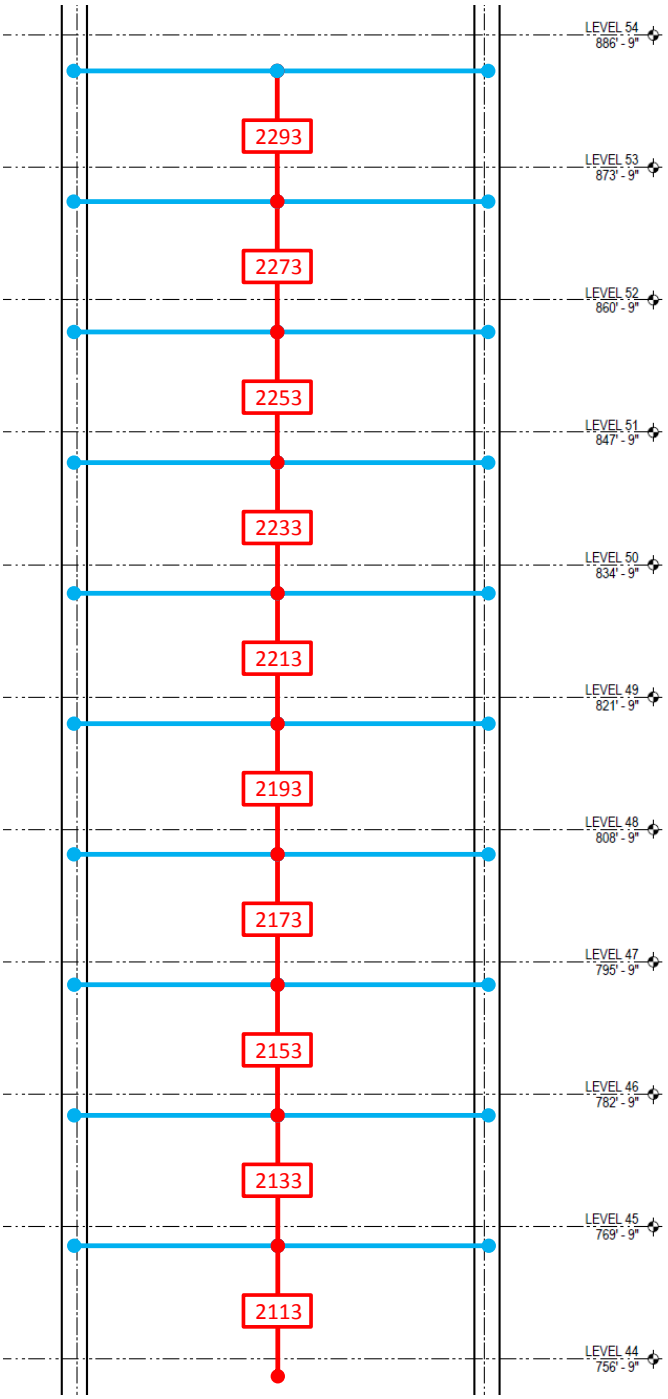
LEVEL 54
886' - 9"
2293
LEVEL 53
873' - 9"
2273
LEVEL 52
860' - 9"
2253
LEVEL 51
847' - 9"
2233
LEVEL 50
834' - 9"
2213
LEVEL 49
821' - 9"
2193
LEVEL 48
808' - 9"
2173
LEVEL 47
795' - 9"
2153
LEVEL 46
782' - 9"
2133
LEVEL 45
769' - 9"
2113
LEVEL 44
756' - 9"

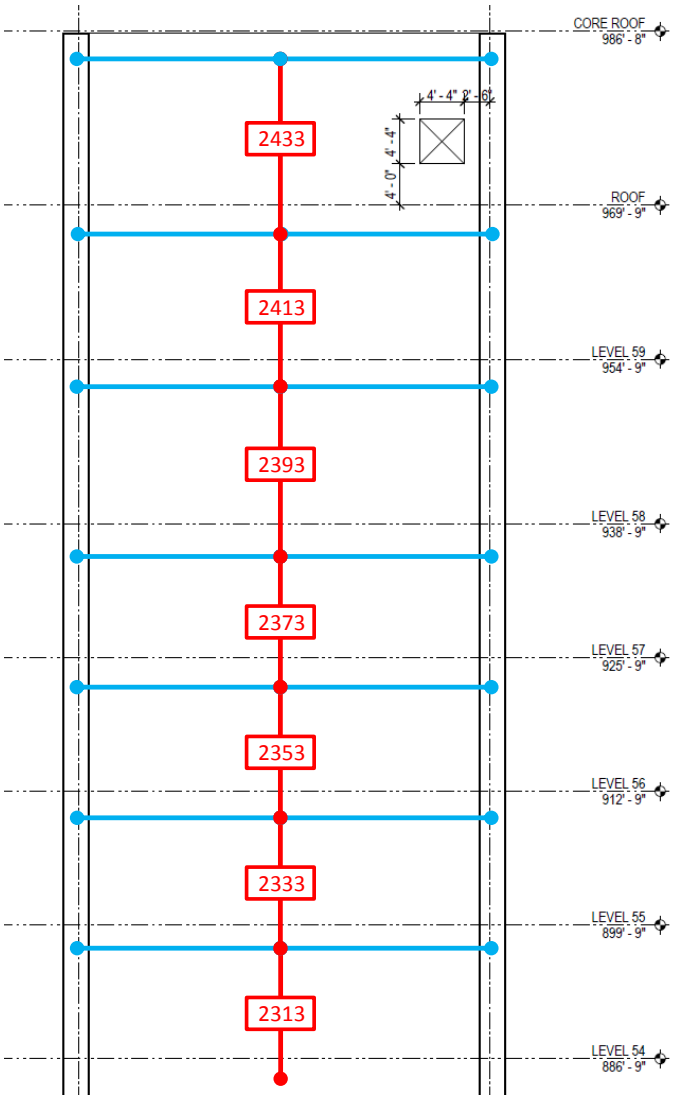
CORE ROOF
986' - 8"
ROOF
969' - 9"
LEVEL 59
954' - 9"
LEVEL 58
938' - 9"
LEVEL 57
925' - 9"
LEVEL 56
912' - 9"
LEVEL 55
899' - 9"
LEVEL 54
886' - 9"
2433
2413
2393
2373
2353
2333
2313
4' - 4"
2' - 6"
4' - 4"
4' - 0"

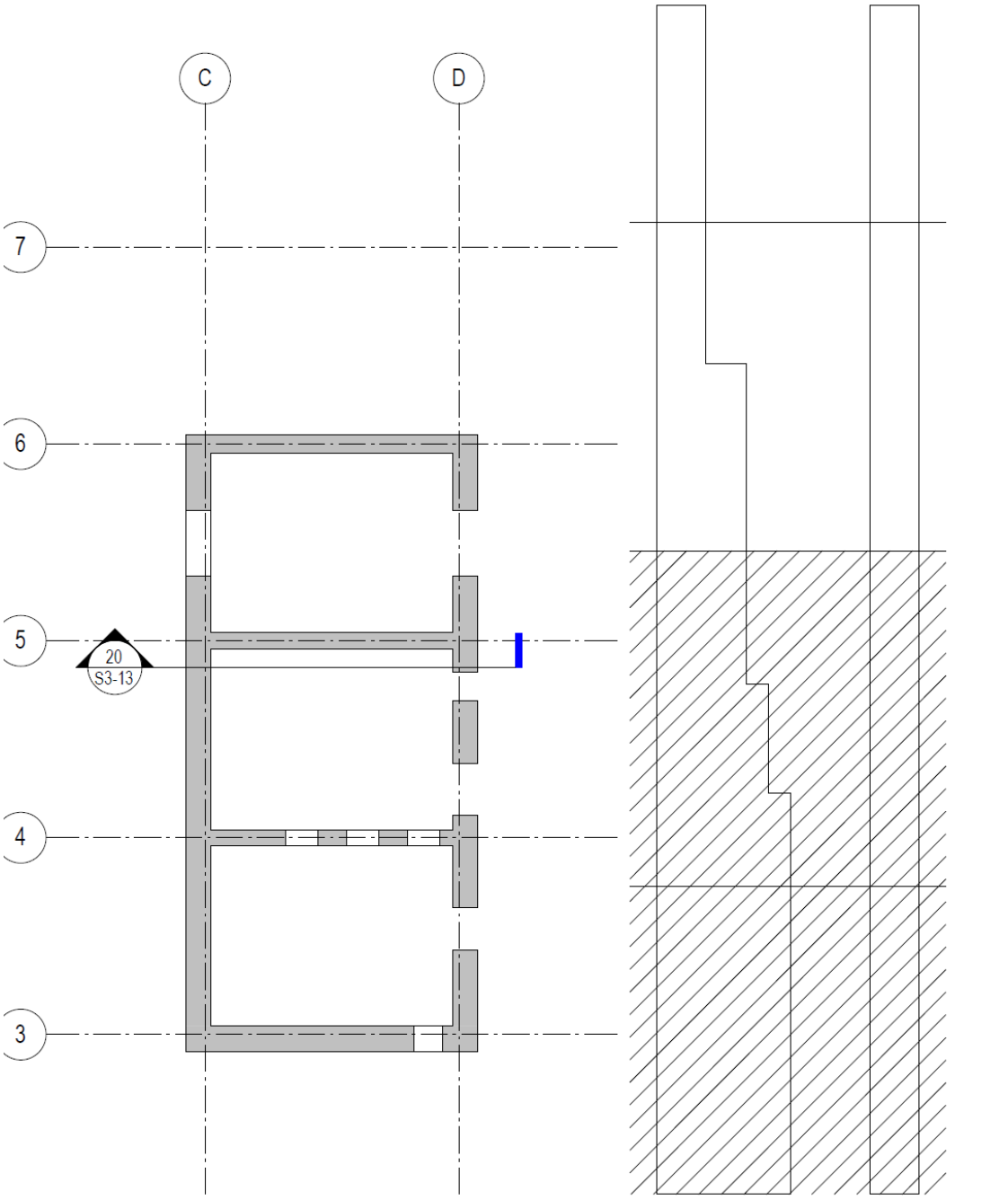

KEY PLAN

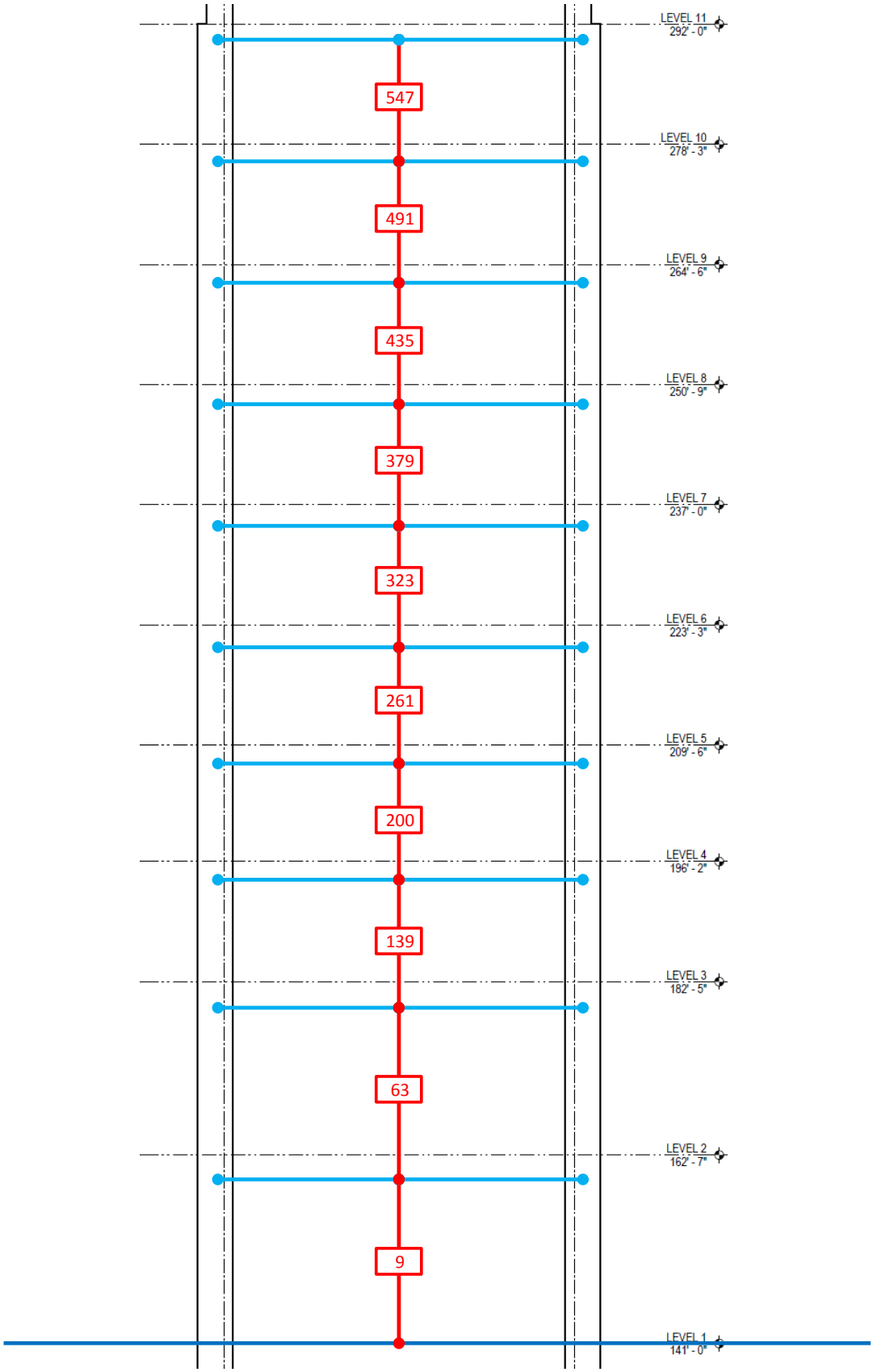
LEVEL 11
292' - 0"
547
LEVEL 10
278' - 3"
491
LEVEL 9
264' - 6"
435
LEVEL 8
250' - 9"
379
LEVEL 7
237' - 0"
323
LEVEL 6
223' - 3"
261
LEVEL 5
209' - 6"
200
LEVEL 4
196' - 2"
139
LEVEL 3
182' - 5"
63
LEVEL 2
162' - 7"
9
LEVEL 1
141' - 0"

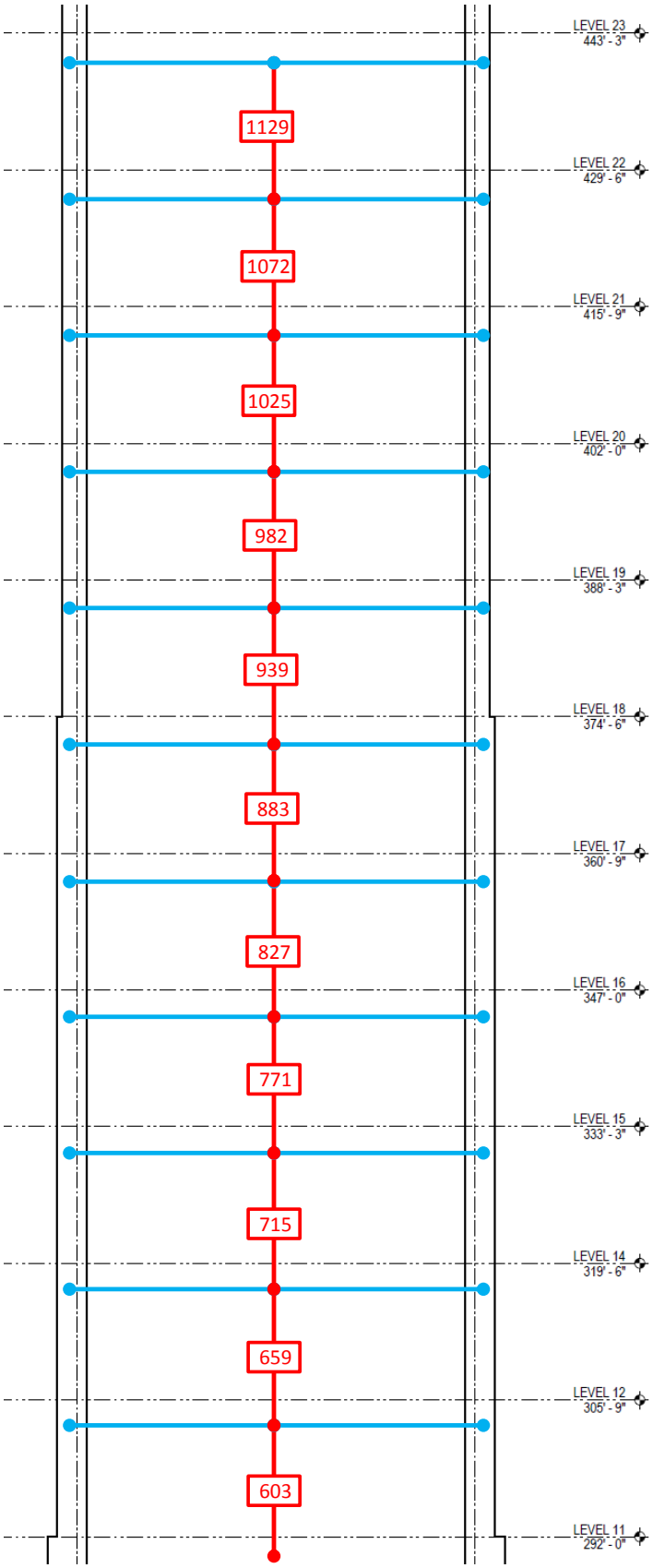
LEVEL 23
443' - 3"
1129
LEVEL 22
429' - 6"
1072
LEVEL 21
415' - 9"
1025
LEVEL 20
402' - 0"
982
LEVEL 19
388' - 3"
939
LEVEL 18
374' - 6"
883
LEVEL 17
360' - 9"
827
LEVEL 16
347' - 0"
771
LEVEL 15
333' - 3"
715
LEVEL 14
319' - 6"
659
LEVEL 12
305' - 9"
603
LEVEL 11
292' - 0"

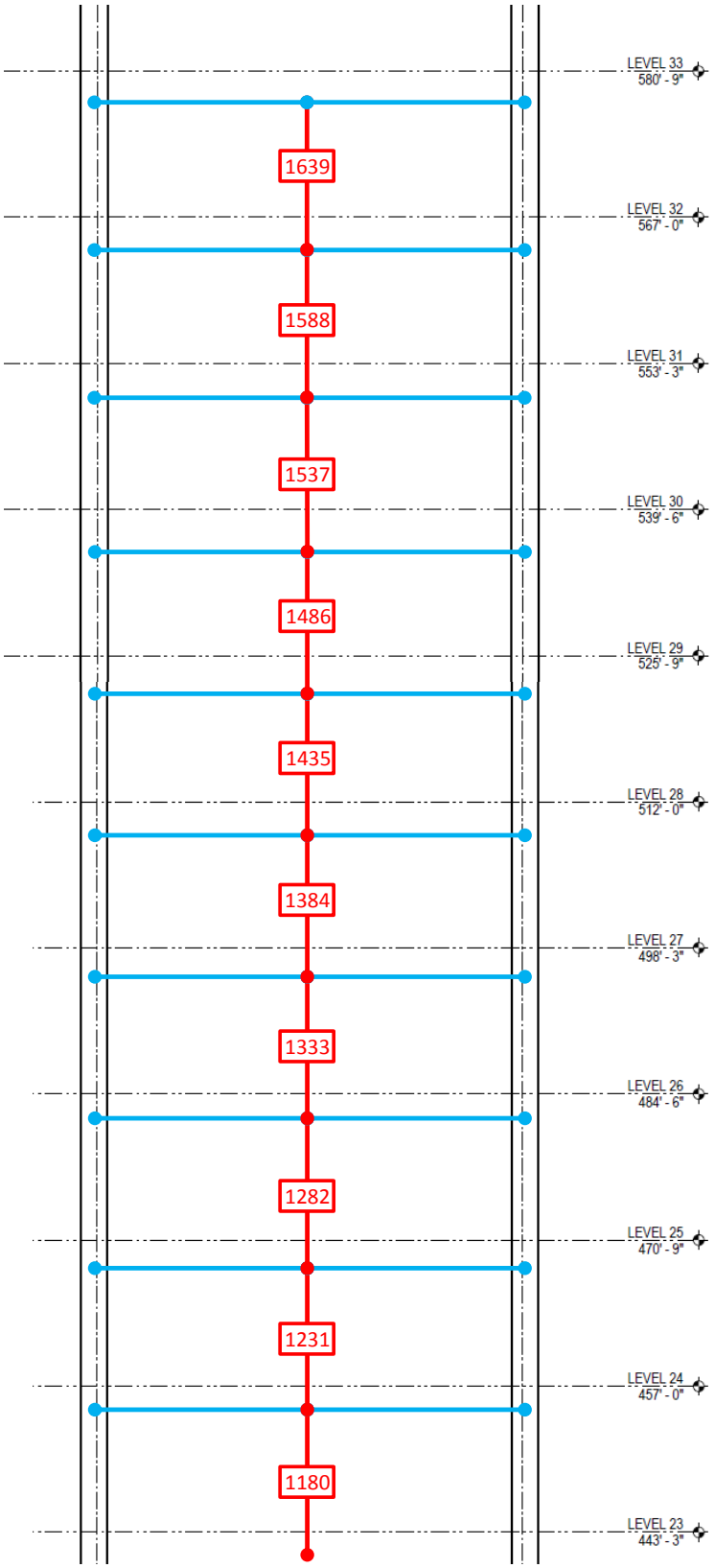
LEVEL 33
580' - 9"
1639
LEVEL 32
567' - 0"
1588
LEVEL 31
553' - 3"
1537
LEVEL 30
539' - 6"
1486
LEVEL 29
525' - 9"
1435
LEVEL 28
512' - 0"
1384
LEVEL 27
498' - 3"
1333
LEVEL 26
484' - 6"
1282
LEVEL 25
470' - 9"
1231
LEVEL 24
457' - 0"
1180
LEVEL 23
443' - 3"

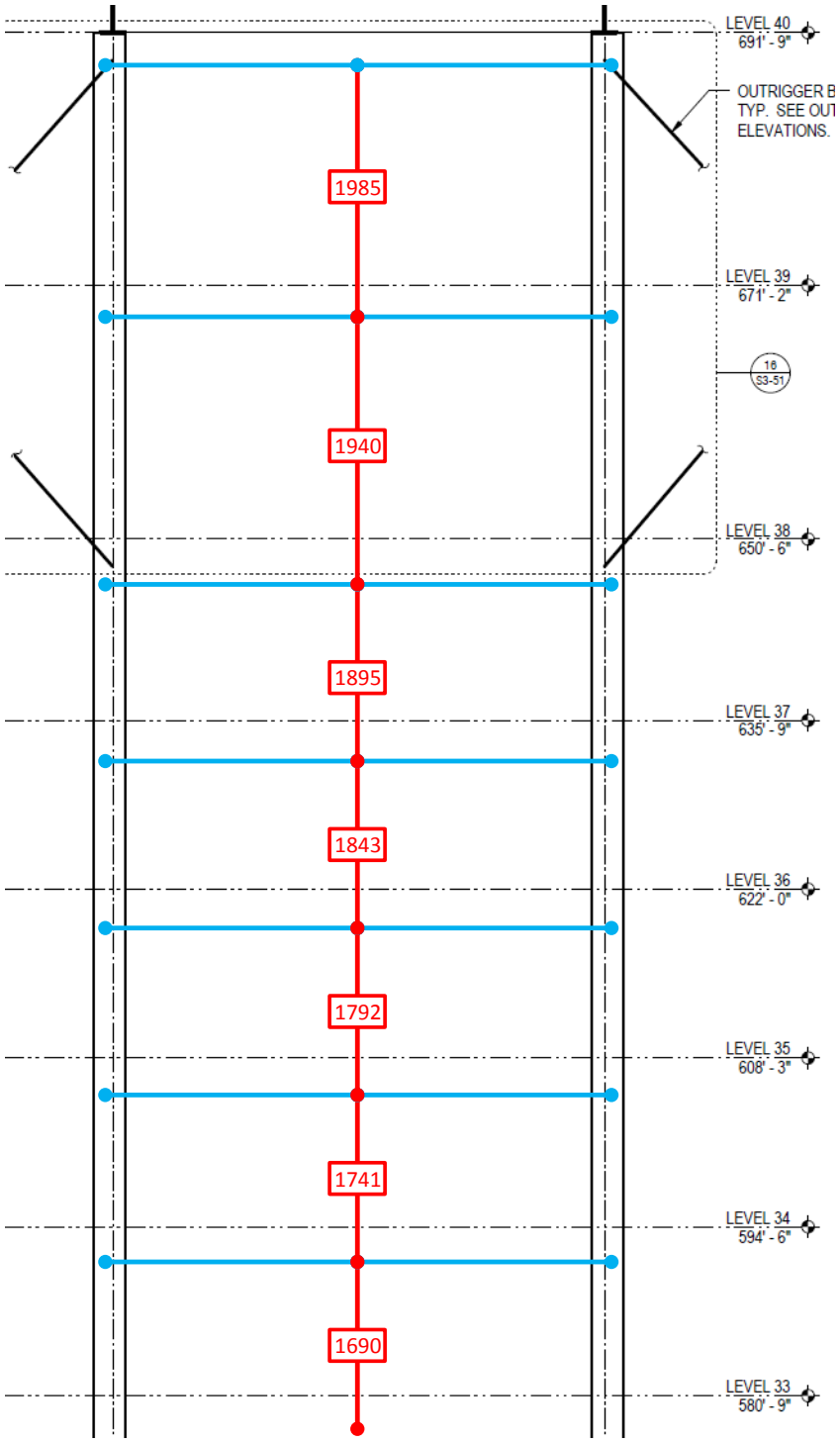
LEVEL 40
691' - 9"
OUTRIGGER B
TYP. SEE OUT
ELEVATIONS.
1985
LEVEL 39
671' - 2"
16
S3-51
1940
LEVEL 38
650' - 6"
1895
LEVEL 37
635' - 9"
1843
LEVEL 36
622' - 0"
1792
LEVEL 35
608' - 3"
1741
LEVEL 34
594' - 6"
1690
LEVEL 33
580' - 9"

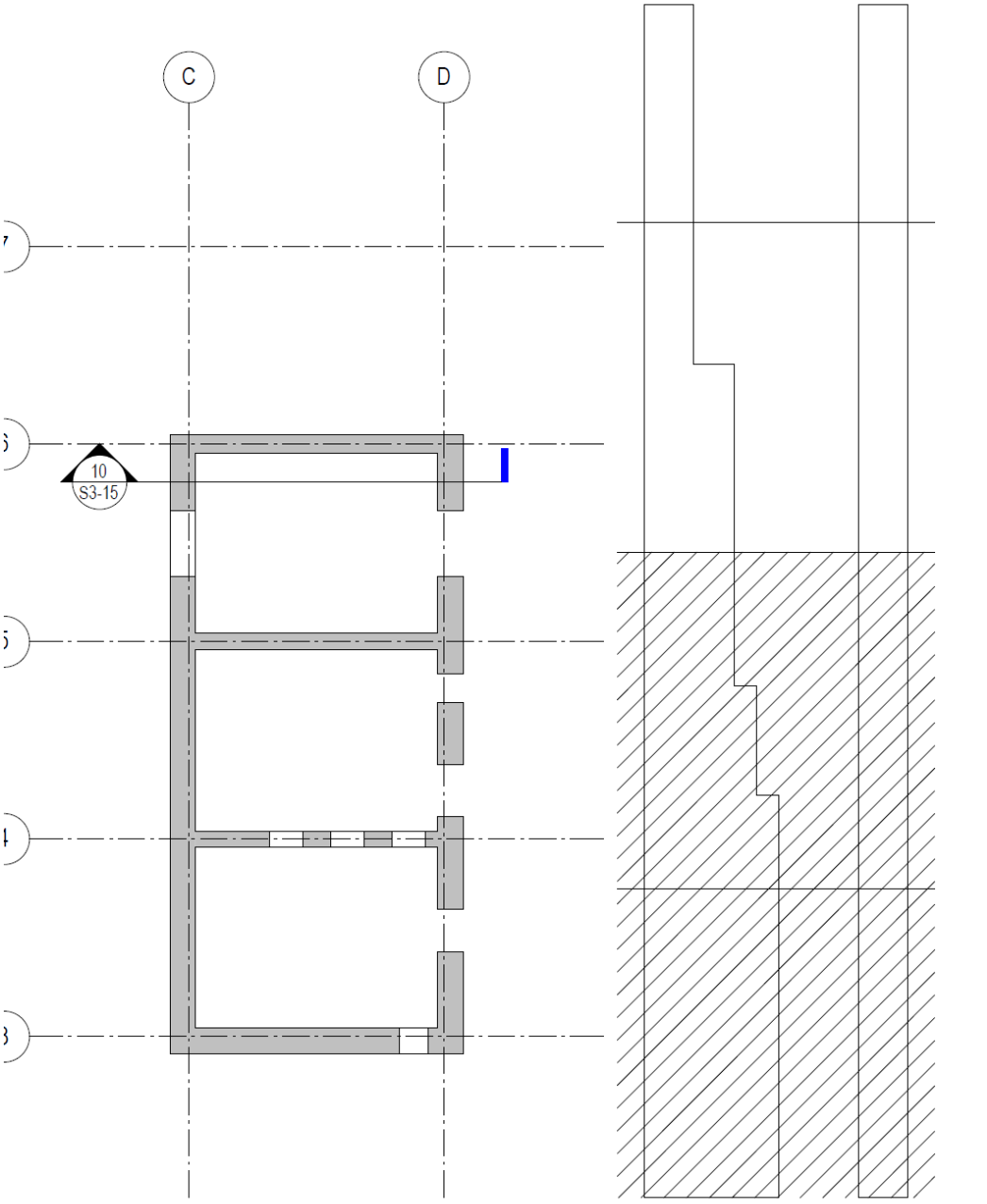

KEY PLAN

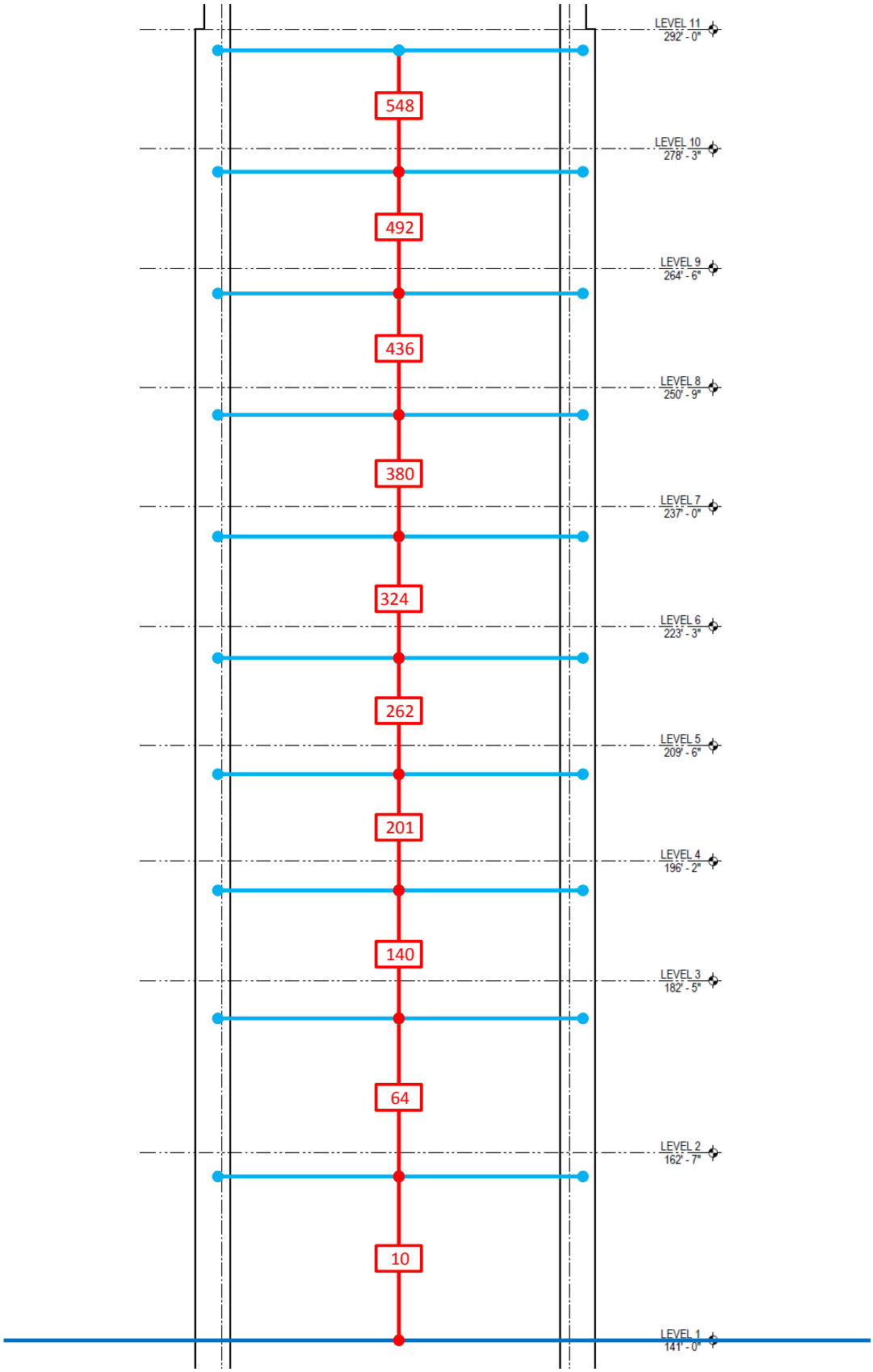
LEVEL 11
292' - 0"
548
LEVEL 10
278' - 3"
492
LEVEL 9
264' - 6"
436
LEVEL 8
250' - 9"
380
LEVEL 7
237' - 0"
324
LEVEL 6
223' - 3"
262
LEVEL 5
209' - 6"
201
LEVEL 4
196' - 2"
140
LEVEL 3
182' - 5"
64
LEVEL 2
162' - 7"
10
LEVEL 1
141' - 0"

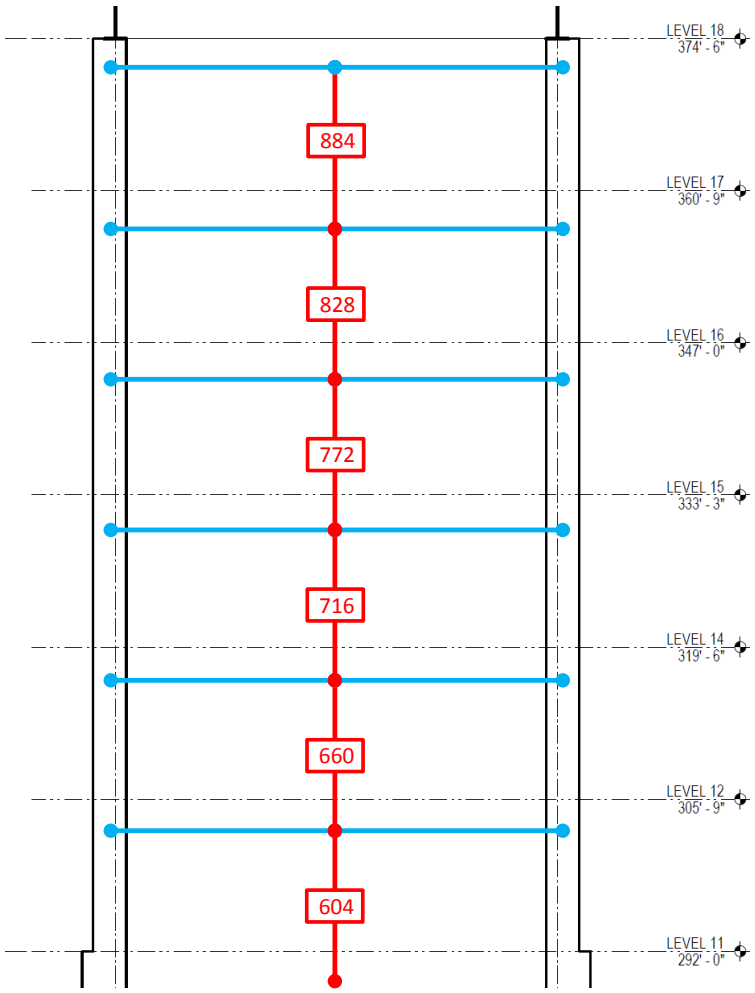
LEVEL 18
374' - 6"
884
LEVEL 17
360' - 9"
828
LEVEL 16
347' - 0"
772
LEVEL 15
333' - 3"
716
LEVEL 14
319' - 6"
660
LEVEL 12
305' - 9"
604
LEVEL 11
292' - 0"

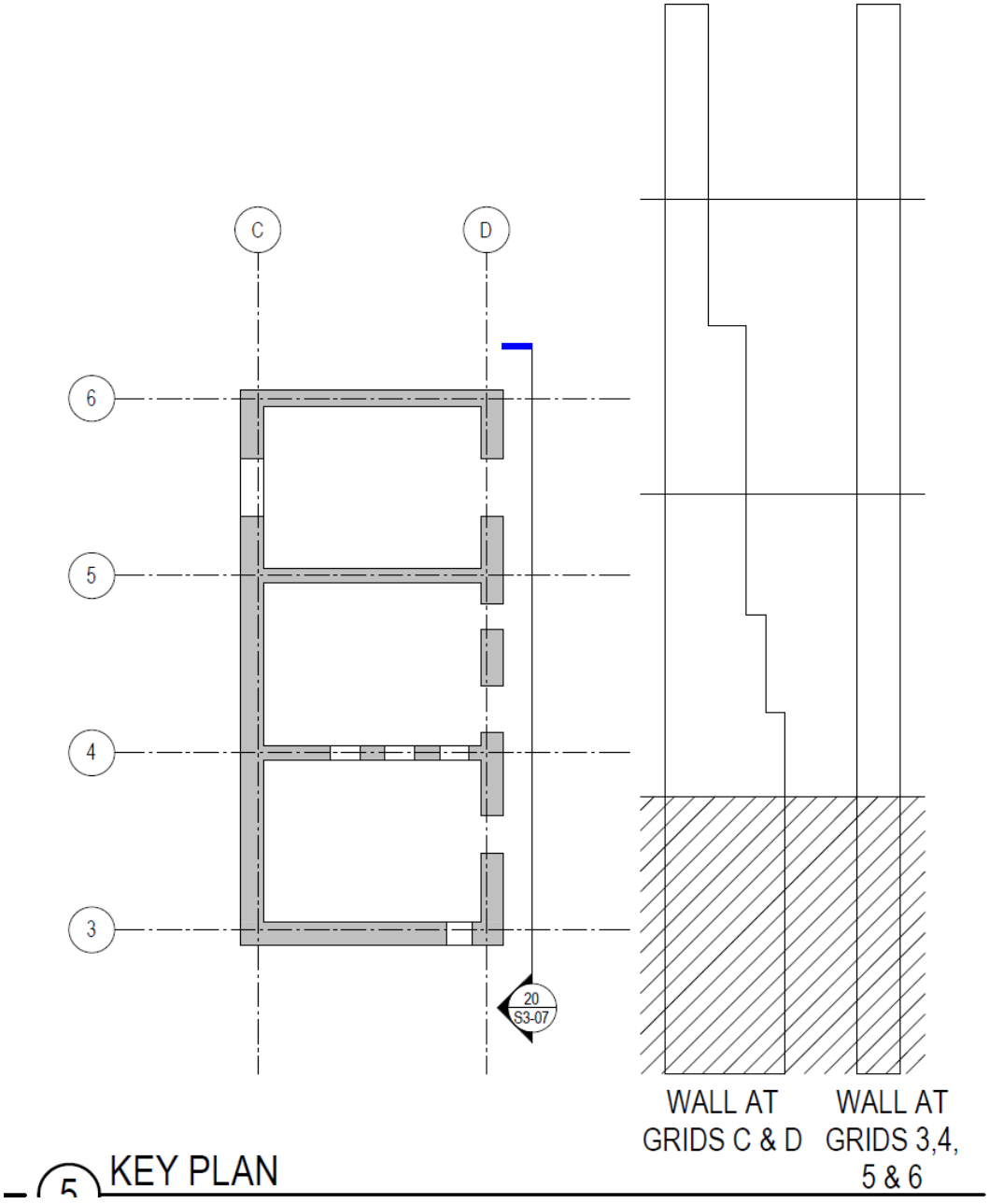

5 KEY PLAN

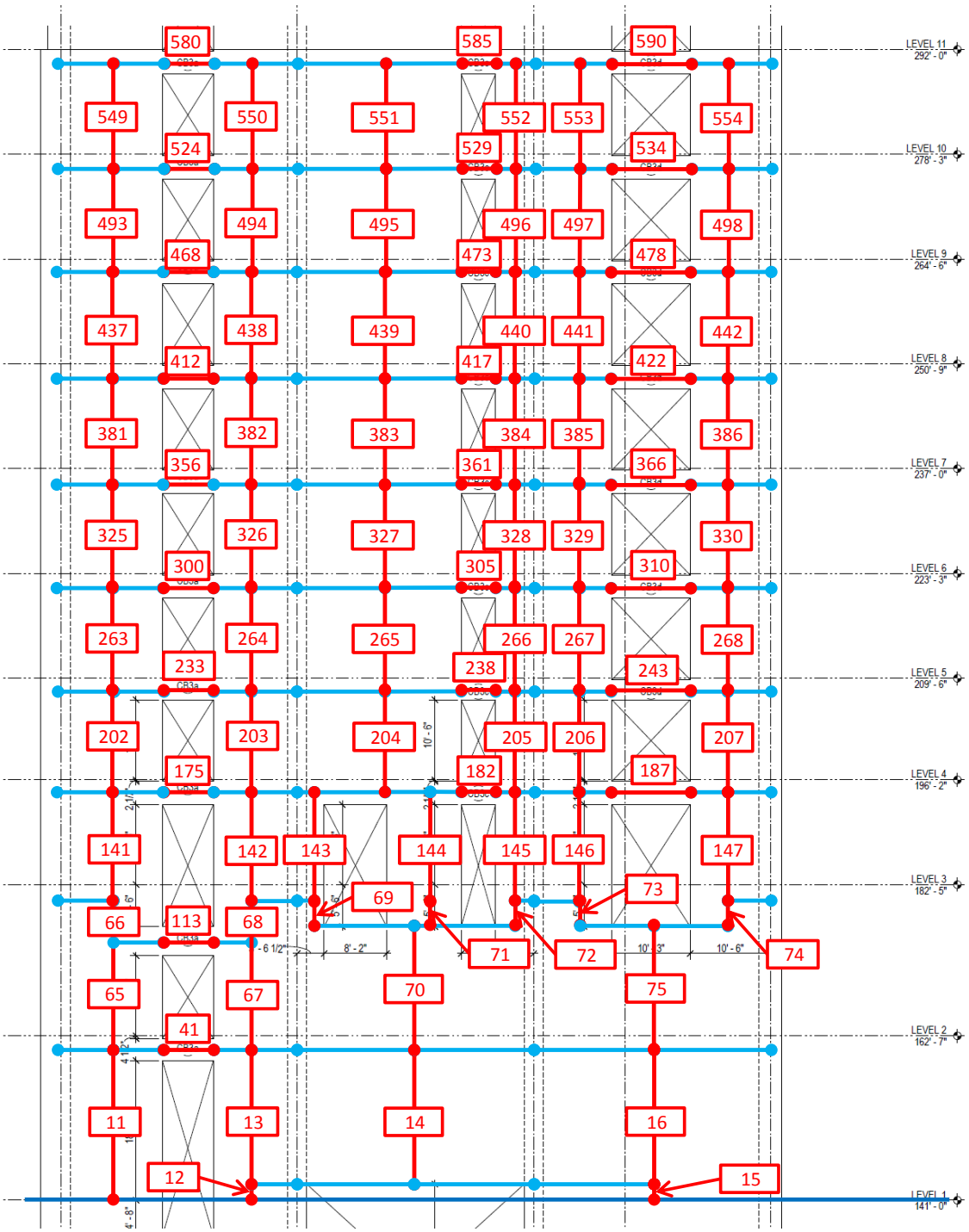
580
585
590
549
550
551
552
553
554
524
529
534
493
494
495
496
497
498
468
473
478
437
438
439
440
441
442
412
417
422
381
382
383
384
385
386
356
361
366
325
326
327
328
329
330
300
305
310
263
264
265
266
267
268
233
238
243
202
203
204
205
206
207
175
182
187
141
142
143
144
145
146
147
66
113
68
69
71
72
73
74
65
67
70
75
41
11
13
14
16
12
15
LEVEL 11
292' - 0"
LEVEL 10
278' - 3"
LEVEL 9
264' - 6"
LEVEL 8
250' - 9"
LEVEL 7
237' - 0"
LEVEL 6
223' - 3"
LEVEL 5
209' - 6"
LEVEL 4
196' - 2"
LEVEL 3
182' - 5"
LEVEL 2
162' - 7"
LEVEL 1
141' - 0"

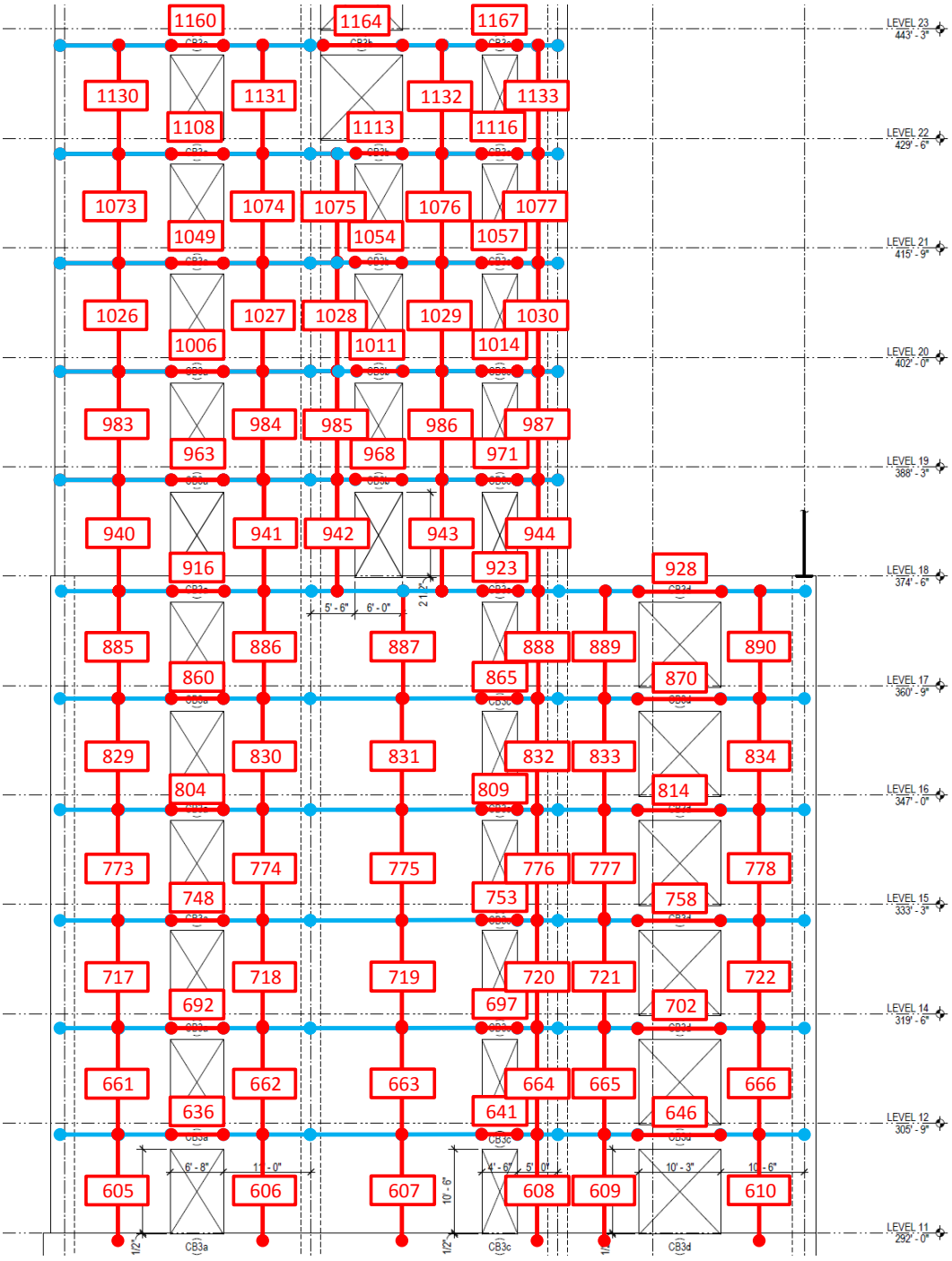
1160
1164
1167
1130
1131
1132
1133
1108
1113
1116
1073
1074
1075
1076
1077
1049
1054
1057
1026
1027
1028
1029
1030
1006
1011
1014
983
984
985
986
987
963
968
971
940
941
942
943
944
916
923
928
885
886
887
888
889
890
860
865
870
829
830
831
832
833
834
804
809
814
773
774
775
776
777
778
748
753
758
717
718
719
720
721
722
692
697
702
661
662
663
664
665
666
636
641
646
605
606
607
608
609
610
LEVEL 23
443' - 3"
LEVEL 22
429' - 6"
LEVEL 21
415' - 9"
LEVEL 20
402' - 0"
LEVEL 19
388' - 3"
LEVEL 18
374' - 6"
LEVEL 17
360' - 9"
LEVEL 16
347' - 0"
LEVEL 15
333' - 3"
LEVEL 14
319' - 6"
LEVEL 12
305' - 9"
LEVEL 11
292' - 0"
5' - 6"
6' - 0"
6' - 8"
11' - 0"
4' - 6"
5' - 0"
10' - 3"
10' - 6"
10' - 6"
CB3a
CB3c
CB3d

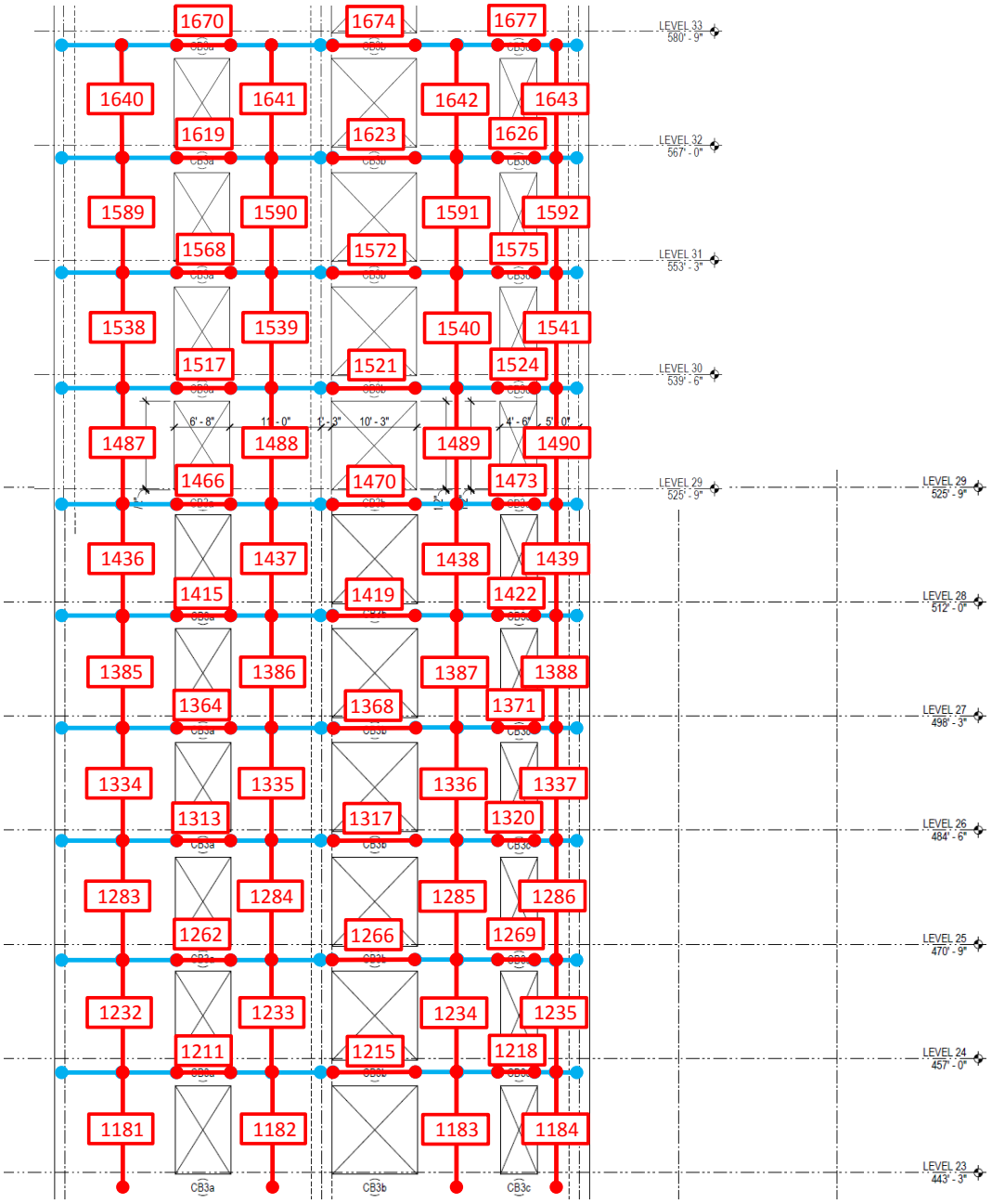
1670
1674
1677
1640
1641
1642
1643
1619
1623
1626
1589
1590
1591
1592
1568
1572
1575
1538
1539
1540
1541
1517
1521
1524
1487
1488
1489
1490
1466
1470
1473
1436
1437
1438
1439
1415
1419
1422
1385
1386
1387
1388
1364
1368
1371
1334
1335
1336
1337
1313
1317
1320
1283
1284
1285
1286
1262
1266
1269
1232
1233
1234
1235
1211
1215
1218
1181
1182
1183
1184
LEVEL 33
580' - 9"
LEVEL 32
567' - 0"
LEVEL 31
553' - 3"
LEVEL 30
539' - 6"
LEVEL 29
525' - 9"
LEVEL 28
512' - 0"
LEVEL 27
498' - 3"
LEVEL 26
484' - 6"
LEVEL 25
470' - 9"
LEVEL 24
457' - 0"
LEVEL 23
443' - 3"
CB3a
CB3b
CB3c

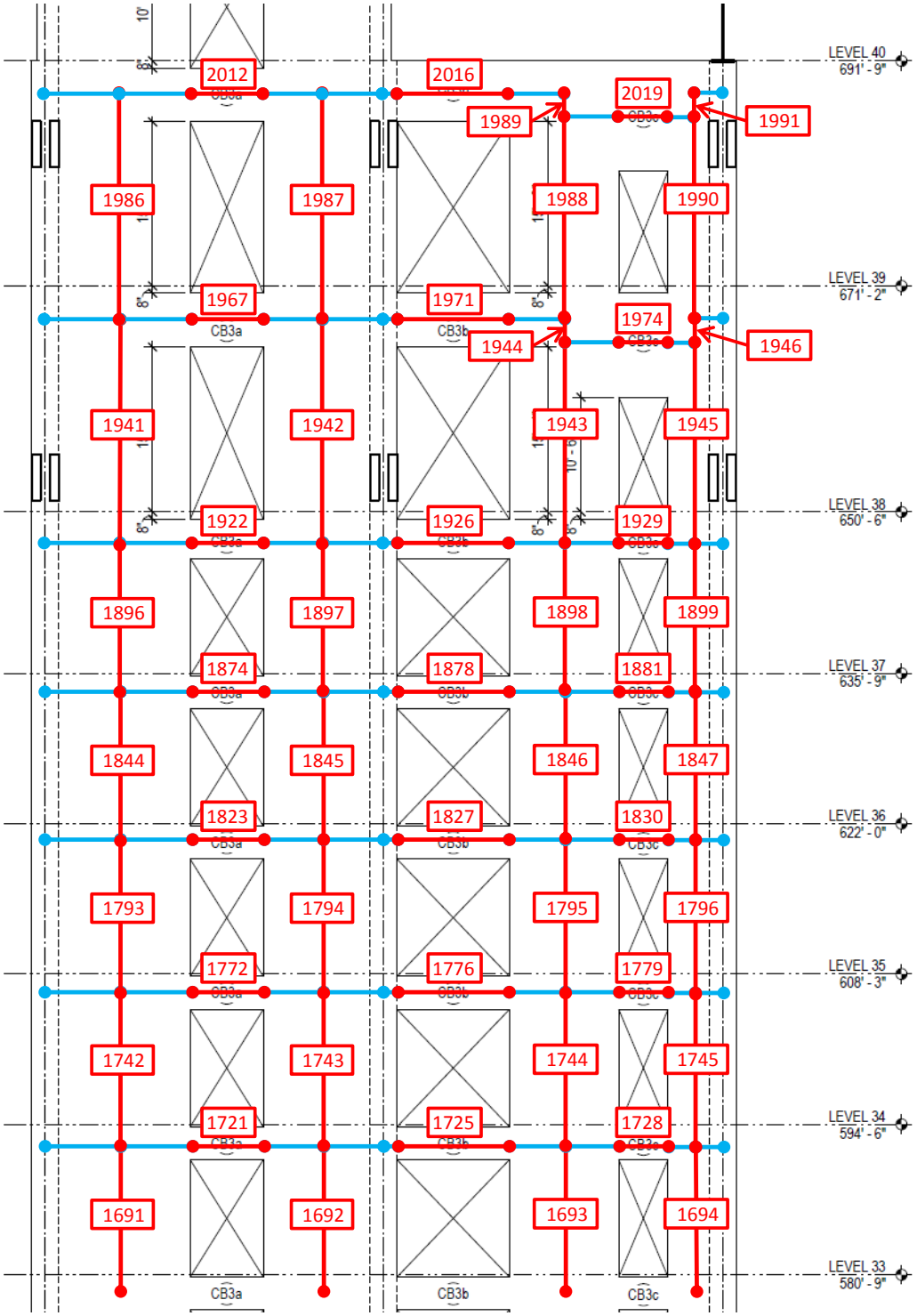
LEVEL 40
691' - 9"
LEVEL 39
671' - 2"
LEVEL 38
650' - 6"
LEVEL 37
635' - 9"
LEVEL 36
622' - 0"
LEVEL 35
608' - 3"
LEVEL 34
594' - 6"
LEVEL 33
580' - 9"
2012
2016
2019
1989
1991
1986
1987
1988
1990
1967
1971
1974
1944
1946
1941
1942
1943
1945
1922
1926
1929
1896
1897
1898
1899
1874
1878
1881
1844
1845
1846
1847
1823
1827
1830
1793
1794
1795
1796
1772
1776
1779
1742
1743
1744
1745
1721
1725
1728
1691
1692
1693
1694
CB3a
CB3b
CB3c

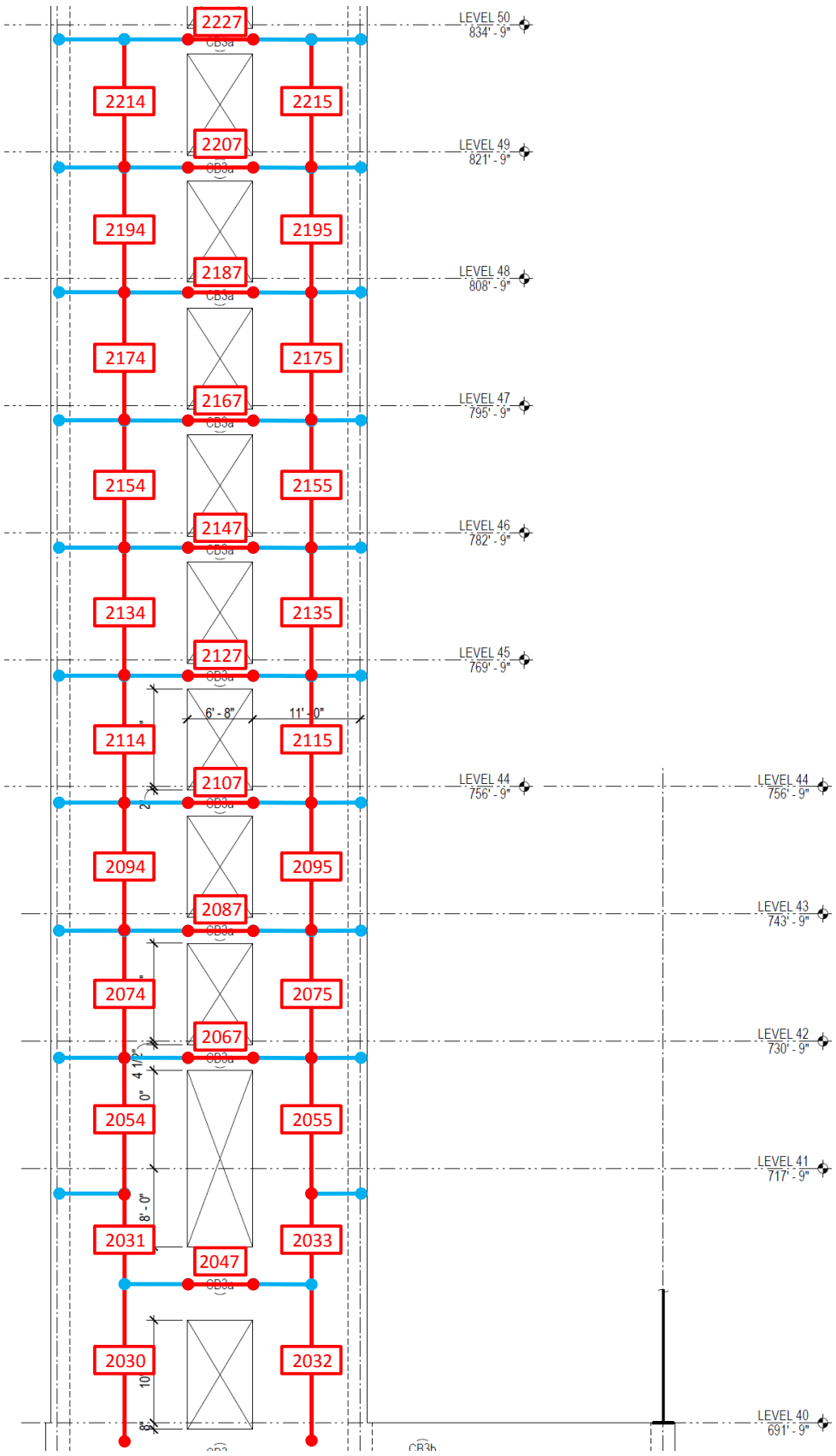
2227
2214
2215
2207
2194
2195
2187
2174
2175
2167
2154
2155
2147
2134
2135
2127
2114
2115
2107
2094
2095
2087
2074
2075
2067
2054
2055
2031
2033
2047
2030
2032
LEVEL 50
834' - 9"
LEVEL 49
821' - 9"
LEVEL 48
808' - 9"
LEVEL 47
795' - 9"
LEVEL 46
782' - 9"
LEVEL 45
769' - 9"
LEVEL 44
756' - 9"
LEVEL 43
743' - 9"
LEVEL 42
730' - 9"
LEVEL 41
717' - 9"
LEVEL 40
691' - 9"
6' - 8"
11' - 0"
8' - 0"
CB3a
CB3b

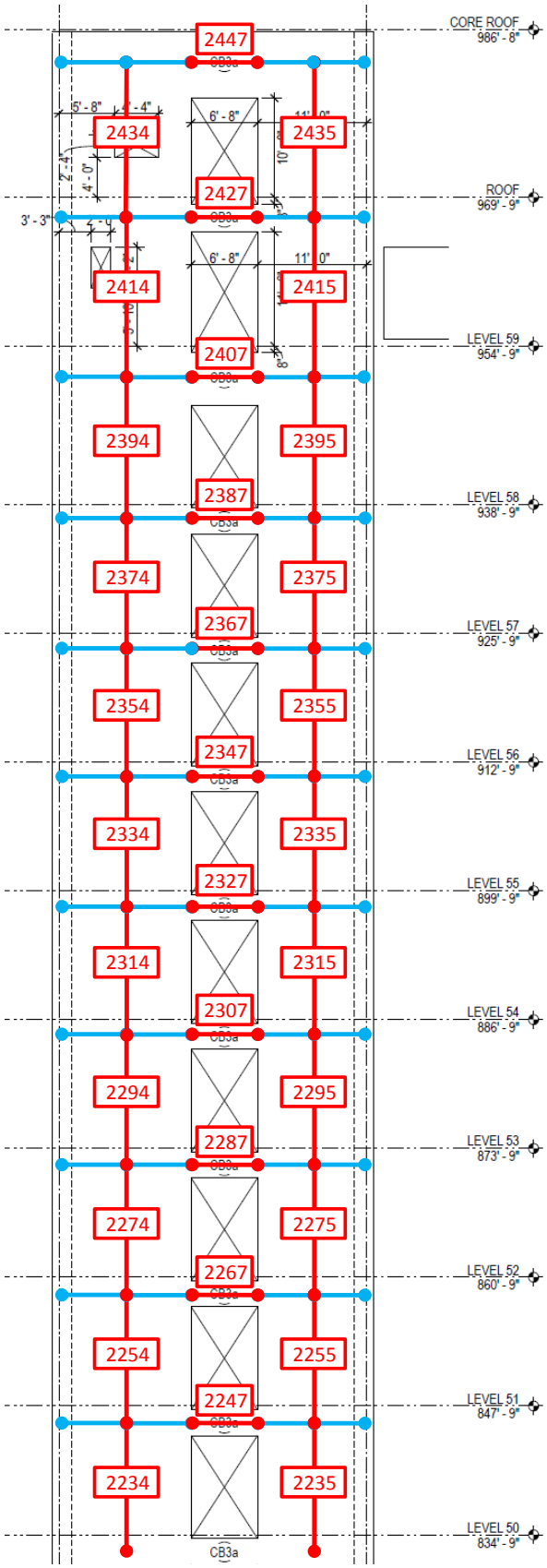
CORE ROOF
986' - 8"
ROOF
969' - 9"
LEVEL 59
954' - 9"
LEVEL 58
938' - 9"
LEVEL 57
925' - 9"
LEVEL 56
912' - 9"
LEVEL 55
899' - 9"
LEVEL 54
886' - 9"
LEVEL 53
873' - 9"
LEVEL 52
860' - 9"
LEVEL 51
847' - 9"
LEVEL 50
834' - 9"
2447
2434
2435
2427
2414
2415
2407
2394
2395
2387
2374
2375
2367
2354
2355
2347
2334
2335
2327
2314
2315
2307
2294
2295
2287
2274
2275
2267
2254
2255
2247
2234
2235
CB3a
6' - 8"
11' - 0"
10' - 0"
5' - 8"
4' - 0"
3' - 3"

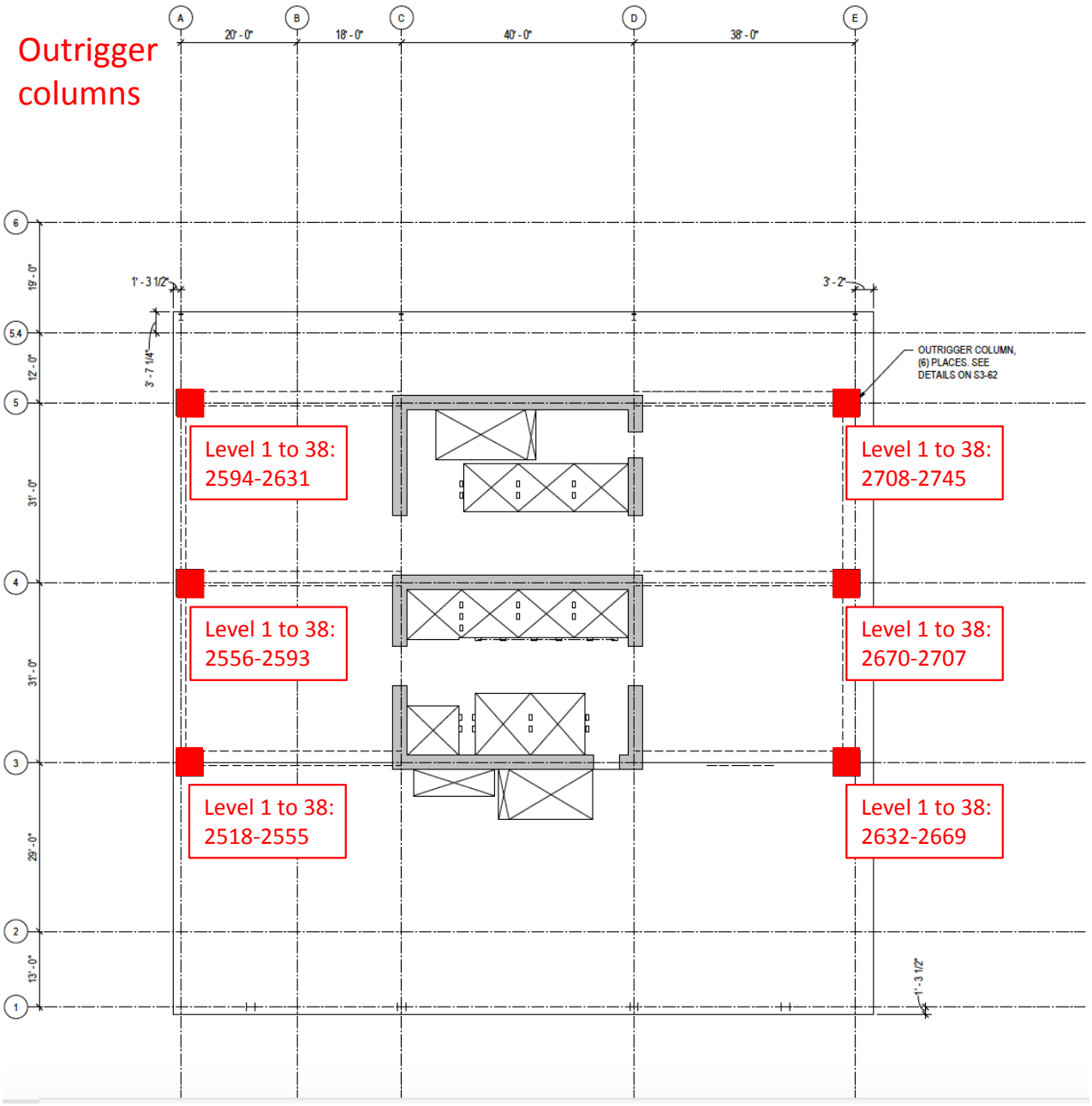
Outrigger columns
A
B
C
D
E
20' - 0"
18' - 0"
40' - 0"
38' - 0"
6
5.4
5
4
3
2
1
19' - 0"
12' - 0"
31' - 0"
31' - 0"
29' - 0"
13' - 0"
1' - 3 1/2"
3' - 7 1/4"
3' - 2"
OUTRIGGER COLUMN, (6) PLACES. SEE DETAILS ON S3-62
Level 1 to 38: 2594-2631
Level 1 to 38: 2708-2745
Level 1 to 38: 2556-2593
Level 1 to 38: 2670-2707
Level 1 to 38: 2518-2555
Level 1 to 38: 2632-2669
1' - 3 1/2"

APPENDIX C

Inclusion of wind tunnel uncertainties

As presented in Section 4.4.1, the stochastic wind loads $\mathbf{F}(t)$ corresponding to the intensity measure $\tilde{V}_H$ and the wind direction α is represented by the superposition of N_l independent vector-valued subprocesses as follows:

$$\mathbf{F}(t;\tilde{V}_H,\alpha)=\sum_{j=1}^{N_l}\mathbf{F}_j(t;\tilde{V}_H,\alpha) \tag{C.1}$$

where $\mathbf{F}_j(t)$ is the jth vector-valued subprocess given by:

$$\mathbf{F}_j(t;\tilde{V}_H,\alpha)=\sum_{k=1}^{N_f}|\mathbf{\Psi}_j(\omega_k;\alpha)|\sqrt{2\Lambda_j(\omega_k;\tilde{V}_H,\alpha)\Delta\omega_k}\times\cos(\omega_k t+\vartheta_{kj}+\boldsymbol{\theta_j}(\omega_k)) \tag{C.2}$$

where $\mathbf{\Psi}_j(\omega_k)$ and $\Lambda_j(\omega_k)$ are the jth frequency dependent eigenvector and eigenvalue of $\mathbf{F}(t)$, N_f is the total number of discrete frequencies considered in the interval $[0,N_f\Delta\omega_k]$ with $\Delta\omega_k$ representing the frequency increment, ϑ_{kj} are independent and uniformly distributed random variables in $[0,2\pi]$, while $\boldsymbol{\theta}_j$ is a vector of complex angles. In particular, $\Lambda_j(\omega_k)$ and $\mathbf{\Psi}_j(\omega_k)$ are related to eigenvalues and eigenvectors of scaled experimental loads, $\mathbf{F}_w(\tilde{t})$, through the following scheme:

$$\Lambda_j(\omega_k;\tilde{V}_H)=\left[\left(\frac{\tilde{V}_H}{\bar{v}_w}\right)^2\right]^2\left(\frac{\bar{v}_w}{\tilde{V}_H}\right)\Lambda_j^{(w)}(\tilde{\omega}_k) \tag{C.3}$$

$$\boldsymbol{\Psi}_j(\omega_k) = \boldsymbol{\Psi}_j^{(w)}(\tilde{\omega}_k) \tag{C.4}$$

where $\bar{v}_w$ is the mean hourly wind speed at the reference height to which the wind tunnel loads $\mathbf{F}_w(\tilde{t})$ were scaled, $\omega_k = \frac{\tilde{V}_H}{\bar{v}_w}\tilde{\omega}_k$ with $\tilde{\omega}_k$ the kth frequency step at the wind tunnel reference speed, while $\Lambda_j^{(w)}(\tilde{\omega}_k)$ and $\boldsymbol{\Psi}_j^{(w)}(\tilde{\omega}_k)$ are eigenvalues and eigenvectors of $\mathbf{F}_w(\tilde{t})$ determined from the following eigenvalue problem:

$$[\mathbf{S}_{\mathbf{F}_w}(\tilde{\omega}_k; \bar{v}_w, \alpha) - \Lambda^{(w)}(\tilde{\omega}_k; \bar{v}_w, \alpha)\mathbf{I}]\boldsymbol{\Psi}^{(w)}(\tilde{\omega}_k; \alpha) = 0 \tag{C.5}$$

where $\mathbf{S}_{\mathbf{F}_w}$ is the cross power spectral density of $\mathbf{F}_w(\tilde{t})$. To consider uncertainties associated with the use of wind tunnel data, the wind tunnel loads $\mathbf{F}_w(\tilde{t})$ should be multiplied by the uncertain parameters w_1, w_2 and w_3 of Table 7.1. This multiplication will obviously affect the simulated wind loads $\mathbf{F}(t)$. To model this effect, consider a corrected wind tunnel load, i.e. $\tilde{\mathbf{F}}_w(\tilde{t}) = w_1 w_2 w_3 \mathbf{F}_w(\tilde{t})$. The associated cross power spectral density is:

$$\tilde{\mathbf{S}}_{\mathbf{F}_w} = (w_1 w_2 w_3)^2 \mathbf{S}_{\mathbf{F}_w} \tag{C.6}$$

The corresponding eigenvalues become $\tilde{\Lambda}_j^{(w)}(\tilde{\omega}_k) = (w_1 w_2 w_3)^2 \Lambda_j^{(w)}(\tilde{\omega}_k)$, while the eigenvectors remain the same. The eigenvalues of the simulated wind loads $\mathbf{F}(t)$ can then be determined through the transformation of Eq. (C.3), which yields $\tilde{\Lambda}_j(\omega_k; \tilde{V}_H) = (w_1 w_2 w_3)^2 \Lambda_j(\omega_k; \tilde{V}_H)$. Hence, by substituting into Eq. (C.2) and summing over all N_l modes, the corrected stochastic wind loads can be expressed as:

$$\tilde{\mathbf{F}}(t; \tilde{V}_H, \alpha) = w_1 w_2 w_3 \mathbf{F}(t; \tilde{V}_H, \alpha) \tag{C.7}$$

BIBLIOGRAPHY

BIBLIOGRAPHY

Abramowitz, M., and I. A. Stegun (1972), *Handbook of Mathematical Functions: with Formulas, Graphs, and Mathematical Tables*, Dover Publications.

AISC 360-16 (2016), *Specification for Structural Steel Buildings*, American Institute of Steel Construction (AISC), Chicago, IL.

Almufti, I., and M. Willford (2013), *Resilience-based earthquake design initiative (REDi) for the next generation of buildings*.

Antoniou, S., and R. Pinho (2004), Advantages and limitations of adaptive and non-adaptive force-based pushover procedures, *J. Earthquake Eng.*, *8*(4), 497–522.

Applied Technology Council (ATC) (1996a), *Seismic design criteria for California bridges: provisional recommendations (Report no. ATC-32)*, Redwood City, CA.

Applied Technology Council (ATC) (1996b), *Seismic evaluation and retrofit of concrete buildings (Report no. ATC-40)*, Redwood City, CA.

ASCE 7-16 (2016), *Minimum design loads and associated criteria for buildings and other structures*, American Society of Civil Engineers (ASCE), Reston, VA.

Bartlett, F., R. Dexter, M. Graeser, J. Jelinek, B. Schmidt, and T. Galambos (2003), Updating standard shape material properties database for design and reliability, *Engineering Journal*, *40*, 2–14.

Bashor, R., T. Kijewski-Correa, and A. Kareem (2005a), On the wind-induced response of tall buildings: the effect of uncertainties in dynamic properties and human comfort thresholds, in *10th Americas Conference on Wind Engineering*, cD-ROM.

Bashor, R., T. Kijewski-Correa, and A. Kareem (2005b), On the wind-induced response of tall buildings: the effects of uncertainties in dynamic properties and human comfort thresholds, in *Proc. of the 10^{th} Americas Conference on Wind Engineering*.

Beck, A. T., I. A. Kougioumtzoglou, and K. R. M. dos Santos (2014), Optimal performance-based design of non-linear stochastic dynamical RC structures subject to stationary wind excitation, *Engineering Structures*, *78*, 145–153.

Bernardini, E., S. M. J. Spence, and A. Kareem (2013), A probabilistic approach for the full response estimation of tall buildings with 3D modes using the HFFB, *Structural Safety*, *44*, 91–101.

Bernardini, E., S. M. J. Spence, D.-K. Kwon, and A. Kareem (2015), Performance-based design of high-rise buildings for occupant comfort, *Journal of Structural Engineering*, *141*(10).

Billings, S. A. (2013), *Nonlinear system identification: NARMAX methods in the time, frequency, and spatio-temporal domains*, Wiley.

Billings, S. A., and H. Wei (2008), An adaptive orthogonal search algorithm for model subset selection and non-linear system identification, *International Journal of Control*, *81*(5), 714–724.

Bobby, S., S. M. J. Spence, E. Bernardini, and A. Kareem (2014), Performance-based topology optimization for wind-excited tall buildings: A framework, *Engineering Structures*, *74*, 242–255.

Bonowitz, D. (2011), *Resilience Criteria for Seismic Evaluation of Existing Buildings*, A 2008 Special Projects Initiative Report to Structural Engineers Association of Northern California (SEAONC).

Caracoglia, L. (2014), A stochastic model for examining along-wind loading uncertainty and intervention costs due to wind-induced damage on tall buildings, *Engineering Structures*, *78*, 121–132.

Casciaro, R., and G. Garcea (2002), An iterative method for shakedown analysis, *Computer Methods in Applied Mechanics and Engineering*, *191*, 5761–5792.

Casciaro, R., and G. Garcea (2006), Erratum to "An iterative method for shakedown analysis", *Computer Methods in Applied Mechanics and Engineering*, *196*, 714–715.

Ceradini, G. (1969), On shakedown of elastic-plastic solids under dynamic actions, *Giornale del Genio Civile*, *107*, 239–250.

Ceradini, G. (1980), Dynamic shakedown in elastic-plastic bodies, *Journal of the Engineering Mechanics Division*, *106*, 481–499.

Chen, D., and A. G. Davenport (2000), Vulnerability of tall buildings in typhoons, in *Advances in structural dynamics*, vol. 2, pp. 1455–1462.

Chen, X., and A. Kareem (2005), Proper orthogonal decomposition-based modeling, analysis, and simulation of dynamic wind load effects on structures, *Journal of Engineering Mechanics*, *131*(4), 325–339.

Chen, Z.-H., and Y.-Q. Ni (2011), On-board identification and control performance verification of an mr damper incorporated with structure, *Journal of Intelligent Material Systems and Structures*, *22*, 1551–1565.

Chuang, W.-C., and S. M. J. Spence (2017), A performance-based design framework for the integrated collapse and non-collapse assessment of wind excited buildings, *Engineering Structures*, *150*, 746–758.

Ciampoli, M., F. Petrini, and G. Augusti (2011a), Performance-Based Wind Engineering: Towards a general procedure, *Structural Safety*, *33*(6), 367–378.

Ciampoli, M., F. Petrini, and G. Augusti (2011b), Performance-based wind engineering: Towards a general procedure, *Structural Safety*, *33*(6), 367–378.

Clough, R. W., K. L. Benuska, , and E. L. Wilson (1965), Inelastic earthquake response of tall buildings, in *3rd World Conference on Earthquake Engineering*, Wellington, New Zealand.

Cook, R. D., et al. (2001), *Concepts and Applications of Finite Element Analysis*, Wiley.

Corradi, L., and G. Maier (1974), Dynamic non-shakedown theorem for elastic perfectly-plastic continua, *Journal of the Mechanics and Physics of Solids*, *22*, 401–413.

Cui, W., and L. Caracoglia (2015), Simulation and analysis of intervention costs due to wind-induced damage on tall buildings, *Engineering Structures*, *87*, 183–197.

Cui, W., and L. Caracoglia (2017), Exploring hurricane wind speed along us atlantic coast in warming climate and effects on predictions of structural damage and intervention costs, *Engineering Structures*, *122*, 209–225.

Deodatis, G. (1996), Simulation of ergodic multivariate stochastic processes, *Journal of Engineering Mechanics*, *122*(8), 778–787.

Diniz, S. M. C., and E. Simiu (2005), Probabilistic descriptions of wind effects and wind-load factors for database-assisted design, *Journal of Structural Engineering*, *131*(3), 507–516.

Diniz, S. M. C., F. Sadek, and E. Simiu (2004a), Wind speed estimation uncertainties: effects of climatological and micrometeorological parameters, *Probabilistic Engineering Mechanics*, *19*, 361–371.

Diniz, S. M. C., F. Sadek, and E. Simiu (2004b), Wind speed estimation uncertainties: Effects of climatological and micrometeorological parameters, *Probabilistic Engineering Mechanics*, *19*(4), 361–371.

D.Morris, M., and T. J. Mitchell (1995), Exploratory designs for computational experiments, *Journal of Statistical Planning and Inference*, *43*(3), 381–402.

Echard, B., N. Gayton, and M. Lemaire (2011), Ak-mcs: An active learning reliability method combining kriging and monte carlo simulation, *Structural Safety*, *33*(2), 145–154.

Ellingwood, B., J. G. MacGregor, T. V. Galambos, and C. A. Cornell (1982), Probability based load criteria: Load factors and load combinations, *Journal of the Structural Division*, *108*, 978–997.

Eman, H., H. J. Pradlwarter, and G. I. Schuëller (2000), A computational procedure for the implementation of equivalent linearization in finite element analysis, *Earthquake Engineering and Structural Dynamics*, *29*, 1–17.

Federal Emergency Management Agency (FEMA) (1996), *NEHRP Guidelines for the Seismic Rehabilitation of Buildings (FEMA Publication 273)*, Washington, DC.

Federal Emergency Management Agency (FEMA) (2012a), *Seismic performance assessment of buildings, Volume 1 - Methodology (FEMA Publication P-58-1)*, Washington, DC.

Federal Emergency Management Agency (FEMA) (2012b), *Seismic performance assessment of buildings, Volume 2 - Implementation (FEMA Publication P-58-2)*, Washington, DC.

Federal Emergency Management Agency (FEMA) (2012c), *Seismic performance assessment of buildings, Volume 3 - Supporting electronic materials and background documentation (FEMA Publication P-58-3)*, Washington, DC.

Feng, C., and X. Chen (2017), Crosswind response of tall buildings with nonlinear aerodynamic damping and hysteretic restoring force character, *Journal of Wind Engineering and Industrial Aerodynamics*, *167*, 62–74.

Feng, C., and X. Chen (2018), Inelastic responses of wind-excited tall buildings: Improved estimation and understanding by statistical linearization approaches, *Engineering Structures*, *159*, 141–154.

Feng, C., X. Chen, and D. Liang (2016), Inelastic crosswind responses of tall buildings with bilinear hysteretic restoring force characteristics, in *8th International Colloquium on Bluff Body Aerodynamics and Applications (BBAA VIII)*, pp. 1207–1214, Boston, Massachusetts, USA.

Filippou, F. C., and A. Issa (1988), Non linear analysis of reinforced concrete frames under cyclic load reversals, *Tech. rep.*, Earthquake Engineering Research Centre, University of California.

Forrester, A., A. Sobester, and A. Keane (2008), *Engineering Design via Surrogate Modelling: A Practical Guide*, John Wiley & Sons.

Gani, F., and F. Légeron (2011), Relationship between specified ductility and strength demand reduction for single degree-of-freedom systems under extreme wind events, *Journal of Wind Engineering and Industrial Aerodynamics*, *109*, 31–45.

Garcea, G., G. Armentano, S. Petrolo, and R. Casciaro (2005), Finite element shakedown analysis of two-dimensional structures, *International Journal for Numerical Methods in Engineering*, *63*, 1174–1202.

Giberson, M. F. (1967), *The response of nonlinear multi-story structures subjected to earthquake excitation. Dissertation (Ph.D.)*, California Institute of Technology.

Healey, J., S. Wu, and M. Murga (1980), *Structural building response review. NUREG/CR1423, vol. I*, US Nuclear Regulatory Commission, Washington, DC.

Hilburg, J. (2018), Seattle's second tallest tower rises on steel plates, without rebar, *The Architect's Newspaper*.

Hong, H. P. (2004), Accumulation of wind induced damage on bilinear sdof systems, *Wind and Structures*, *7*, 145–158.

Huang, M. F., Q. Li, C. M. Chan, W. J. Lou, and K. C. S. Kwok (2015), Performance based design optimization of tall concrete framed structures subject to wind excitations, *Journal of Wind Engineering and Industrial Aerodynamics*, *139*, 70–81.

Hughes, T. J. R. (2000), *The Finite Element Method: Linear Static and Dynamic Finite Element Analysis*, Dover Publications, Mineola, New York.

Jensen, H. A., and A. A. Catalan (2007), On the effects of non-linear elements in the reliability based optimal design of stochastic dynamical systems, *International Journal of Non-Linear Mechanics*, *42*, 802–816.

Judd, J., and F. Charney (2015), Inelastic behavior and collapse risk for buildings subjected to wind loads, in *Structures Congress 2015*, edited by N. Ingraffea and M. Libby, pp. 2483–2496, April 23-25, Portland, Oregon, USA.

Koiter, W. T. (1960), *Shakedown of elastic-plastic structures*, North-Holland, Amsterdam.

Krawinkler, H., and G. D. P. K. Seneviratna (1998), Pros and cons of a pushover analysis of seismic performance evaluation, *Engineering Structures*, *20*(4-6), 452–464.

Lagarias, J. C., J. A. Reeds, M. H. Wright, and P. E. Wright (1998), Convergence properties of the nelder-mead simplex method in low dimensions, *SIAM Journal of Optimization*, *9*(1), 112–147.

Larsen, R., R. Klemencic, J. Hooper, and K. Aswegan (2016), Engineering objectives for performance-based wind design, in *Proceedings of the Geotechnical and Structural Engineering Congress*, Phoenix, AZ, USA.

Li, Y., and A. Kareem (1991), Simulation of multivariate nonstationary random processes by FFT, *Journal of Engineering Mechanics*, *117*(5), 1037–1058.

Li, Y., and A. Kareem (1993), Simulation of multivariate random processes: Hybrid DFT and digital filtering approach, *Journal of Engineering Mechanics*, *119*(5), 1078–1098.

Li, Y., and A. Kareem (1997), Simulation of multivariate nonstationary random processes: Hybrid DFT and digital filting approach, *Journal of Engineering Mechanics*, *123*(12), 1302?1310.

Mai, C. V. (2016), Polynomial chaos expansions for uncertain dynamical systems – applications in earthquake engineering, Ph.D. thesis, ETH Zurich, Switzerland.

Mai, C. V., M. D. Spiridonakos, E. N. Chatzi, and B. Sudret (2016), Surrogate modelling for stochastic dynamical systems by combining NARX models and polynomial chaos expansions, *International Journal for Uncertainty Quantification*, *6*, 313–339.

Malena, M., and R. Casciaro (2008), Finite element shakedown analysis of reinforced concrete 3D frames, *Computers and Structures*, *86*, 1176–1188.

Minciarelli, F., M. Gioffrè, M. Grigoriu, and E. Simiu (2001), Estimates of extreme wind effects and wind load factors: Influence of knowledge uncertainties, *Probabilistic Engineering Mechanics*, *16*, 331–340.

Mitseas, I. P., I. A. Kougioumtzoglou, and M. Beer (2016), An approximate stochastic dynamics approach for nonlinear structural system performance-based multi-objective optimum design, *Structural Safety*, *60*, 67–76.

Moehle, J., and G. G. Deierlein (2004), A framework methodology for performance-based earthquake engineering, in *13th World Conference on Earthquake Engineering*, Vancouver.

Moustapha, M., B. Sudret, J.-M. Bourinet, and B. Guillaume (2016), Quantile-based optimization under uncertainties using adaptive kriging surrogate models, *Structural and Multidisciplinary Optimization*, *54*(6), 1403–1421.

Neuenhofer, A., and F. C. Filippou (1997), Evaluation of nonlinear frame finite-element models, *Journal of Structural Engineering*, *123*(7), 958–966.

Nowak, A. S., and K. R. Collins (2013), *Reliability of Structures*, CRC Press.

Ohkuma, T., T. Kurita, and M. Ninomiya (1998), Response estimation based on energy balance for elasto-plastic vibration of tall building in across-wind direction, in *Proceedings of the 7th International Conference on Structural Safety and Reliability (ICOSSAR 97)*, pp. 1379–1386, Kyoto, Japan.

Ouyang, Z., and S. M. Spence (2019), A performance-based wind engineering framework for envelope systems of engineered buildings subject to directional wind and rain hazards, *Journal of Structural Engineering*, p. Submitted.

Peng, L., G. Huang, X. Chen, and A. Kareem (2017), Simulation of multivariate nonstationary random processes: Hybrid stochastic wave and proper orthogonal decomposition approach, *Journal of Engineering Mechanics*, *143*(9).

Petrini, F., and M. Ciampoli (2012), Performance-based wind design of tall buildings, *Structure and Infrastructure Engineering*, *8*(10), 954–966.

Polizzotto, C. (1984), Dynamic shakedown by modal analysis, *Meccanica*, *19*, 133–144.

Polizzotto, C., G. Borino, S. Caddemi, and P. Fuschi (1993), Theorems of restricted dynamic shakedown, *International Journal of Mechanical Sciences*, *35*(9), 787–801.

Pradlwarter, H. J., G. I. Schuëller, and C. A. Schenk (2003), A computational procedure to estimate the stochastic dynamic response of large non-linear fe-models, *Computer Methods in Applied Mechanics and Engineering*, *192*, 777–801.

Riks, E. (1979), An incremental approach to the solution of snapping and buckling problems, *International Journal of Solids and Structures*, *15*, 529–551.

Sadek, F., S. Diniz, M. Kasperski, M. Gioffrè, and E. Simiu (2004), Sampling errors in the estimation of peak wind-induced internal forces in low-rise structures, *Journal of Engineering Mechanics*, *130*(2), 235–239.

Schenk, C. A., H. J. Pradlwarter, and G. I. Schuëller (2004), On the dynamic stochastic response of fe models, *Probabilistic Engineering Mechanics*, *19*, 161–170.

Seo, D. W., and L. Caracoglia (2013), Estimating life-cycle monetary losses due to wind hazards: Fragility analysis of long-span bridges, *Engineering Structures*, *56*, 593–1606.

Spacone, E., and S. El-Tawil (2004), Nonlinear analysis of steel-concrete composite structures: State of the art, *Journal of Structural Engineering*, *130*(2), 159–168.

Spacone, E., V. Ciampi, and F. C. Filippou (1996), Mixed formulation of nonlinear beam finite element, *Computers and Structures*, *58*(1), 71–83.

Spence, S. M. J., and M. Gioffrè (2012), Large scale reliability-based design optimization of wind excited tall buildings, *Probabilistic Engineering Mechanics*, *28*, 206–215.

Spence, S. M. J., and A. Kareem (2014a), Tall buildings and damping: a concept-based data-driven model, *Journal of Structural Engineering*, *140*(5), 04014,005–1–15.

Spence, S. M. J., and A. Kareem (2014b), Performance-based design and optimization of uncertain wind-excited dynamic building systems, *Engineering Structures*, *78*, 133–144.

Spence, S. M. J., E. Bernardini, Y. Guo, A. Kareem, and M. Gioffrè (2014), Natural frequency coalescing and amplitude dependent damping in the wind-excited response of tall buildings, *Probabilistic Engineering Mechanics*, *35*, 108–117.

Spiridonakos, M. D., and E. N. Chatzi (2015), Metamodeling of dynamic nonlinear structural systems through polynomial chaos narx models, *Computers and Structures*, *157*, 99–113.

Structural Engineers Association of California (SEAOC) (1996), *Vision 2000, conceptual framework for performance-based seismic design. Recommended Lateral Force Requirements and Commentary*, Sacramento, CA.

Symans, M. D., and M. C. Constantinou (1998), Passive fluid viscous damping systems for seismic energy dissipation, *Journal of Earthquake Technology*, *35*(4), 185–206.

Tabbuso, P., S. M. J. Spence, L. Palizzolo, A. Pirrotta, and A. Kareem (2016), An efficient framework for the elasto-plastic reliability assessment of uncertain wind excited systems, *Structural Safety*, *58*, 69–78.

Tamura, Y., H. Yasui, and H. Marukawa (2001), Non-elastic responses of tall steel buildings subjected to across-wind forces, *Wind and Structures*, *4*(2), 147–162.

Tokyo polytechnic university (TPU) Wind Pressure Database (2008), http://wind.arch.t-kougei.ac.jp/system/eng/contents/code/tpu.

Tsujita, O., Y. Hayabe, and T. Ohkuma (1998), A study on wind-induced response for inelastic structure, in *Proceedings of the 7th International Conference on Structural Safety and Reliability (ICOSSAR 97)*, pp. 1359–1366, Kyoto, Japan.

Valdebenito, M. A., and G. I. Schuëller (2011), Efficient strategies for reliability-based optimization involving non-linear, dynamical structures, *Computers and Structures*, *89*, 1797–1811.

Vamvatsikos, D., and C. A. Cornell (2002), Incremental dynamic analysis, *Earthquake Engineering and Structural Dynamics*, *31*(3), 491–514.

Vickery, B. J. (1970), Wind action on simple yielding structures, *Journal of Engineering Mechanics Division*, *96*, 107–120.

Wei, H. L., and S. A. Billings (2008), Model structure selection using an integrated forward orthogonal search algorithm assisted by squared correlation and mutual information, *International Journal of Modelling, Identification and Control*, *3*(4), 341–356.

Whittaker, A. S., R. Hamburger, and M. Mahoney (2003), Performance based engineering of buildings and infrastructure for extreme events, in *Proceedings of the AISC-SINY Symposium on Resisting Blast and Progressive Collapse*, American Institute of Steel Construction, New York, NY.

Wight, J. K. (2015), *Reinforced Concrete: Mechanics and Design (7th ed.)*, Pearson.

Wilson, E. L. (2002), *Three dimensional static and dynamic analysis of structures: A physical approach with emphasis on earthquake engineering*, Computers and Structures, Inc., Berkeley, California, USA.

Wyatt, T. A., and H. I. May (1971), The ultimate load behavior of structures under wind loading, in *Proceedings of the 3rd International Conference on Wind Effects on Buildings and Structures*, pp. 501–510, Tokyo, Japan.

Yang, T. Y., J. Moehle, B. Stojadinovic, and A. Der Kiureghian (2009), Seismic performance evaluation of facilities: methodology and implementation, *Journal of Structural Engineering*, *135*(10), 1146–1154.

Zhang, H., B. R.Ellingwood, and K. J. Rasmussen (2014), System reliabilities in steel structural frame design by inelastic analysis, *Engineering Structures*, *81*, 341–348.